



Max-Planck Institut für Kolloid- und Grenzflächenforschung

COVALENT ANODE MATERIALS FOR HIGH-ENERGY SODIUM-ION BATTERIES

Dissertation

zur Erlangung des akademischen Grades

"doctor rerum naturalium"

(Dr. rer. nat.)

in der Wissenschaftsdisziplin "Materialwissenschaft"

eingereicht an der Mathematisch-Naturwissenschaftlichen Fakultät

der Universität Potsdam

von

Enis Oğuzhan Eren

Geboren am 14.03.1990 in Altındağ

Potsdam, 2023

Unless otherwise indicated, this work is licensed under a Creative Commons License Attribution 4.0 International.

This does not apply to quoted content and works based on other permissions.

To view a copy of this licence visit:

<https://creativecommons.org/licenses/by/4.0>

Hauptbetreuer	Prof. Dr. Dr. h.c. Markus Antonietti
Zweitbetreuer	Prof. Dr. Yan Lu
Mentorin	Dr. Paolo Giusto

Gutachter/innen	Prof. Dr. Dr. h.c. Markus Antonietti
	Prof. Dr. Yan Lu
	Prof. Dr. Martin Oschatz

Published online on the

Publication Server of the University of Potsdam:

<https://doi.org/10.25932/publishup-62258>

<https://nbn-resolving.org/urn:nbn:de:kobv:517-opus4-622585>

To the Universe

ACKNOWLEDGMENT

First and foremost, I would like to convey my sincere appreciation to Prof. Dr. Dr. h.c. Markus Antonietti for allowing me to pursue my Ph.D. under his supervision at one of the world's leading institutes. His guidance and expertise have been invaluable in the success of this thesis. I would also like to extend my appreciation to Prof. Dr. Yan Lu, my second supervisor.

Dr. Paolo Giusto deserves special thanks for his continuous encouragement and mentorship, which empowered me to explore new ideas and push the boundaries of my knowledge. His insightful ideas and constructive feedback have significantly influenced the direction and methodology of this study.

I am deeply grateful to my research group, "2D-Covalent Thin Films for Energy Storage," for their collaborative and stimulating environment, which has significantly impacted my research. I would like to express my thanks, especially to Dr. Evgeny Senokos "COF," Dr. Zihan Song "Maestro," Elif Begüm Yılmaz "Kumbi," Tim Horner, and Irina Shekova for their unwavering support.

Furthermore, I would like to acknowledge Dr. Cansu Esen, Dr. Ernesto Scoppola, Dr. Baris Kumru, Dr. Majd-Al Naji, Dr. Nadezda V. Tarakina, Dr. Hannes Zschiesche, Dr. Iver Lauer mann, Dr. Daniel Cruz, and Bolortuya Badamdorj who participated in the part of experimental results presented in this work. I am also grateful to all technicians for helping me with part of the materials' characterizations.

Special recognition goes to TOMBEE for enlightening me on how music drives motivation in science.

Lastly, I would like to extend my sincere appreciation to my family, starting from my dear spouse, Ayse Altunbas Eren; my brother, Meric Eren; my father and mother, Mustafa Arif Eren & Ergül Eren; and as well as my friend, Ömer Burak Akgün, and many others, for their support, patience, and encouragement throughout this journey.

CONTENTS

LIST OF FIGURES	IX
LIST OF TABLES.....	XI
MOTIVATION	1
OUTLINE.....	3
CHAPTER 1. INTRODUCTION	5
1.1. ELECTROCHEMICAL ENERGY STORAGE.....	7
1.2. ALKALI-ION BATTERIES	9
1.2.1. COMMERCIALIZATION OF SIBS	11
1.2.2. OPERATING PRINCIPLE OF ALKALI-ION BATTERIES.....	13
1.2.3. COMPONENTS OF A BATTERY CELL	14
1.3. BACKGROUND ON HARD CARBON MATERIALS	25
1.3.1. SODIUM STORAGE IN HARD CARBONS	27
1.3.2. STRATEGIES FOR ENHANCING THE ELECTROCHEMICAL PERFORMANCE OF ANODE MATERIALS IN SIBS	29
BIGLIOGRAPHY FOR MOTIVATION, OUTLINE, AND CHAPTER 1	33
CHAPTER 2. CONFORMAL CARBON NITRIDE THIN FILM AS AN ARTIFICIAL SEI ENHANCING SODIUM STORAGE.....	41
2.1. CNS: FUNDAMENTALS AND APPLICATIONS.....	42
2.1.1. CHEMICAL VAPOR DEPOSITION	44
2.2. PREPARATION OF CARBON ELECTRODE AND CN FILM	44
2.3. RESULTS AND DISCUSSION	45
2.3.1. PHYSICO-CHEMICAL CHARACTERIZATIONS.....	45
2.3.2. SODIUM STORAGE BEHAVIOR OF MATERIALS.....	52
2.4. CONCLUSIONS.....	59
BIGLIOGRAPHY FOR CHAPTER 2.....	60
CHAPTER 3. SULFUR-RICH CARBON AS A HIGH-PERFORMING ANODE MATERIAL	65
3.1. SULFUR HETEROATOM EFFECT.....	66
3.2. PREPARATION OF SULFUR-CARBON.....	67
3.3. RESULTS AND DISCUSSION	68
3.3.1. PHYSICO-CHEMICAL CHARACTERIZATIONS.....	68

3.3.2.	SODIUM STORAGE BEHAVIOR OF MATERIALS	76
3.3.3.	BOOSTING ELECTROCHEMICAL STORAGE BY SODIUM PLATING AND STRIPPING	82
3.3.4.	ELUCIDATING THE PORE-FILLING MECHANISM BY IN-OPERANDO SAXS	84
3.4.	CONCLUSIONS	89
	BIGLIOGRAPHY FOR CHAPTER 3	90
CHAPTER 4. HIGH-CAPACITY SUSTAINABLE HARD CARBON FOR SIBs		95
4.1.	PARAMETERS TO IMPROVE THE ELECTROCHEMICAL PERFORMANCE	96
4.2.	THE EFFECT OF PRECURSORS ON STRUCTURE	98
4.3.	PRODUCTION OF HMF	100
4.4.	PREPARATION OF HARD CARBON DERIVED FROM HMF	101
4.5.	RESULTS AND DISCUSSION	102
4.5.1.	PHYSICO-CHEMICAL CHARACTERIZATIONS	102
4.5.2.	SODIUM STORAGE BEHAVIOR OF THE MATERIAL	104
4.6.	CONCLUSIONS	108
	BIGLIOGRAPHY FOR CHAPTER 4	109
CHAPTER 5. SUMMARY AND OUTLOOK		111
APPENDICES.....		115
A1.	ABBREVIATIONS AND VARIABLES	116
A2.	SUPPLEMENTARY INFORMATION FOR CHAPTER 2	119
A3.	SUPPLEMENTARY INFORMATION FOR CHAPTER 3	133
A4.	SUPPLEMENTARY INFORMATION FOR CHAPTER 4	147
	LIST OF PUBLICATIONS.....	151
	DECLARATION	153

LIST OF FIGURES

FIGURE 1.1. COMPARATIVE ANALYSIS OF ENERGY STORAGE SYSTEMS	6
FIGURE 1.2. COMMERCIAL EXAMPLES OF SIBs	11
FIGURE 1.3. DRIVING RANGE ANALYSIS IN RELATION TO THE BATTERY PACK ENERGY DENSITIES.....	12
FIGURE 1.4. OPERATING PRINCIPLE OF A TYPICAL SIB.....	14
FIGURE 1.5. CURRENT CATHODE MATERIALS FOR SIBs REPRESENTED IN A RAGONE PLOT.....	17
FIGURE 1.6. CURRENT ANODE MATERIALS FOR SIBs REPRESENTED IN A RAGONE PLOT.....	19
FIGURE 1.7. TEM AND SEM IMAGES OF A TYPICAL NON-GRAPHITIC CARBON.....	26
FIGURE 1.8. X-RAY SCATTERING PROFILE OF HARD CARBON AND ILLUSTRATION OF SURFACE- AND DIFFUSION-CONTROLLED STORAGE REGIONS	27
FIGURE 1.9. THE EFFECT OF ARTIFICIAL SEI ON METAL PLATING AND STRIPPING PROCESSES.....	31
FIGURE 2.1. SYNTHETIC STEPS FOR CN FROM MELAMINE.....	43
FIGURE 2.2. SCHEME FOR THE PREPARATION OF LSC AND LSC/CN.....	45
FIGURE 2.3. SEM, XRD, AND RAMAN OF THE LSC.....	46
FIGURE 2.4. THICKNESS OF THE CN LAYER FROM ADF-STEM AND ELECTRONIC STATES FROM VBEELS	48
FIGURE 2.5. SCHEMATIC DIAGRAM DEPICTING THE VARIATION IN CN LAYER	49
FIGURE 2.6. PSD FROM GAS PHYSISORPTION AND XPS SPECTRA OF MATERIALS	51
FIGURE 2.7. NYQUIST PLOTS OF THE MATERIALS	52
FIGURE 2.8. INITIAL AND 10 TH GCD CYCLES OF THE MATERIALS	53
FIGURE 2.9. RATE PERFORMANCE OF THE MATERIALS	54
FIGURE 2.10. SODIUM STORAGE MECHANISM VIA CV.....	55
FIGURE 2.11. SODIUM STORAGE MECHANISM VIA GITT.....	56
FIGURE 2.12. CYCLING STABILITY OF THE MATERIALS	57
FIGURE 2.13. ILLUSTRATION OF HOW SODIUM IS ACCUMULATED AT THE INTERFACE.....	58
FIGURE 3.1. SYNTHETIC STEPS FOR THE MATERIALS.....	67
FIGURE 3.2. FTIR SPECTRUM OF OLIGO-EDOT.....	68
FIGURE 3.3. SEM IMAGES OF THE MATERIALS	69
FIGURE 3.4. EDX MAP, HRTEM IMAGE, AND FFT PROFILE	70
FIGURE 3.5. RAW VS. NORMALIZED INTENSITIES IN SAXS	71
FIGURE 3.6. XRD PATTERNS AND RAMAN SPECTRA OF THE MATERIALS	72
FIGURE 3.7. GAS PHYSISORPTION AND PSD OF THE MATERIALS	74
FIGURE 3.8. XPS AND EELS SPECTRA OF THE MATERIALS	75
FIGURE 3.9. INITIAL AND 10 TH GCD CYCLE OF THE MATERIALS	76
FIGURE 3.10. SODIUM STORAGE MECHANISM VIA CV AND GITT.....	78
FIGURE 3.11. SODIUM STORAGE MECHANISM, RATE PERFORMANCE, AND CYCLING STABILITY	79
FIGURE 3.12. COMPARISON OF SODIATION CURVES AT DIFFERENT RATES.....	80

FIGURE 3.13. XRD AND HALF-CELL PERFORMANCE OF NVP CATHODE, AND FULL-CELL TRIAL	81
FIGURE 3.14. OVERPOTENTIAL SODIUM DEPOSITION PERFORMANCE.....	82
FIGURE 3.15. SEM AFTER SODIUM PLATING AND STRIPPING	83
FIGURE 3.16. IN-OPERANDO SAXS SETUP.....	85
FIGURE 3.17. PORE-FILLING MECHANISM VIA SAXS.....	86
FIGURE 3.18. QUALITY OF THE FITTINGS FROM IN-OPERANDO SAXS.....	88
FIGURE 4.1. STRUCTURAL COMPARISON OF GRAPHITE, SOFT, AND HARD CARBONS.....	97
FIGURE 4.2. DIAGRAM SHOWING CARBONIZATION PROCESS OF GRAPHITE, SOFT, AND HARD CARBONS ...	99
FIGURE 4.3. SYNTHESIS OF HMF FROM BIOMASSES IN DIFFERENT PATHWAYS.....	100
FIGURE 4.4. RESULTS FROM MAIN PHYSICO-CHEMICAL CHARACTERIZATIONS	103
FIGURE 4.5. OVERALL SODIUM STORAGE PERFORMANCE WITH RATE AND CYCLING PERFORMANCE	106
FIGURE 4.6. COMPARISON OF HMF CARBON WITH COMMERCIAL HC, GLUCOSE- AND FRUCTOSE-DERIVED CARBON.	107
FIGURE 4.7. SODIUM STORAGE MECHANISM VIA CV AND GITT.....	108
FIGURE A2.1. PHYSICAL APPEARANCE OF LSC CARBON AND AFTER CN DEPOSITION	122
FIGURE A2.2. SEM IMAGES OF THICK AND THIN CN COATINGS	123
FIGURE A2.3. XRD PATTERNS OF THE BULK CN, AND LSC WITH CN	124
FIGURE A2.5. TGA PROFILES IN SYNTHETIC AIR AND NITROGEN.....	126
FIGURE A2.6. NITROGEN PHYSISORPTION ISOTHERMS OF THE MATERIALS.....	127
FIGURE A2.7. CO ₂ PHYSISORPTION ISOTHERMS OF THE MATERIALS	128
FIGURE A2.8. XPS OF THE LSC.....	129
FIGURE A2.9. FTIR OF THE MATERIALS	130
FIGURE A2.10. FIRST AND 10 TH GCD CURVES OF THE UNTREATED LSC AND BULK CN.....	131
FIGURE A2.11. LINEAR FIT TO SIMPLIFY WEPPNER AND HUGGINS MODEL	132
FIGURE A3.1. TGA-MS PROFILE OF OLIGO-EDOT.....	136
FIGURE A3.2. ELEMENTAL MAPPINGS OF THE MATERIALS	137
FIGURE A3.3. HRTEM IMAGES OF THE MATERIALS	138
FIGURE A3.4. HRTEM IMAGE, IMAGE INTENSITY PERIODICITY, AND FFT OF SC-800	139
FIGURE A3.5. HRTEM IMAGE, IMAGE INTENSITY PERIODICITY, AND FFT OF SC-900	139
FIGURE A3.6. PSD FROM NITROGEN PHYSISORPTION	140
FIGURE A3.7. O1s CORE-LEVEL XPS OF THE MATERIALS	141
FIGURE A3.8. LOW-LOSS EELS OF THE MATERIALS.....	142
FIGURE A3.9. CV CURVES OF THE MATERIALS	143
FIGURE A3.10. GITT CURVES AND LINEAR FITS OF THE MATERIALS	144
FIGURE A3.11. NYQUIST PLOTS AND RELATIVE RANGLES CIRCUIT MODELS OF THE MATERIALS.....	145
FIGURE A3.12. REPRODUCIBILITY OF THE SCATTERING PROFILES FROM IN-OPERANDO SAXS	146
FIGURE A4.1. SAXS PROFILES OF THE HMF-CARBON AND SULFUR-CARBON	149
FIGURE A4.1. EIS PROFILE OF THE HMF IN DIFFERENT ELECTROLYTES.....	150

LIST OF TABLES

TABLE 2.1. ELEMENTAL COMPOSITIONS FROM EDX ANALYSIS	47
TABLE 2.2. INTERNAL AND CHARGE TRANSFER RESISTIVITIES FROM EIS	52
TABLE 3.2. ELEMENTAL COMPOSITIONS FROM EA AND EDX.....	69
TABLE 3.3. RATIO OF DECONVOLUTED PEAK AREAS FROM S2P AND C1s REGIONS OF THE XPS.....	75
TABLE A3.1. INTERNAL, CHARGE, AND SEI-RELATED RESISTIVITIES OF THE MATERIALS FROM EIS	145

MOTIVATION

The evolutionist nature of humankind has always been an instinctual motivation for seeking a plausible energy source. Recently, the quest for energy, which further emerged in the 20th century, arising from scientific, technological, and industrial advancement, led to a situation affecting every aspect of our lives. The global population has grown significantly throughout the past century, leading to a considerable surge in total energy requirements.^[1] In addition to population growth, political tensions, and globalization further fueled the demand for energy.^[2] Major fossil fuels, including coal, oil, and natural gas, have been the primary sources of supply in order to fulfill this expanding demand. This contributed to an increase in polluting agents released into the atmosphere, causing climate change, also recognized as the global climate crisis.^[3] The concentration of atmospheric greenhouse gases has reached an all-time high, surpassing the values of the past 800,000 years.^[4] The abnormal rise in average temperatures is expected to cause several problems, including the potential extinction of many living organisms. Emergency plans, such as the Kyoto Protocol and its follow-ups, i.e., the Doha Amendment, are currently under action to mitigate the effects of the climate crisis.^[5] Nevertheless, in order to achieve the pre-determined objectives, it is compulsory to speed up the action and adopt more sustainable solutions. Notably, among these initiatives, boosting the proportion of renewables in the overall energy mix occupies a key position.^[6]

Given all the above, a rapid transition to renewable energy sources has already started. However, the efficient utilization of renewable energy resources is as important as putting them into service. Electrochemical energy storage systems, primarily batteries, are commonly recognized as one of the most efficient ways to store energy among the options available.^[7] Batteries serve as a source of electrical power and comprise multiple components designed for chemical energy conversion and storage. Upon the presence of an electric load, a redox reaction takes place, storing the electrical energy and releasing it when needed.

Batteries have become one of the essential components of human life since they were introduced and have been used in many fields, from simple to critical applications.^[8] However, technology and green energy transformation have increased the prominence of

MOTIVATION

batteries several times and made them one of the priority investment areas in the 2020s.^[9] For instance, due to the expanding market, global demand is estimated to increase several times over by 2030.^[10] This significant increase in demand is driving a surge in investment, leading to the planning and construction of numerous Gigafactories worldwide.^[11] The majority of this demand is primarily attributable to portable applications, particularly for passenger transportation. Additionally, batteries are recognized as the principal component for grid energy storage, which is crucial in facilitating the integration of renewable energy sources.^[7b] A closer look shows that a larger portion of this demand is covered by lithium-ion batteries (LIBs).^[12] Due to their outstanding electrochemical performance in both stationary and portable applications, LIBs are widely considered the current industry standard for rechargeable battery systems.^[12-13] Nonetheless, concerns regarding the extraction, availability, and geopolitical implications of lithium and associated materials raise doubts about the ability of LIBs to meet the market demand in near future.^[14] The search for substitute rechargeable batteries goes on unabatedly.

Sodium-ion batteries (SIBs) are seen to be a potential substitute for LIBs due to their similar operating principle and lower manufacturing cost.^[15] Sodium is far more abundant and evenly distributed in the crust, making it easier and less expensive to isolate than lithium.^[15-16] However, because of the mysterious nature of its underlying components, SIBs are not yet sufficiently advanced to take the place of LIBs. While lithium and sodium have several similarities, as conformed by their location in the periodic table, their distinct physicochemical properties necessitate fundamental changes to develop efficient active materials for SIBs. Specifically, sodium exhibits a more metallic character and a larger ionic radius, which hinders the formation of a stable sodium-carbon intercalation compound on the anode side, resulting in a different ion storage mechanism utilized in LIBs.^[17] Innovations in synthetic methods, post-treatments, and interface engineering clearly demonstrate the significance of developing high-performance carbonaceous anode materials for SIBs.^[18] This dissertation aims to give a systematic approach to fabricating efficient, high-performance, and sustainable carbonaceous anode materials for SIBs. This will involve a comprehensive investigation of different chemical environments and post-modification techniques as well.

OUTLINE

As the statement made by Max Planck, “*Insight must precede application,*” points out the necessity of fundamental research and its potential impact on innovations. With this quote as the primary motivation, **Chapter 1** aims to provide a comprehensive and informative introduction to the topic, including a general overview and setting the ground for more specific discussions. The chapter discusses a wide range of subjects, beginning with a global overview of energy storage systems and moving on to development methods for high-performing carbonaceous anode materials for SIBs.

Chapter 2 focuses on the crucial role of post-synthetic methods in designing interfaces. In this chapter, a conformal carbon nitride (CN) coating with a thickness lower than 100 nm is deposited on a carbon electrode, creating an artificial passivation layer and a heterojunction effect that enhances the electrode’s electrochemical performances, i.e., initial Coulombic efficiency, rate performance, and total capacity. The mesoporous carbon material is synthesized from the sodium lignosulfonate precursor, which is a byproduct of the paper/pulp industry. Thin CN layers are eventually deposited on the substrate using the chemical vapor deposition (CVD) technique, which enables precise control of the film thickness. Conclusively, this electroactive interface is found crucial in achieving the desired performance with a minimum change in the materials’ structure.

Along the lines of sulfur-containing carbons, the purpose of **Chapter 3** is to present an easy and effective process for preparing sulfur-rich carbon as a high-performing anode material tailored for SIBs. The technique employs a thiophene-containing precursor, namely oligo-3,4-ethylenedioxythiophene (oligo-EDOT), to convey a fundamental understanding of the sulfur heteroatom effect on the electrochemical sodium storage mechanism.^[17a, 19] By optimizing the condensation temperature, the materials’ nanostructure undergoes a significant transformation that improves the electrochemical performance. Moreover, the method yields reversible overpotential sodium plating and stripping that further increases the specific capacity, which is attributed to the controlled nucleation of sodium in confined pore spaces. This increases the electrode’s energy density and ensures safe operation under overload conditions that may occur in real

OUTLINE

applications. To further support the pore-filling sodium storage mechanism, a technique for *in-operando* small-angle X-ray scattering (SAXS) characterization is presented, providing valuable insights into how the electron density difference changes during the electrochemical processes by demonstrating the interaction between micropores and the sodium ions.

Two key methods for introducing high-performing and effective carbonaceous anode materials for SIBs have been covered in earlier chapters. One of these methods comprises introducing an artificial passivation layer to the carbon electrode to improve its performance, while the other involves investigating the impact of sulfur heteroatoms. The method for making a high-performance anode material from sustainable sources for electrochemical sodium storage is presented in **Chapter 4**. This chapter focuses on the development of high-capacity hard carbon with a specific capacity of more than 370 mAh g⁻¹. The hard carbon is made of 5-hydroxymethyl furfural (HMF), a saccharide dehydration product performing admirably at low and high current densities. Additionally, extensive electrochemical and physicochemical characterizations are used to understand the sodium storage mechanism in relation to the chemical environment. The material is found to be well-stable and promising for potential implementations.

CHAPTER 1. INTRODUCTION

Concept of energy storage – Energy storage is a process of balancing energy demand and energy supply by allowing energy to be consumed at a different time than when it is produced. Energy is available in several forms, including radiation, electrical, gravitational, heat, and kinetic. The critical function of energy storage is to interconnect energy from its hard-to-store form to more convenient and efficient forms. The most commonly available energy storage methods are thermal, mechanical, and electrical.^[20] The commonly employed methods for storage include chemical storage, such as batteries, and mechanical means, such as pumped hydro storage. It is important to note that diverse energy systems have different requirements for their own to operate wisely. The main reason is that the energy demand and supply are typically asynchronous, making it necessary to have a buffer solution to minimize losses.^[21]

Renewable energy sources have gained significant attraction due to the decrease in operating and manufacturing costs.^[22] Additionally, the need to reduce carbon emissions in the industrial sectors has further highlighted the importance of green energy. To ensure a continuous and uninterrupted power supply, reliable energy storage technologies are necessary, considering the non-constant nature of renewable energy sources.^[23] Energy storage systems typically comprise three phases: an energy uptake phase, a storage phase, and an energy release phase. Primary storage systems are those that can only undergo a single cycle of energy storage, while secondary storage systems can undergo multiple operating cycles.^[24] Examples of primary storage systems include fossil fuels and single-use batteries, while rechargeable batteries are an example of secondary storage systems. Capacitors are examples of pure electrical energy storage devices that use just electrical storage, commonly referred to as electric-double layer systems. In contrast, batteries encompass the conversion of energy through chemical reactions and use a combination of electrical and chemical storage mechanisms. Conversely, pure chemical energy storage systems entail the storage of energy within chemical species or materials. Fossil fuels are an example of chemical energy sources. Mechanical energy storage systems include potential energy, such as storage reservoirs, and kinetic energy, such as flywheels. Thermal energy storage systems rely on the principle of heat dissipation.^[20b] To accurately

describe these systems, it is necessary to understand the terminology related to power (Watt), energy (Watt hour), and their quantitative derivations, such as specific and volumetric power/energy. A system with a high energy capacity may not be well-suited for a particular application due to its large size, which decreases its energy density. As previously noted, each energy storage system is unique in terms of its application field and usability.^[24] Due to space constraints, high power and energy densities are vital in portable applications, while stationary applications might sometimes tolerate lower energy densities.^[25] For instance, regarding electrochemical energy storage in passenger vehicles, strict requirements mandate the selection of cutting-edge battery systems owing to their varying energy densities.^[26] In passenger vehicles, it is necessary to have high-performing packs, whereas moderate ones can be used on large public transportation systems.^[27] **Figure 1.1** displays the typical energy storage systems according to their rated power versus discharge time.^[28] With regard to the flexibility and scalability of energy systems, batteries hold a significant advantage for having excellent energy and power densities. Considering the future volume of the renewables in the energy mix, batteries are expected to be the essential constituents in the grid energy storage systems.^[29]

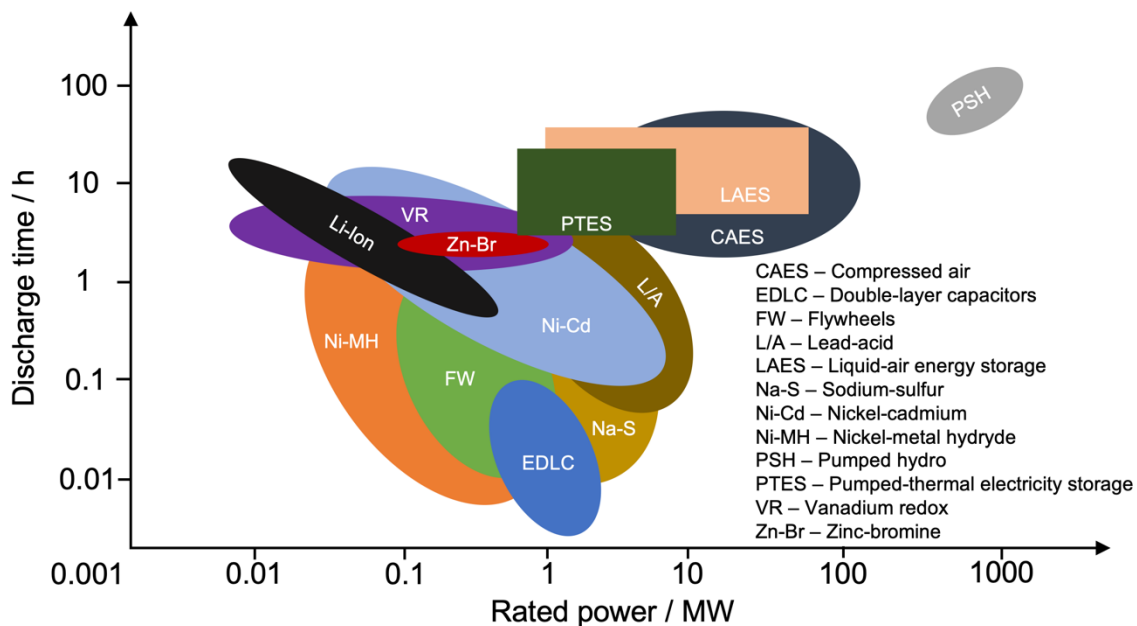


Figure 1.1. Energy storage systems intended for commercial applications based on their rated power and discharge time, adapted from Georgiou et al., *Applied Energy*, **2018**, 226, 1119-1133.

1.1. Electrochemical energy storage

Electrochemical energy storage systems are known as a favorable choice of energy storage thanks to their applicability and notable efficiency in energy conversion. With a variety of available sizes, these systems can be used in a diverse range of applications, from compact, portable electronic devices to large-scale electrical grids. In secondary systems where the process is reversible, electrochemical energy storage involves the conversion of chemical energy into electrical energy and the opposite. To better understand the driving forces behind this process, consider a simplified example of a thermodynamic system in which two metals, X and Y, combine to form an electrically conductive XY compound (Eq. 1.1). Gibbs free energy associated with the reaction can be expressed in Eq. 1.2.



$$\Delta G_r^\circ = \Delta G_f^\circ (XY) \quad (1.2)$$

In a system where two metals, X and Y, are separated, the formation of XY products requires diffusion, for example, X to Y. During the diffusion process, the X/XY interface shifts gradually towards the X side.^[30] The driving force behind the chemical reaction is the difference in chemical potential between the two electrodes. With a decrease in the concentration of species X, chemical potential decreases correspondingly. When the chemical potentials of the species are equal, diffusion stops.^[30] This condition is usually referred to as equilibrium.

An electrolyte is required in an electrochemical reaction in order to facilitate the transport of ionic species while impeding electronic species. Completing the reaction requires an external electrical circuit that connects X and Y, allowing for electron transfer through the system. If there is any obstruction in the flow of the ionic or electronic paths, the entire reaction will stop. When the electronic circuit is open and no current is flowing, the ionic species within the mobile electrolyte encounter a chemical driving force that propels them in a specific direction. However, this gradient is counterbalanced by an electrostatic driving force acting in the opposite direction.^[30]

The Gibbs free energy is a quantitative measure of the work performed in a thermodynamic system, in this case, the transfer of electrons from reducing agents to oxidizing agents. This work can also be represented as the per-mole electrostatic energy of a charged species, as demonstrated in Eq. 1.3. Here, ΔG_r° is the standard Gibbs free energy change per mole fraction; n is the charge number of the transferred ionic species; F is the Faraday constant (96,485 C per mole); and E is the potential difference between two electrodes.

$$\Delta G_r^\circ = -nFE \quad (1.3)$$

In discussions related to electrochemistry, it is important to consider not only the chemical perspective but also include other relevant terms such as “anode” and “cathode.” The terms “positive” or “negative” electrode can often be complex when defining anode and cathode because the sign changes depending on the presence of load or charging. It is noteworthy to emphasize that the anode is a terminal where the oxidation reaction takes place, causing electron transfer to the opposite side. In contrast, at the cathode, reduction takes place. The term “cell potential” (also known as “open circuit voltage”) refers to the difference in potential between the anode and the cathode.^[30]

In addition, other common terminologies in electrochemistry include specific energy, specific capacity, and specific power. These terms represent physical quantities that are typically divided by the mass of active material to obtain specific units such as mAh g⁻¹ or Wh kg⁻¹. The terminologies used in electrochemical systems, such as specific energy, specific capacity, and specific power, are crucial for understanding the basics and making relative comparisons. Specific energy is the total energy divided by the mass of the active material, which is commonly used for describing the energy density of batteries and supercapacitors. Specific capacity describes how much charge is stored in a given amount of active material. Specific power denotes the power output achievable from the electrochemical cell per unit mass of active material. By comprehending these terminologies, one can effectively analyze and delve into more specific discussions.^[30]

Common reactions in electrochemical energy storage systems – Having discussed the fundamental principles of electrochemical cells, it is now essential to examine the common reactions that occur in these devices. The most frequent reaction types can be categorized as formation reactions, displacement reactions, and insertion reactions.^[30] In formation reactions, a new phase is created, such as the XY compound in Eq. 1.1. This process involves the diffusion of a single species through an electrolyte, forming a new phase at the opposite electrode. Various examples of formation reactions exist, with the Li-Si/Sn/Sb systems being the most prevalent ones.^[31] Another common type of reaction is the displacement reaction, which occurs when two species displace each other within a binary phase. One example of a displacement reaction is Li with Cu₂O, resulting in Li₂O,^[32] as represented in Eq. 1.4.



In the insertion (or intercalation) reactions, guest species occupy the interstitial sites within the host material, also known as intercalation material. Such reactions generally occur within layered crystal structures. Guest species can change the composition of the present phase, and this phenomenon can be viewed as the solubilization of the guest in

the host substance. Consequently, these reactions are usually called “solid solution reactions.” One example of this reaction involves the insertion of lithium into TiS_2 ,^[33] as shown in Eq. 1.5.



Probably the most common example in terms of modern-day application is lithium in graphite, which is the operating principle of LIBs. In this case, highly crystalline and stable graphite can host lithium atoms, resulting in the formation of the LiC_6 compound.^[34] From established principles, contemporary secondary batteries often employ this reaction mechanism, with particular emphasis on alkali-ion batteries, which have been considered the leading technology in this field over the last few decades.

1.2. Alkali-ion batteries

The term “alkali-ion battery” generally refers to battery chemistries involving lithium, sodium, and potassium.^[35] The development of portable electronic devices necessitated the introduction of rechargeable battery systems. The first rechargeable batteries were made from nickel-cadmium (NiCd) cells, which were subsequently replaced by nickel-metal hydride (NiMH) batteries due to concerns about the environmental impact and toxicity of cadmium.^[36] However, major drawbacks of NiMH batteries were their limited energy density, memory effect, and more, leading to the search for alternative solutions.

Lithium-based batteries were identified as a potential secondary battery system in the late 20th century owing to their high specific capacity, low self-discharge, and readiness.^[37] Early applications of lithium-based batteries utilized metallic lithium anodes, which were difficult to recharge due to the dendritic growth of the metal after a few cycles. Therefore, an alternative negative and positive electrode was sought, resulting in the introduction of graphite as an effective negative electrode due to its theoretical specific capacity of 372 mAh g⁻¹.^[38] Most of the capacity can be stored at a plateau close to zero versus the lithium reference electrode without significant irreversible side reactions. However, the lack of modern manufacturing techniques and laboratory equipment made graphite obsolete for commercial use for some time. In early trials, propylene carbonate (PC) was introduced as an electrolyte, which was not compatible with graphite, resulting in an undemanding performance for scale-up demonstrations.^[39] As a follow-up, the introduction of soft carbons, graphitizable carbons, enabled the use of such electrolytes and additives in LIBs, as they were already compatible with the other chemical constituents.^[40]

Sony introduced the first commercial LIB in 1991, consisting of soft carbon and LiCoO_2 as anode and cathode materials, respectively.^[41] Meanwhile, modified soft carbons and

even hard carbons, which are non-graphitizable carbons, were being tried in LIB systems. However, soft and hard carbons were considered inefficient for large-scale productions. The introduction of advanced electrolytes, such as ethylene carbonate (EC), dimethyl carbonate (DMC), and diethyl carbonate (DEC), allowed graphite to be used in LIBs.^[42] Since then, LIBs have remained dominant in the market in most aspects, although the extraction and production of cathode materials remain complicated. A typical LIB consists of graphite as an anode, LiCoO_2 as a cathode, a separator (such as Celgard), and a carbonate-based electrolyte. The use of graphite in LIBs is notable due to its excellent performance, which includes a capacity of more than 300 mAh g^{-1} and an initial coulombic efficiency (ICE) of more than 90%.^[39] Moreover, graphite possesses good conductivity, reducing the amount of additional conductive additives like carbon black. The energy density of LIBs is typically between 150 and 250 Wh kg^{-1} , depending on the application, subject to real-world operating conditions, representing an impressive metric.^[43]

LIBs have been considered a marvel of modern technology since their introduction. They continue to dominate the market, particularly in mobile applications where high energy density and electrochemical performance are required. In contrast, research interest in sodium-ion batteries (SIBs) was previously limited due to the challenges associated with working with sodium due to the need for highly specialized production equipment, as well as the need for more controlled environments that require costly systems.^[44] Moreover, the elusive nature of cathode materials, such as NaCoO_2 , which exhibits a complicated charge and discharge profile compared to its analogous LiCoO_2 , has hindered early research efforts.^[45] As such, scientific research on SIBs before the turn of the millennium was negligible compared to that on LIBs. However, as technological advances in LIBs continued, research interest in SIBs has also gained momentum, given their analogous operating principles. The increased interest in SIBs is driven not only by scientific advances but also by techno-economic and geopolitical issues related to LIBs. As a readily available battery system, SIBs have received increasing attention not only in laboratory-scale research but also in industrial applications. The first commercial SIB was introduced by CATL Company (with a specific energy of 160 Wh kg^{-1} and 15 min to 80% state of charge (SoC)) (**Figure 1.2a**) and followed by Company HiNa Battery Systems (140 Wh kg^{-1}), and the latter has been successfully applied to an electric vehicle (**Figure 1.2b** and **Figure 1.2c**), demonstrating its promising potential for further implementations,^[46] despite its technical specifications not yet matching those of state-of-the-art LIBs. Still, the goal of achieving an energy density of 200 Wh kg^{-1} in SIBs is still a horizon of development.

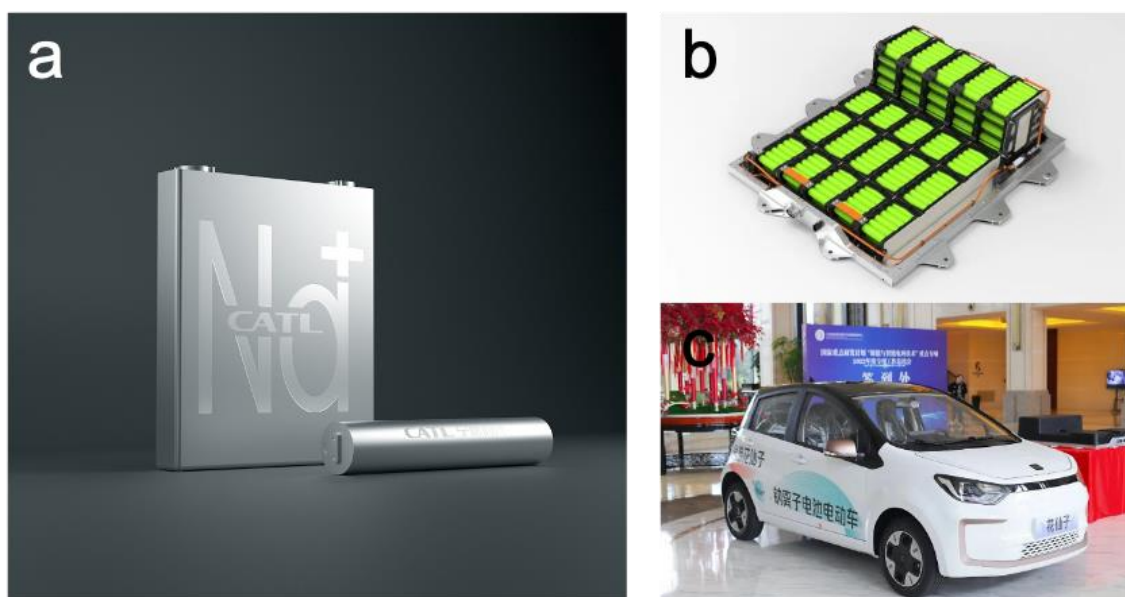


Figure 1.2. (a) The first commercial SIB introduced by CATL, (b) commercial SIB stacks from HiNa Battery, and (c) the first application of SIB in an electric vehicle (JAC SEHOL E10X), which provides a range of approximately 300 km when used with 140 Wh kg^{-1} battery packs. (Copyright, CATL, HiNa Battery, and JAC)

Alkali-ion batteries have gained significant attention in scientific research, and it is worth mentioning that potassium-ion batteries (KIBs) have also been studied in this field.^[47] While the current state of research on KIBs does not yet match that of SIBs, it is essential to recognize the value of understanding the fundamentals of ion storage mechanisms provided by alkali-ion batteries. The lesser investment in KIB research can be attributed to challenges in developing battery components, specifically for the anode side. Due to the larger covalent radius of potassium, the storage mechanism and electrode materials are significantly different than those for LIBs and SIBs. Furthermore, the identification of stable cathode material for KIBs remains an area of active investigation, along with electrolyte restrictions.^[47] Nevertheless, research on KIBs is increasing, and similar operating principles among alkali-ion batteries suggest that advances in KIB technology will contribute to broader improvements across the whole field.

1.2.1. Commercialization of SIBs

While SIBs and LIBs share similar principles in processing and integrating battery components, SIBs were considered supplementary battery systems to LIBs in the medium term due to their lower electrochemical performances.^[48] Nevertheless, SIBs can be effectively utilized in upcoming mobile applications due to their promising energy

densities. Manufacturers currently aim to expand SIB technology to cover the entire range of LIB applications, but this objective is not yet feasible. Nonetheless, promising results are emerging for industrial-scale applications, and global manufacturing lines can be swiftly adapted to SIB technology without requiring substantial investments.^[46]

The most significant advantage of SIBs, for now, is their considerably lower cost compared to LIBs. The supply chain for LIBs is expected to be distorted, not only due to the challenging extraction of expensive cobalt but also due to environmental concerns. The total cost of lithium, nickel, and cobalt in the typical battery pack is roughly 30%, which is remarkably high, and a further reduction in cost is essential.^[46] To reduce costs, some manufacturers have returned to LiFePO_4 (LFP) cathodes for some applications, even though they have lower energy densities than LiCoO_2 (NMC)-based packs. Nevertheless, even eliminating cobalt from the cathode is insufficient to make LIBs more appealing. For example, lithium carbonate, the primary chemical source of lithium, is significantly more expensive than sodium carbonate (roughly 27,000 USD/Ton compared to 300 USD/Ton as of April 2023, tradingeconomics.com), and sodium is also significantly more abundant.

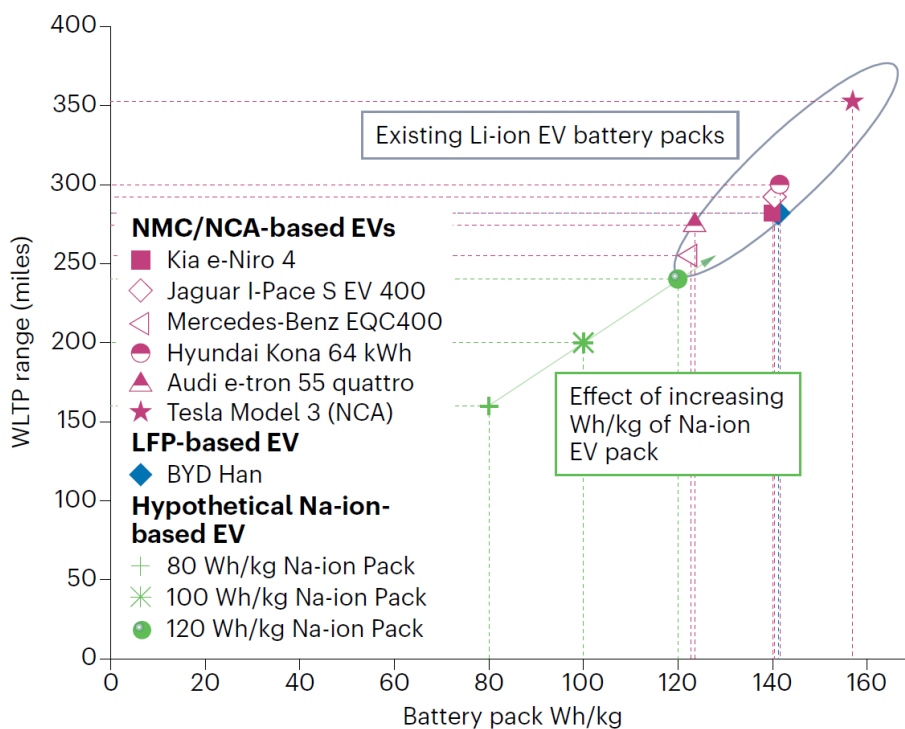


Figure 1.3. Analysis of the driving range in relation to the battery pack energy densities of current SIBs, NCM- and LFP-based LIBs. Reprinted with permission from Figure 3 in Rudola et al., *Nat. Energy*, **2023**, 8, 215-218. (Copyright (2023) Nature Publishing Group, copyright granted through Copyright Clearance Center, Inc.)

In the past decade, several endeavors have been undertaken to show the prospective capabilities of SIBs at an industrial level. Some of these attempts have reported comparable results to LFP-based LIBs.^[46] Naturally, the main focus of interest lies in the electric vehicle (EV) market, which is the largest potential market for the battery industry. Initially, SIBs were deemed unfit for numerous aspects, but current scientific and technological developments suggest that they might actually have a chance. **Figure 1.3** demonstrates the typical cell-to-pack strategies for SIBs and compares them with the already available approaches in the EV market. If appropriate pack-level energy densities can be attained, the performance of SIBs can compete with the NCM- and LFP-based LIBs.^[46]

Pack engineering is one of the main obstacles faced by SIBs. It is a complex task that requires careful consideration. In general, there is no reason why SIB packs can't be employed in these kinds of applications. However, it may be necessary to develop a unique structural battery solution. According to the most recent US transportation statistics, 95% of all trips in 2021 were less than 80 km, indicating that SIB deployment might begin with small city vehicles.^[46] Considering the sustainability and cost benefits of SIB chemistry, they could be a promising candidate for moderate-range EV applications.

1.2.2. Operating principle of alkali-ion batteries

As previously discussed, alkali-ion batteries primarily comprise LIBs, SIBs, and KIBs, which do not rely on similar storage mechanisms, i.e., insertion (intercalation). The fundamental operating principle of these batteries involves pairing each electrode with an appropriate counterpart and combining them with an electrolyte, separator, current collector, and other components.

In most cases, layered oxides are used as cathodes and carbonaceous materials as anodes. In the presence of an electric load, redox reactions happen at the active sites, and the ions migrate to the other terminal. Then, these ions are stored in the structure. Simultaneously, the flow of electrons generated within the system travels through an external circuit, resulting in the generation of a current (**Figure 1.4**).

The insertion mechanism in this context is broadly defined, as the stable intercalation compound is not uniform across all types of alkali-ion batteries. For instance, the energy barrier for the formation of an alkali-ion-carbon compound is relatively low for LIBs (LiC_6 , with a theoretical capacity of 372 mAh g^{-1}) and even for KIBs (KC_8 , with a theoretical capacity of 279 mAh g^{-1}).^[49] However, for SIBs, the nature of sodium makes its intercalation into carbon inconvenient (NaC_{64} , with a theoretical capacity of 35 mAh

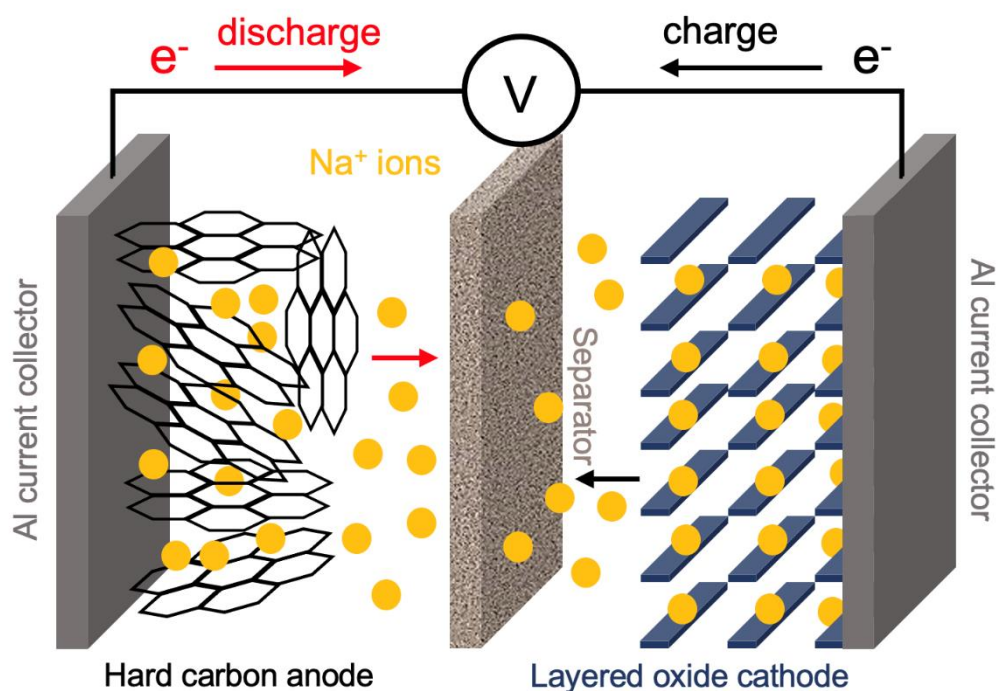


Figure 1.4. Operating principle of a typical SIB is illustrated.

g^{-1}).^[50] Consequently, the primary mechanism usually occurs through the pore-filling in SIBs, which involves the diffusion-controlled transport of sodium ions into the micropores (open or closed) of the carbon anode.^[51]

From a more scientific standpoint, “alkali-ion battery” refers to systems in which ions do not participate in further chemical reactions apart from intercalation. When these materials undergo different reactions with the active materials in electrodes (i.e., compounds found in cathode materials, such as transition metal oxides, phosphates, coordination polymers, or polyanionic compounds), they are classified as different battery types. A couple of examples of those kinds of systems are the lithium-sulfur (Li-S) and sodium-sulfur (Na-S) battery systems, which involve the formation of alkali-ion-sulfur species during operation and are distinct from LIBs, SIBs, and KIBs.

1.2.3. Components of a battery cell

Cathodes – In many cases, performance parameters, such as energy density, are significantly influenced by the cathode chemistry, as the cell potential is crucial for high energy density. While this holds true for all batteries, the range of cathode materials that

have been studied under several conditions is particularly extensive for LIBs, which are currently the only commercially available alkali-ion battery systems.

The materials that have received the most attention in this context are metal oxides with layered structures, specifically those denoted as LiMO_2 , where M represents elements such as Co, Ni, and Al. These oxides allow for the intercalation of Li ions at very high potentials, such as over 4.0 V (vs. Li^+/Li), and possess a stable plateau region.^[40] Consequently, these materials are currently the most efficient cathode materials due to their high theoretical capacity and stable potential, ultimately leading to a remarkable energy density. However, there is a limitation associated with these materials. At the potential at around 4.6 V (vs. Li^+/Li), the oxygen evolution reaction occurs, and the flammable electrolyte poses a danger of reacting with it, leading to thermal failure.^[52] For mobile applications, currently, there is no other feasible solution beyond the use of oxide layers. However, for large-scale applications where energy density is not the main performance metric, other types of cathode materials are considered. Especially given that cobalt is the most widely used element on commercial LIBs, its availability is also highly localized in the crust. In such cases, nickel or manganese could replace cobalt, although their performance may not stand for direct comparison.^[53] Alternative cathode materials are mixed crystals, such as lithium-nickel-cobalt-aluminum oxide ($\text{Li}(\text{Ni}_{0.8}\text{Co}_{0.15}\text{Al}_{0.05})\text{O}_2$), which is the preferred choice when a balance is required in terms of energy density, power density, safety, and availability. Recently, most of the commercial LIBs have also used mixed crystals, such as lithium-nickel-manganese-cobalt oxide ($\text{Li}(\text{Ni}_{0.33}\text{Mn}_{0.33}\text{Co}_{0.33})\text{O}_2$). In this case, nickel reduces the amount of cobalt used in the cathode, and manganese stabilizes the lattice.^[53-54]

Spinel represents another type of cathode material, with LiMn_2O_4 (LMO) and LiNi_2O_4 being the typical compositions. These materials can provide high operating voltages, reaching up to 5.0 V vs. Li^+/Li , almost above the oxidative stability of electrolytes.^[53, 55] LMO is the most well-known member of this group and has been studied for use in commercial applications. It is sometimes blended with NCM to reduce the amount of cobalt used in the cathode. The performance of LMO at high temperatures is not sufficient in terms of cyclic stability and rate-capability. Moreover, there are various types of LMO cathodes, which can lead to the generation of lower-performance variants (due to their different chemical structure) during battery operation.

Metal phosphates, denoted as LiMPO_4 (where M indicates Fe, Mn, Co, or Ni), represent another important type of cathode material.^[55a, 56] LiFePO_4 (LFP) is the most commonly used variant of these cathodes, providing a relatively high specific capacity of approximately 160 mAh g^{-1} at around 3.4 V (vs. Li^+/Li). The unique property of LFP is its flat plateau, along with its superior rate performance and capacity retention. However, the drawback of this kind of cathode is its low electrical conductivity, which requires costly

fabrication techniques to be improved. Despite this limitation, metal phosphates are promising cathode materials, and research in this field is proceeding at a fast pace. However, due to the performance of NCM cathodes in mobile applications, LFP cathodes currently lag behind.

On the SIBs side, it has been observed that several cathode materials can be made compatible to some extent by substituting Li with Na, resulting in stable and similar compounds. The discovery of efficient cathode material is essential to achieve the desired level of energy density for mobile applications. Indeed, the cathode constitutes the heaviest part of the battery, accounting for almost half of the cell weight, which is nearly twice the weight of the anode. The molar mass of Na is higher compared to Li (i.e., 23.0 vs. 6.9 g mol⁻¹); hence, energy densities of analogous cathodes for SIBs are expected to be lower. For instance, the theoretical capacity of NaCoO₂ is approximately 15% lower than that of LiCoO₂. Additionally, the lower redox potential of Na decreases the cell potential, resulting in a lower energy density in the full-cell. The full-cell voltage is primarily driven by the cathode potential since the anode plateau usually hovers close to 0 V (vs. reference electrodes) in both LIBs and SIBs using graphite and hard carbons, respectively.^[51] A direct substitution of Na for Li in cathode materials is not suitable for practical applications. As an example, NaCoO₂ exhibits different plateaus at different potentials, making it unfeasible for commercial use.^[57] Conversely, NaFeO₂ can serve as a stable cathode material, albeit with a lower specific capacity. It can provide a stable plateau at 3.4 V (vs. Na⁺/Na).^[58] However, this material is susceptible to irreversible phase transitions, leading to faster decay. Mn-based analogs are also under investigation, but their lower cyclic stability and less flat voltage profiles also put them in a disadvantageous place.

The superior affinity of polyanionic compounds to Na compared to Li has made them a desirable candidate for efficient cathode materials. In this regard, NaFePO₄, close to its Li counterpart (LFP), has demonstrated similar cycling properties with a flat plateau profile at two different potentials while effectively utilizing most of its theoretical capacity.^[59] However, low conductivity has posed a significant challenge, necessitating the adoption of advanced treatment techniques to decrease particle size. The replacement of phosphate with pyrophosphates has also been considered; in this case, energy density is lower, but power density and stability are higher. Optimization with Mn and F has also been explored, with the introduction of F leading to the development of a relatively stable compound, Na₂FePO₄F. This material can provide a reversible capacity of approximately 110 mAh g⁻¹ and exhibits two plateaus around 3.0 V (vs. Na⁺/Na).^[45, 60]

The current consensus deems NASICON (Na Super Ionic Conductor) type Na₃V₂(PO₄)₃ (NVP) cathode materials as the most promising in the field,^[61] even for commercial purposes. With a capacity of approximately 117 mAh g⁻¹ and a plateau at 3.4 V (vs.

evident that the performance of SIB cathodes falls short of replacing their LIB counterparts in mobile applications in many performance metrics, such as stable operating voltages, cyclic stability, and rate capability. Nevertheless, ongoing research endeavors aim to discover much more efficient cathode materials for the future. Alternatively, these materials may be employed for stationary applications that do not require very high energy densities. In **Figure 1.5**, a comparison of cathode materials is visualized in terms of their fundamental electrochemical performances.^[64]

Anodes – After an extensive discussion over several decades, it has been observed at a theoretical level that the optimal negative electrodes for alkali-ion batteries are bare metals, which offer overseen energy densities.^[65] However, the irreversible plating and stripping of metals lead to distortion of surfaces over cycling. This results in the formation of dendrites, which pose a potential danger of causing short circuits and, thus, failure. Given these challenges, the anode material should be lightweight and have a consistent working potential to maintain a stable full-cell voltage during operation and preserve high energy density. Furthermore, it is essential to consider additional performance metrics that are just as crucial as energy density, such as cycling stability, chemical stability, wide operating window, safety, and sustainability.^[66] Consequently, it is essential to develop anode materials that meet these criteria while holding high-performance standards to attain sustainable and efficient energy storage solutions.

When compared to the cathode side, the anode exhibits a much narrower range of useful product scales for both LIBs and SIBs. Titanium-based anodes, such as TiO_2 , can be utilized in both cases and offer a lithiation potential of approximately 1.5 V (vs. Li^+/Li) and above 0.5 V (vs. Na^+/Na).^[66b, 67] However, the high voltages associated with LIBs make them unsuitable for high-energy-density applications. In the case of SIBs, the modification of electrochemical properties may be achieved through the partial replacement of Ti atoms with Li, Cr, Co, or Ni. Titanites, being one of the most promising insertion materials in both cases according to scientific research, led to the introduction of various chemical structures, such as $\text{Li}_4\text{Ti}_5\text{O}_{12}$ and $\text{Na}_2\text{Ti}_6\text{O}_{13}$, among others. Nevertheless, their low specific capacity and low conductivity remain their primary drawbacks.^[68]

Meanwhile, alloys have also captured the attention, given their significant theoretical capacities. However, the formation of alloys is usually accompanied by substantial volume changes during phase transitions, resulting in a rapid failure of the battery.^[66b, 69] Si and Sb are widely regarded in this context due to their very high capacity. For instance, $\text{Li}_{22}\text{Si}_5$ can offer capacities of approximately 4200 mAh g^{-1} with lithium. However, the alloying process is sometimes sequential and challenging due to the formation of amorphous compounds at near-room temperatures. Notably, no alloy formation has been observed between Na and Si in practical tests, while alloy formation does occur with Sb and Sn,

which is theoretically expected.^[69b, 70] However, controlling the intermediate species is difficult, leading to volume changes that are detrimental to battery stability. Therefore, it is crucial to continue exploring advanced materials that meet the requirements for high performance, safety, and environmental sustainability in order to develop next-generation energy storage solutions that must be implemented at a large scale.

An alternative strategy for the advancement of anodes in SIBs involves the utilization of phosphorous.^[71] Phosphorous has the ability to react smoothly with sodium, leading to outstanding electrochemical properties. For example, the redox potential of the formation of Na_3P is less than 0.5 (vs. Na^+/Na), a relatively low value when compared to other alloy-based anodes, making it a valuable alternative to obtain a high energy density. Still, there are challenges associated with phosphorous. White phosphorous is out of discussion in the use of batteries as they are extremely toxic and flammable. Red phosphorous provides good stability. Black phosphorous offers high conductivity and possesses a layered structure similar to graphite, with four phosphorous atoms binding to each sodium atom.^[71]

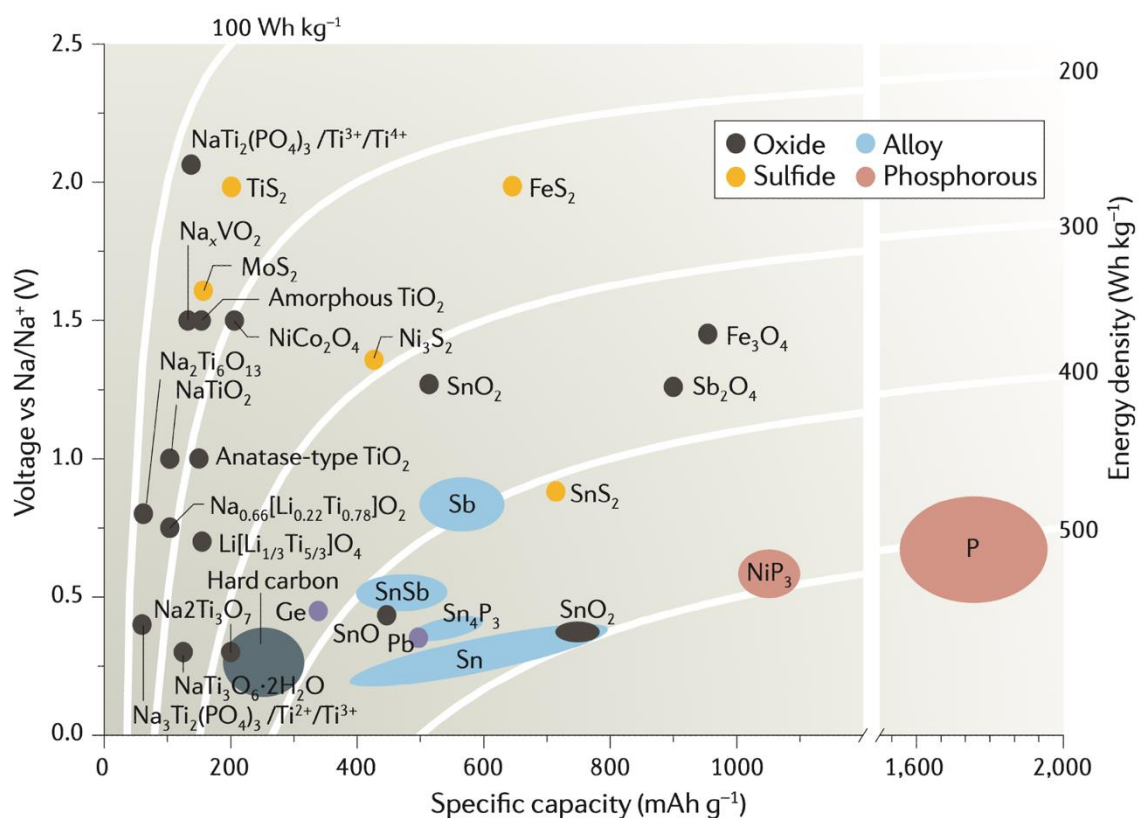


Figure 1.6. In a Ragone plot, the anode materials for SIBs is represented by their energy density, specific capacity, and voltage. Reprinted with permission from Figure 7b in Choi & Aurbach, *Nat. Rev. Mater.*, **2016**, 1, 16013-16013. (Copyright (2016) Nature Publishing Group, copyright granted through Copyright Clearance Center, Inc.)

Despite these advantages, this class of materials also faces specific problems, such as low processability and undemanding real-world electrochemical performance. Additives and custom facilities/devices are required to achieve the desired particle size and ensure proper conductivity. Nonetheless, using phosphorous anodes is considered a promising area of research in developing high-performance batteries.

Carbonaceous materials are frequently thought to be the best for LIBs and SIBs. These materials are readily available and exhibit remarkable electrochemical performance in various aspects. In the case of LIBs, commercial batteries typically utilize graphite as an anode due to its ability to form stable intercalation compounds. The theoretical capacity of graphite in LIBs is 372 mAh g^{-1} , with most of this capacity being close to 0 V (vs. Li^+/Li), which allows for its broad use in a variety of applications. Aside from graphite, non-graphitic carbons can also be employed in some instances while remaining compatible with LIBs.^[49a]

In SIBs, graphite is not supported because of the aforementioned limitations. However, non-graphitic carbons, such as hard carbons, can be used and exhibit similar electrochemical behavior to graphite in LIBs. Hard carbons can provide more than 300 mAh g^{-1} , with most of their capacity being stored close to the plateau.^[18a, 18b, 72] Nevertheless, these materials do have some drawbacks, such as capacity degradation at high currents due to harsh ion insertion processes, which can distort their structures and negatively impact their long-term cycling performance. Section 1.3.1 delves into the sodium storage behavior of hard carbon in more detail. **Figure 1.6** presents a comparative analysis of various anode materials in terms of their fundamental electrochemical characteristics.^[64]

Solid electrolyte interphase (SEI) – In light of the discussion on anodes, it is worthwhile to mention the role of solid-electrolyte interphase (SEI) layers in alkali-ion battery systems. Despite exhibiting distinct chemical structures in LIBs and SIBs, these layers share fundamental characteristics. The SEI layer is a natural passivation layer consisting of the decomposition products of the electrolyte. It occurs when the redox potentials of the electrodes exceed the electrolyte's stable electrochemical window, particularly during the initial operating cycle.^[73] SEI layers are mostly inorganic layers that chemically coat the active surfaces of the electrodes. While this mechanism manifests in both negative and positive electrodes, the latter is often referred to as cathode-electrolyte interphase (CEI) layers.

In the late 1970s, Peled and colleagues first introduced the concept of SEI while studying the electrodeposition of alkali and alkaline earth metals in different electrolytes.^[74] Their investigation resulted in a thin, electronically insulating but ionically conductive layer on the current collector, which, due to its properties resembling those of the liquid electrolyte,

was referred to as the SEI.^[74] SEI layers are of paramount importance in numerous respects, including their ability to enhance cycling stability, rate capability, safety, and other critical factors. However, as previously noted, their formation during the initial cycle is unavoidable and can significantly impact capacity loss and electrolyte consumption. Thus, the controlled formation, growth, and chemical composition of SEI layers require meticulous study.

SEIs in both LIBs and SIBs primarily comprise heterogeneous mixtures of organic and inorganic species, with the latter being more dominant.^[75] Consequently, SEIs exhibit sensitivity to different chemical environments, including salts and electrolyte solvents. In the case of graphite in LIBs, SEI formation typically occurs lower than 0.3 V (vs. Li⁺/Li), resulting in a relatively stable structure.^[76] However, this is not possible for hard carbons in SIBs, given that the half-cell potential is higher, leading to considerably lower SEI stability.^[76] The diffusion-controlled mechanism of storage for alkali-ion batteries, such as the pore-filling in SIBs, is more detrimental to the structure. For example, the harsh ion insertion process distorts the structure and generates additional surfaces, resulting in the growth of the SEI layer that consumes electrolytes and decreases the Coulombic efficiency. Additionally, SEIs in SIBs have been found to be more fragile, which causes cracking and decomposition after operating for a while.^[77]

Controllable formation and growth of SEIs can be done in several ways. One such approach involves modifying the electrolytes with various additives (as discussed in the electrolyte section), although this practice is seldom used. Another technique consists of utilizing electrodes with relatively low surface areas accessible to the electrolyte, thereby impeding the formation and growth of excessive passivation, as it consumes electrolytes and may affect the charge transfer resistivity. However, this strategy has been found to be controversial, as certain anode materials in SIBs rely on these surface areas to enable efficient ion storage, such as mesopores that facilitate surface-controlled sodium adsorption. Another modification method is introducing an artificial passivation layer, namely an artificial-SEI (*a*-SEI), as a post-synthetic process to suppress the growth of naturally forming SEI. Chapter 2 mainly explores this phenomenon experimentally by introducing carbon nitride (CN) thin film as an *a*-SEI layer and provides positive outcomes.^[78] Further discussions on *a*-SEI layers can also be found in Section 1.3.2.

Electrolytes – In both LIBs and SIBs, electrolytes must meet several requirements, including electrochemical and thermal stability, plus ionic conductivity, while remaining electrically insulating. These electrolytes should be synthesized from feasible and abundant sources, as they occupy a significant amount of space within the battery. Given the highly reactive environment on the cathode and anode sides, the electrolyte must also have a highly stable potential window.^[79] Thermal stability is also critical since, as a liquid phase, the electrolyte should resist thermal decomposition and prevent phase changes

within the thermal operating window, e.g., -30 to 50°C. The ionic conductivity plays a crucial role in providing fast ion transfer and reducing charge transfer resistivity, which is essential for the state of health (SoH, an actual condition compared to the ideal) of the battery.

Electrolytes typically consist of salts, solvents, and sometimes additives.^[73b] The alkali salt, containing either sodium or lithium, is the critical parameter. As the diameter of the anion in the salt is much larger than that of the cation, it conveys the ionic transportation kinetics to a greater extent. After desolvation, the cations are transferred to the electrodes and stored through redox reactions or surface-controlled processes. The selection of salts is crucial, as they have significantly different solubilities in various solvents and electrochemical stability.^[73b] Alkali salt decomposition usually occurs as an anodic process; thus, they should be paired with electron-withdrawing atoms to provide weaker coordination with the alkali atom. Common anions paired with Na⁺ and Li⁺ cations include ClO₄⁻, BF₄⁻, PF₆⁻, [N(FSO₂)₂]⁻ (FSI), and [N(CF₃SO₂)₂]⁻ (TFSI).^[73b, 80] The selection of these anions should be based on several performance criteria. However, ClO₄⁻ is a potential danger to safety, while FSI and TFSI are rather costly.^[76, 81] Among these, PF₆⁻ can be considered a good compromise despite being highly moisture-sensitive.

Electrolyte solvent is as significant as the alkali salt due to the solvent's crucial role in the formation of the SEI and its effect on various other critical factors. The most frequently exploited solvents are organic polar solvents, such as organic carbonate esters and glycol ethers. Among the glycol ether solvents, bis(2-methoxyethyl) ether (diglyme) has garnered much scientific interest owing to its many favorable outcomes.^[82] For instance, in Chapter 4, it is found that the material investigated with diglyme-based electrolyte solution exhibits better performance than with carbonate-based electrolytes. However, due to their higher stability, carbonate-based solvents are the primary choice in real-world applications. In particular, ethylene carbonate (EC) and propylene carbonate (PC) are often preferred due to their high dielectric constants.^[83] However, the use of PC in LIBs is unfeasible as it exfoliates the graphite over time, while in the case of SIBs, it triggers excessive SEI formation with the hard carbons. EC stands out for its performance and stability, but its melting temperature of 36°C precludes it from being employed as a standalone solvent, as it is solid at room temperature. For this reason, it is frequently blended with other carbonate-based solvents to create binary solvent mixtures. Dimethyl carbonate (DMC), ethyl-methyl carbonate (EMC), and diethyl carbonate (DEC) are all highly-miscible options that can be employed in varying volumetric ratios with EC. In SIBs, the most common electrolyte is 1M NaPF₆ in EC/DEC (or EMC), while in LIBs, it is 1M LiPF₆ in EC/DMC, as the use of EC with DMC yields much higher ionic conductivities.^[80, 84]

It is worth noting that there are certain additives that can be introduced into the electrolyte solution to enhance its performance further. Although scale-up demonstrations may pose additional challenges, promising results have been shown at the lab-scale level. Notably, fluoroethylene carbonate (FEC) is a common additive and is usually added to the electrolyte solution at levels ranging from 1 to 5 wt. %.^[85] It has been demonstrated that the inclusion of such additives increases the stability of the SEI, leading to its thickening with improved protection. In turn, this mitigates the creation of new surfaces and thereby hinders the uncontrolled growth of the SEI and electrolyte consumption. A drawback of such additives is reducing the storage capacity, particularly in the case of SIBs, as hard carbon stores sodium in its micropores, and a thicker SEI can block the sodium diffusion channels. Therefore, the amount of additives should be investigated in detail before implementation.^[86]

An alternative class of electrolytes, known as room-temperature ionic liquids (RTILs), has garnered considerable attention in academic research.^[73b, 80, 87] These RTILs exhibit improved thermal stability and stable potential windows in many cases. However, compared to carbonate-based electrolytes, their extreme cost makes them unsuitable for commercial applications. Similarly, solid-state electrolytes have recently been investigated due to their exceptional thermal stability, lower flammability, improved durability, and more. However, low ionic conductivity still remains their biggest drawback, and further investigation is essential for implementation.

Binders and additives – The coating of active material on the surface of the current collector is required for the assembly of an electrode. For this purpose, electrode slurry usually contains some adhesive and performance enhancer additives. Binders represent a crucial class of additives in electrode slurry, serving as the principal agents for furnishing adhesive strength in the active material and attaching it firmly to the current collector. In tandem with other components, binders also have requirements that must be met to ensure high performance. These requirements include the ability to adhere firmly utilizing both chemical interactions with the other components and good mechanical properties, sufficient wettability to provide seamless compatibility with the electrolyte, and thermal stability. Various binder types are available, such as conductive, cross-linking, self-healing, and many others.^[88] Nonetheless, the most prevalent and suitable varieties for commercial applications are derived from linear polymers.

Polyvinylidene fluoride (PVDF), polyacrylic acid (PAA), sodium alginate (SA), and carboxymethyl cellulose (CMC) are linear polymers that are commonly employed as binders. PVDF, a fluoropolymer, is renowned for its excellent electrochemical stability. However, its relatively weak intermolecular forces often result in significant volume expansion during cycling.^[89] Furthermore, to facilitate its usage, hazardous solvents are used, such as *N*-Methyl-2-pyrrolidone (NMP), as they are toxic and have a high boiling

point (i.e., 202°C for NMP). PAA, on the other hand, is an amorphous polymer that is capable of establishing robust mechanical properties. It provides a desirable electrode elasticity, enabling it to revert to its initial dimensions even after undergoing volumetric expansion resulting from sodiation and desodiation during cycling.^[89] SA, a natural polysaccharide, can facilitate bond formation under protonation conditions, thereby improving the SEI stability and increasing the initial Coulombic efficiency. Last but not least, CMC, a cellulose-derived polymer with numerous hydroxyl and carboxymethyl groups, might interact chemically with the active components to improve bonding efficiency.^[89] As a binder, CMC yields superior electrochemical performance when compared to the conventional PVDF binder in SIBs.^[90]

In addition, styrene-butadiene rubber/carboxymethylcellulose (SBR/CMC) offers some advantages for the negative electrodes, given their enhanced stability properties.^[91] The implementation of such binders is excluded on the cathode side owing to the oxidation of unsaturated bonds present in SBR at high cathodic potentials. Hence, they are not preferred in cathode slurries.

It is critical in battery technology to discuss the role of conductive compounds in the positive and negative electrodes. In LIBs, thanks to the conductive nature of the graphite, the use of an additional conductive additive is often unnecessary.^[92] However, the cathode side of the battery, which typically consists of layered metal oxides, exhibits lower conductivity, thereby necessitating the use of such additives. In the case of SIBs, both the anode and the cathode require conductive additives because hard carbon is a non-graphitic carbon and does not provide sufficient electrical conductivity. Hence, the use of conductive additives is unavoidable for the efficiency of SIBs.

Several batteries contain conductive additives, such as carbon nanotubes (CNTs), graphene, or carbon black, which are combined into a mixed slurry comprising two or more components.^[93] The integration of such conductive additives into a conductive paste is necessary for industrial purposes, and it arises from the collective efforts of these additives to encourage their utilization. Carbon black (such as Super-P), graphene, or carbon nanotubes (CNTs) are challenging to be dispersed homogeneously. For this reason, before their inclusion in the electrode slurry and subsequent utilization, it is necessary to disperse these additives thoroughly. Ideally, conductive additives should exhibit excellent dispersion in the dispersing agent (such as NMP) to provide effective electrical conduction with a minimum amount. However, in some cases, the amount of additive binder in the electrode mixture can exceed 20 wt.%, leading to a decrease in energy density, as their contribution to the capacity is negligible. Nevertheless, they can enhance electrolyte adsorption and diffusion by improving the ionic conductivity of the electrodes. Furthermore, conductive additives should be cost-effective and practical for large-scale

utilization. Carbon black is preferred over CNTs and other additives due to its significantly lower cost.^[93]

1.3. Background on hard carbon materials

Graphite is the most common carbon allotrope characterized by a layered structure of sp^2 -hybridized carbon atoms. Meanwhile, hard carbons represent another type of carbon allotropes with a disordered, non-graphitizable structure, even at very high temperatures.^[18a, 18b, 72] Hard carbons typically lack long-range order, yet they may exhibit locally ordered graphitic-like stacking, sometimes referred to as pseudo-graphitic. These carbons usually possess a high degree of open and closed porosity, which arises from their structural features derived from defects and short-range orders. The local pseudo-graphitic stacking of hard carbons in their (002) planes is larger compared to the one in graphite (ca. >0.36 vs. 0.34 nm), leading to a lower density compared to graphite (ca. 1.5 to 2.2 g cm^{-3}).^[94] By increasing the condensation temperature, these hard carbons exhibit an increase in the conjugation length, i.e., higher sp^2 degree with a local structural order. Hard carbons, however, have a minor change in structural order as compared to soft carbons, which can be graphitized at higher temperatures.^[72] If the treatment temperature increases, the available surface area of hard carbons to the gas decreases, and the closed pores inside of the material become a crucial measure.

Designing the physicochemical properties of carbonaceous materials is an art that is still a very active area of investigation. The structural features of these materials are dependent on the precursors, temperature, environment, and other parameters. For instance, when coal and petroleum pitch are treated, they transform into soft carbons that are graphitizable at above 2000°C due to the arrangement of their turbostratic disordered layers.^[95] Meanwhile, hard carbons may be generated from a variety of sources, including cross-linked polymers and biomasses.^[96] During thermal condensation, carbon atoms possess limited mobility, which restricts the rearrangement of sp^2 -based units. Therefore, they may preserve the precursor morphology during condensation, controlling the closed and open porosity. It is noteworthy that it is controversial to classify soft and hard carbons as completely amorphous since they still contain locally arranged graphitic units and do not have fully localized π orbitals.

The complex structure of hard carbons can be analyzed through several characterization techniques, which are thoroughly discussed in Chapter 4. Transmission and scanning electron microscopy (TEM and SEM) are used for obtaining an overview of structures on the μm to nm scale. The disordered structure of hard carbons, which typically takes the form of entangled noodle-like graphitic layers (**Figure 1.7a**), is explored using TEM. At the larger-scale, the morphology of hard carbon often appears as larger chunks with

distinct boundaries and smooth surfaces (**Figure 1.7b**) in the absence of surface treatments. Diffraction techniques, such as X-ray diffraction (XRD), enable the characterization of the interlayer distance and comparison to one of the graphitic carbons. The (002) reflections are observed at lower diffraction angles, indicating increased stacking distance.^[19, 97] The porous nature of hard carbons is also characterized by other techniques, such as gas physisorption analysis for open surfaces that are available for gas adsorption. In this case, N₂ adsorption and desorption are the most common methods used for the quantification of such surfaces by applying several methods (such as density-functional-theory (DFT) and beyond). However, such carbons usually possess micropores that are not available for N₂ since the gas kinetic radius may be larger than potentially available micropores (such as ultramicropores $d < 0.7$ nm (IUPAC)), depending on the nanostructure. The utilization of different gases, e.g., CO₂, He, or Ar, can be employed to delve into such analysis.^[98] Closed pores cannot be characterized with gas physisorption analysis and can be analyzed using scattering techniques. Small-angle X-ray scattering (SAXS) is a useful method for analyzing structural changes in materials, including surfaces, interfaces, and crystal structures.^[99] In particular, SAXS is a conventional method for analyzing the closed porosity of hard carbons both qualitatively and quantitatively. The scattering curve of a typical hard carbon sample is presented in **Figure 1.8a**, where the scattering from microporous regions is usually associated with the mid-range (i.e., 0.5 to 8.0 nm⁻¹) of the scattering vector (q).^[99b] At the same time, additional structural features such as sharp boundaries, lateral imperfections, and the radius of gyration can be obtained from the lower q ranges in the Porod region.

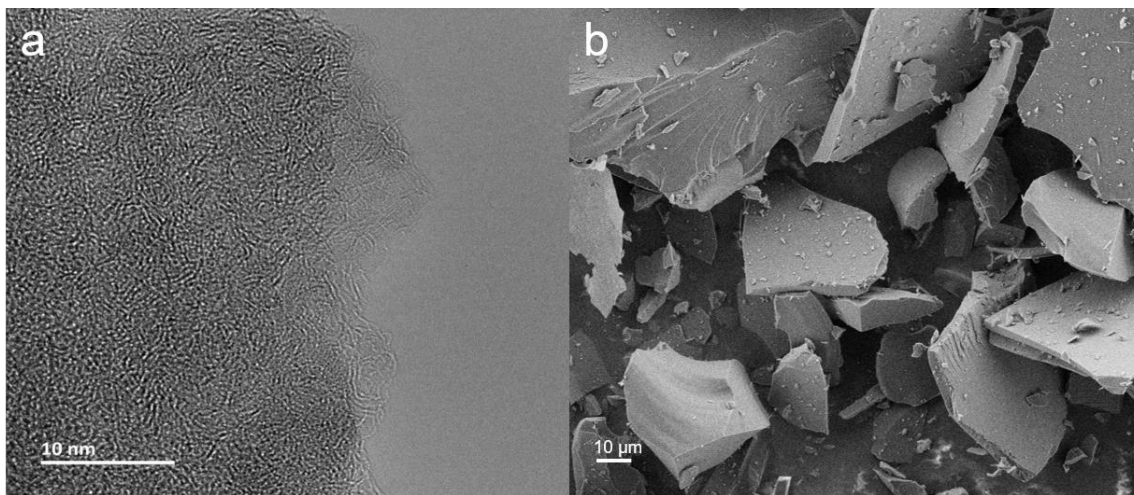


Figure 1.7. (a) TEM image of a typical non-graphitic carbon with a short-range order. (b) SEM images of the same material, revealing the sharp edges and smooth surfaces of the structure.

1.3.1. Sodium storage in hard carbons

As previously mentioned, the sodium storage mechanism in hard carbons differs significantly from the lithium storage mechanism in graphite. This is due to the physicochemical properties of the materials that prevent the formation of a stable intercalation compound. Despite this difference, the electrochemical behavior of these materials, as observed in their galvanostatic charge and discharge (GCD) profiles, exhibits similarities.^[17b] The GCD curve of hard carbons typically includes three distinct regions (**Figure 1.8b**). In the beginning, a sharp decrease in the potential to approximately 1.0 V (vs. Na⁺/Na) occurs, which is due to the activation with SEI (not to confuse it with the desolvation process) and is negligibly involved in the energy storage. The second region, where a “sloping region” occurs, is a surface-controlled storage mechanism that arises due to the broad energy distribution of adsorption sites for the sodium ions. This happens due to the capacitive-like storage behavior of the active material (e.g., surfaces and defect sites). The last region, which is referred to as the diffusion-controlled “plateau region,” exhibits a relatively constant voltage profile close to 0 V (vs. Na⁺/Na) and accounts for the most significant part of the sodium-storage mechanism, as it is important for many performance metrics, such as obtaining higher cell potential and energy density.^[18a, 18b, 72] This storage mechanism involves the intercalation and diffusion of sodium ions into the carbon framework, where redox reactions may occur.

In addition to the GCD measurements, ion storage mechanisms can be assessed using a number of electrochemical techniques, including galvanostatic intermittent titration tests (GITT) and cyclic voltammetry (CV). For diffusion-controlled storage, the redox peaks close to 0 V (vs. Na⁺/Na) are suppressed at high scan rates in CV due to the limited time available for the diffusion, while the capacitive sloping region that mainly relies on fast

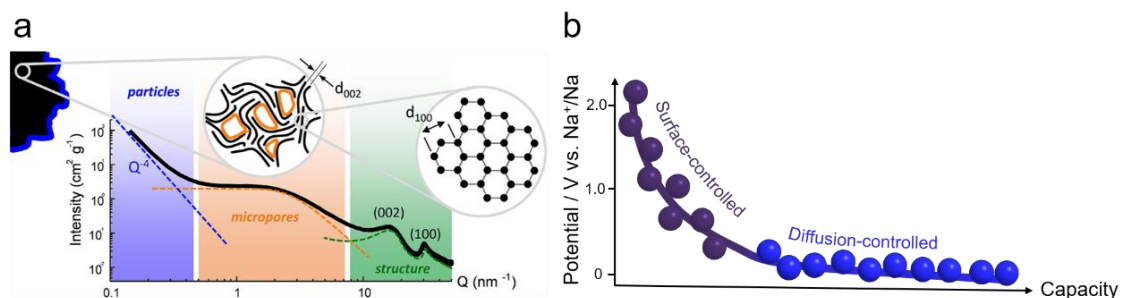


Figure 1.8. (a) X-ray scattering profile of a hard carbon in terms of normalized intensity versus scattering vector (q). Graphical abstract in Saurel et al., *Energy Storage Mater.*, **2019**, 21, 162-173. (Copyright (2019) Elsevier) (b) Illustration of surface- and diffusion-controlled sodium storage regions of hard carbons.

near-surface kinetics is less affected by the scan rate. In GITT, a current pulse is applied for a specific time and then removed, monitoring the relaxation of the potential. This approach allows for the calculation of sodium-ion diffusion coefficients based on Fick's law of diffusion. As the electrochemical reduction and oxidation reactions happen close to 0 V (vs. Na⁺/Na) at the plateau, a sharp decrease in the sodium-ion diffusion coefficients is expected.

The sodium storage mechanism in the plateau region is of particular interest to several studies, and it is still under debate.^[100] Some studies associate this mechanism with pore-filling, which occurs through the diffusion of sodium ions into the micropores present within the material.^[101] Other studies propose that sodium ions can be stored within the structure, such as between pseudo-graphitic planes and associated defect sites.^[101] However, the most widely accepted opinion is that the mechanism is a combination of these two processes,^[18c] as both have been confirmed by *ex-situ*, *in-situ*, and *in-operando* measurements. The structural changes in the material during sodiation can be evaluated through X-ray techniques such as *in-operando* small-angle and wide-angle X-ray scatterings (SAXS and WAXS).^[51, 102] In the former case, variation in electron energy density difference in tiny pores provides robust evidence to support the pore-filling mechanism, which is also evaluated in Chapter 3. In the latter case, a shift in the scattering peaks accounts for the increase in stacking distance, which happens because of the distortion of the planes by sodium. However, in the case of intercalation, the question of whether sodium forms a stable intercalation compound remains still unanswered. Sodium nuclear magnetic resonance (²³Na NMR) is also a useful tool for monitoring the formation of sodium clusters in pores.^[103]

Hard carbons have a wide range of electrochemical properties, making them a promising material for SIBs. They usually have more than 300 mAh g⁻¹ capacities and, in some cases, even reach up to 400 mAh g⁻¹,^[104] as also presented in Chapter 4. Currently, hard carbons are the only material class that has progressed to commercialization in SIBs. However, the practical use of hard carbons depends on their feasibility, as their performances are usually demonstrated only on a small scale. The most common precursors for hard carbons are derived from biomasses and carbohydrates (i.e., glucose).^[105] Performance improvements can be achieved through appropriate synthesis schemes and precursors. One issue with hard carbons is that they are typically treated at relatively high temperatures (e.g., above 1300°C) to achieve good performance.^[49b] At lower condensation temperatures, the materials may not provide the prolonged plateau capacity required for high-energy-density applications. Therefore, developing high-performance anode materials through processes with a low energy footprint remains a challenging endeavor for future implementation. Despite being known for many years, hard carbons have recently received more attention due to their promising performance for different

applications. Technological advancements have introduced discussions of several approaches to improve these materials further for specific applications.

1.3.2. Strategies for enhancing the electrochemical performance of anode materials in SIBs

In order to examine potential techniques to enhance the performance of carbons in SIBs, it is essential first to consider some of the challenges associated with them. Sodium possesses a larger ionic radius, which can negatively impact its diffusion kinetics when compared to lithium. This presents a significant obstacle to achieving fast operation in SIBs. Additionally, non-graphitic carbons used in SIBs usually have lower conductivity compared to graphite in LIBs. This is because the hard carbons are less organized and present fewer sp^2 bonds. Other challenges include low sodium ion affinity of active materials, as well as efficient diffusion channels. Several methods have been proposed to address these complications as promising techniques for enhancing electrochemical sodium storage performance.

Heterojunctions for increasing ionic and electronic conductivity – The concept of heterojunctions emerged within semiconductor materials and has demonstrated significant potential for various applications, ranging from transistors to solar cells.^[106] A heterojunction is a barrier formed by the contact of two semiconductors with comparable thermal expansion coefficients, interatomic distances, and crystal structures but different bandgaps.^[106] In this regard, two parameters are critical, namely the work function (ϕ) and the Fermi level. The work function is defined as the least amount of energy required to extract an electron from a substance and convey it to a vacuum. The variation in the work function of materials substantially influences band alignment and electron flow. Meanwhile, the Fermi level represents the maximum energy level attainable by an electron at absolute zero. Alignment of the Fermi levels between materials potentially removes the barrier for electron flow.^[106] Due to concentration polarization, when two semiconductors are integrated, carriers on one side of the interface migrate spontaneously to the opposing side. This results in the formation of a space charge area near the interface of the two semiconductors, and the uneven charge distribution causes an electric field. By adjusting the bandgap, sodium storage can potentially be enhanced.^[107] In this way, heterojunctions can be utilized for several purposes, such as increasing ionic and electronic conductivity in anode materials. Although carbon is commonly linked with semiconductors, its job, in this case, is to act as the metal in heterostructures. Several studies have demonstrated an increase in the ionic conductivity of electrodes via this mechanism while also improving the electronic conductivity.^[107]

The junction formed between conductive materials and semiconductors, resulting from differences in work functions that cause free electrons to flow at the interface, is usually called the Mott-Schottky junction. Although not typically associated with carbon materials, some carbons can create a Mott-Schottky junction with semiconductors to enhance the electronic properties of electrodes.^[78b] The *a*-SEI used in Chapter 2 involves a carbon/CN heterojunction.

Artificial SEI (*a*-SEI) concept – The SEI is an irregular and inhomogeneous layer that happens through the side reactions accumulated during the initial operating cycle of the battery. The formation of SEI is difficult to control; hence, it is crucial for numerous performance metrics.^[78a, 108] For example, excessive formation of SEI boosts electrolyte consumption, eventually leading to failure. Moreover, the heterogeneous nature of the SEI creates “hotspots” for faster ion transport, thus accelerating the kinetics for the nucleation and growth of metal dendrites on some areas of the electroactive surface.^[108] To overcome the issues arising from natural SEI layers, the concept of an *a*-SEI was initially introduced for lithium- and sodium-based batteries and is now extended to conventional designs. In this case, the physicochemical properties of the *a*-SEIs are meant to improve the electrochemical performance. Designing effective *a*-SEI relies on three main principles:^[108] (i) mechanical stability, where *a*-SEI should be dense and rigid to avoid cracking since natural SEI is brittle and prone to cracks, allowing for the dendrite growth on the surfaces. (ii) Uniform ion transport should be provided by *a*-SEI to avoid localization, which damages the structure, as performance decay is significantly faster due to inhomogeneous ion flux. (iii) Chemical passivation is the critical parameter, as SEI should be able to passivate the active surface contact with the liquid electrolyte to prevent additional parasitic reactions. In **Figure 1.9**, three main design principles are visualized to show the importance of a stable *a*-SEI layer.^[108] Note that all design requirements for lithium-based batteries are also valid for sodium-based batteries.

Scientists are exploring different techniques to induce a stable and thin conformal layer that can provide stability during operation, such as preventing dendrite formation and improving electronic structures by even creating heterostructures with the electrode.^[78a] Even though the concept of *a*-SEI is typically exploited in the metal anode (sometimes also referred to as anode-free) batteries, inhomogeneous and highly porous carbons can also be covered with a very thin layer of conformal *a*-SEI with appropriate deposition methods. In Chapter 2, the chemical vapor deposition (CVD) method is used to introduce a CN conformal *a*-SEI and enhance the performance of biowaste-derived carbon, addressing the heterojunction effect.

Heteroatom effect – Extensive research has been conducted to explore the heteroatom effect to enhance the electrochemical performance, focusing on nitrogen, phosphorus, and sulfur as the most widely studied atoms integrated into the carbon structure.^[78b, 109] Studies

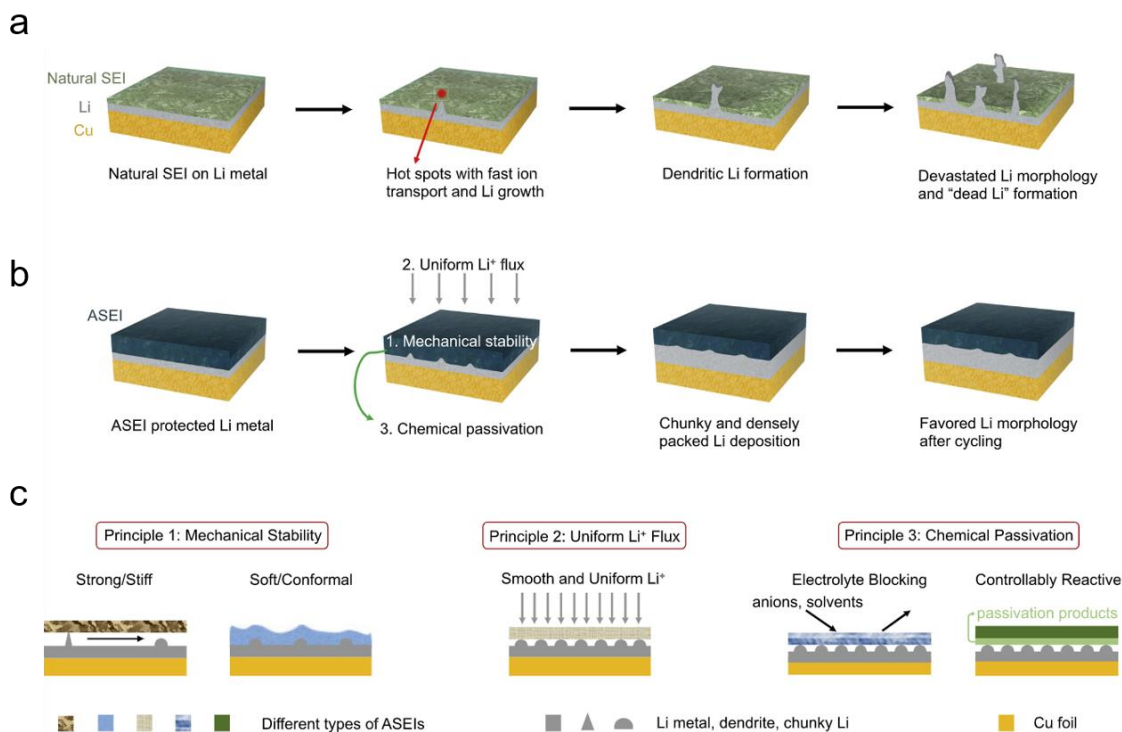


Figure 1.9. (a) Scheme showing the effect of Li-metal plating/stripping on surface with natural SEI and (b) with *a*-SEI. (c) Scheme showing three main design principles for an effective *a*-SEI. Figure 1 in Yu et al. *Cell Rep. Phys. Sci.*, **2020**, 1, 100119. (Copyright (2020) Elsevier)

have revealed that nitrogen and phosphorus can enhance first-cycle efficiencies even though the sodium storage performance is not affected much. Meanwhile, sulfur has been considered an up-and-coming solution for SIBs owing to its larger covalent radius and chemical properties, which increase the interlayer spacing of graphitic planes while introducing the preferential adsorption sites for sodium ions.^[17a, 19] These carbons entail chemical features that are energetically favorable for the surface adsorption of sodium ions, potentially increasing the capacity.^[19b] However, reports indicate that the sulfur-containing carbons typically lack a diffusion-controlled plateau region, suggesting lower energy densities in full-cell devices.^[16a, 17a, 110] Nevertheless, the design of sulfur-rich carbonaceous anodes can be used for high-power applications due to the improved surface affinity. Sulfur heteroatoms for efficient sodium storage are widely investigated in Chapter 3.

The effect of oxygen heteroatoms on electrochemical sodium storage, which can be positive and negative, is also not ignorable.^[107, 111] When oxygen is present, the desired structure of hard carbons can be achieved due to the step-wise condensation process, as

oxygen plays a critical function in controlling structural stability, e.g., with terminal groups. At high temperatures, oxygen-bonded species may be removed from the framework, serving as a pore-forming agent within the material. Thus, they are typically considered necessary for the fabrication of high-performing carbon materials.^[49b] However, a high oxygen concentration is often linked to an unstable SEI. For this reason, the most promising hard carbons are usually synthesized at very high temperatures, which has positive outcomes in both cases: (i) oxygen-containing species leave the framework, creating internal pores for the efficient sodium storage, and (ii) decreased amount of oxygen brings the formation of a more stable SEI layer. In Chapter 4, high-capacity hard carbon is introduced in this way, where achieving over 70% ICE with a total capacity of more than 370 mAh g⁻¹.

Surface engineering – The relationship between the open surface area of hard carbons and the electrochemical performance is widely discussed in the literature. However, a high concentration of mesopores on the surface can reduce ICE as the SEI is usually formed on these surfaces.^[112] Hard carbons with very high open surface areas sometimes bring ICE below 30%,^[113] causing significant irreversibility. Many studies have, therefore, focused on reducing the open surface area of hard carbons through various techniques. For instance, conformal coating methods, such as those used in the formation of artificial SEIs (*a*-SEIs),^[114] can be employed to reduce the surface area. However, this may also have some drawbacks, such as decreased total capacity and rate capability, as surface-controlled processes play a critical role in fast sodium storage.

Bibliography for Motivation, Outline, and Chapter 1

- [1] G. A. Jones, K. J. Warner, *Energy Policy* **2016**, *93*, 206-212.
- [2] A. Månsson, *Energy Res. Soc. Sci* **2014**, *4*, 106-116.
- [3] D. Archer, S. Rahmstorf, *The Climate Crisis: An Introductory Guide to Climate Change*, Cambridge University Press, Cambridge, **2009**.
- [4] M. Meinshausen, E. Vogel, A. Nauels, K. Lorbacher, N. Meinshausen, D. M. Etheridge, P. J. Fraser, S. A. Montzka, P. J. Rayner, C. M. Trudinger, P. B. Krummel, U. Beyerle, J. G. Canadell, J. S. Daniel, I. G. Enting, R. M. Law, C. R. Lunder, S. O'Doherty, R. G. Prinn, S. Reimann, M. Rubino, G. J. M. Velders, M. K. Vollmer, R. H. J. Wang, R. Weiss, *Geosci. Model Dev.* **2017**, *10* (5), 2057-2116.
- [5] B. R. Gearey, W. Fletcher, R. Fyfe, *Conserv. Manag. Archaeol. Sites* **2014**, *16* (3), 236-244.
- [6] O. Edenhofer, R. Pichs-Madruga, Y. Sokona, K. Seyboth, S. Kadner, T. Zwickel, P. Eickemeier, G. Hansen, S. Schlömer, C. von Stechow, P. Matschoss, *Renewable Energy Sources and Climate Change Mitigation*, Cambridge University Press, Cambridge, **2011**.
- [7] a) M. Chen, Y. Zhang, G. Xing, S.-L. Chou, Y. Tang, *Energy Environ. Sci.* **2021**, *14* (6), 3323-3351; b) Z. Yang, J. Zhang, M. C. W. Kintner-Meyer, X. Lu, D. Choi, J. P. Lemmon, J. Liu, *Chem. Rev.* **2011**, *111* (5), 3577-3613.
- [8] a) P. Simon, Y. Gogotsi, B. Dunn, *Science* **2014**, *343* (6176), 1210-1211; b) J. B. Goodenough, *Energy Environ. Sci.* **2014**, *7* (1), 14-18.
- [9] S. Dühnen, J. Betz, M. Kolek, R. Schmuck, M. Winter, T. Placke, *Small Methods* **2020**, *4* (7), 2000039.
- [10] C. Xu, P. Behrens, P. Gasper, K. Smith, M. Hu, A. Tukker, B. Steubing, *Nat. Commun.* **2023**, *14* (1), 119.
- [11] M. Beuse, T. S. Schmidt, V. Wood, *Science* **2018**, *361* (6407), 1075-1077.
- [12] T. Kim, W. Song, D.-Y. Son, L. K. Ono, Y. Qi, *J. Mater. Chem. A* **2019**, *7* (7), 2942-2964.
- [13] a) M. Armand, J. M. Tarascon, *Nature* **2008**, *451* (7179), 652-657; b) J. B. Goodenough, K. S. Park, *J. Am. Chem. Soc.* **2013**, *135* (4), 1167-1176.
- [14] G. N. Newton, L. R. Johnson, D. A. Walsh, B. J. Hwang, H. X. Han, *Acs Sustainable Chem. Eng.* **2021**, *9* (19), 6507-6509.
- [15] N. Yabuuchi, K. Kubota, M. Dahbi, S. Komaba, *Chem. Rev.* **2014**, *114* (23), 11636-11682.
-

CHAPTER 1. INTRODUCTION

-
- [16] a) J. Y. Hwang, S. T. Myung, Y. K. Sun, *Chem. Soc. Rev.* **2017**, *46* (12), 3529-3614; b) S. W. Kim, D. H. Seo, X. H. Ma, G. Ceder, K. Kang, *Adv. Energy Mater.* **2012**, *2* (7), 710-721; c) Z. Xu, J. Wang, *Adv. Energy Mater.* **2022**, *12* (29), 2201692.
- [17] a) W. Li, M. Zhou, H. Li, K. Wang, S. Cheng, K. Jiang, *Energy Environ. Sci.* **2015**, *8* (10), 2916-2921; b) L. F. Zhao, Z. Hu, W. H. Lai, Y. Tao, J. Peng, Z. C. Miao, Y. X. Wang, S. L. Chou, H. K. Liu, S. X. Dou, *Adv. Energy Mater.* **2020**, *11* (1), 2002704.
- [18] a) J. W. Choi, D. Aurbach, *Nat. Rev. Mater.* **2016**, *1* (4), 16013-16013; b) H. M. Zhang, Y. X. Huang, H. Ming, G. P. Cao, W. F. Zhang, J. Ming, R. J. Chen, *J. Mater. Chem. A* **2020**, *8* (4), 1604-1630; c) X. Chen, J. Tian, P. Li, Y. Fang, Y. Fang, X. Liang, J. Feng, J. Dong, X. Ai, H. Yang, Y. Cao, *Adv. Energy Mater.* **2022**, *12* (24), 2200886.
- [19] a) L. Qie, W. Chen, X. Xiong, C. Hu, F. Zou, P. Hu, Y. Huang, *Adv. Sci.* **2015**, *2* (12), 1500195; b) J. Yang, X. Zhou, D. Wu, X. Zhao, Z. Zhou, *Adv. Mater.* **2017**, *29* (6), 1604108-1604108.
- [20] a) L. Wagner, in *Future Energy (Second Edition)* (Ed.: T. M. Letcher), Elsevier, Boston, **2014**, pp. 613-631; b) H. Ibrahim, A. Ilinca, J. Perron, *Renew. Sust. Energ. Rev* **2008**, *12* (5), 1221-1250.
- [21] J. Torriti, *Energy Res. Soc. Sci* **2017**, *25*, 37-47.
- [22] R. Gross, M. Leach, A. Bauen, *Environ. Int.* **2003**, *29* (1), 105-122.
- [23] A. Azarpour, S. Suhaimi, G. Zahedi, A. Bahadori, *Arab. J. Sci. Eng.* **2013**, *38* (2), 317-328.
- [24] M. S. Guney, Y. Tepe, *Renew. Sust. Energ. Rev.* **2017**, *75*, 1187-1197.
- [25] S. C. Singhal, *Solid State Ion.* **2002**, *152-153*, 405-410.
- [26] M. Einhorn, F. V. Conte, C. Kral, J. Fleig, *IEEE Trans. Power Electron.* **2013**, *28* (3), 1429-1437.
- [27] M. Koniak, A. Czerepicki, *IOP Conf. Ser.: Mater. Sci. Eng.* **2017**, *211* (1), 012005.
- [28] S. Georgiou, N. Shah, C. N. Markides, *Appl. Energy* **2018**, *226*, 1119-1133.
- [29] T. Chen, Y. Jin, H. Lv, A. Yang, M. Liu, B. Chen, Y. Xie, Q. Chen, *Trans. Tianjin Univ.* **2020**, *26* (3), 208-217.
- [30] R. A. Huggins, in *Energy Storage: Fundamentals, Materials and Applications* (Ed.: R. Huggins), Springer International Publishing, Cham, **2016**, pp. 119-144.
- [31] W.-J. Zhang, *J. Power Sources* **2011**, *196* (1), 13-24.
- [32] L. Zhang, Q. Li, H. Xue, H. Pang, *ChemSusChem* **2018**, *11* (10), 1581-1599.
-

CHAPTER 1. INTRODUCTION

- [33] M. Wagemaker, W. J. H. Borghols, F. M. Mulder, *J. Am. Chem. Soc.* **2007**, *129* (14), 4323-4327.
- [34] J. Xie, Y.-C. Lu, *Nat. Commun.* **2020**, *11* (1), 2499.
- [35] A. Van der Ven, Z. Deng, S. Banerjee, S. P. Ong, *Chem. Rev.* **2020**, *120* (14), 6977-7019.
- [36] M. Assefi, S. Maroufi, Y. Yamauchi, V. Sahajwalla, *Curr. Opin. Green Sustain. Chem.* **2020**, *24*, 26-31.
- [37] M. Li, J. Lu, Z. Chen, K. Amine, *Adv. Mater.* **2018**, *30* (33), 1800561.
- [38] P. Bernard, M. Lippert, in *Electrochemical Energy Storage for Renewable Sources and Grid Balancing* (Eds.: P. T. Moseley, J. Garche), Elsevier, Amsterdam, **2015**, pp. 223-251.
- [39] J. Xu, Y. Dou, Z. Wei, J. Ma, Y. Deng, Y. Li, H. Liu, S. Dou, *Adv. Sci.* **2017**, *4* (10), 1700146.
- [40] Y. Nishi, *Chem. Rec.* **2001**, *1* (5), 406-413.
- [41] Y. Nishi, *J. Power Sources* **2001**, *100* (1), 101-106.
- [42] S.-K. Jeong, M. Inaba, Y. Iriyama, T. Abe, Z. Ogumi, *J. Power Sources* **2008**, *175* (1), 540-546.
- [43] G. Zhou, H. Chen, Y. Cui, *Nat. Energy* **2022**, *7* (4), 312-319.
- [44] K. Kubota, N. Yabuuchi, H. Yoshida, M. Dahbi, S. Komaba, *MRS Bull.* **2014**, *39* (5), 416-422.
- [45] N. Yabuuchi, K. Kubota, M. Dahbi, S. Komaba, *Chem. Rev.* **2014**, *114* (23), 11636-11682.
- [46] A. Rudola, R. Sayers, C. J. Wright, J. Barker, *Nat. Energy* **2023**, *8* (3), 215-218.
- [47] W. Zhang, J. Lu, Z. Guo, *Mater. Today* **2021**, *50*, 400-417.
- [48] K. Chayambuka, G. Mulder, D. L. Danilov, P. H. L. Notten, *Adv. Energy Mater.* **2020**, *10* (38), 2001310.
- [49] a) Y. Li, Y. Lu, P. Adelhelm, M.-M. Titirici, Y.-S. Hu, *Chem. Soc. Rev.* **2019**, *48* (17), 4655-4687; b) L.-F. Zhao, Z. Hu, W.-H. Lai, Y. Tao, J. Peng, Z.-C. Miao, Y.-X. Wang, S.-L. Chou, H.-K. Liu, S.-X. Dou, *Adv. Energy Mater.* **2021**, *11* (1), 2002704.
- [50] H. Moriwake, A. Kuwabara, C. A. J. Fisher, Y. Ikuhara, *RSC Advances* **2017**, *7* (58), 36550-36554.
- [51] A. Brennhagen, C. Cavallo, D. S. Wragg, J. Sottmann, A. Y. Kozlov, H. Fjellvåg, *Batteries & Supercaps* **2021**, *4* (7), 1039-1063.
-

CHAPTER 1. INTRODUCTION

-
- [52] a) G. X. Wang, M. J. Lindsay, M. Ionescu, D. H. Bradhurst, S. X. Dou, H. K. Liu, *J. Power Sources* **2001**, 97-98, 298-302; b) G. G. Amatucci, J. M. Tarascon, L. C. Klein, *Solid State Ion.* **1996**, 83 (1), 167-173.
- [53] a) C. Graf, in *Lithium-Ion Batteries: Basics and Applications* (Ed.: R. Korthauer), Springer Berlin Heidelberg, Berlin, Heidelberg, **2018**, pp. 29-41; b) C. H. Chen, J. Liu, M. E. Stoll, G. Henriksen, D. R. Vissers, K. Amine, *J. Power Sources* **2004**, 128 (2), 278-285.
- [54] L. Wang, J. Li, X. He, W. Pu, C. Wan, C. Jiang, *J. Solid State Electrochem.* **2009**, 13 (8), 1157-1164.
- [55] a) A. K. Padhi, K. S. Nanjundaswamy, J. B. Goodenough, *J. Electrochem. Soc.* **1997**, 144 (4), 1188; b) N. Ravet, Y. Chouinard, J. F. Magnan, S. Besner, M. Gauthier, M. Armand, *J. Power Sources* **2001**, 97-98, 503-507; c) T. Drezen, N.-H. Kwon, P. Bowen, I. Teerlinck, M. Isono, I. Exnar, *J. Power Sources* **2007**, 174 (2), 949-953.
- [56] B. Kang, G. Ceder, *J. Electrochem. Soc.* **2010**, 157 (7), A808.
- [57] A. Kanwade, S. Gupta, A. Kankane, M. K. Tiwari, A. Srivastava, J. A. Kumar Satrughna, S. Chand Yadav, P. M. Shirage, *RSC Advances* **2022**, 12 (36), 23284-23310.
- [58] H. Yoshida, N. Yabuuchi, S. Komaba, *Electrochem. Commun.* **2013**, 34, 60-63.
- [59] a) K. Zaghib, J. Trottier, P. Hovington, F. Brochu, A. Guerfi, A. Mauger, C. M. Julien, *J. Power Sources* **2011**, 196 (22), 9612-9617; b) M. Avdeev, Z. Mohamed, C. D. Ling, J. Lu, M. Tamaru, A. Yamada, P. Barpanda, *Inorg. Chem.* **2013**, 52 (15), 8685-8693.
- [60] X. Xiang, K. Zhang, J. Chen, *Adv. Mater.* **2015**, 27 (36), 5343-5364.
- [61] K. Saravanan, C. W. Mason, A. Rudola, K. H. Wong, P. Balaya, *Adv. Energy Mater.* **2013**, 3 (4), 444-450.
- [62] Z.-Y. Gu, J.-Z. Guo, J.-M. Cao, X.-T. Wang, X.-X. Zhao, X.-Y. Zheng, W.-H. Li, Z.-H. Sun, H.-J. Liang, X.-L. Wu, *Adv. Mater.* **2022**, 34 (14), 2110108.
- [63] L. Wang, J. Song, R. Qiao, L. A. Wray, M. A. Hossain, Y.-D. Chuang, W. Yang, Y. Lu, D. Evans, J.-J. Lee, S. Vail, X. Zhao, M. Nishijima, S. Kakimoto, J. B. Goodenough, *J. Am. Chem. Soc.* **2015**, 137 (7), 2548-2554.
- [64] J. W. Choi, D. Aurbach, *Nat. Rev. Mater.* **2016**, 1 (4), 16013.
- [65] M. Wang, F. Zhang, C.-S. Lee, Y. Tang, *Adv. Energy Mater.* **2017**, 7 (23), 1700536.
- [66] a) H. Liu, X.-B. Cheng, Z. Jin, R. Zhang, G. Wang, L.-Q. Chen, Q.-B. Liu, J.-Q. Huang, Q. Zhang, *EnergyChem* **2019**, 1 (1), 100003; b) T. Perveen, M. Siddiq, N. Shahzad, R. Ihsan, A. Ahmad, M. I. Shahzad, *Renew. Sust. Energ. Rev.* **2020**, 119, 109549.
- [67] G.-N. Zhu, Y.-G. Wang, Y.-Y. Xia, *Energy Environ. Sci.* **2012**, 5 (5), 6652-6667.
-

CHAPTER 1. INTRODUCTION

- [68] a) Z. Liang, P. Hui-Lin, H. Yong-Sheng, L. Hong, C. Li-Quan, *Chin. Phys. B* **2012**, *21* (2), 028201; b) J. C. Pérez-Flores, A. Kuhn, F. García-Alvarado, *J. Power Sources* **2011**, *196* (3), 1378-1385; c) A. Rudola, K. Saravanan, S. Devaraj, H. Gong, P. Balaya, *Chem. Commun.* **2013**, *49* (67), 7451-7453.
- [69] a) X. Wang, G. Pawar, Y. Li, X. Ren, M. Zhang, B. Lu, A. Banerjee, P. Liu, E. J. Dufek, J.-G. Zhang, J. Xiao, J. Liu, Y. S. Meng, B. Liaw, *Nat. Mater.* **2020**, *19* (12), 1339-1345; b) W.-J. Zhang, *J. Power Sources* **2011**, *196* (3), 877-885.
- [70] C.-M. Park, H.-J. Sohn, *J. Electrochem. Soc.* **2010**, *157* (1), A46.
- [71] L. Wang, J. Światowska, S. Dai, M. Cao, Z. Zhong, Y. Shen, M. Wang, *Materials Today Energy* **2019**, *11*, 46-60.
- [72] X. Dou, I. Hasa, D. Saurel, C. Vaalma, L. Wu, D. Buchholz, D. Bresser, S. Komaba, S. Passerini, *Mater. Today* **2019**, *23*, 87-104.
- [73] a) P. Verma, P. Maire, P. Novák, *Electrochim. Acta* **2010**, *55* (22), 6332-6341; b) A. Ponrouch, D. Monti, A. Boschini, B. Steen, P. Johansson, M. R. Palacín, *J. Mater. Chem. A* **2015**, *3* (1), 22-42.
- [74] E. Peled, *J. Electrochem. Soc.* **1979**, *126* (12), 2047.
- [75] S. Komaba, W. Murata, T. Ishikawa, N. Yabuuchi, T. Ozeki, T. Nakayama, A. Ogata, K. Gotoh, K. Fujiwara, *Adv. Funct. Mater.* **2011**, *21* (20), 3859-3867.
- [76] G. G. Eshetu, S. Grugeon, H. Kim, S. Jeong, L. Wu, G. Gachot, S. Laruelle, M. Armand, S. Passerini, *ChemSusChem* **2016**, *9* (5), 462-471.
- [77] a) V. A. Oltean, B. Philippe, S. Renault, R. Félix Duarte, H. Rensmo, D. Brandell, *Chem. Mater.* **2016**, *28* (23), 8742-8751; b) R. Mogensen, D. Brandell, R. Younesi, *ACS Energy Lett.* **2016**, *1* (6), 1173-1178.
- [78] a) W. Liu, P. Liu, D. Mitlin, *Adv. Energy Mater.* **2020**, *10* (43), 2002297; b) E. O. Eren, E. Senokos, Z. Song, E. B. Yılmaz, I. Shekova, B. Badamdorj, I. Laueremann, N. V. Tarakina, M. Al-Naji, M. Antonietti, P. Giusto, *J. Mater. Chem. A* **2023**, *11* (3), 1439-1446.
- [79] Y. You, A. Manthiram, *Adv. Energy Mater.* **2018**, *8* (2), 1701785.
- [80] C. Bommier, X. Ji, *Small* **2018**, *14* (16), 1703576.
- [81] Q. Li, J. Chen, L. Fan, X. Kong, Y. Lu, *Green Energy Environ.* **2016**, *1* (1), 18-42.
- [82] K. Westman, R. Dugas, P. Jankowski, W. Wiczorek, G. Gachot, M. Morcrette, E. Irisarri, A. Ponrouch, M. R. Palacín, J. M. Tarascon, P. Johansson, *ACS Appl. Energy Mater.* **2018**, *1* (6), 2671-2680.
-

CHAPTER 1. INTRODUCTION

- [83] H. Che, S. Chen, Y. Xie, H. Wang, K. Amine, X.-Z. Liao, Z.-F. Ma, *Energy Environ. Sci.* **2017**, *10* (5), 1075-1101.
- [84] A. V. Cresce, S. M. Russell, O. Borodin, J. A. Allen, M. A. Schroeder, M. Dai, J. Peng, M. P. Gobet, S. G. Greenbaum, R. E. Rogers, K. Xu, *Phys. Chem. Chem. Phys.* **2017**, *19* (1), 574-586.
- [85] a) M. Winter, P. Novák, A. Monnier, *J. Electrochem. Soc.* **1998**, *145* (2), 428; b) F. Béguin, F. Chevallier, C. Vix-Guterl, S. Saadallah, V. Bertagna, J. N. Rouzaud, E. Frackowiak, *Carbon* **2005**, *43* (10), 2160-2167; c) Y. Jin, S. Sun, M. Ou, Y. Liu, C. Fan, X. Sun, J. Peng, Y. Li, Y. Qiu, P. Wei, Z. Deng, Y. Xu, J. Han, Y. Huang, *ACS Appl. Energy Mater.* **2018**, *1* (5), 2295-2305.
- [86] E. Memarzadeh Lotfabad, P. Kalisvaart, A. Kohandehghan, D. Karpuzov, D. Mitlin, *J. Mater. Chem. A* **2014**, *2* (46), 19685-19695.
- [87] C.-Y. Chen, T. Kiko, T. Hosokawa, K. Matsumoto, T. Nohira, R. Hagiwara, *J. Power Sources* **2016**, *332*, 51-59.
- [88] R.-R. Li, Z. Yang, X.-X. He, X.-H. Liu, H. Zhang, Y. Gao, Y. Qiao, L. Li, S.-L. Chou, *Chem. Commun.* **2021**, *57* (93), 12406-12416.
- [89] J. Patra, P. C. Rath, C. Li, H.-M. Kao, F.-M. Wang, J. Li, J.-K. Chang, *ChemSusChem* **2018**, *11* (22), 3923-3931.
- [90] M. Dahbi, T. Nakano, N. Yabuuchi, T. Ishikawa, K. Kubota, M. Fukunishi, S. Shibahara, J.-Y. Son, Y.-T. Cui, H. Oji, S. Komaba, *Electrochem. Commun.* **2014**, *44*, 66-69.
- [91] J. Park, N. Willenbacher, K. H. Ahn, *Colloids Surf., A* **2019**, *579*, 123692.
- [92] S. Hein, T. Danner, D. Westhoff, B. Prifling, R. Scurtu, L. Kremer, A. Hoffmann, A. Hilger, M. Osenberg, I. Manke, M. Wohlfahrt-Mehrens, V. Schmidt, A. Latz, *J. Electrochem. Soc.* **2020**, *167* (1), 013546.
- [93] Y. H. Chen, C. W. Wang, G. Liu, X. Y. Song, V. S. Battaglia, A. M. Sastry, *J. Electrochem. Soc.* **2007**, *154* (10), A978.
- [94] X. Wu, D. P. Leonard, X. Ji, *Chem. Mater.* **2017**, *29* (12), 5031-5042.
- [95] D. Saurel, B. Orayech, B. Xiao, D. Carriazo, X. Li, T. Rojo, *Adv. Energy Mater.* **2018**, *8* (17), 1703268.
- [96] a) J. Baek, H.-M. Lee, J.-S. Roh, H.-S. Lee, H. S. Kang, B.-J. Kim, *Microporous Mesoporous Mater.* **2016**, *219*, 258-264; b) J. Górka, C. Vix-Guterl, C. Matei Ghimbeu, in *C, Vol. 2*, **2016**.
- [97] C. Li, Y. Sun, Q. Wu, X. Liang, C. Chen, H. Xiang, *Chem. Commun. (Camb)* **2020**, *56* (45), 6078-6081.
-

CHAPTER 1. INTRODUCTION

- [98] A. Beda, C. Vaultot, C. Matei Ghimbeu, *J. Mater. Chem. A* **2021**, 9 (2), 937-943.
- [99] a) C. J. Jafta, A. Petzold, S. Risse, D. Clemens, D. Wallacher, G. Goerigk, M. Ballauff, *Carbon* **2017**, 123, 440-447; b) D. Saurel, J. Segalini, M. Jauregui, A. Pendashteh, B. Daffos, P. Simon, M. Casas-Cabanas, *Energy Storage Mater.* **2019**, 21, 162-173.
- [100] N. Sun, J. Qiu, B. Xu, *Adv. Energy Mater.* **2022**, 12 (27), 2200715.
- [101] X. Chen, C. Liu, Y. Fang, X. Ai, F. Zhong, H. Yang, Y. Cao, *Carbon Energy* **2022**, 4 (6), 1133-1150.
- [102] a) D. A. Stevens, J. R. Dahn, *J. Electrochem. Soc.* **2000**, 147 (12), 4428; b) G. Alvarez Ferrero, G. Åvall, K. A. Mazzio, Y. Son, K. Janßen, S. Risse, P. Adelhelm, *Adv. Energy Mater.* **2022**, 12 (47), 2202377.
- [103] J. M. Stratford, P. K. Allan, O. Pecher, P. A. Chater, C. P. Grey, *Chem. Commun.* **2016**, 52 (84), 12430-12433.
- [104] A. Kamiyama, K. Kubota, D. Igarashi, Y. Youn, Y. Tateyama, H. Ando, K. Gotoh, S. Komaba, *Angew. Chem. Int. Ed.* **2021**, 60 (10), 5114-5120.
- [105] Y. Long, J. Zhang, P. Li, J. Han, C. Geng, Q.-H. Yang, in *Encyclopedia of Energy Storage* (Ed.: L. F. Cabeza), Elsevier, Oxford, **2022**, pp. 47-65.
- [106] J. T. Calow, P. J. Deasley, S. J. T. Owen, P. W. Webb, *J. Mater. Sci.* **1967**, 2 (1), 88-96.
- [107] S. Xiao, X. Li, T. Li, Y. Xiang, J. S. Chen, *J. Mater. Chem. A* **2021**, 9 (12), 7317-7335.
- [108] Z. Yu, Y. Cui, Z. Bao, *Cell Rep. Phys. Sci.* **2020**, 1 (7), 100119.
- [109] a) Z. Li, C. Bommier, Z. S. Chong, Z. Jian, T. W. Surta, X. Wang, Z. Xing, J. C. Neufeind, W. F. Stickle, M. Dolgos, P. A. Greaney, X. Ji, *Adv. Energy Mater.* **2017**, 7 (18), 1602894-1602894; b) W. Chen, M. Wan, Q. Liu, X. Xiong, F. Yu, Y. Huang, *Small Methods* **2019**, 3 (4), 1800323-1800323.
- [110] X. Yuan, S. Chen, J. Li, J. Xie, G. Yan, B. Liu, X. Li, R. Li, L. Pan, W. Mai, *Carbon Energy* **2021**, 3 (4), 615-626.
- [111] C. Chen, Y. Huang, Y. Zhu, Z. Zhang, Z. Guang, Z. Meng, P. Liu, *ACS Sustainable Chem. Eng.* **2020**, 8 (3), 1497-1506.
- [112] a) W. Luo, C. Bommier, Z. Jian, X. Li, R. Carter, S. Vail, Y. Lu, J. J. Lee, X. Ji, *ACS Appl. Mater. Interfaces* **2015**, 7 (4), 2626-2631; b) B. H. Hou, Y. Y. Wang, Q. L. Ning, W. H. Li, X. T. Xi, X. Yang, H. J. Liang, X. Feng, X. L. Wu, *Adv. Mater.* **2019**, 31 (40), e1903125.
- [113] N. T. Aristote, K. Zou, A. Di, W. Deng, B. Wang, X. Deng, H. Hou, G. Zou, X. Ji, *Chin. Chem. Lett.* **2022**, 33 (2), 730-742.
-

- [114] a) J. H. Song, B. W. Xiao, Y. H. Lin, K. Xu, X. L. Li, *Adv. Energy Mater.* **2018**, 8 (17), 1703082; b) C.-C. Wang, W.-L. Su, *ACS Appl. Energy Mater.* **2021**, 5 (1), 1052-1064; c) Q. W. Chen, H. He, Z. Hou, W. M. Zhuang, T. X. Zhang, Z. Z. Sun, L. M. Huang, *J. Mater. Chem. A* **2020**, 8 (32), 16232-16237; d) J. Lee, J. Kim, S. Kim, C. Jo, J. Lee, *Mater. Adv.* **2020**, 1 (9), 3143-3166; e) C. X. Yu, Y. Li, H. X. Ren, J. Qian, S. Wang, X. Feng, M. Q. Liu, Y. Bai, C. Wu, *Carbon Energy* **2022**, n/a (n/a); f) G.-H. Lee, T. Hwang, J.-B. Kim, J. Yang, F. Zou, M. Cho, Y.-M. Kang, *J. Mater. Chem. A* **2022**, 10 (31), 16506-16513; g) E. O. Eren, E. Senokos, Z. Song, E. B. Yilmaz, I. Shekova, B. Badamdorj, I. Lauermann, N. V. Tarakina, M. Al-Naji, M. Antonietti, P. Giusto, *J. Mater. Chem. A* **2023**.

CHAPTER 2. CONFORMAL CARBON NITRIDE THIN FILM AS AN ARTIFICIAL SEI ENHANCING SODIUM STORAGE

The results presented in this chapter can be found as, E. O. Eren, E. Senokos, Z. Song, E. B. Yilmaz, I. Shekova, B. Badamdorj, I. Lauer mann, N. V. Tarkina, M. Al-Naji, M. Antonietti, P. Giusto, *J. Mater. Chem. A*, **2023**, 11 (3), 1439-1446.^[1]

Notion – A novel method for improving the hard carbons involves the development of an artificial interphase at the electrodes' surface to adjust its electronic and chemical structure, enhancing the stability and performance of SIBs.^[2] For this purpose, it is essential to develop materials that demonstrate exceptional durability both chemically and mechanically. Additionally, these materials should possess high ionic and low electrical conductivity and exhibit favorable wetting properties in contact with the electrolyte, all while maintaining a clearly defined structure. Carbon nitride (CN) demonstrates great potential as a suitable material for fulfilling these requirements. It possesses a low electrical conductivity, exhibits high thermal stability, and showcases notable ionic conductivity.^[3] Importantly, CN is not considered an active material for sodium storage.^[4] Additionally, its in-plane structural pores have the potential to facilitate the diffusion of sodium ions while effectively obstructing the negative counter ions present in the electrolyte. An efficient technique for applying CN thin films with adjustable thicknesses onto different substrates has already been documented through chemical vapor deposition (CVD).^[3b, 3h]

In this section, the synthesis of a carbonaceous anode material derived from sodium lignosulfonate, which is a byproduct of the paper and pulp industry, is conducted.^[5] Carbon materials derived from lignin have shown promise as electrochemically active materials in various applications.^[6] Here, lignosulfonate-based carbon (LSC) with a high sulfur content is chosen to produce a “sulfur-rich” carbon, the positive impact of which has been discussed in detail in Chapters 1 and 3. To enhance the electrochemical

performance of the LSC electrode material, it is coated with thin films of CN using CVD. The thickness of the CN film is controlled by adjusting the amount of precursor used in the process. This coating technique leads to significant improvements in the electrochemical performance of the electrode material. Specifically, the first-cycle Coulombic efficiency of the coated electrode material is twice as high as that of the pristine material. The total specific capacity of the LSC is increased by 30%, and there is a notable enhancement in the diffusion-controlled plateau region at lower current densities. Moreover, the CN-coated samples exhibit improved rate capability. This innovative approach emphasizes the importance of designing and controlling interfaces in carbonaceous anode materials for sodium-ion batteries (SIBs). It demonstrates the potential for enhancing the performance of SIBs by manipulating the interactions between different materials at the electrode interfaces.

2.1. CNs: Fundamentals and applications

Semiconductors have emerged as one of the most important classes of materials in the 20th century despite their reliance on metal and silicon-based constituents. However, the pursuit of covalent semiconductors remains, and graphene is believed to be a promising candidate for future electronic materials.^[7] Nevertheless, the absence of a distinct energy bandgap is regarded as a constraint, resulting in numerous attempts to manipulate the bandgap at the nanoscale level.^[8] Ongoing research also persists in exploring alternative covalent semiconductors, and one promising, in this case, is the carbon nitride family.^[9]

As far back as 1834, Berzelius and Liebig reported the “melon,” one of the earliest members reported of the CN family.^[10] However, due to the limited availability of advanced characterization tools at the time, the in-depth features of CN materials remained hidden until the late 20th century.^[11] Since then, several attempts to synthesize carbon nitride materials have undergone and were accompanied by theoretical investigations.^[12] Notably, g-C₃N₄ has gained attention due to its distinctive properties as a sustainable, fully-organic semiconductor that can be thermally synthesized from cost-effective precursors.^[13]

Thermal condensation of CN is utilized with a diverse range of precursors, primarily composed of organic molecules possessing high nitrogen content, including cyanamide, dicyanamide, melamine, and others.^[13] At temperatures around 550°C, a polymeric architecture consisting of tri-s-triazine units, interconnected through amino groups, is formed. The polycondensation reactions involved in the transformation of melamine into g-C₃N₄ necessitate the continuous removal of ammonia to drive the reactions to the end (**Figure 2.1**).^[13-14] As a result, the material possesses an ideal composition of “C₃N₄” or a C/N ratio of 0.75. However, due to incomplete condensation, small amounts of unreacted

terminal groups (amino groups) may still be present within the material.^[13-14] Structurally, g-C₃N₄ exhibits an arrangement of graphitic-like stacked layers with an interplanar spacing of 0.32 nm, primarily governed by “van der Waals” interactions.^[15] This particular arrangement, coupled with a high degree of condensation, contributes significantly to the chemical and thermal stability of g-C₃N₄. Notably, the depolymerization of g-C₃N₄ initiates only slightly above 600°C and leaves no residual matter even at temperatures as high as 750°C, thus establishing its position among the thermally stable organic materials known to date.

The electronic properties of g-C₃N₄ are exciting. The conjugated polymeric structure exhibits anisotropic semiconducting behavior, with an indirect bandgap typically reported as 2.7 eV, enabling its suitability for applications involving visible light.^[13] For example, g-C₃N₄ serves as a metal-free n-type semiconductor, demonstrating the remarkable potential for harnessing visible light and generating electron-hole pairs, making it highly attractive for photocatalytic applications.^[16] Band engineering and manipulating semiconductor properties from n-type to p-type are crucial to achieving efficient heterojunctions and devices.^[3] Designing appropriate band alignments between semiconductors is commonly employed to enhance exciton dissociation and facilitate the separation of charges at the interface of two semiconductors, thereby reducing charge recombination, which is fundamental for some semiconductor applications. As demonstrated, g-C₃N₄ is an exceptionally versatile organic semiconductor that lends itself to easy modification through non-metal doping, thereby opening up a wide array of potential applications.

It is noteworthy that g-C₃N₄ has proven successful not only in photocatalysis but also in various other fields.^[3g, 13, 17] It has been utilized in fluorescence and electrochemical sensors, biomedical applications, and the development of batteries and supercapacitors.^[3g, 13, 17] Among those, one potential application of g-C₃N₄ is their use as an artificial

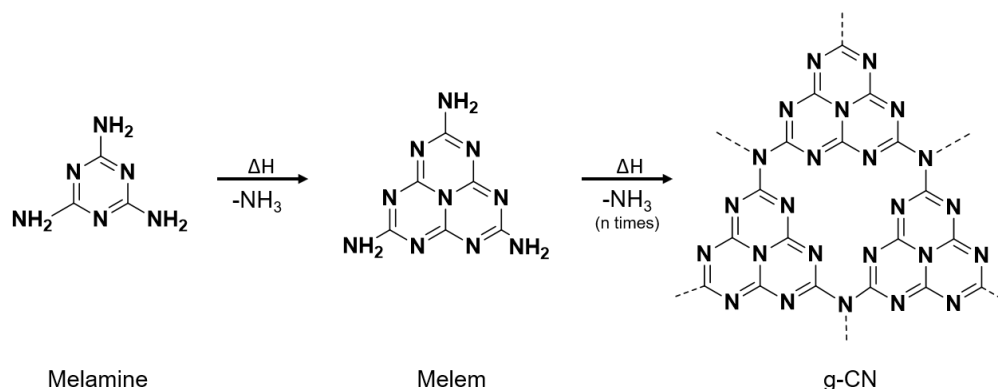


Figure 2.1. The synthetic steps for g-CN from melamine precursor.

passivation layer, specifically as an artificial solid electrolyte interphase (*a*-SEI), in negative electrodes for alkali-ion battery applications. CNs possess the necessary characteristics for an effective *a*-SEI layer, as discussed in Chapter 1. They exhibit ionic conductivity and stability while being electrically insulators. The ability to tune the bandgap of g-C₃N₄ presents a multitude of opportunities for diverse applications. However, in order to establish an efficient heterojunction at the interface, careful consideration of band alignment is crucial, as it facilitates exciton dissociation and charge separation. This enables efficient charge transfer while forming Mott-Schottky junctions with the host materials. Positive outcomes have been reported in applications where CN was utilized as a passivation layer, as it enhanced the efficiency of alkali-ion transfer and redox reactions.^[3g]

2.1.1. Chemical vapor deposition

In contemporary practice, distinguishing between physical and chemical deposition methods has become challenging, as many techniques combine both approaches. However, as a general guideline, physical methods are associated with deposition techniques wherein the resulting film possesses the same composition as the source material.^[18] Meanwhile, in CVD, the film's composition differs from that of the precursor due to chemical reactions occurring during the process.^[19] CVD holds particular significance for the deposition and integration of carbon-based films in cutting-edge organic devices, such as integrated electronics and laser technology. It is a highly effective technique for achieving high-quality, uniform deposition of thin films, irrespective of substrate topography.^[20] CVD finds extensive application across various materials, ranging from metal oxide coatings to polymer and hybrid materials.

The design of a CVD experiment necessitates an interdisciplinary understanding encompassing chemical principles (i.e., reactions and reaction kinetics), physical considerations (i.e., thermodynamics and fluid dynamics), and engineering aspects (i.e., reactor design) that collectively determine the deposition process onto the substrate.^[21] Several CVD methods are available, such as thermal, plasma-enhanced, photo-enhanced, and more. These configurations are often coupled with vacuum systems to enable low-pressure deposition. The selection of a specific CVD setup is closely linked to the desired film material, making it a critical decision point in the development process.

2.2. Preparation of carbon electrode and CN film

The synthesis methods applied here are explained in detail in “**A2.1. Preparation of sulfur-containing carbon and CN thin film application using the CVD method**” in

Appendices. For the details of electrochemical and physicochemical characterization methods, please see “**A2.2. Electrode preparation**” and “**A2.3. Physico-chemical characterizations**” in **Appendices**.

Briefly, the carbon source consists of sodium-lignosulfonate, urea, D-glucose anhydrous, and deionized water, along with ZnO nanoparticles as a porogen, which is mixed using a kneader and then extruded into pellets.^[22] The as-prepared pellets are thermally condensated at 950 °C. The carbonized pellets are ground into a powder, washed with HCl solution to remove residual Zn, and referred to as LSC (**Figure 2.2a**). For CN coating, the CVD method is applied, already developed by Giusto et al.^[3h] LSC powder is placed in the downstream chamber, while a melamine precursor is placed in the upstream. The melamine precursor undergoes sublimation and subsequently deposits onto the target carbon substrate at a higher temperature of 550 °C. The melamine precursor is heated and held at a specific temperature (**Figure 2.2b**). After cooling, a color change is observed in the samples based on the amount of melamine precursor used (**Figure A2.1**).

2.3. Results and Discussion

2.3.1. Physico-chemical characterizations

The **structure of LSC** – ZnO nanoparticles is utilized as porogen in the synthesis of LSC. The stepwise thermal process leads to condensation, followed by ZnO carbothermal reduction at temperatures exceeding 907°C with consequent sublimation of zinc.^[23] The

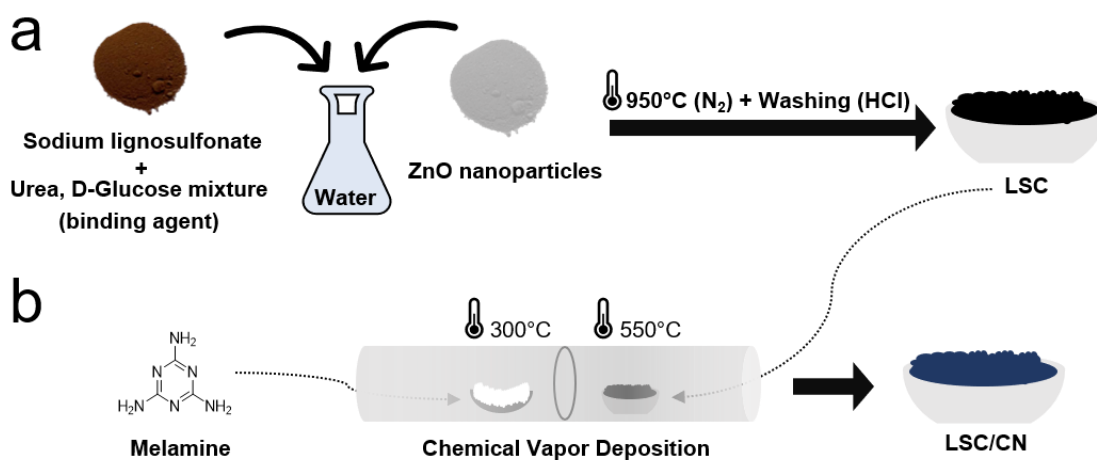


Figure 2.2. Scheme for the preparation of LSC and LSC coated with carbon nitride (LSC/CN) anode material. **(a)** Synthesis of LSC from a sodium lignosulfonate precursor and ZnO porogen. **(b)** Deposition of CN onto LSC via CVD method. (Copyright (2023) The Royal Society of Chemistry)

residual Zn is eliminated by washing with HCl at room temperature. By means of inductively coupled plasma optical emission spectrometry (ICP-OES), trace amounts of residual zinc and sodium (<1.0 wt. %) are identified. Scanning electron microscopy (SEM) images reveal the LSC morphology at the macroscale, as depicted in **Figure 2.3a**. The non-graphitic nature of LSC is confirmed through X-ray diffraction (XRD) by exhibiting two broad peaks at approximately 23° and 43° , which correspond to the (002) and (100) reflections of hard carbons, as shown in **Figure 2.3b**.^[24] The average interlayer distance of the pseudo-graphitic stacking is found to be 0.39 nm, slightly larger than that of graphite (0.34 nm). This difference can be attributed in part to the structural impact of sulfur, as indicated in **Table 2.1**.^[25] Raman spectroscopy, displayed in **Figure 2.3c**, is utilized to assess the level of order in the carbonaceous materials. The *G* band at around 1600 cm^{-1} represents graphite-like sp^2 hybridization, while the *D* band at 1350 cm^{-1} represents disordered breathing mode oscillations.^[26] The I_D/I_G ratio is determined to be 1.0 based on the intensity of the fitted peaks, typical of non-graphitic carbon materials.

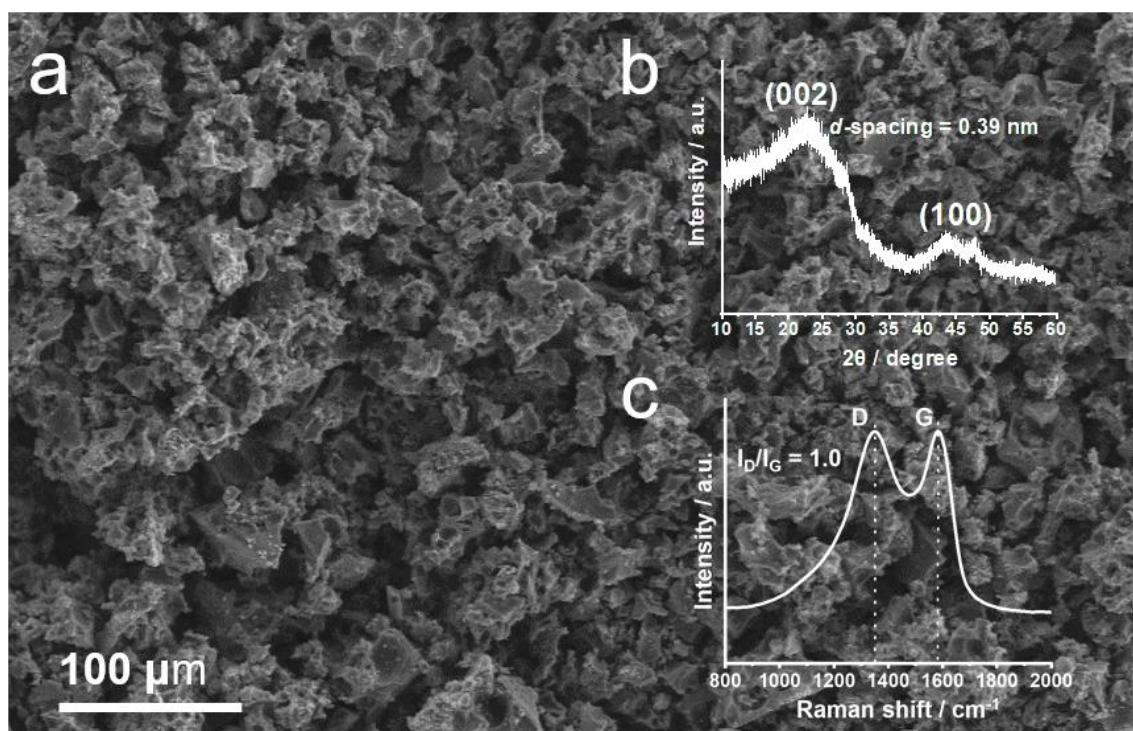


Figure 2.3. (a) SEM image depicting the final LSC powder. (b) XRD pattern with the calculated *d*-spacing from Bragg's law. (c) A Raman spectrum showing the I_D/I_G peak intensity ratio. (Copyright (2023) The Royal Society of Chemistry)

Table 2.1. Elemental compositions (wt. %) from EDX analysis.

Sample	C	O	N	S	Zn/Na
LSC	87.3 ± 2.7	4.4 ± 0.6	n/a	4.2 ± 1.5	4.1 ± 1.1
LSC/ThinCN	82.7 ± 3.7	1.7 ± 0.5	11.6 ± 2.8	1.3 ± 1.2	2.7 ± 0.6
LSC/MediumCN	71.5 ± 3.0	3.7 ± 0.3	17.7 ± 3.4	2.6 ± 1.1	4.5 ± 1.2
LSC/ThickCN	63.1 ± 3.2	3.6 ± 1.0	25.9 ± 3.3	3.0 ± 0.5	4.4 ± 3.4

Conformal α -SEI preparation – Following that, the LSC carbon material is introduced into the CVD system and coated with a CN layer of varying thicknesses. To achieve this, melamine is selected as the solid precursor for CN due to its cost-effectiveness, non-toxic nature, and relatively low sublimation temperature, making it a widely used precursor for the synthesis of CN materials.^[3h] The resulting samples represent different levels of CN layer thickness, as confirmed by examining cross-sectional transmission electron microscopy (TEM) images (**Figure 2.4a**). In the annular dark-field (ADF)-TEM images, the carbon nitride layers appeared brighter compared to the LSC material. Energy-dispersive X-ray (EDX) maps obtained from the same areas further validated that the bright regions corresponded to the denser CN layers, as N is contained only in the CN layer. Through analysis of image intensity contrast, the thicknesses of the CN layers were determined to be 10 ± 2 nm, 26 ± 6 nm, and 69 ± 14 nm for LSC/ThinCN, LSC/MediumCN, and LSC/ThickCN, respectively.

Valence electron energy loss (VEELS) spectral data cubes across the LSC/ThickCN sample are collected to understand the interface between LSC and CN better. These VEELS spectra illustrate the energy loss experienced by the electron beam as a result of inelastic scattering caused by the outer shell electrons of the material (**Figure 2.4b**), providing information about the valence electron density. The width of the VEELS peak reflects the damping effect observed in single-electron transitions.^[27] In the case of LSC, a peak at 6.0 eV was observed, which is characteristic of carbonaceous materials.^[28] On the other hand, the CN coating shows a peak at 4.5 eV, indicating that the electrons were displaced from the sample with lower energies compared to LSC (**Figure 2.4c**). Near the interface, the electron beam induced the flow of electron density from LSC towards CN, resembling the behavior observed in the depletion region of a Schottky contact, which effectively reduces the energy barrier at the interface. The maximum intensity of the peak showed a slight red shift, suggesting a coupling between the electronic states of CN and LSC. This electron flow from LSC to the CN layer, accompanied by the generation of a negative potential at the CN coating, is expected to enhance the transport of sodium towards the LSC electrode and improve the electrochemical properties. It is worth noting

that the electron density components are located outside the material, extending several nanometers, indicating the presence of transient low-energy electrons that are plasmonically or excitonically bound to the surface of the material.

The influence of the CN layer thickness on the morphology of the materials is examined using SEM. The findings indicate that the thinnest CN coating does not visibly alter the carbon surface morphology compared to the bare LSC material. However, as the amount of melamine and, consequently, the thickness of the CN film is increased, the LSC surface becomes entirely covered by a CN layer that is superimposed onto the carbon structure (**Figure 2.5a** and **Figure A2.2**). Elemental maps obtained through EDX analysis (**Figure 2.5b**) reveal that nitrogen is uniformly distributed on the carbon material without any

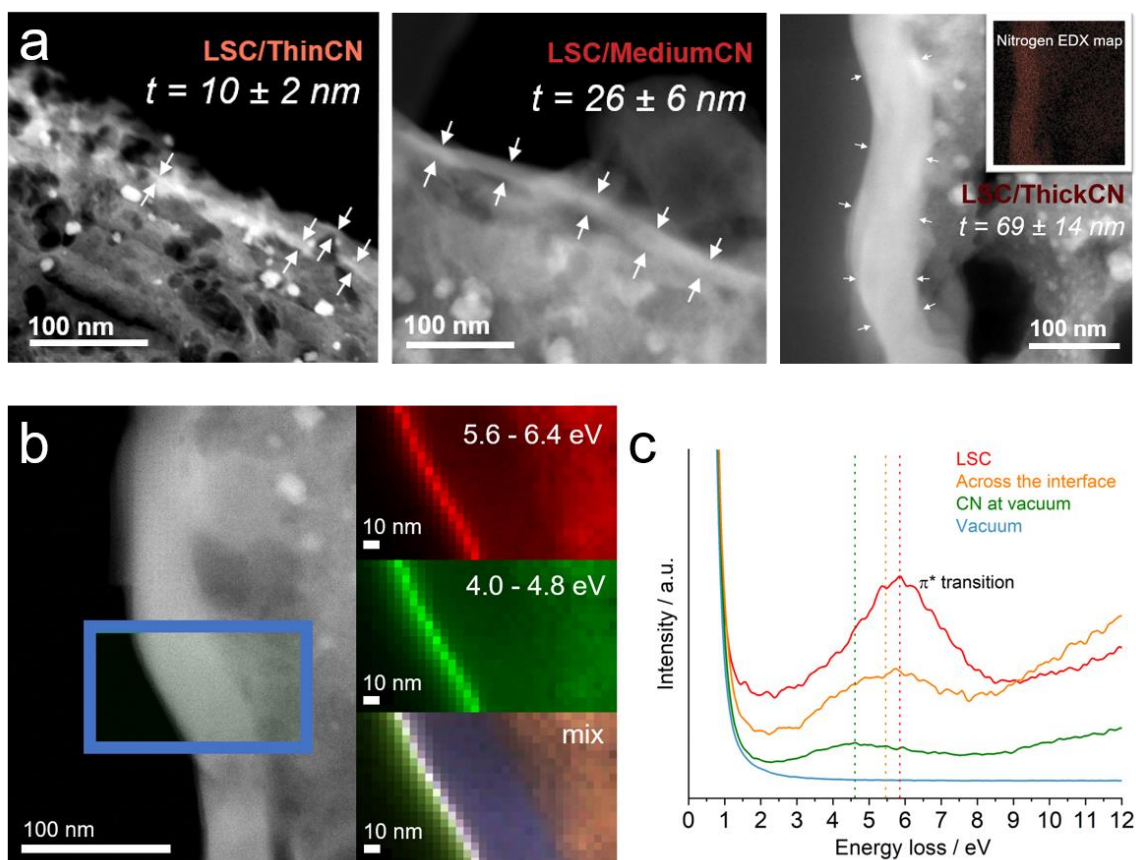


Figure 2.4. (a) The thicknesses of the CN layers determined by analyzing the intensity change in the images collected from different locations. (b) ADF-STEM image of the LSC/ThickCN sample. The area from which the VEELS spectral data cube is marked by a white rectangle. Spectral imaging maps for different energy windows (c) EELS spectra acquired at the vacuum region, CN, interface, and LSC are compared. (Copyright (2023) The Royal Society of Chemistry)

noticeable phase segregations. The nitrogen content increases as the thickness of the CN film increases (Figure 2.5a and Table 2.1).

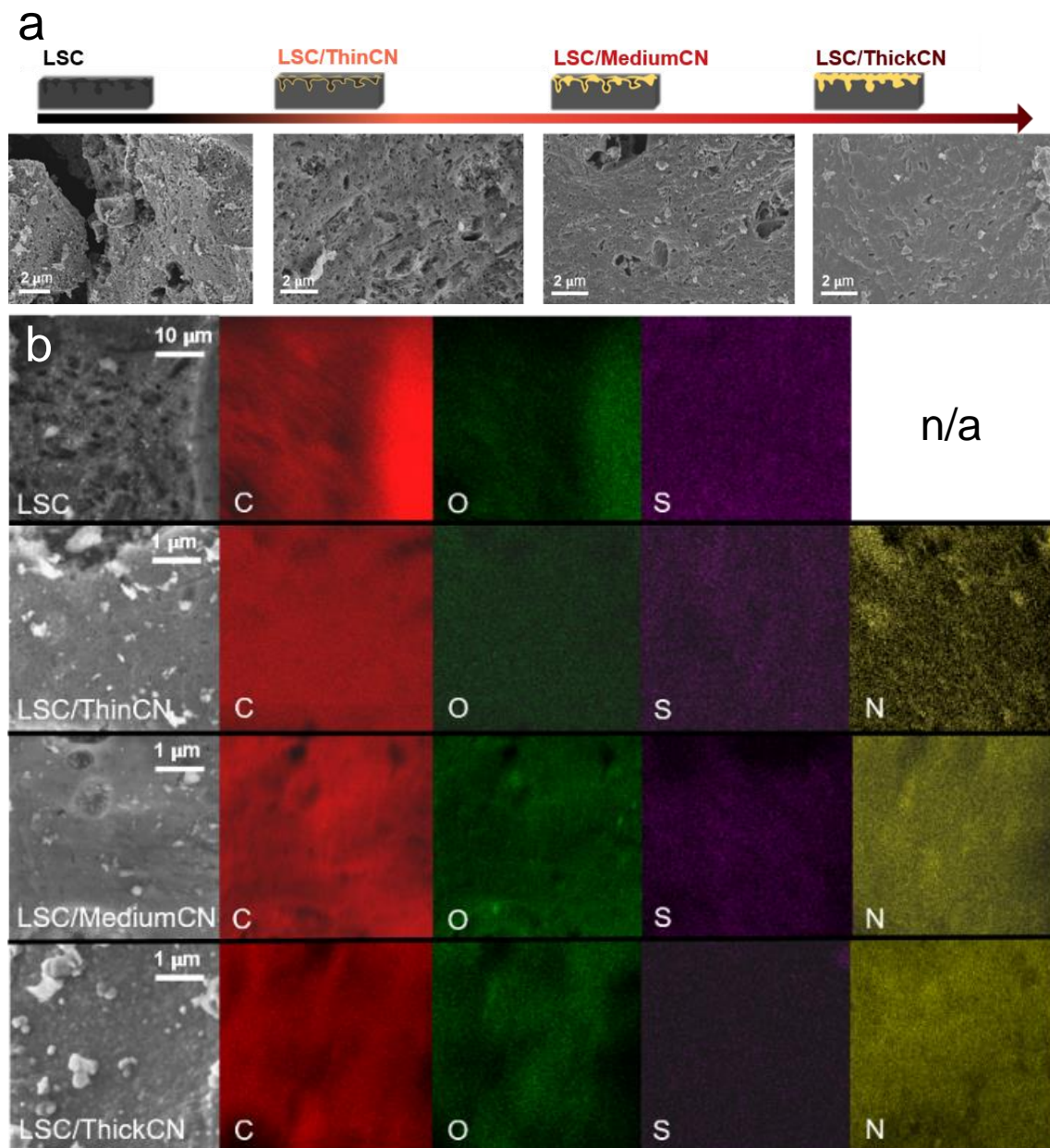


Figure 2.5. (a) A schematic diagram depicting the variation in CN layer thickness as a function of the amount of melamine precursor used is presented. The nitrogen content for each sample is determined by EDX. (b) Elemental mappings of C, O, S, and N, obtained from EDX, illustrate that these elements are homogeneously distributed along the framework without any significant localizations. (Copyright (2023) The Royal Society of Chemistry) (Copyright (2023) The Royal Society of Chemistry)

Note that the amount of N in the bare LSC is lower than the detection limit of the EDX (confirmed later via XPS), pointing to the increase in N content associated with the CN film on top. The bulk CN has characteristic peaks at 13.0° (100) and 27.5° (002) in the XRD pattern, the latter being more pronounced.^[29] After CN deposition on LSC, it is observed that the typical (002) peak of CN can be seen in the patterns (**Figure A2.3**). However, the (100) peak is not visible as (002) due to the significant contribution from LSC. Raman spectra (**Figure A2.4**) do not exhibit any significant differences.

Thermogravimetric analysis (TGA) is conducted under synthetic air and nitrogen atmospheres (**Figure A2.5**). The results indicated that the presence of the CN coating notably improves the thermal stability of the pristine LSC material. This enhancement demonstrates the close interaction between the two materials, leading to a higher thermal degradation resistance than their individual components. This behavior is characteristic of composite materials, where the combination of different constituents results in improved thermal properties.^[3c, 3f] As an illustration, composite materials, such as LSC/ThinCN, demonstrate a remarkable increase in thermal stability when exposed to air. At 900°C , approximately 24% of the composite material remains, whereas the pristine LSC carbon only retains about 10% under the same conditions (**Figure A2.5**). This observation is noteworthy, considering that the CN thin films completely decompose at a lower temperature of 650°C under synthetic air. The enhanced thermal stability exhibited by the composite material highlights the synergistic effect between LSC and CN, resulting in improved resistance to high-temperature degradation.^[3f]

The N_2 sorption isotherms, specifically Type IV isotherms (**Figure A2.6**), indicate that both the pristine LSC and the composite materials possess a mesoporous structure. This is characterized by multilayer adsorption of nitrogen followed by capillary condensation within the mesopores. Using the density-functional-theory (DFT) model, the nitrogen available surface area of the pure LSC is determined to be $498 \text{ m}^2 \text{ g}^{-1}$. However, as the thickness of the CN film increases, this surface area is reduced to $4 \text{ m}^2 \text{ g}^{-1}$. This reduction confirms the growth of the CN thin film and the subsequent decrease in the available surface area for nitrogen adsorption. The decrease in the nitrogen-available surface area also limits the surface available for the growth of the natural passivation layer, known as the solid-electrolyte interphase (SEI), which typically forms on the electrode's surface during initial sodiation.^[30] When comparing the cumulative micropore volume ($d_{\text{pore}} < 2.0 \text{ nm}$) of LSC and LSC/ThinCN, the difference is found to be minimal (**Figure 2.6a**). CO_2 sorption experiments are conducted at room temperature (**Figure A2.7**) to investigate the microporous surface area.^[31] Generally, the CN coating layer reduces the volume of micropores, except for the CO_2 -accessible ultramicropore volume ($d_{\text{pore}} < 0.7 \text{ nm}$) of LSC/ThinCN, which remains similar to that of LSC. However, as the coating thickness

increases, a barrier forms ahead of the ultramicroporous texture, significantly reducing the CO₂-accessible area for both LSC/MediumCN and LSC/ThickCN (**Figure 2.6a**).

The chemical composition and states of the CN film deposited on LSC are verified using X-ray photoelectron spectroscopy (XPS) and Fourier-transform infrared spectroscopy (FTIR). In the N1s core level deconvolution (**Figure 2.6b**), the peak at 400.9 eV is attributed to terminal amino groups (-NH_x), while the peaks at 399.4 eV and 398.6 eV correspond to central heptazine-based nitrogen (N-(C)₃) and aromatic nitrogen (C=N-C), respectively.^[32] The ratio of aromatic to central nitrogen remains constant, indicating that the film maintains its structural integrity without an increase in terminal edge groups associated with defect sites. Furthermore, XPS analysis of pure LSC before CN deposition reveals negligible nitrogen content (**Figure A2.8**), supporting the findings from EDX analysis (**Table 2.1**). The pristine LSC material exhibits sulfur features in the form of -C-SO_x and -C-S- states (**Figure A2.8**). The features at approximately 170 eV are attributed to -C-SO_x units, while those around 164 eV correspond to covalent -C-S- bonds of the thiophene type.^[24a, 25b, 33] The sulfur content in LSC is estimated to be approximately 4.1 wt. %. In the C1s spectra (**Figure 2.6c**), the peak at 284.6 eV is assigned to C-C bonds, while the peaks at 286.4 eV and 288.3 eV are associated with the carbon bonds to amino-terminal groups and heptazine rings (-N=C-N-), respectively.^[3h] The chemical structure of

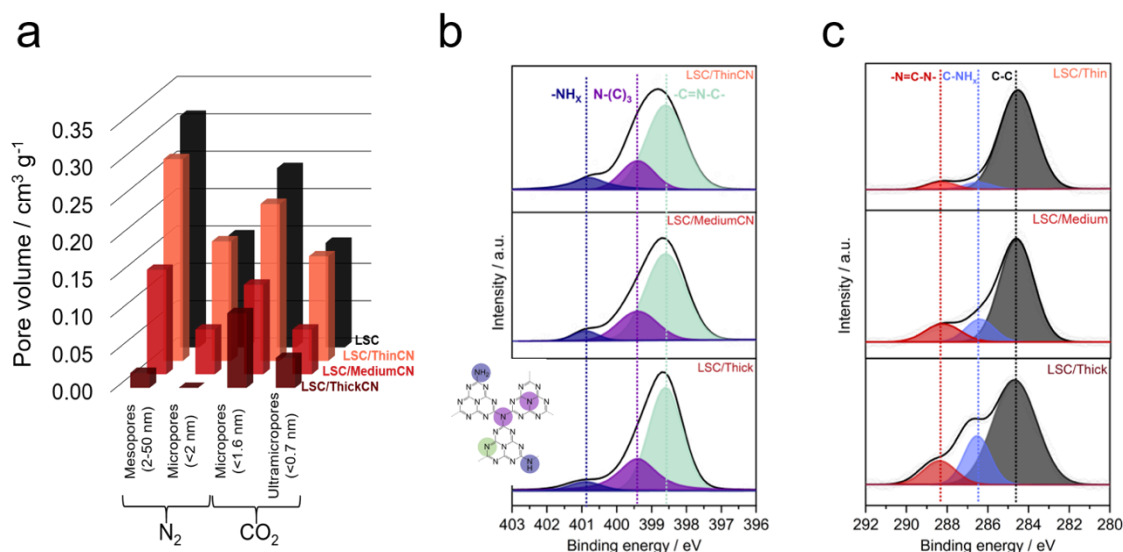


Figure 2.6. (a) The cumulative meso- and micro-pore volumes of the materials from N₂ and CO₂ physisorption. (b) The XPS N1s core levels of the materials, and the corresponding chemical structure of the CN-cycle (inset). (c) The C1s core levels of materials. Increasing the coating thickness leads to a decrease in the signal from pristine LSC, resulting significant increase in C-NH_x and CN₂ to C-C ratio. (Copyright (2023) The Royal Society of Chemistry)

the films is further examined using FTIR (**Figure A2.9**). While the pristine LSC material does not exhibit distinct features in the IR range, the introduction of the CN film with increasing thickness results in the emergence of characteristic CN peaks. The observed peaks, such as the CN-heterocycle heptazine breathing mode (810 cm^{-1}) and the CN-cycle vibrations (1258 cm^{-1} to 1630 cm^{-1}), are consistent with previous reports on CN materials.^[34]

2.3.2. Sodium storage behavior of materials

CN thickness effect on electrochemical impedance spectroscopy (EIS) – The impact of CN thickness on electrochemical impedance spectroscopy (EIS) is investigated to assess the overall resistance of the electrode and the contribution of the CN coating. **Figure 2.7** demonstrates that EIS is conducted on the electrodes to compare the equivalent series resistance (ESR), which combines the resistances from the bulk electrolyte and the electrode itself among varying CN thicknesses. Analysis of the Randles circuit model reveals that the difference in ESR is negligible across the electrodes with different CN thicknesses (R_2 , **Table 2.2**). However, the results indicate that the deposition of a 69 nm-thick CN layer raises the charge transfer resistance from 86.8 Ohm cm^{-2} to 396.5 Ohm cm^{-2} (R_1 , **Table 2.2**). This substantial increase is attributed to the insulating behavior of the CN layer.^[3c]

Galvanostatic charge and discharge (GCD) measurements – The initial galvanostatic charge-discharge (GCD) curves presented in **Figure 2.8a** demonstrate that the application of a CN coating enhances the initial coulombic efficiency (ICE) of the active electrode material. In its pristine form, the LSC electrode exhibits a modest ICE of 25%. However, when coated with CN, the LSC electrode consistently achieves an ICE of over 40%. This improvement validates the notion that a durable CN coating limits the surface area of the electrode available for electrolyte decomposition, thereby mitigating the formation of the

Table 2.2. Internal and charge transfer resistivities of materials from Randles circuit model.

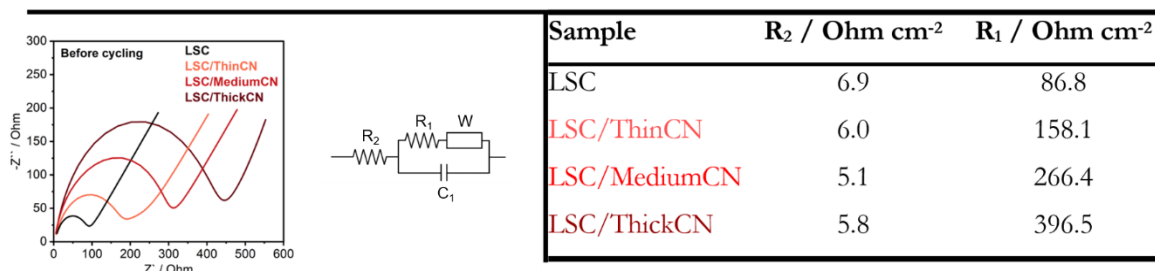


Figure 2.7. Nyquist plots of the materials before cycling and relative Randles circuit model. (Copyright (2023) The Royal Society of Chemistry)

SEI layer.^[35] After the stable formation of the SEI layer, the reversible capacities of electrodes are as follows: LSC (214 mAh g⁻¹), LSC/ThinCN (275 mAh g⁻¹), LSC/MediumCN (220 mAh g⁻¹), and LSC/ThickCN (190 mAh g⁻¹), all measured at 30 mA g⁻¹ during the 10th cycle (**Figure 2.8b**). In all cases, Coulombic efficiencies surpass 99%. Interestingly, the deposition of a 10 nm-thick and uniformly distributed CN film positively influences the sodium storage capacity, increasing it by more than 30%. This outcome indicates that the artificial passivation layer has an electronic impact on the carbon electrode, particularly in the non-capacitive Faradaic storage mode. A significant enhancement in battery performance is observed by controlling the film thickness during CVD. The structural characteristics of the materials and the electronic/chemical interactions between the CN film and the electrode create synergies that enhance the sodium storage performance. Similar to other multilayer configurations,^[3g] the carbon electrode, with its high electron mobility, rapidly transfers electrons to the CN layer, which possesses a relatively positive work function, establishing a Schottky transfer layer.^[36] This LSC/CN electrode, with a thickness of approximately 10 nm (comparable to the Schottky length), exhibits the lowest charge transfer resistivity compared to other CN-coated electrodes. The electron-rich CN layer then attracts sodium ions, which are subsequently directed toward the carbon electrode for storage. In this process, sodium ions undergo reduction to sodium metal close to 0 V (vs. Na⁺/Na). The resulting electron-rich sodium species then donate electrons back to the carbon electrode, which, in turn, transfers its electron to the CN layer, completing the cycle. This polarization-backdonation-stabilization effect explains to the broader plateau with minimal changes in the capacitive range at lower potentials below 1.0 V (vs. Na⁺/Na). However, as the thickness of the CN layer increases, this effect diminishes and eventually reverses due the

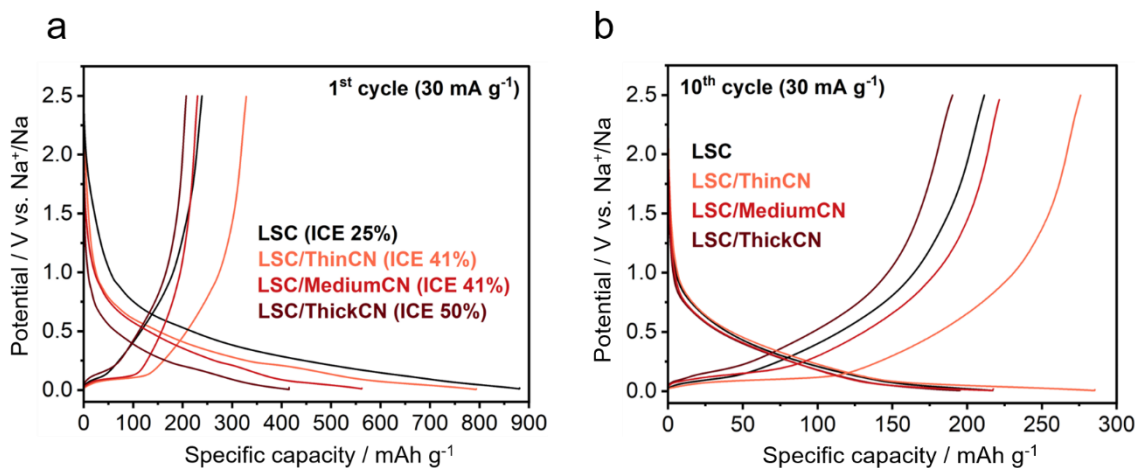


Figure 2.8. (a) The initial and (b) 10th cycles of the half-cells at 30 mA g⁻¹. (Copyright (2023) The Royal Society of Chemistry)

charge transfer resistivity. Importantly, the improved electrochemical performance cannot be attributed to the vacuum thermal treatment during the CVD process or the contributions solely from the CN material. To demonstrate that the observed enhancement in sodium storage performance is indeed a result of the heterojunction effect, pure LSC material undergoes the same heat treatment without the presence of the melamine precursor, thus avoiding the deposition of any CN film. This experiment (**Figure A2.10**) reveals a decrease in capacity for the pristine LSC material while the ICE remains similar. This finding reinforces the idea that the substantial improvement in electrochemical performance is indeed due to the presence of the conformal CN layer. Furthermore, it is observed that bulk CN material makes a negligible contribution to sodium storage (**Figure A2.10**) due to its high electrical resistivity, making it unsuitable as an active material for sodium storage under the same electrochemical conditions. Eventually, the observed enhancement in electrochemical performance arises from the synergistic contribution between LSC and CN materials rather than from the properties of each material individually.

Rate performance – At higher current densities, where electrodes primarily rely on pseudo-capacitive storage, the introduction of a CN coating enhances the rate capability of pristine LSC, as depicted in **Figure 2.9**. For example, when charged at rates of 300 mA g^{-1} and 600 mA g^{-1} , the specific capacity of pristine LSC is doubled when combined with ThinCN. Also, even though the storage capacities of pristine LSC and LSC/MediumCN are similar at 30 mAh g^{-1} , LSC/MediumCN exhibits superior rate performance at higher current densities due to the presence of the CN film.

The plateau capacity, resulting from the intercalation of sodium ions within planes and micropores found in the disordered carbons, is achieved when low-energy supercapacitive adsorption reaches saturation, as depicted by the intercalation/filling-based model. This model suggests that the effect of the CN film on the supercapacitive mode, represented by

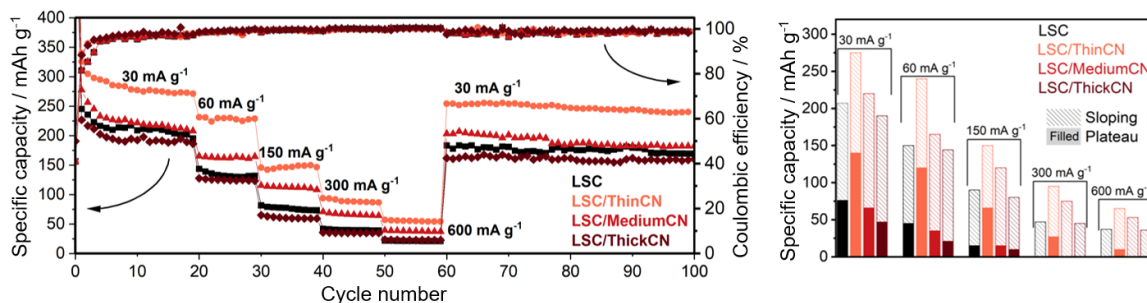


Figure 2.9. Rate capability performance of materials and associated column chart showing distribution of plateau and sloping capacities. (Copyright (2023) The Royal Society of Chemistry)

the sloping region of the GCD curve, is negligible as the electrodes display almost identical sloping behavior. However, a substantial change in performance, primarily in the plateau region, is observed at approximately 0.1 V (vs. Na⁺/Na), where the plateau capacity of pristine LSC is extended from 80 mAh g⁻¹ (a total of 214 mAh g⁻¹) to 140 mAh g⁻¹ (a total of 275 mAh g⁻¹).

Evaluating the sodium storage mechanism using cyclic voltammetry (CV) – CV with the different scan rates is used for the evaluation of the ion storage mechanism (**Figure 2.10a**).^[37] An analysis is achieved by plotting the “log(*i*, peak anodic current)” versus “log(*v*, scan rate)” (Eq. 2.1).

$$i = av^b \quad (2.1)$$

A slope “*b*-value” value close to 1 indicates a convective storage mechanism related to surface-controlled processes. Conversely, bulk-diffusion-controlled mechanisms exhibit *b*-values close to 0.5.^[38] Here, “*b*-values” (**Figure 2.10b**) for LSC and LSC/ThinCN are 0.65 and 0.55, respectively. This is consistent with the GCD data revealing the extended plateau region of the LSC/ThinCN is related to diffusion-controlled storage.

Sodium ion diffusion coefficients from galvanostatic intermittent titration technique (GITT) – The “apparent sodium-ion diffusion” coefficients are determined via the GITT measurements. The GITT is a convenient method for estimating the ion diffusion coefficients in electrochemical environments. However, it relies on certain assumptions and estimations based on Fick’s law of diffusion. Here, it has been confirmed that the potential response shows a linear correlation when plotted against the square root of the

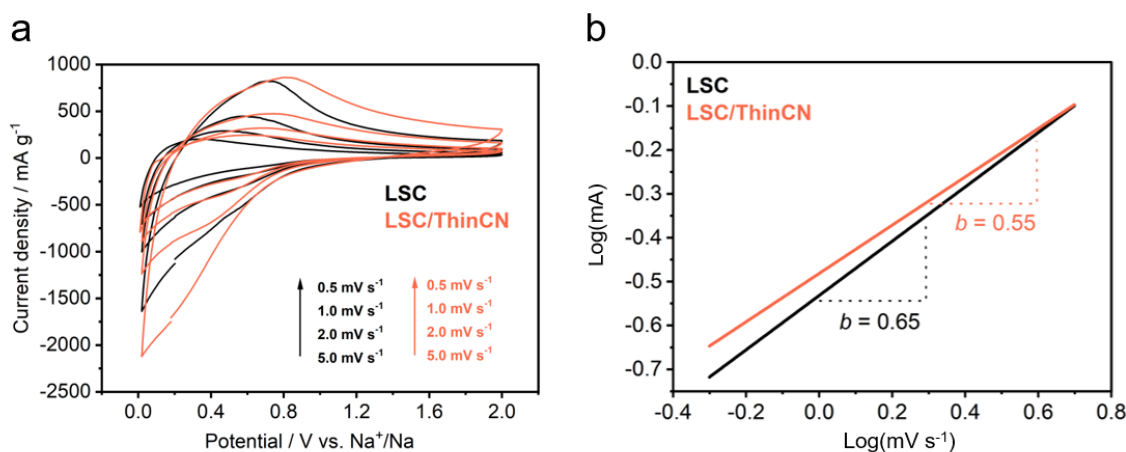


Figure 2.10. (a) CV plots of LSC and LSC/ThinCN with different scan rates. (b) log(*i*, peak anodic current) vs. log(*v*, scan rate) plots of LSC and LSC/ThinCN from CV. (Copyright (2023) The Royal Society of Chemistry)

step time, as shown in **Figure A2.11**. Consequently, the “first-order approximation” proposed by Weppner and Huggins can be employed for these materials.^[39] This approximation is applicable to both spherical and planar geometries. However, it is important to note that this approach relies on a set of assumptions.^[40]

- i. The step time is significantly shorter than the effective diffusion time.
- ii. The transient data is sufficiently extensive to exclude ohmic and kinetic overpotential.

The diffusion coefficients from GITT can be calculated using the simplified equation (Eq. 2.2) based on these assumptions.

$$D_{Na} = \frac{4}{\pi\tau} \left(\frac{m_B V_M}{M_B S} \right)^2 \left(\frac{\Delta E_S}{\Delta E_\tau} \right)^2 \quad (2.2)$$

In the equation, τ represents the pulse duration, m_B and M_B denote the actual and molar mass of the active material, respectively. V_m is the molar volume, while S denotes the surface area of the electrodes. Therefore, $(m_B V_M / M_B)$ corresponds to the electrode volume, and dividing it by S yields the electrode thickness. The changes in steady-state voltage (ΔE_S) and cell voltage (ΔE_τ) during a single GITT pulse can be obtained from the typical GITT curve of the material, as illustrated in **Figure 2.11a** and **Figure 2.11b**.^[41] The diffusion coefficients are calculated from 1.0 to 0.2 V (vs. Na⁺/Na) with a step size of 0.05 V. According to **Figure 2.11c**, the diffusion coefficients of the materials exhibit variations within the range of 10⁻⁹ and 10⁻¹¹ cm² s⁻¹, depending on the potential of sodiation and desodiation. During the sodiation, the diffusion coefficients of LSC/MediumCN and LSC/ThickCN are significantly lower compared to those of LSC and LSC/ThinCN. However, during desodiation, there is a noticeable decrease in the diffusion coefficient of

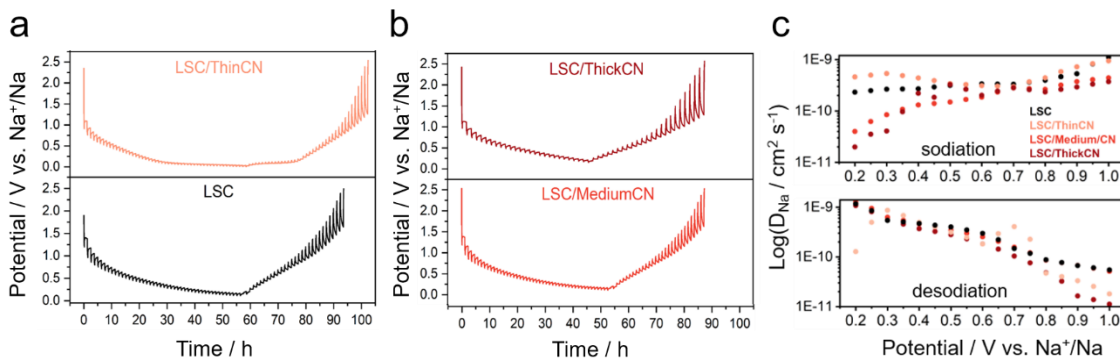


Figure 2.11. GITT profiles of the (a) LSC and LSC/ThinCN; (b) LSC/MediumCN and LSC/ThickCN during sodiation and desodiation at 30 mA g⁻¹. (c) Variation of material diffusion coefficients obtained from GITT as a function of sodiation and desodiation potentials. (Copyright (2023) The Royal Society of Chemistry)

LSC/ThinCN, indicated by the plateau around 0.3 V (vs. Na⁺/Na). This behavior has been previously documented and attributed to the occurrence of specific electrochemical reactions^[41b, 42] (such as the oxidation/reduction of sodium) that occur only for LSC/ThinCN in this particular case.

Based on the analysis conducted, it is argued that the CN coating serves multiple purposes. Firstly, it acts as an artificial interphase, providing mechanical stability, ionic conductivity, and chemical passivation.^[3g, 3h, 43] Additionally, the CN coating plays a crucial role in reducing the plateau potential through the heterojunction effect at the interface. This is facilitated by the charge transfer from carbon nitride to the LSC carbon, thereby increasing the number of accessible active sites in the underpotential mode. In these findings, it is proposed to label this type of interphase as an “inter-active interphase.” The improved storage of sodium ions, which leads to a significant portion of capacity being stored at approximately 0.1 V (vs. Na⁺/Na), enhances the expected energy density in the full-cell configuration.

Long-term stability – To assess the durability of the electrodes, both LSC and LSC/ThinCN undergo 1000 cycles at a rate of 300 mA g⁻¹, as depicted in **Figure 2.12**. The capacity retentions of LSC and LSC/ThinCN are 88% and 78%, respectively. The higher capacity retention of the pristine LSC electrode can be attributed to the predominant pseudo-capacitive adsorption of sodium ions, which is less detrimental to the electrode structure compared to the slower process of ion insertion that can lead to localized disruptions of graphitic-like domains in carbons.^[44] Nevertheless, LSC/ThinCN still provides a 65% higher capacity at the 1000th cycle compared to pure LSC.

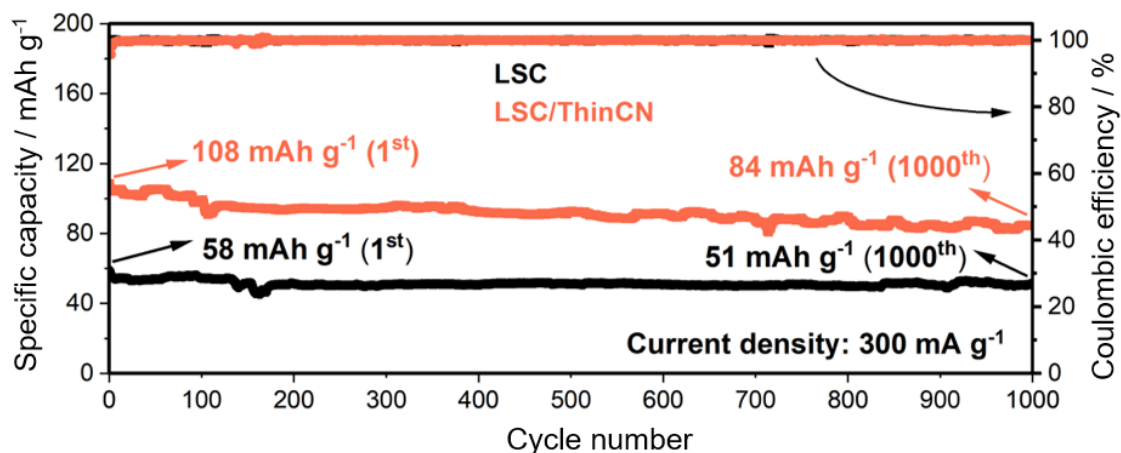


Figure 2.12. The durability of LSC and LSC/ThinCN electrodes is evaluated through stability tests involving 1000 cycles at a constant current density of 300 mA g⁻¹. (Copyright (2023) The Royal Society of Chemistry)

The application of a conformal coating made of CN plays a crucial role in enhancing the electrochemical properties of carbon obtained from sustainable sources. The thickness of the coating is identified as a critical parameter for improving sodium storage, particularly in the non-capacitive Faradaic storage mode. This improvement can be attributed to the heterojunction effect between CN and lignosulfonate-derived carbon. Unlike noble carbon, lignosulfonate-derived carbon is a reductive carbon with a higher Fermi level compared to the α -SEI.^[3h, 22a, 45] As a result, LSC donates electrons to CN, leading to sodium ions accumulation through the polarization effect, as illustrated in **Figure 2.13**. The positive polarization of LSC facilitates the stabilization of reduced sodium at the solid-solid interface, creating a polarization-backdonation-stabilization effect that enhances sodium storage in the composite electrode. The charge transfer and increased polarity also improve the ion transfer by enhancing wettability, adsorption enthalpy, and intercalation. However, excessively thick CN layers can hinder diffusion and shift the dominant storage mechanism from diffusion-controlled to surface-controlled. In **Figure 2.13**, the proportion of plateau capacity in pristine LSC increases from 36% to 51% with a thin CN coating, but further deposition reduces its contribution to only 25%.

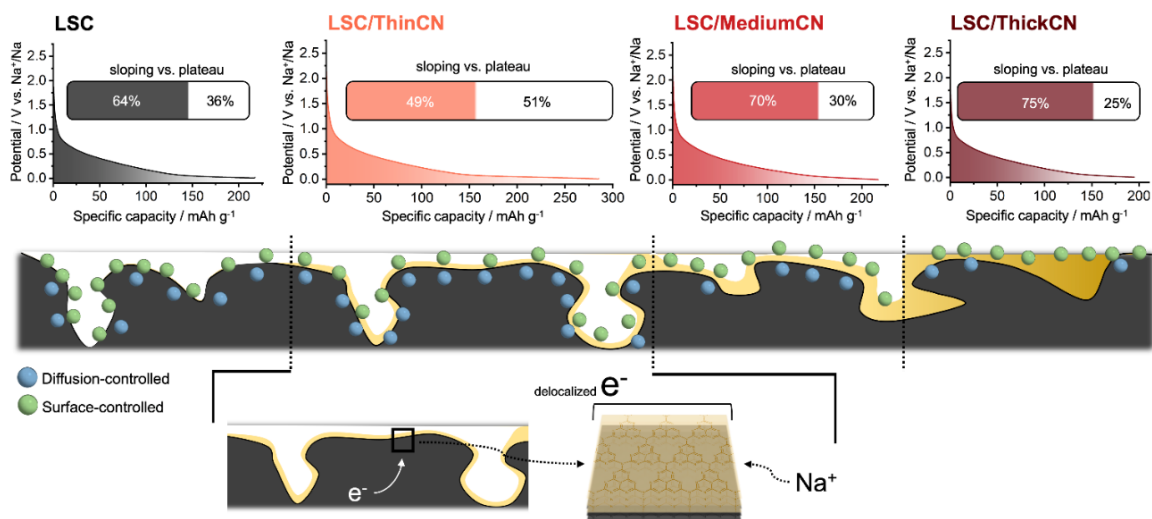


Figure 2.13. At 30 mA g⁻¹, the sodiation curves provide insight into the impact of sloping and plateau capacities on sodium storage. Additionally, illustration of how sodium is accumulated at the interface. (Copyright (2023) The Royal Society of Chemistry)

2.4. Conclusions

The composite material consisting of carbon and CN exhibits remarkable improvements in various electrochemical performance metrics such as ICE, rate capability, and total specific capacity when a 10 nm thickness of the CN film is applied. Importantly, the plateau capacity of the original electrode is extended significantly, indicating a potential increase in energy density for full-cell devices as the *a*-CN layer exhibits a negligible increase in the electrode's weight. The effective utilization of the heterojunction effect at the interfaces between materials is made possible by combining reductive carbon with precisely controlled deposition of the CN film. Going beyond this thickness does not enhance the overall specific capacity and diffusion-controlled sodium storage, but it does improve the rate capability compared to the pristine lignosulfonate-derived carbon. In particular, the thin CN film shows promise as an artificial interphase, enhancing the sodium storage performance of carbon-based anode materials derived from abundant sources and industrial byproducts.

Bibliography for Chapter 2

- [1] E. O. Eren, E. Senokos, Z. Song, E. B. Yılmaz, I. Shekova, B. Badamdorj, I. Lauermann, N. V. Tarakina, M. Al-Naji, M. Antonietti, P. Giusto, *J. Mater. Chem. A* **2023**, *11* (3), 1439-1446.
- [2] a) J. H. Song, B. W. Xiao, Y. H. Lin, K. Xu, X. L. Li, *Adv. Energy Mater.* **2018**, *8* (17), 1703082; b) C.-C. Wang, W.-L. Su, *ACS Appl. Energy Mater.* **2021**, *5* (1), 1052-1064; c) Q. W. Chen, H. He, Z. Hou, W. M. Zhuang, T. X. Zhang, Z. Z. Sun, L. M. Huang, *J. Mater. Chem. A* **2020**, *8* (32), 16232-16237; d) J. Lee, J. Kim, S. Kim, C. Jo, J. Lee, *Mater. Adv.* **2020**, *1* (9), 3143-3166; e) C. X. Yu, Y. Li, H. X. Ren, J. Qian, S. Wang, X. Feng, M. Q. Liu, Y. Bai, C. Wu, *Carbon Energy* **2022**, *n/a* (n/a); f) G.-H. Lee, T. Hwang, J.-B. Kim, J. Yang, F. Zou, M. Cho, Y.-M. Kang, *J. Mater. Chem. A* **2022**, *10* (31), 16506-16513.
- [3] a) J. Wu, L. Tian, H. Duan, Y. Cheng, L. Shi, *ACS Appl. Mater. Interfaces* **2021**, *13* (39), 46821-46829; b) K. Schutjajew, P. Giusto, E. Hark, M. Oschatz, *Carbon* **2021**, *185*, 697-708; c) J. Liu, H. Wang, M. Antonietti, *Chem. Soc. Rev.* **2016**, *45* (8), 2308-2326; d) V. W. h. Lau, B. V. Lotsch, *Adv. Energy Mater.* **2021**, *12* (4), 2101078; e) P. Zhai, T. Wang, H. Jiang, J. Wan, Y. Wei, L. Wang, W. Liu, Q. Chen, W. Yang, Y. Cui, Y. Gong, *Adv. Mater.* **2021**, *33* (13), e2006247; f) P. Giusto, B. Kumru, J. Zhang, R. Rothe, M. Antonietti, *Chem. Mater.* **2020**, *32* (17), 7284-7291; g) L. Chen, R. Yan, M. Oschatz, L. Jiang, M. Antonietti, K. Xiao, *Angew. Chem. Int. Ed.* **2020**, *59* (23), 9067-9073; h) P. Giusto, D. Cruz, T. Heil, H. Arazoe, P. Lova, T. Aida, D. Comoretto, M. Patrini, M. Antonietti, *Adv. Mater.* **2020**, *32* (10), e1908140.
- [4] M. Hankel, D. Ye, L. Wang, D. J. Searles, *J. Phys. Chem. C* **2015**, *119* (38), 21921-21927.
- [5] a) T. Aro, P. Fatehi, *ChemSusChem* **2017**, *10* (9), 1861-1877; b) F. Brandi, M. Antonietti, M. Al-Naji, *Green Chem.* **2021**, *23* (24), 9894-9905.
- [6] a) H. Y. Jung, J. S. Lee, H. T. Han, J. Jung, K. Eom, J. T. Lee, *Polymers (Basel)* **2022**, *14* (4); b) C. Matei Ghimbeu, B. Zhang, A. Martinez de Yuso, B. Réty, J.-M. Tarascon, *Carbon* **2019**, *153*, 634-647; c) L. Mo, S. Jia, S. Lin, Z. Shao, F. Wang, *Int. J. Energy Res.* **2022**, *46* (3), 2373-2384.
- [7] A. K. Geim, K. S. Novoselov, *Nat. Mater.* **2007**, *6* (3), 183-191.
- [8] G. Algara-Siller, N. Severin, S. Y. Chong, T. Björkman, R. G. Palgrave, A. Laybourn, M. Antonietti, Y. Z. Khimyak, A. V. Krashennikov, J. P. Rabe, U. Kaiser, A. I. Cooper, A. Thomas, M. J. Bojdys, *Angew. Chem. Int. Ed.* **2014**, *53* (29), 7450-7455.
- [9] J. Zhang, X. Chen, K. Takanabe, K. Maeda, K. Domen, J. D. Epping, X. Fu, M. Antonietti, X. Wang *Angew. Chem. Int. Ed.* **2010**, *49* (2), 441-444.
- [10] V. W.-h. Lau, B. V. Lotsch, *Adv. Energy Mater.* **2022**, *12* (4), 2101078.
-

-
- [11] E. Kroke, M. Schwarz, *Coord. Chem. Rev.* **2004**, 248 (5), 493-532.
- [12] a) A. Y. Liu, M. L. Cohen, *Science* **1989**, 245 (4920), 841-842; b) D. M. Teter, R. J. Hemley, *Science* **1996**, 271 (5245), 53-55.
- [13] J. Liu, H. Wang, M. Antonietti, *Chem. Soc. Rev.* **2016**, 45 (8), 2308-2326.
- [14] S. T. A. G. Melissen, S. N. Steinmann, T. Le Bahers, P. Sautet, *J. Phys. Chem. C* **2016**, 120 (43), 24542-24550.
- [15] a) A. Thomas, A. Fischer, F. Goettmann, M. Antonietti, J.-O. Müller, R. Schlögl, J. M. Carlsson, *J. Mater. Chem.* **2008**, 18 (41), 4893-4908; b) X. Wang, S. Blechert, M. Antonietti, *ACS Catalysis* **2012**, 2 (8), 1596-1606.
- [16] a) J. Wu, Z. Liu, X. Lin, E. Jiang, S. Zhang, P. Huo, Y. Yan, P. Zhou, Y. Yan, *Nat. Commun.* **2022**, 13 (1), 6999; b) Q. Lu, K. Eid, W. Li, A. M. Abdullah, G. Xu, R. S. Varma, *Green Chem.* **2021**, 23 (15), 5394-5428.
- [17] X. Zhang, H. Wang, H. Wang, Q. Zhang, J. Xie, Y. Tian, J. Wang, Y. Xie, *Adv. Mater.* **2014**, 26 (26), 4438-4443.
- [18] S. M. Rosnagel, *J. Vac. Sci. Technol. A* **2003**, 21 (5), S74-S87.
- [19] J. E. Crowell, *J. Vac. Sci. Technol. A* **2003**, 21 (5), S88-S95.
- [20] a) Y. Li, D. Mann, M. Rolandi, W. Kim, A. Ural, S. Hung, A. Javey, J. Cao, D. Wang, E. Yenilmez, Q. Wang, J. F. Gibbons, Y. Nishi, H. Dai, *Nano Lett.* **2004**, 4 (2), 317-321; b) M. J. Bozack, L. Muehlhoff, J. N. Russell, Jr., W. J. Choyke, J. T. Yates, Jr., *J. Vac. Sci. Technol. A* **1987**, 5 (1), 1-8; c) G. Su, V. G. Hadjiev, P. E. Loya, J. Zhang, S. Lei, S. Maharjan, P. Dong, P. M. Ajayan, J. Lou, H. Peng, *Nano Lett.* **2015**, 15 (1), 506-513.
- [21] M. Ohring, in *Materials Science of Thin Films (Second Edition)* (Ed.: M. Ohring), Academic Press, San Diego, **2002**, pp. 277-355.
- [22] a) F. Brandi, M. Bäuml, V. Molinari, I. Shekova, I. Laueremann, T. Heil, M. Antonietti, M. Al-Naji, *Green Chem.* **2020**, 22 (9), 2755-2766; b) M. Al-Naji, F. Brandi, B. Kumru, M. Antonietti, *ChemCatChem* **2022**, n/a (n/a).
- [23] R. B. Gordon, T. E. Graedel, M. Bertram, K. Fuse, R. Lifset, H. Rechberger, S. Spatari, *Resour., Conserv. Recycl.* **2003**, 39 (2), 107-135.
- [24] a) L. Qie, W. Chen, X. Xiong, C. Hu, F. Zou, P. Hu, Y. Huang, *Adv. Sci.* **2015**, 2 (12), 1500195; b) C. Li, Y. Sun, Q. Wu, X. Liang, C. Chen, H. Xiang, *Chem. Commun. (Camb)* **2020**, 56 (45), 6078-6081.
- [25] a) J. Yang, X. Zhou, D. Wu, X. Zhao, Z. Zhou, *Adv. Mater.* **2017**, 29 (6), 1604108; b) W. Li, M. Zhou, H. Li, K. Wang, S. Cheng, K. Jiang, *Energy Environ. Sci.* **2015**, 8 (10), 2916-2921.
-

-
- [26] A. C. Ferrari, J. Robertson, *Phys. Rev. B* **2000**, *61* (20), 14095-14107.
- [27] R. F. Egerton, in *Electron Energy-Loss Spectroscopy in the Electron Microscope* (Ed.: R. F. Egerton), Springer US, Boston, MA, **2011**, pp. 419-422.
- [28] L. Calliari, S. Fanchenko, M. Filippi, *Carbon* **2007**, *45* (7), 1410-1418.
- [29] F. Fina, S. K. Callear, G. M. Carins, J. T. S. Irvine, *Chem. Mater.* **2015**, *27* (7), 2612-2618.
- [30] a) W. Luo, C. Bommier, Z. Jian, X. Li, R. Carter, S. Vail, Y. Lu, J. J. Lee, X. Ji, *ACS Appl. Mater. Interfaces* **2015**, *7* (4), 2626-2631; b) B. H. Hou, Y. Y. Wang, Q. L. Ning, W. H. Li, X. T. Xi, X. Yang, H. J. Liang, X. Feng, X. L. Wu, *Adv. Mater.* **2019**, *31* (40), e1903125.
- [31] a) A. Beda, C. Vaulot, C. Matei Ghimbeu, *J. Mater. Chem. A* **2021**, *9* (2), 937-943; b) J. Yang, X. Wang, W. Dai, X. Lian, X. Cui, W. Zhang, K. Zhang, M. Lin, R. Zou, K. P. Loh, Q.-H. Yang, W. Chen, *Nano-Micro Lett.* **2021**, *13* (1), 98-98; c) S.-W. Zhang, W. Lv, C. Luo, C.-H. You, J. Zhang, Z.-Z. Pan, F.-Y. Kang, Q.-H. Yang, *Energy Storage Mater.* **2016**, *3*, 18-23.
- [32] a) J. Li, B. Shen, Z. Hong, B. Lin, B. Gao, Y. Chen, *Chem. Commun. (Camb)* **2012**, *48* (98), 12017-12019; b) A. Thomas, A. Fischer, F. Goettmann, M. Antonietti, J. O. Muller, R. Schlogl, J. M. Carlsson, *J. Mater. Chem.* **2008**, *18* (41), 4893-4908; c) J. Yu, K. Wang, W. Xiao, B. Cheng, *Phys. Chem. Chem. Phys.* **2014**, *16* (23), 11492-11501.
- [33] T. Wu, M. Jing, L. Yang, G. Zou, H. Hou, Y. Zhang, Y. Zhang, X. Cao, X. Ji, *Adv. Energy Mater.* **2019**, *9* (9), 1803478-1803478.
- [34] a) M. Shen, L. X. Zhang, M. Wang, J. J. Tian, X. X. Jin, L. M. Guo, L. Z. Wang, J. L. Shi, *J. Mater. Chem. A* **2019**, *7* (4), 1556-1563; b) M. Kim, S. Hwang, J. S. Yu, *J. Mater. Chem.* **2007**, *17* (17), 1656-1659.
- [35] Q. Liu, A. M. Rao, X. Han, B. Lu, *Adv. Sci.* **2021**, *8* (9), 2003639.
- [36] Z.-H. Xue, J.-T. Han, W.-J. Feng, Q.-Y. Yu, X.-H. Li, M. Antonietti, J.-S. Chen, *Angew. Chem. Int. Ed.* **2018**, *57* (10), 2697-2701.
- [37] Q. Li, H. Wang, X. Tang, M. Zhou, H. Zhao, Y. Xu, W. Xiao, Y. Lei, *Adv. Funct. Mater.* **2021**, *31* (24), 2101081.
- [38] T. S. Mathis, N. Kurra, X. H. Wang, D. Pinto, P. Simon, Y. Gogotsi, *Adv. Energy Mater.* **2019**, *9* (39), 1902007.
- [39] a) W. Weppner, R. A. Huggins, *J. Electrochem. Soc.* **1977**, *124* (10), 1569; b) C. Delacourt, M. Ati, J. M. Tarascon, *J. Electrochem. Soc.* **2011**, *158* (6), A741.
- [40] J. S. Horner, G. Whang, D. S. Ashby, I. V. Kolesnichenko, T. N. Lambert, B. S. Dunn, A. A. Talin, S. A. Roberts, *ACS Appl. Energy Mater.* **2021**, *4* (10), 11460-11469.
-

- [41] a) E. Deiss, *Electrochim. Acta* **2005**, *50* (14), 2927-2932; b) Y. Li, Y.-S. Hu, M.-M. Titirici, L. Chen, X. Huang, *Adv. Energy Mater.* **2016**, *6* (18), 1600659.
- [42] K. Wang, Y. Jin, S. Sun, Y. Huang, J. Peng, J. Luo, Q. Zhang, Y. Qiu, C. Fang, J. Han, *ACS Omega* **2017**, *2* (4), 1687-1695.
- [43] Z. Yu, Y. Cui, Z. Bao, *Cell Rep. Phys. Sci.* **2020**, *1* (7), 100119.
- [44] R. C. Massé, C. Liu, Y. Li, L. Mai, G. Cao, *Natl. Sci. Rev.* **2016**, *4* (1), 26-53.
- [45] M. Antonietti, M. Oschatz, *Adv. Mater.* **2018**, *30* (21), 1706836.

CHAPTER 3. SULFUR-RICH CARBON AS A HIGH-PERFORMING ANODE MATERIAL

The results presented in this chapter can be found as, E. O. Eren, C. Esen, E. Scoppola, Z. Song, E. Senokos, H. Zschiesche, D. Cruz, I. Lauermann, N. V. Tarakina, B. Kumru, M. Antonietti, P. Giusto, Microporous sulfur-carbon materials with extended sodium storage window. *Adv. Sci.*, **2024**, In press.

Notion – Developing carbonaceous anode materials for high-performance SIBs is an essential endeavor toward a sustainable future of energy storage. One of the most promising strategies for developing highly efficient anode materials is the introduction of sulfur atoms within a carbon framework. This induces an expansion in pseudo-graphitic stacking, distorts the structure, and creates favorable sites for sodium ions. In this chapter, a microporous sulfur-rich carbon anode is developed from a liquid sulfur-containing precursor, namely 3,4-Ethylenedioxythiophene (EDOT). At higher condensation temperatures, the sodium storage mechanism shifts from surface-controlled to diffusion-controlled. This change in storage mechanism is found to be independent of interplanar spacing; instead, it anticipated an increased microporosity and a thiophene-rich chemical environment. These properties enable the extension of the underpotential plateau region and reversible overpotential sodium storage. Moreover, *in-operando* small-angle X-ray scattering (SAXS) is utilized to corroborate the pore-filling mechanism. This technique reveals variations in electron density differences throughout the sloping and plateau regions. Overall, the framework presented in this chapter has the potential to enable the design of high-performance anodes for sodium-ion batteries with competitive energy density.

Herewith, an innovative method is introduced for preparing sulfur-containing carbon anode with a high sulfur content using a stable thiophene-containing oligomer (oligo-EDOT). By increasing the condensation temperature, a significant change in the nanostructure and sodium storage mechanism is observed, which results in a higher

plateau capacity while maintaining a larger interlayer distance than graphite. Notably, the resulting material exhibits an unprecedented plateau capacity of 165 mAh g⁻¹ compared to other sulfur-containing carbonaceous materials (as listed in **Table 3.1**). In addition, it is demonstrated for the first time reversible overpotential sodium deposition, which is attributed to the controlled nucleation of sodium in confined pore spaces, a crucial tool for increasing the electrode energy density and ensuring safe operation under potential overload. Therefore, a larger interplanar spacing in the turbostratic structure is not the sole parameter for improving performance, as it is proven that (ultra-)microporosity and the chemical environment are crucial factors for designing novel anode materials for SIBs as well.

Table 3.1. Comparison of recent studies regarding sulfur-carbon materials in Na-ion and RT Na-S batteries.

Material	System	S content / wt. %	Heat treatment / °C	Max. Capacity / mAh g ⁻¹	Plateau Capacity / mAh g ⁻¹	ICE / %	Reference
SC-800	Na-ion	14.9	800	255	-	50	This work
SC-900	Na-ion	10.3	900	325	55	53	This work
SC-1000	Na-ion	7.3	1000	325	165	50	This work
SC	Na-ion	5.5	1100	243	90	36	[1]
S, N-C	RT Na-S	9.1	650	350	-	44	[2]
S-HC	RT Na-S	13.6	600	430	-	56	[3]
SC	RT Na-S	15.6	700	482	-	74	[4]
DC-S	RT Na-S	26.9	500	516	-	63	[5]
S-CS-600	RT Na-S	32.0	600	520	-	72	[6]
SHC-500	RT Na-S	15.9	500	678	-	84	[7]
NSC2	Na-ion	n/a	800	280	-	38	[8]
S-Cmph-700	RT Na-S	n/a	700	373	-	66	[9]

3.1. Sulfur heteroatom effect

The sulfur heteroatom effect has already been discussed in previous chapters, such as the conceptual introduction in Chapter 1 and Chapter 2, in which the latter utilizes sulfur-containing carbon, namely LSC, as a substrate for CN deposition. This chapter focuses on

a model material to investigate the effects of sulfur heteroatoms alone on the sodium storage mechanism.

The introduction of heteroatoms in carbonaceous anodes has been extensively studied to enhance the sodium storage performance of non-graphitic carbons.^[10] Among various heteroatoms, sulfur doping is considered a promising approach for SIBs due to the larger covalent radius and the chemical properties of sulfur, which lead to an increase in the interlayer distance between pseudo-graphitic planes and the creation of preferential adsorption sites for sodium ions. The performance improvements achieved by sulfur doping are often linked to changes in the local packing geometry and chemical structure induced by specific bonding motifs.^[2, 5, 11] However, carbons with high sulfur content are typically exploited as an electrode material for room-temperature sodium-sulfur batteries (RT Na-S) due to the formation of Na_xS_y compounds during electrochemical processes.^[12] With a decrease in the amount of sulfur in the carbon, the electrochemical reaction between sodium and sulfur is suppressed, leading to the benefit of surface adsorption for SIBs. Nonetheless, even in SIBs, sulfur-containing carbons usually lack the diffusion-controlled plateau region, decreasing average cell potential in a full-cell and thus lowering the energy density.^[5-6, 13] In order to attain favorable performance in applications, it is necessary to achieve a balance, which may involve control over the chemical structure, morphology, and sulfur content in the material.

3.2. Preparation of sulfur-carbon

The procedure for synthesizing Oligo-EDOT is conducted through photooxidative polymerization.^[14] In brief, 3,4-ethylenedioxythiophene (EDOT, 97% purity, Sigma-Aldrich, 10 mL) is mixed with graphitic carbon nitride (g-CN, 500 mg) as photocatalyst and sonicated for approximately 10 minutes in a vial. The photopolymerization process involves placing the vial in front of a 50 W visible light source and stirring continuously for 24 hours at room temperature. Following filtration of the g-CN, Oligo-EDOT is

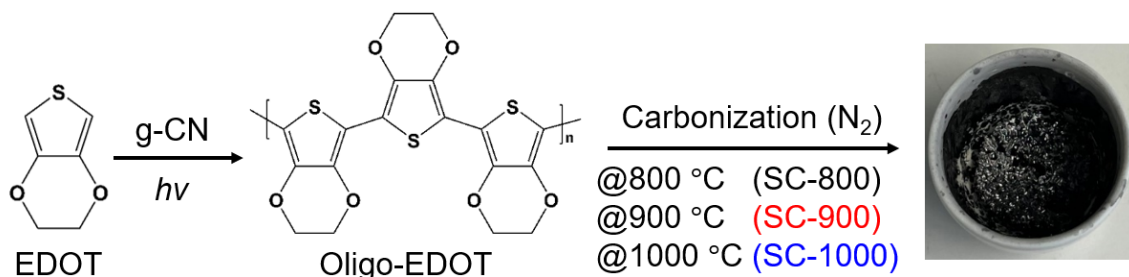


Figure 3.1. Synthetic steps for SC-800, SC-900, and SC-1000. (Copyright (2024) Wiley)

obtained as a viscous honey-like fluid. For thermal condensation, the Oligo-EDOT is subjected to a target temperature (800°C for SC-800, 900°C for SC-900, and 1000°C for SC-1000) at a heating rate of 3.15 K min⁻¹ under a nitrogen atmosphere in a furnace and held at this temperature for 2 hours (**Figure 3.1**). The resulting material exhibits a thin, crispy film with a metallic sheen appearance and is subsequently ground into a fine powder. The details of the electrochemical and physicochemical characterization methods can be found in “**A3.1 Electrode preparation and electrochemical characterizations**” and “**A3.2 Physico-chemical characterizations**” in the **Appendices**.

3.3. Results and Discussion

3.3.1. Physico-chemical characterizations

Characterization of oligo-EDOT – The linear non-doped oligomer, oligo-EDOT, is synthesized by means of the oxidative photopolymerization of EDOT, using CN as a photoinitiator,^[14] yielding a viscous fluid. The chemical structure of oligo-EDOT is confirmed using Fourier-transform infrared (FTIR) spectroscopy. The FTIR analysis reveals the presence of characteristic peaks corresponding to C=C, C–C stretching, and C–S vibrations in the thiophene ring and the conjugations in the polymeric structure, as shown in **Figure 3.2**.^[14-15]

The thermal behavior of the oligomer is evaluated using thermogravimetric analysis-mass spectroscopy (TGA-MS). The TGA-MS profile shows that there is stepwise thermal condensation of oligo-EDOT (**Figure A3.1**). The intense signals observed in the mass spectrum above 600°C are attributed to fragments such as C_xH_y⁺, CO⁺, CO₂⁺²⁺, and OH⁺. The signals at 32 (*m/z*) are assigned to S⁺ and O₂⁺ fragments, which show a steady decrease even at temperatures above 800°C, indicating the presence of significant amounts of sulfur

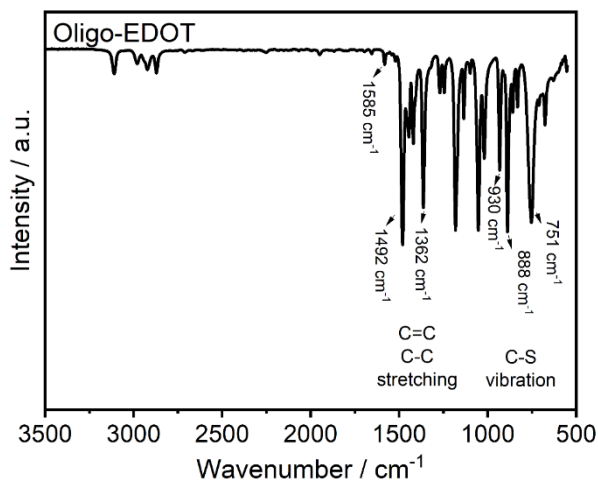


Figure 3.2. FTIR spectrum of oligo-EDOT. (Copyright (2024) Wiley)

at high temperatures. However, no significant mass losses over 50 (m/z) are observed to mirror the SO_x^+ and CS_2^+ fragments. The precursor is then subjected to thermal condensation at 800°C, 900°C, and 1000°C, resulting in carbon materials that are referred below to as SC-800, SC-900, and SC-1000, respectively.

Characterizations of sulfur carbons – Scanning electron microscopy (SEM) provides insights into the material’s physical appearance, revealing that it condenses into large chunks with sharp edges, which appear as a lustrous metallic sheen (as depicted in **Figure 3.3**). Increasing the carbonization temperature caused a decrease in sulfur content, from approximately 15 wt. % at 800°C to 10 wt. % at 900°C and 7 wt. % at 1000°C, characterized by elemental analysis (EA). Meanwhile, the oxygen content remains constant at all three temperatures, hovering around 3 wt. %, as shown in **Table 3.2**.

Table 3.2. Elemental compositions of the materials via EA and EDX.

		Elemental Compositions [wt. %]		
		C	S	O
SC-800	(EA)	81.9 ± 0.1	14.9 ± 0.3	3.1 ± 0.3
	(EDX)	85.3 ± 1.7	13.2 ± 2.0	1.5 ± 0.4
SC-900	(EA)	86.1 ± 0.1	10.3 ± 0.1	3.6 ± 0.6
	(EDX)	89.2 ± 0.3	8.3 ± 0.7	2.5 ± 0.5
SC-1000	(EA)	89.6 ± 0.3	7.3 ± 0.1	3.1 ± 0.2
	(EDX)	90.5 ± 0.4	7.2 ± 0.8	2.2 ± 0.4

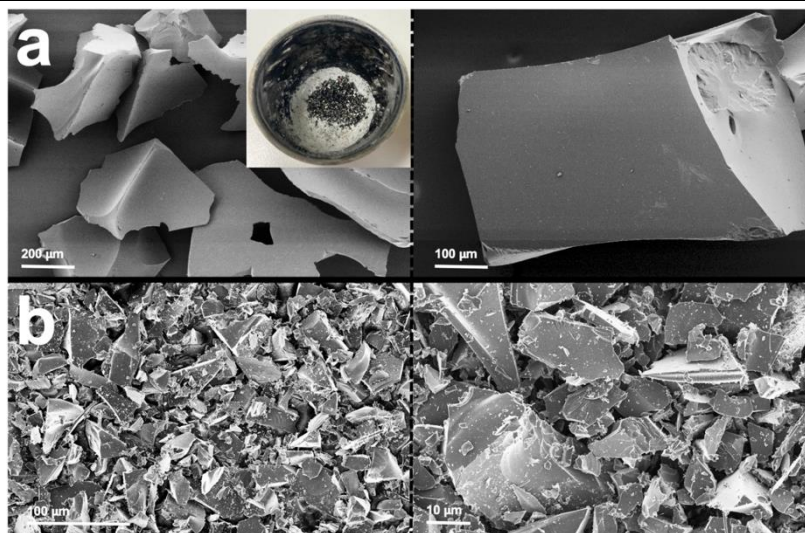


Figure 3.3. The SEM images of the material at various magnifications. Panel (a) displays pre-grinded monolith-like structures (SC-800). The inset in the figure depicts a powder with a metallic sheen appearance. Panel (b) exhibits post-grinded glitter-like powder (SC-900 and SC-1000). (Copyright (2024) Wiley)

Energy-dispersive X-ray (EDX) spectroscopy confirms that the C, S, and O elements are uniformly distributed throughout the material without any significant phase segregation at the sub-micrometer level. This is supported by the elemental maps displayed in **Figure 3.4a** and **Figure A3.2**. Morphological analysis, carried out using high-resolution transmission electron microscopy (HRTEM), reveals that the samples appear to be homogeneous. The fast Fourier transform (FFT) profiles obtained from HRTEM images of various sections of the samples show one diffuse ring, indicating the absence of long-range order at the nanoscale. However, features such as periodic intensity alternations in one direction and layer-like structures are observed locally, which reveal the presence of non-graphitic domains typical of turbostratic and ramen-like structures (as shown in **Figure 3.4b** and **Figure A3.3**).^[16] The distances between these short-range graphitic stacks are directly measured in the image and found to be consistent across all samples, measuring 0.38 nm (as depicted in **Figure 3.4b**; inset, **Figure A3.4**, and **Figure A3.5**).

Small-angle X-ray scattering (SAXS) is a robust technique utilized for comprehending the topological information of complex porous structures at a relatively large scale.^[17] Data processing requires several steps of corrections to take into account the contribution from the beam flux, transmission, and backgrounds (empty capillary and beam).^[17b] In

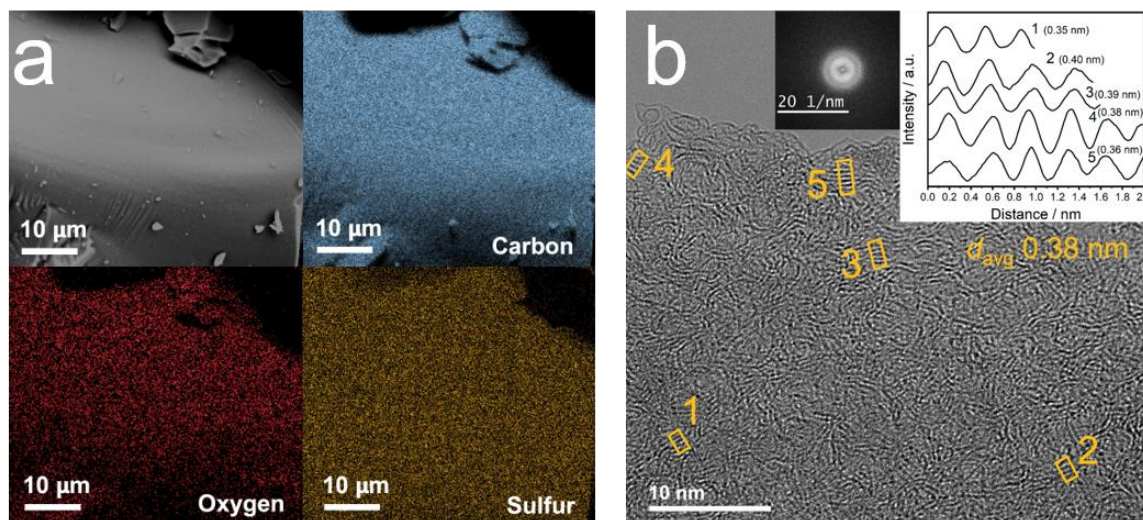


Figure 3.4. (a) An image obtained through secondary electron SEM of SC-1000, along with SEM-EDX maps depicting the distribution of carbon, sulfur, and oxygen in the chosen region of interest. (b) HR-TEM image of SC-1000, revealing the presence of short-range order pseudo-graphitic stacks in the disordered framework of the material. The inset of the image showcases line profiles of SC-1000, which are obtained through analyzing the average distances between locally stacked graphitic-like sheets using the image intensity function from FFT profile. (Copyright (2024) Wiley)

summary, the raw intensity (**Figure 3.5a**) obtained from the measurement can be reduced by the following equations.

$$I_{pixel} = I_0 \cdot e \cdot t \cdot \frac{d\Sigma}{d\Omega} \cdot \Delta\Omega_{pixel} \quad (3.1)$$

Here, I_0 denotes the intensity of the beam in cps, e represents the thickness of the sample (for powders, it is the thickness of the capillary sample holder without walls, which is 0.048 cm), t stands for the angle-dependent transmission of the sample, $d\Sigma/d\Omega$ is the scattering cross-section per unit volume in cm^{-1} , and $\Delta\Omega_{pixel}$ represents the solid angle of the pixel. The value of $\Delta\Omega_{pixel}$ is calculated based on equations 3.2, 3.3, and 3.4. A_0 denotes the geometrical surface area of the pixel in cm^2 ($68 \times 68 \mu\text{m}$), D_0 is the sample-detector distance in cm (28.3), and 2θ is the angle between the sample-pixel axis and the beam axis. The scattering cross-section per unit volume ($d\Sigma/d\Omega$) (q) is then calculated and plotted with respect to the scattering vector (q), as illustrated in **Figure 3.5b**.

$$\Delta\Omega_{pixel} = \frac{A_{pixel}(2\theta)}{D(2\theta)^2} \quad (3.2)$$

$$A_{pixel}(2\theta) = A_{pixel}^0 \cos(2\theta) \quad (3.3)$$

$$D(2\theta) = \frac{D_0}{\cos(2\theta)} \quad (3.4)$$

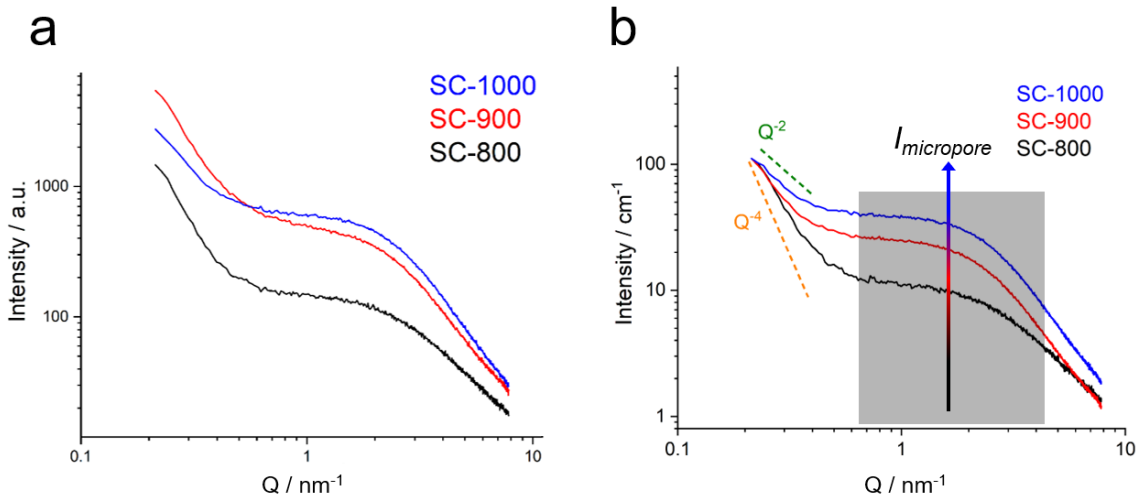


Figure 3.5. (a) Raw intensities vs. scattering vectors of the materials. (b) SAXS patterns of the materials with normalized intensities in cm^{-1} . (Copyright (2024) Wiley)

Upon analysis, two primary contributions are observed in the final pattern. Porod's law of scattering from sharp interfaces, such as macroscopic surfaces, corresponded to a particular slope in q^{-4} at low angles.^[17b] However, it is elucidated by Ruland et al. that the decay through q^{-2} is observed due to the defective nature of carbonaceous materials, which brings the total scattering intensity to q^{-3} .^[17a, 18] Although SC-800 shows an almost q^{-3} behavior, the pattern is shifted through the q^{-2} for SC-900 and SC-1000, possibly due to an increase in mass and surface fractals.^[19a] Meanwhile, the signal in the intermediate q ranges is attributed to the microporous nature of the materials.^[17b, 19] The scattering intensities at the mid- q range reveal an increase in micropore volume at higher temperatures (**Figure 3.5b**).

The X-ray diffraction (XRD) patterns presented in **Figure 3.6a** exhibit two broad peaks at 22° and 43° , which can be attributed to the (002) and (100) planes of disordered carbons, respectively.^[2, 11, 20] These findings are consistent with previous studies. By utilizing Bragg's law, the interlayer distances are calculated from the highest intensity of the (002) reflection, resulting in an average value of 0.40 nm for all samples. This indicates that the larger d -spacing observed compared to that of graphite (0.34 nm) is not significantly affected by the sulfur content or the temperature increase within the range considered. The stacking distances derived from the XRD analysis are in good agreement with the results obtained from HRTEM investigations.

In addition, the trend in the graphitization degree of the carbonaceous materials can be monitored using Raman spectroscopy, where the G ($\sim 1580\text{ cm}^{-1}$) and D ($\sim 1345\text{ cm}^{-1}$) bands are analyzed. The G band represents sp^2 hybridization, while the D band reflects

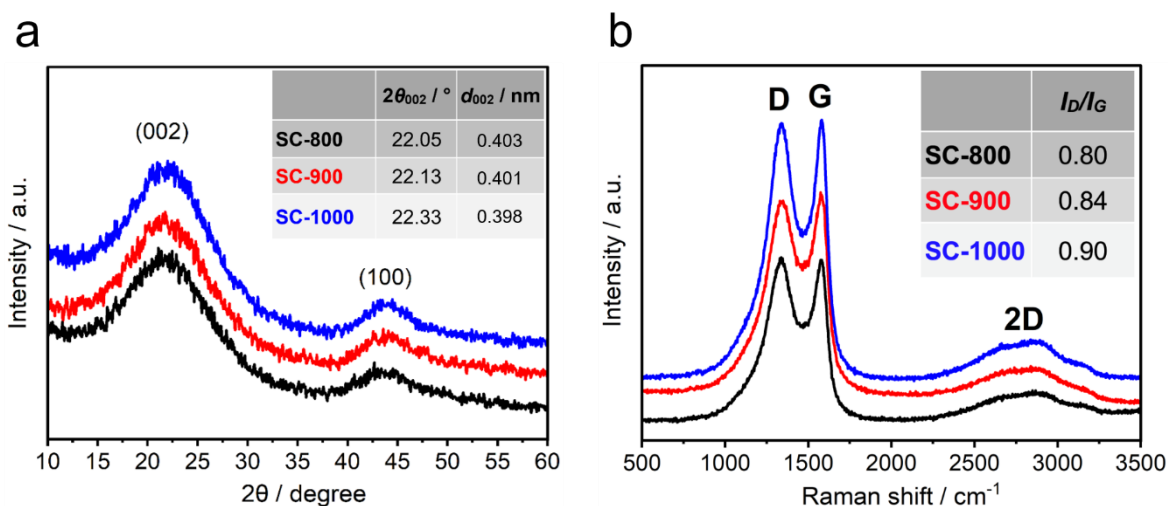


Figure 3.6. (a) XRD patterns of materials. Inset: Table presenting $2\theta_{002}$ (degree) vs. d_{002} (nm). (b) Raman spectra of materials showing D and G bands. Inset: Peak intensity ratios of D (Lorentzian) and G (BWF) bands. (Copyright (2024) Wiley)

the oscillations of the breathing mode.^[21] From the spectra shown in **Figure 3.6b**, all materials exhibit broad *D* and *G* bands, as well as a very broad *2D* region. An increase in the absolute intensity of the *D* band is associated with an increased order in disordered carbons, whereas it suggests the opposite trend for graphitized carbons.^[21] The I_D/I_G ratio, determined by measuring the peak intensity using Lorentzian fit for the *D* band and the Breit-Wigner-Fano (BWF) model for the *G* band, is found to increase from 0.80 to 0.90 upon increasing the pyrolysis temperature from 800°C to 1000°C. This implies that the carbons are at the second stage of their amorphization trajectory, which was proposed by Ferrari and Robertson.^[21] Furthermore, a slight increase in the I_D/I_G ratio at higher pyrolysis temperatures suggests a tendency to increase graphitic units in the materials.

Accurate characterization of porosity and available surface area is essential for the successful development of high-performance anode materials. To this end, valuable information is obtained through the use of N₂ and CO₂ gas sorption measurements, which can be analyzed using appropriate models such as the density functional theory (DFT) model. Here, DFT is utilized to assess the pore size distribution in disordered carbons. DFT is a reliable method for estimating pore structure parameters, in contrast to conventional methods based on the Kelvin equation.^[22] DFT is frequently applied to a wide range of porous materials with various pore structures.^[23] The approach involves using a mathematical model to calculate theoretical isotherms for individual pores of a particular adsorbate-adsorbent system. Combinations of the theoretical isotherms are then fitted to the experimental data using the adsorption isotherm, resulting in a final pore size distribution (PSD) that reflects the volumetric contributions of pores with different sizes whose theoretical isotherm best fits the experimental data. Additional information about the DFT approach to pore size analysis can be found in relevant literature.^[24]

Analysis of N₂ sorption indicates that the surface area available for N₂ is less than 10 m² g⁻¹ (S_{BET}) for all samples, with a negligible amount of mesopores (**Figure A3.6**). While many studies aim to synthesize electrodes with high N₂ surface area, electrodes with a low amount of macro and mesopores have a positive effect on the performance of SIBs. Indeed, low surface area suppresses the excessive growth of the solid electrolyte interphase (SEI) during the first loading cycle, which primarily affects the initial Coulombic efficiency (ICE), as previously reported in Chapter 2.^[25] This is important because excessive SEI growth can significantly decrease battery performance and consume the electrolyte. To explore the potential presence of smaller pores, a CO₂ sorption experiment is conducted, which is a more suitable method for examining the microporosity of hard carbons (**Figure 3.7**), as the kinetic radius of CO₂ is significantly smaller than that of N₂.^[26] The results confirm the sub-microporous nature of the samples, which is consistent with previous studies on high-capacity hard carbons.^[27] The volume

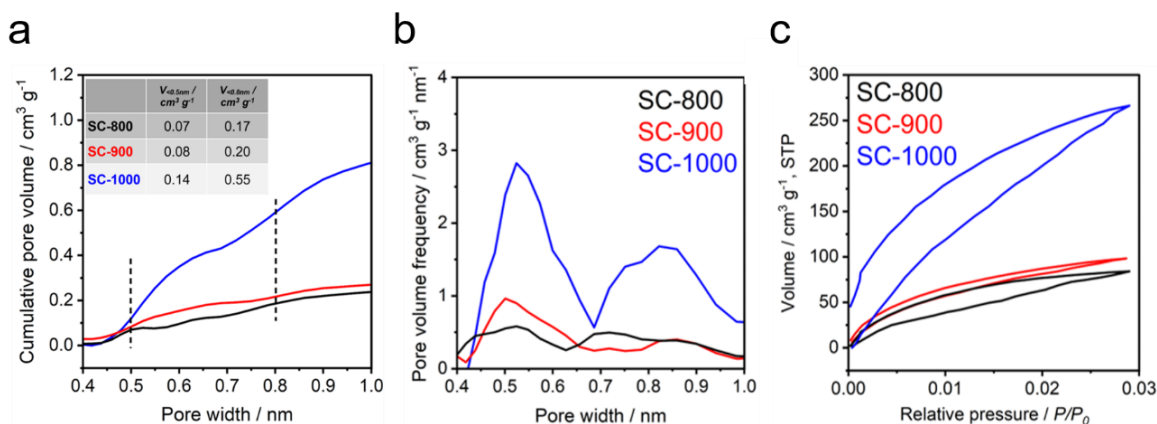


Figure 3.7. CO₂ sorption analysis; **(a)** cumulative micropore volume. Inset: statistical summary from DFT method; **(b)** PSD, and **(c)** isotherms. (Copyright (2024) Wiley)

of micropores and ultramicropores is instead significantly affected by the pyrolysis temperature. For instance, the cumulative volume of micropores ($d_{\text{pore}} < 0.8 \text{ nm}$) more than doubles as the pyrolysis temperature increases, particularly from 900°C to 1000°C (e.g., from 0.20 cm³ g⁻¹ to 0.55 cm³ g⁻¹) (**Figure 3.7; inset table**), which supports the trends observed in SAXS. The removal of heteroatoms such as S, O, and pendant groups at higher temperatures might act as a pore-forming agent, subsequently creating a micropore-rich carbon. Importantly, the pores with a diameter below 0.8 nm can allow the diffusion of sodium ions while hindering the transport of the counter ion in the electrolyte (in this case, PF₆⁻), even for surfaces with a neutral charge (referring to the absence of a net positive or negative charge).^[28]

The X-ray photoelectron spectra (XPS) spectra of the S2p core level presented in **Figure 3.8a** exhibit an intense doublet peak at 163.8 eV (S2p_{3/2}) and 165.0 eV (S2p_{1/2}), as well as two broader peaks at 167.8 eV and 169.1 eV. The doublet peaks at 163.8 eV and 165.0 eV correspond to the spin-orbital splitting peaks and can be attributed to the covalent –C–S– bonds found in thiophene-type compounds. On the other hand, the peaks at 167.8 eV and 169.1 eV correspond to –C–SO_x units, which are primarily attributed to –C–SO₂–C– sulfone bridges.^[5, 11, 29] The signals of all peaks in the S2p core level decrease with increasing pyrolysis temperature in relation to the C1s peaks. However, the relative ratio of the –C–SO_x peak to the –C–S– peak increases at higher temperatures (**Table 3.3**), indicating that the sulfur in the –C–SO₂–C– configuration is more stable compared to the –C–S– sulfur. The shoulder at 284.5 eV in the C1s region of the XPS survey (**Figure 3.8b**) corresponds to the *sp*² carbon, while the intense peak at 285.5 eV is attributed to the *sp*³ carbon and contributions from C–S bonds.^[30] An increase in temperature also increases the relative area of the *sp*² peak, in agreement with observations made using Raman-

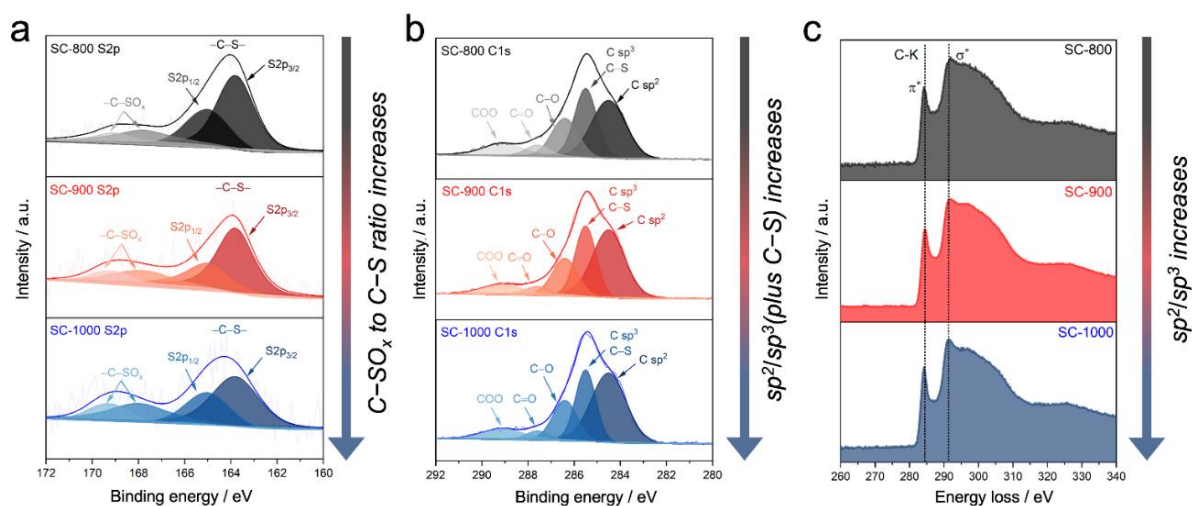


Figure 3.8. XPS spectra of the materials analyzed, with **(a)** representing the S2p core level and **(b)** showing the C1s core level. In addition, **(c)** illustrates EELS spectra of the materials, exhibiting the carbon K-edge with both π^* and σ^* states. (Copyright (2024) Wiley)

Table 3.3. The ratio of deconvoluted peak areas from the S2p and C1s regions of the XPS survey is calculated based on SC-800 as a reference.

Sample	XPS S2p	XPS C1s
	C-SO _x to C-S ratio	sp^2/sp^3 (plus C-S)
SC-800	x	y
SC-900	1.2x	1.1y
SC-1000	1.4x	1.2y

spectroscopy. Peaks at 286.4 eV, 287.6 eV, and 289.1 eV correspond to the C_xO_y species and are also observed in the O1s core level.^[31] In the O1s core level (**Figure A3.7**), the peak centered at 530 eV corresponds to both the indium oxide foil utilized as a substrate, which does not impact the S2p and C1s regions and the O-S bonds. In contrast, the wider peak represents the oxygen-carbon species, along with the hydroxide.^[32]

Electron energy loss spectroscopy (EELS) spectra can provide insights into the chemical environment at the atomic/nanoscale. The features between 280 and 320 eV representing the carbon K energy-loss near-edge structure (ELNES) can be qualitatively used to estimate changes in the sp^2 to sp^3 carbon ratio (**Figure 3.8c**). The sharp peak at 284.5 eV and the features around 292 eV correspond to the $1s \rightarrow \pi^*$ (C=C) and $1s \rightarrow \sigma^*$ (C-C) antibonding states, respectively.^[33] A distinct increase in the π^* states and the onset peak of the σ^* (292.0 eV) indicate the formation of more sp^2 -hybridized carbons, confirming

an increase in graphitic order at higher condensation temperatures.^[34] No significant peak shift is observed in the carbon K-edge. In the low-loss region of SC-800, SC-900, and SC-1000, the plasmon peaks (**Figure A3.8**) at 6.0 eV (only π electrons) and 23.0 eV ($\pi+\sigma$, all valence electrons).^[35] Here, the electronic structure of the materials associated with the low-loss EELS is expected to be similar.

3.3.2. Sodium storage behavior of materials

Galvanostatic charge and discharge (GCD) measurements – Based on the GCD curves, the initial Coulombic efficiencies (ICEs) of SC-800, SC-900, and SC-1000 are determined to be approximately 50%, as depicted in **Figure 3.9a**. The ICE of disordered carbon anodes within carbonate-based electrolytes has been previously reported to range between 30 and 70% in the literature.^[36] Recent research indicates that the ICE can be significantly improved by utilizing ether-based electrolytes, which are believed to enhance the kinetics of the diffusion-controlled plateau region.^[37] However, achieving this goal requires experimentation with various combinations of solvents and salts, as electrolyte compatibility is highly dependent on the physicochemical properties of the materials. In addition, various strategies can be employed to enhance the ICE, including **(i)** Increasing the pyrolysis temperature to create a more ordered carbon texture with fewer defect sites, which are typically responsible for irreversible sodium ion adsorption,^[38] **(ii)** pre-sodiation of the anode material,^[39] **(iii)** surface engineering of the electrode and designing an artificial solid-electrolyte interphase (*a*-SEI) layer,^[40] and **(iv)** optimizing the

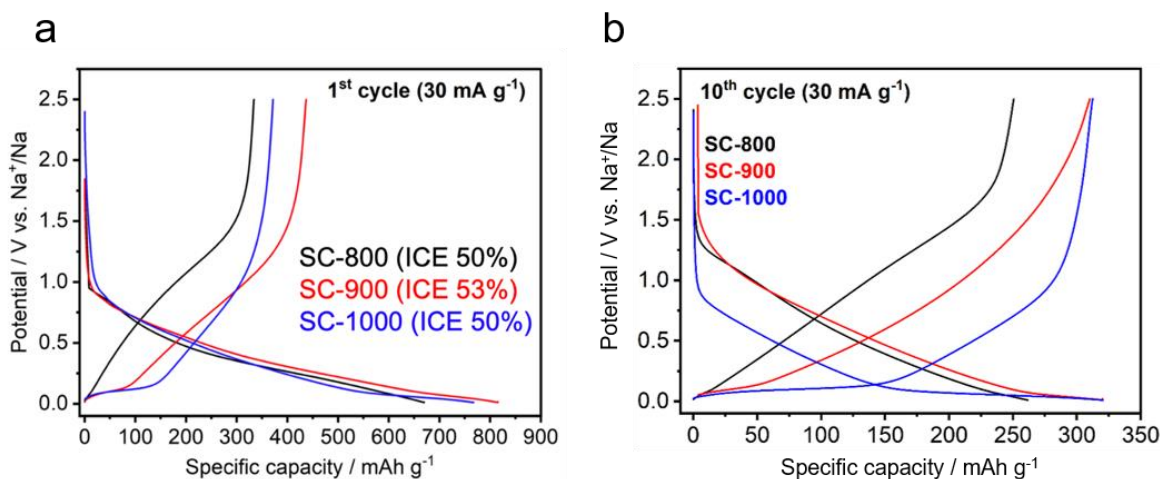


Figure 3.9. (a) The initial cycles of SC-800, SC-900, and SC-1000 with their ICEs. (b) The 10th GCD curve of the electrodes at a specific current density of 0.1C (30 mA g⁻¹). (Copyright (2024) Wiley)

electrolyte.^[41] Among those techniques, the design of an α -SEI is explored as a potential method to improve ICE in Chapter 2. Further, electrolyte optimization, which positively enhances ICE, is also discussed in Chapter 4.

After the formation of a stable SEI, SC-800, SC-900, and SC-1000 exhibit stable capacities of around 250 mAh g⁻¹, 325 mAh g⁻¹, and 325 mAh g⁻¹, respectively, as shown in **Figure 3.9b**. The alteration in the shape of the sodiation and desodiation curves indicates the modification of the sodium storage mechanisms and resembles changes in the structure and chemistry. Here, the plateau region is identified as the point of transition between the capacitive and diffusion-controlled regions, which is found to be approximately 0.1 V (vs. Na⁺/Na). Notably, the SC-1000 exhibits a well-defined extended plateau region with a typical sloping area in a high-voltage region. Conversely, the SC-800 does not show any noticeable plateau region, implying that the sodium storage is primarily governed by a surface-controlled mechanism. The SC-900 represents an intermediate state between SC-800 and SC-1000, exhibiting a small plateau contribution to the overall capacity.

Cyclic voltammetry (CV) and galvanostatic intermittent titration (GITT) measurement

– The examination of the sodium storage mechanism here follows the same concepts outlined in Chapter 2. Precisely, the b -value of the materials is calculated using Eq. 2.1 for the CV analysis (See **Figure A3.9** for CV curves), while the GITT is analyzed using Eq. 2.2 (See **Figure A3.10** for GITT curves).

The concentration of sodium ions at the electrode-electrolyte interface, if the redox reaction of the electroactive species relies mainly on diffusion, is usually time-dependent.^[42] This is demonstrated by the fast rate of the sloping region, as observed with SC-800, which highlights capacitive storage, while the sluggishness of the plateau mode indicates non-capacitive Faradaic behaviors. The slope of the $\log(i, \text{peak anodic current})$ vs. $\log(v, \text{scan rate})$ plots from the CV enables differentiation between surface- or diffusion-controlled mechanisms of sodium-ion storage. A b -value close to 1 indicates a surface-controlled electrochemical process, while a b -value close to 0.5 suggests that the diffusion-controlled mechanism is dominant.^[42] The corresponding b -values confirm that SC-800 is more surface-controlled, while SC-900 and SC-1000 involve more diffusion-controlled storage mechanisms (**Figure 3.10a**). Sodium-ion diffusion coefficients are calculated from GITT (**Figure 3.10b**), revealing that the diffusion coefficients of the electrodes are around 10⁻⁸ and 10⁻⁹ cm² s⁻¹ during the sodiation and desodiation processes, in the range of typical hard carbons.^[43] However, a sharp decrease in diffusion coefficients is observed for SC-900 and SC-1000 during the plateau region (<0.2 V (vs. Na⁺/Na)), indicating a different sodium storage behavior due to the presence of phase-transition reactions at that potential window (such as intercalation and pore-filling), which makes time-dependent processes more prominent.^[43] In contrast, SC-800 does not exhibit such a

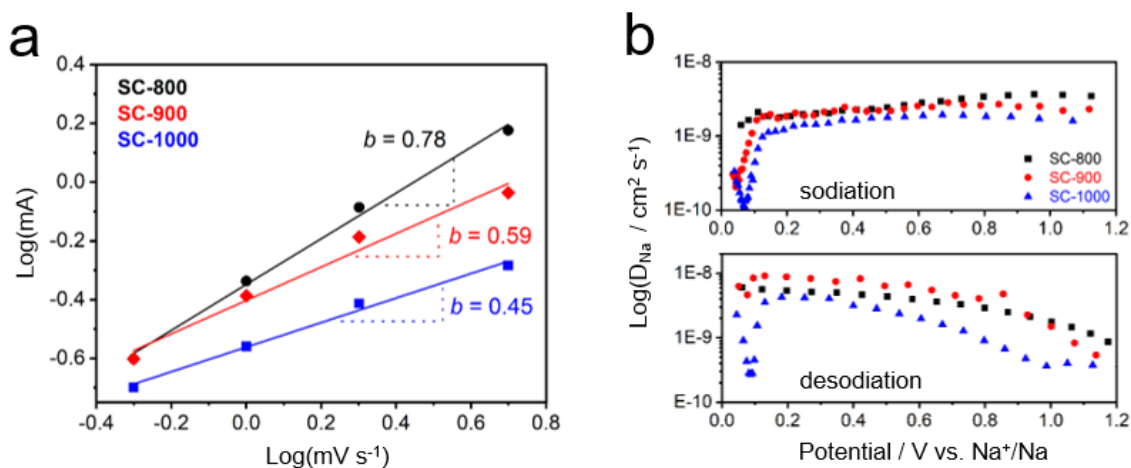


Figure 3.10. (a) b -value plots from CV. (b) Sodium-ion diffusion coefficients of the materials calculated from GITT. (Copyright (2024) Wiley)

sharp decrease in that region as it is purely capacitive until the cutoff potential. The sodium-to-carbon ratio at the non-capacitive Faradaic mode is approximated as $\text{NaC}_{40.7}$ for SC-900 (55 mAh g^{-1}) and $\text{NaC}_{13.6}$ (165 mAh g^{-1}) for SC-1000, considering the theoretical capacity of NaC_{64} , which is 35 mAh g^{-1} .^[44] The sulfur heteroatom is expected to significantly influence the charge distribution on the carbon surface, leading to a stronger binding affinity for sodium ions and reducing the formation energy of sodium-carbon compounds.^[45]

In general, the adequate accommodation of sodium ions necessitates a significant increase in interplanar spacing, as well as the provision of optimal micropores for an adsorption-intercalation/filling model. Sulfur atoms are observed to play a crucial role in distorting the material's structure by increasing the stacking distance of graphitic planes and introducing defect sites. However, the relationship between interplanar distance and the electrochemical properties is not always straightforward, as the sodium storage behavior of pendant groups contributes to surface-controlled sodium storage rather than diffusion-controlled. If the material's structure is sufficiently open for sodium storage, a diffusion-controlled process should occur once the low-energy supercapacitive adsorption reaches saturation. Observations here show no indication of sodium intercalation in the SC-800, as it still has a very high amount of sulfur inside. Increasing the pyrolysis temperature leads to the removal of sulfur-containing fragments from the material, leading to a higher proportion of sp^2 hybridized carbon and fewer edge terminations, which is attributed to be the primary reason for the sharp increase in the CO_2 -accessible micropore volume. An increase in micropores improves the efficiency of the desolvation process, hindering the

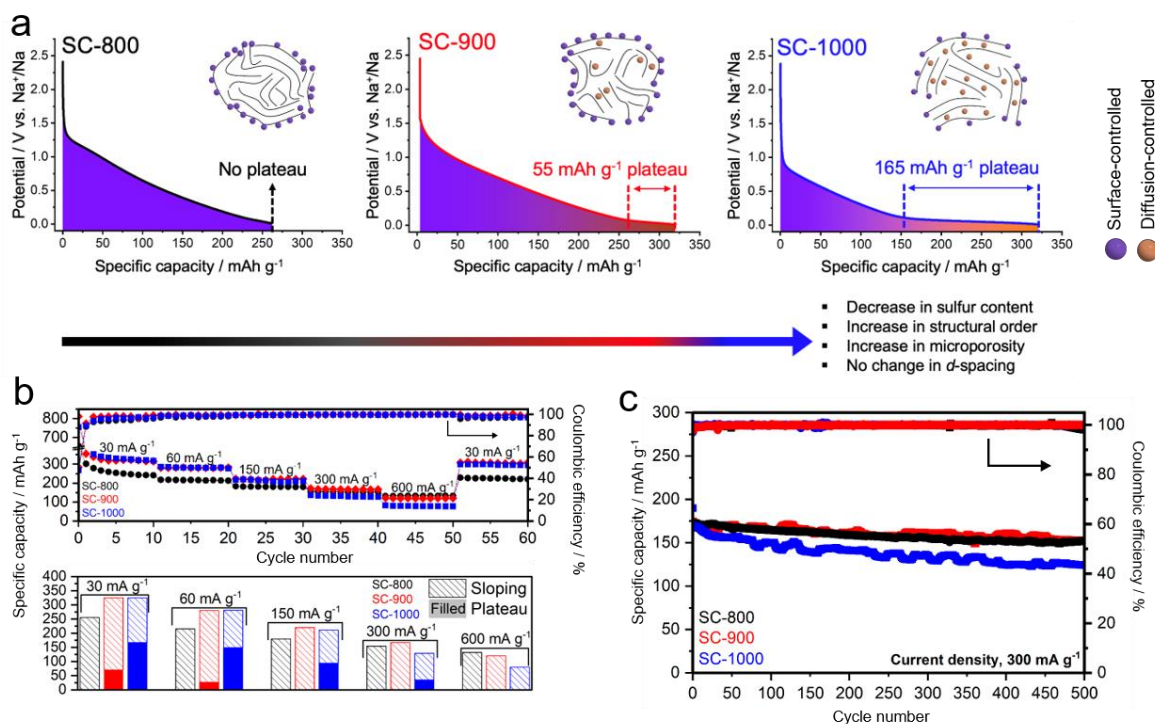


Figure 3.11. (a) The sodiation curves obtained at 0.1C (30 mA g^{-1}) are linked to the adsorption-intercalation model based on the outcomes of physicochemical analyses. (b) The top section of the figure displays the rate performance of the electrodes at various current densities, including 0.1C (30 mA g^{-1}), 0.2C (60 mA g^{-1}), 0.5C (150 mA g^{-1}), 1C (300 mA g^{-1}), and 2C (600 mA g^{-1}). Meanwhile, the bottom section exhibits a column chart of the electrodes at different current densities, illustrating the distribution of the plateau and sloping capacities. (c) results of the 500 cycle stability tests conducted at 1C (300 mA g^{-1}). (Copyright (2024) Wiley)

diffusion of negative ions in the electrolyte (PF_6^-) and also the electroactive area responsible for the redox reactions. Once this volume increases, sodium intercalation becomes more prominent, leading to a sudden and prolonged plateau capacity (**Figure 3.11a**).

At higher current densities, all electrodes tend to be involved in fast-near-surface activities, as semi-infinite diffusion-controlled Faradaic storage in bulk is often slow, as seen in battery devices with Faradaic reactions.^[46] As an example, the rate capability of SC-1000 becomes inferior to that of SC-800 and SC-900 (**Figure 3.11b**), making SC-800 and SC-900 more suitable for fast charging (**Figure 3.12**).

In order to assess the long-term stability of the electrodes, the batteries are subjected to 500 cycles at 1C (300 mA g^{-1}) (**Figure 3.11c**). This is an important measurement to reveal

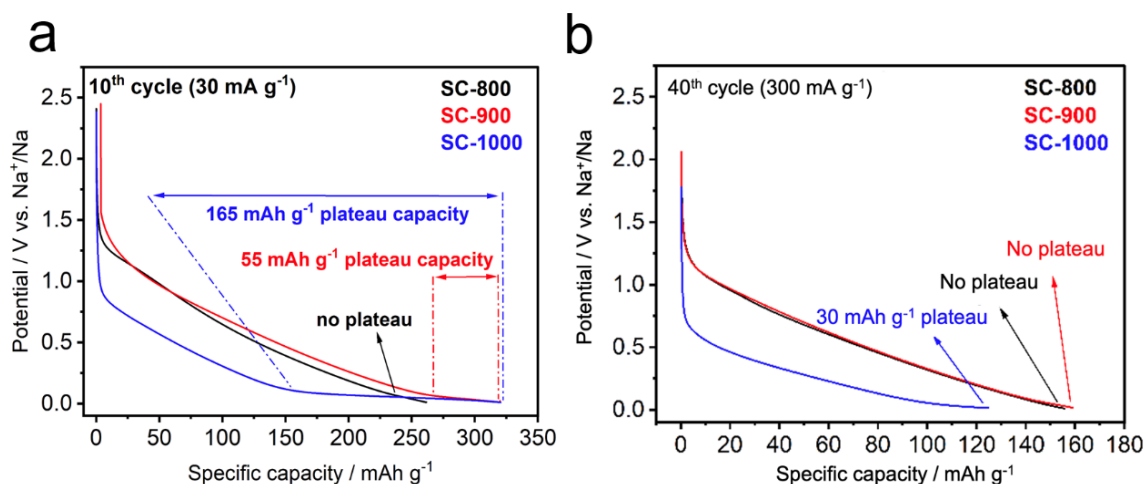


Figure 3.12. (a) 10th and (b) 40th sodiation curves of materials. (Copyright (2024) Wiley)

the cycling stability of the materials to simulate their performance in real applications as the capacity retention is expected to be high under charging and discharging at relatively high current densities. The results show that SC-800, SC-900, and SC-1000 have capacity retention rates of 92%, 90%, and 80%, respectively. The significant capacitive mode provided by SC-800 and SC-900 contributes to excellent stability; however, at this current density, SC-1000 still offers a small plateau region, which can lead to a slight decay during cycling as non-capacitive Faradaic storage tends to cause irreversible decomposition of electrolyte and then reduce the efficiency. Still, results here show that all materials exhibit good capacity retention after 500 cycles.

After GCD cycling, electrochemical impedance spectra (EIS) show double-semi circles (**Figure A3.11**), with the semi-circle in the mid-frequency region commonly associated with SEI formation and contributing significantly to charge transfer resistance. The excessive growth of the passivation layer can affect the state of health (SoH) of the batteries.^[47] The charge transfer resistance (R_t in **Figure A3.11**) of SC-1000 after cycling is the highest among all samples, which might indicate lower SoH than SC-800 and SC-900 due to more harsh electrochemical reactions (**Table A3.1**).

Full-cell using Na₃V₂(PO₄)₃ (NVP) as cathode material – The SC-1000 demonstrates a notable feature in the form of an elongated plateau region, which facilitates most of the sodium storage at an elevated cell potential. As a result, the energy density in full-cell applications is considerably improved in comparison to the SC-800 and SC-900 batteries. To showcase the complete cell functionality of the SC-1000, the NVP cathode material is chosen as a positive electrode.

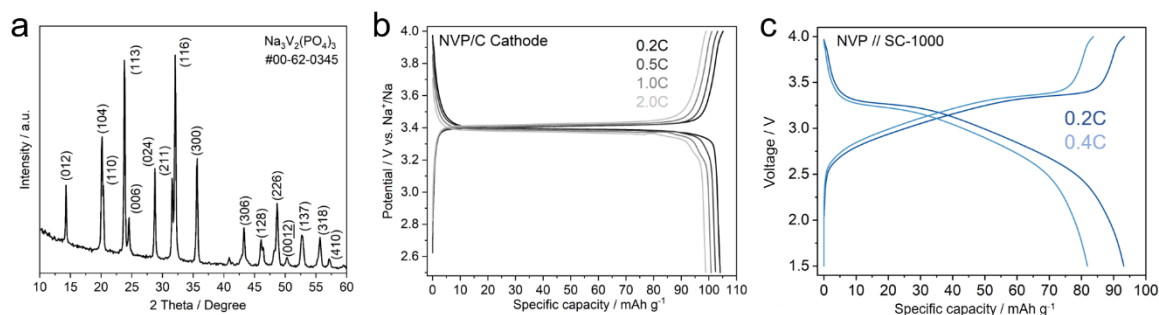


Figure 3.13. (a) The XRD pattern of the NVP cathode material. (b) The half-cell GCD curves of the NVP/C cathode material at various rates with 1M NaPF₆ in EC/DEC (1:1 in vol.) along with 5 wt. % FEC. (c) The GCD of the full-cell, NVP//SC-1000, with the negative electrode being SC-1000 and the positive electrode being NVP/C. The current density and specific capacity are calculated based on the mass of the active material in the positive electrode. (Copyright (2024) Wiley)

The crystal structure of the NVP is validated using XRD (**Figure 3.13a**), and its electrochemical performance is assessed through half-cell GCD measurements (**Figure 3.13b**). The cathode slurry contains an equal proportion of conductive carbon (Super-P, 10 wt. %) as the anode material (SC-1000). Two different electrolytes, namely 1M NaPF₆ in EC/EMC (3:7 in vol.) and 1M NaPF₆ in EC/DEC (3:7 in vol.) with the addition of 5 wt. % FEC, are employed. The latter electrolyte demonstrates slightly better electrochemical performance for the cathode material, yielding a capacity of approximately 105 mAh g⁻¹ at 0.2C, which corresponds to more than 92% of its theoretical capacity (ca. 117 mAh g⁻¹). However, the presence of FEC in the anode side leads to a noticeable reduction in the plateau capacity, which could be attributed to the formation of a thick SEI layer, impeding sodium diffusion. For the purpose of testing the anodes, 1M NaPF₆ in EC/EMC (3:7 in vol.) is chosen as the electrolyte for full-cell measurements. Prior to full-cell testing, the SC-1000 anode material undergoes presodiation to mitigate the effect of initial coulombic efficiency and ensure stability. The energy densities of the full-cells are computed using Eq. 3.5, where Q represents the capacity at a specific rate, m corresponds to the total active material mass, and U denotes the cell voltage.

$$E = \int_0^Q \frac{U}{m} dQ \quad (3.5)$$

Based on the active materials, the energy density is determined to be 170 Wh kg⁻¹ at 0.2C and 149 Wh kg⁻¹ at 0.4C (**Figure 3.13c**).

3.3.3. Boosting electrochemical storage by sodium plating and stripping

Electroplating and stripping sodium is another type of sodium storage widely exploited in metal anode batteries. Having very high theoretical capacities of metal anodes and stable cell potential due to the electroplating process, this type of storage is found to be a novel approach for increasing the energy density of batteries. However, this storage mode is not standard for insertion-based anodes, as the irreversible plating of metal causes the formation of large dendrites and “dead” metal residues, which can adversely affect battery performance and safety. Sodium’s lower cohesion energy with respect to lithium, is enabled it to be more homogeneously nucleated and plated at the electrode, which requires a favorable chemical environment for sodium adsorption and nucleation, as provided by a microporous structure.^[48] This type of storage has also never been proposed for carbon-based electrodes as it destroys the structure and causes the growth of the dendrites.

Based on these considerations, the materials here are subjected to this type of sodium storage mode. Even though the harsh plating and stripping process, the total reversible capacity of SC-1000 can be extended over 380 mAh g^{-1} , with an over 95% Coulombic efficiency, which is an overseen value in this type of storage among the carbon-based electrodes. This is in contrast to SC-800 and SC-900, which do not allow such reversible metal plating and stripping under any of the cutoff conditions (**Figure 3.14a**). The sharp dip in the nucleation overpotential is associated with more dendritic spikes (**Figure 3.15b**).^[49]

To prove it, an *ex-situ* investigation using SEM is conducted (**Figure 3.15**). For the sample preparation, the materials undergo overpotential sodium deposition mode for more than

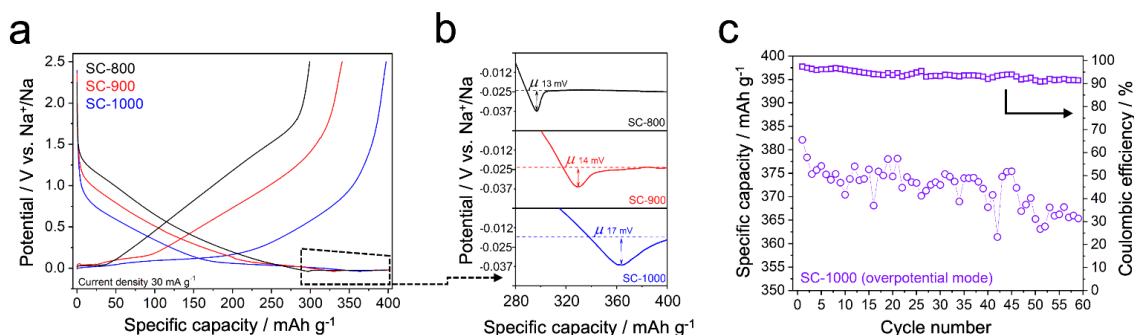


Figure 3.14. (a) Overpotential sodium deposition behavior of materials, where the cutoff conditions for sodiation and desodiation are set to 400 mAh g^{-1} and 2.5 V (vs. Na^+/Na), respectively. Panel (b) presents an enlarged view of the nucleation overpotential regions, which play a critical role in the initial stages of sodium deposition. Panel (c) displays the stability of the SC-1000 during 60 cycles of sodium plating and stripping at a current rate of $0.1C$ (30 mA g^{-1}). (Copyright (2024) Wiley)

ten cycles. After disassembling the half-cells in a glove box, the anode materials are washed with pure DMC organic solvent to eliminate any residual electrolyte. The EDX spectra, as shown in the inset of **Figure 3.15**, confirm that the frameworks are free from the solid electrolyte, as there are no signals from fluorine and phosphorus. The sodium signals observed in the spectra can be mainly attributed to the overpotential deposition of sodium metal. The SEM images of the materials in a sodium-plated state follow the electrochemically observed nucleation kinetics of metal plating, with larger crystallites observed in SC-800 and smaller in SC-900, especially for SC-1000.

In contrast, the broad nucleation dip found for SC-1000 indicates that the growth of sodium crystallites occurs via the formation of a larger number of nuclei on the surface, reflecting a more intimate and thermodynamically favorable interaction between the electrode and the sodium atoms. This dispersity provides promising reversibility and stability, attributed to the high amount of (ultra-) micropores combined with the heteroatomic surface and optimum adsorption enthalpy between sodium metal and the host SC-1000. The (ultra-)micropores behave like “bags” within the electrode to host the

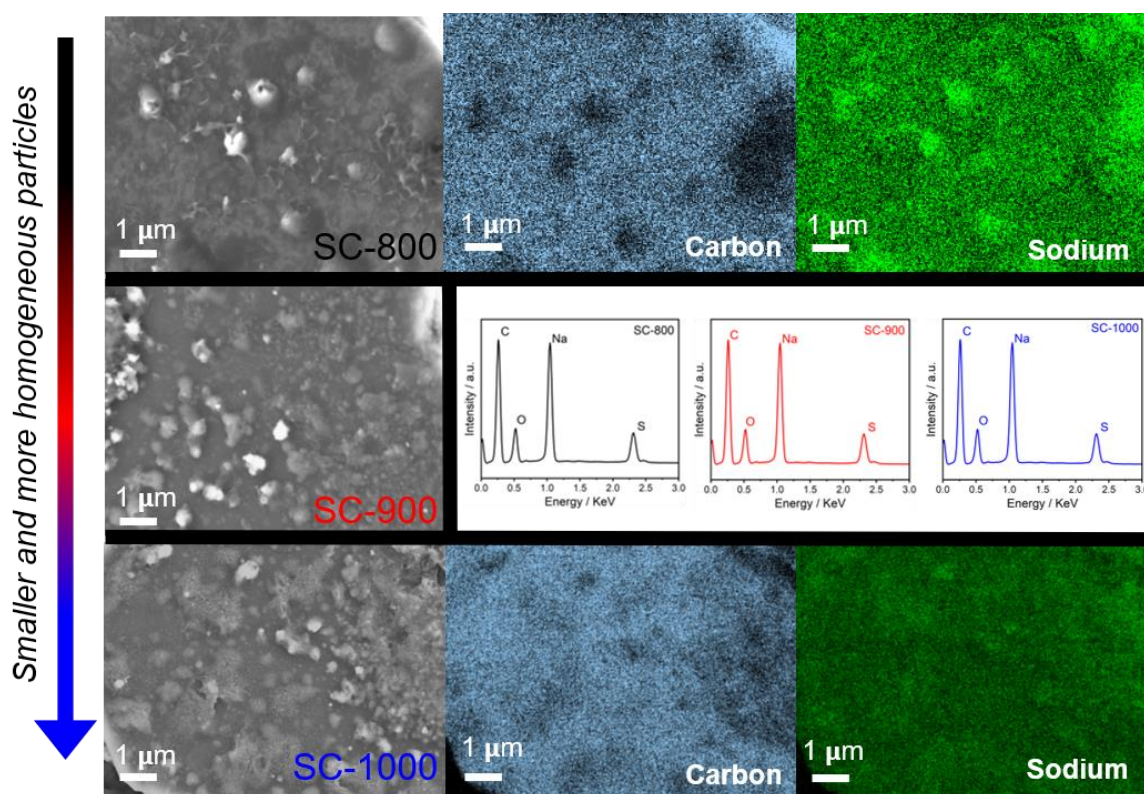


Figure 3.15. The SEM images of the materials after overpotential sodium deposition, and the inset shows the EDX spectra of the frameworks. (Copyright (2024) Wiley)

nucleation of a few sodium atoms to grow out homogeneously at the SC-1000 surface to the plating layer that is again quantitatively removed during stripping.

The amount of plated sodium in this overpotential mode can be approximated using Faraday's law of electrolysis.

$$Q = i \cdot t \quad (3.6)$$

$$m = \left(\frac{Q}{F}\right) \left(\frac{M}{z}\right) \quad (3.7)$$

The equations are related to the total electric charge passed through a substance (Q), the Faraday constant (F), the molar mass of the substance (M), the mass of the substance liberated at the electrode (m), and the valency number of ions (z). The surface plating of sodium takes place after the nucleation dip, as depicted in **Figure 3.14b**, and continues until the cutoff capacity is reached. The period from the nucleation dip (approximately 364 mAh g⁻¹) to the cutoff capacity (400 mAh g⁻¹) is determined to be 4320 seconds, during which a current of 30.3 μA is applied. Therefore, the amount of plated sodium in the first operating cycle of overpotential mode is estimated at 31.2 μg, calculated using Eq. 3.6 and Eq. 3.7, considering the valency number of ions ($z=1$) for the reduction of Na⁺ to Na (0). However, the amount of plated sodium is subject to change due to the shifting of the nucleation dip during cycling. At the 60th cycle, the estimated amount of plated sodium is 17.2 μg.

The shift in the nucleation dip is correlated to the change in the structure caused by the harsh plating and stripping process that reduces the Coulombic efficiency to around 92% at the 60th operating cycle in this mode (**Figure 3.14c**). While overpotential sodium deposition is reversible, the constraints of the process still require more research. Given that this type of sodium storage is not well-studied for carbonaceous materials,^[50] these insights are critical to building more efficient electrochemical sodium-based energy storage systems. For practical applications, reversible overpotential sodium deposition may significantly increase the plateau capacity, average cell potential, and energy density.

3.3.4. Elucidating the pore-filling mechanism by *in-operando* SAXS

It is shown that SAXS is a potent analytical methodology that can effectively study the accessible and bulk porosity of non-graphitic carbons, even when subjected to *in-situ* and *in-operando* measurements.^[51] When utilized in combination with synchrotron light sources, SAXS measurements can detect alterations in the structure of the studied electrodes while operating in ideal conditions. In this regard, the deposition of sodium at under- and over-potential modes on SC-1000 is examined utilizing *in-operando* SAXS. A

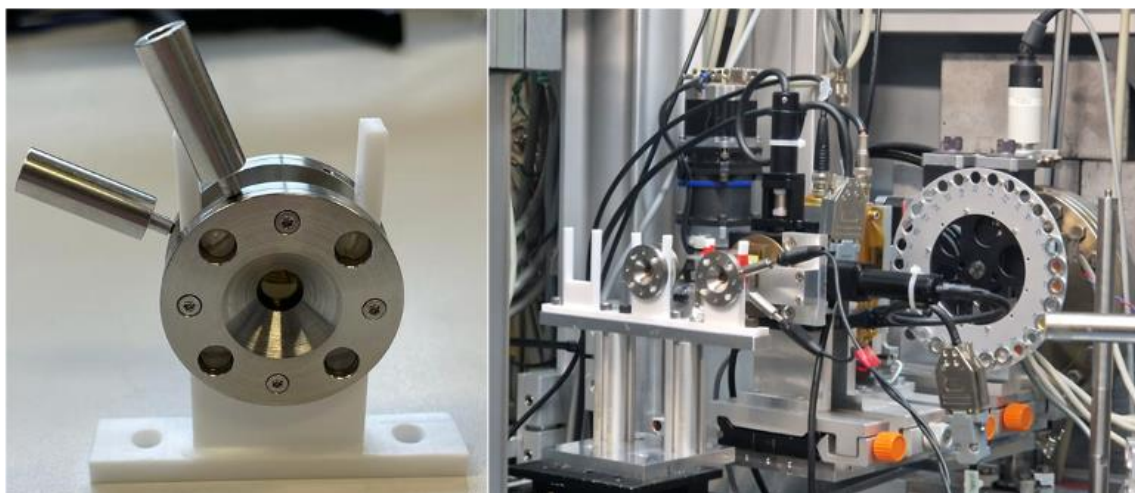


Figure 3.16. A cell made of stainless steel with a specially designed transmission window for operando SAXS measurement (**left**) and experimental setup at BESSY II (**right**). (Copyright (2024) Wiley)

specialized half-cell with a Kapton film on the transmission window is employed for the measurements (**Figure 3.16**).

The scattering intensity, $I(q)$, is mathematically described as a function of the electron density (ρ) difference known as $\Delta\rho$, which represents the disparity in density between particles and their surrounding media. This relationship can be expressed as follows:

$$I(q) = K\Delta\rho^2P(q)S(q) \quad (3.8)$$

In this equation, K is a constant, $P(q)$ represents the form factor function utilized to determine particle shape, and $S(q)$ describes the spatial distribution of particles. The sphere model (Eq. 3.9), which accounts for scattering from both macro- and micro-pores, is employed as a fitting model and fits precisely to the raw data (**Figure 3.17a** and **Figure 3.18**).

$$P(q) = \left[4\pi r^3 \frac{\sin(qr) - qr\cos(qr)}{(qr^3)} \right]^2 \quad (3.9)$$

During the process of sodiation, a noticeable decrease in intensity is observed within the relative q range, indicating the insertion of sodium ions into the microporous structure (**Figure 3.17b**). Upon desodiation, the scaled intensity returns to a state close to its initial condition at the mirroring potential, demonstrating the reversibility of the pore-filling mechanism. This result aligns with previous findings.^[52]

The $\Delta\rho$ is associated with contrast, which is a measure of the intensity of X-ray scattering relative to the surrounding medium.^[53] When alkali ions are inserted into carbon, the $\Delta\rho$ of the structure is expected to increase due to the electron cloud. The fitting model includes two regression models, each corresponding to the fitting of spherical micro- and mesopores within the structural composition:

$$I(q) = K_0\Delta\rho_0^2 \int \varphi(r_0)P(q, r_0)dr_0 + K_1\Delta\rho_1^2 \int \varphi(r_1)P(q, r_1)dr_1 + background \quad (3.10)$$

Through the mathematical transformation of Eq. 3.8 to Eq. 3.10, it can isolate the electron density variation into distinct variables, namely $\Delta\rho_0$ and $\Delta\rho_1$. In this context, the symbol $\Delta\rho_0$ indicates the disparity in electron density between micropores near large particles,

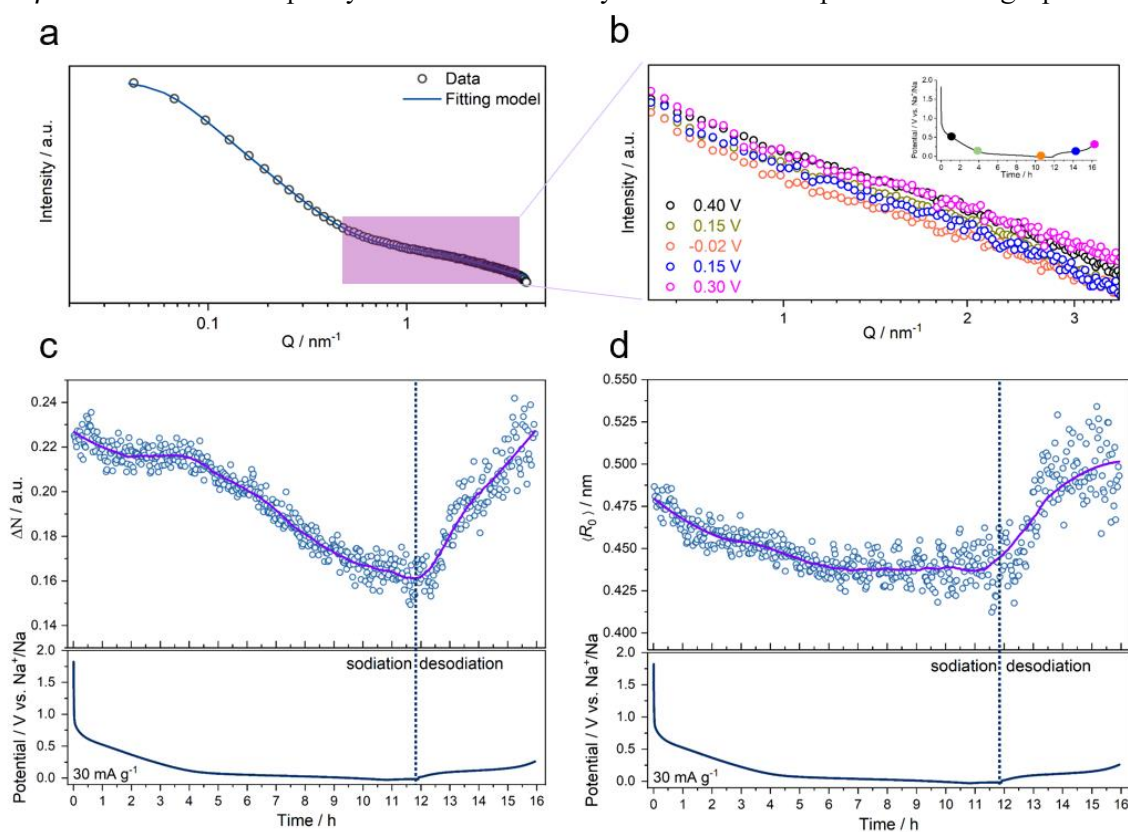


Figure 3.17. (a) A graph depicting the scattering of single particles and the two-sphere fitting model, which indicates a high-degree of accuracy in matching the experimental data. Subfigure (b) provides a closer examination of the scattering patterns from the microporous region during the sodiation and desodiation processes. Subfigure (c) illustrates the alteration in the modified electron density difference (ΔN) of the micropores in relation to the current collector during the sodiation and desodiation processes. Finally, subfigure (d) shows the changes in the average radius of the micropore model during the sodiation and desodiation processes. Smoothing lines are in purple color to show the trend clearly. (Copyright (2024) Wiley)

macropores, and mass fractals. Conversely, $\Delta\rho_l$ denotes the dissimilarity in electron density between those large particles and the aluminum current collector, which exhibits minimal interaction with sodium ions.^[54] As a result, the comprehensive contrast in electron density between the micropores and the current collector can be mathematically expressed as ΔN in Eq. 3.11:

$$\Delta N = \frac{4}{3}\pi\langle R_0 \rangle^3 |\Delta\rho_0 - \Delta\rho_1| \quad (3.11)$$

In the detailed examination presented in **Figure 3.17c**, the variation in electron density follows a similar pattern to that observed in the sodiation and desodiation curves. In the sloping region, changes in ΔN are typically not observed since the storage process is primarily governed by the pore-filling mechanism, whereby sodium ions are strongly adsorbed onto the surface. However, a significant reduction in the overall ΔN is observed in the diffusion-controlled plateau region, indicating a substantial change in electron density difference between the micropores and the surrounding environment associated with the ion diffusion. When the overpotential region is analyzed, its effect on ΔN is slightly reduced, potentially due to the nucleation of sodium starting and growing through the surfaces. During the desodiation process, ΔN returns to its initial state in accordance with the scattering patterns and radius.

Following sodiation, the average radius of particles $\langle R_0 \rangle$ (measured in nm, Eq. 3.12) visibly decreases, which is attributed to sodium ion uptake by the material in micropores (**Figure 3.17d**). This decrease in $\langle R_0 \rangle$ initiated with the surface adsorption of sodium ions and further continues in the plateau region. Conversely, upon desodiation, an opposite trend is observed, with an increase in $\langle R_0 \rangle$ that approaches the initial state.

$$\langle R_0 \rangle = \frac{\int r_0 \varphi(r_0) dr_0}{\int \varphi(r_0) dr_0} \quad (3.12)$$

In the *in-operando* SAXS experiment, diffraction patterns are collected from 16 distinct locations. To demonstrate the consistency of the findings mentioned in the main text, supplementary locations, which reveal similar patterns, are presented in Figure A3.12.

The equation presented in Eq. 3.9, which corresponds to the two-sphere model, exhibits a high level of accuracy in fitting, even when applied to very low q ranges beyond the examined region (**Figure 3.18a**). Furthermore, within the mid- q range, wherein the microporous characteristics of the model material are manifested, the fitting precision is notably enhanced, as exemplified in **Figure 3.18b** and **Figure 3.18c**.

Ex-situ measurements are performed on the precycled electrode, as illustrated in **Figure 3.18d**. The results obtained indicate a significant decrease in the intensity of the micropore

region, indicating the presence of electrolytes leftover, which may exist as oxidized compounds that are entrapped within the micropores and cannot be removed without additional treatment. The identification of such phenomena presents a noteworthy challenge in *ex-situ* investigations and warrants careful consideration when comparing them with *in-operando* studies.

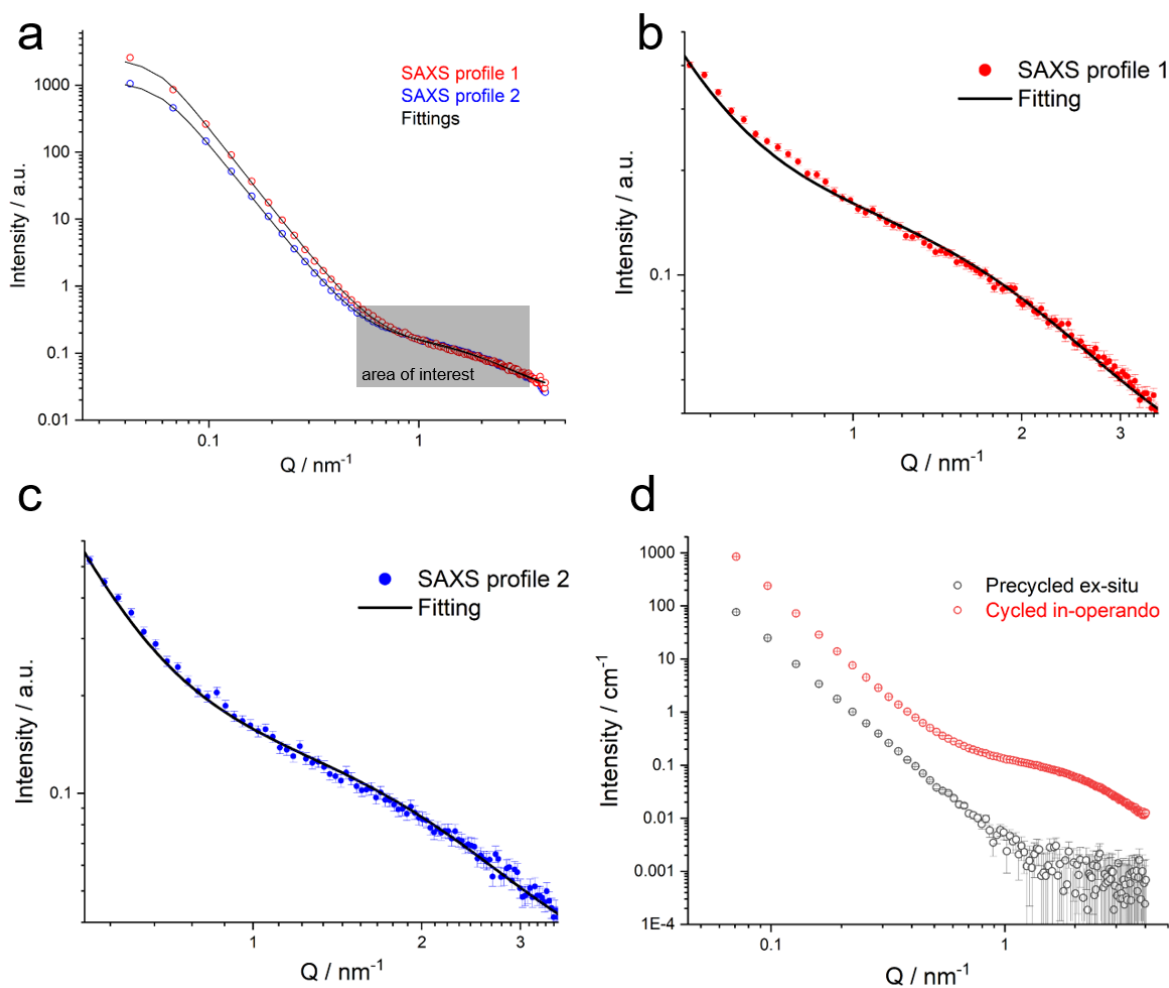


Figure 3.18. The fitting quality of the two-sphere model for the raw data (consisting of two randomly selected profiles) is shown in panel (a). An enlarged view of profile 1 and profile 2 is presented in (b) and (c), respectively. (d) A comparison of the SAXS profile between the cycled electrode and the *ex-situ* electrode that are precycled. (Copyright (2024) Wiley)

3.4. Conclusions

This chapter presents a novel method for producing sulfur-rich carbons possessing a high sulfur heteroatom content through the pyrolysis of oligo-EDOT. The unique chemical and nanostructural characteristics of the material lead to excellent electrochemical properties, resulting in a reversible capacity exceeding 320 mAh g^{-1} in underpotential deposition mode. Increasing the condensation temperature makes it possible to generate materials with significantly different sodium storage mechanisms, ranging from high-rate capable surface-controlled capacitive storage at higher sulfur contents to non-capacitive Faradaic storage at lower sulfur contents, which is essential for high energy density applications. The physico-chemical and structural properties of the anode material allow for promising overpotential sodium deposition in the latter case. The transition between surface-controlled to diffusion-controlled sodium storage mechanisms at different pyrolysis temperatures is thoroughly examined and correlated with the (ultra-)microporosity and short-range nanostructural order of the electrode materials. The uniqueness of the synthesized material enables the achievement of an unprecedented reversible overpotential deposition, which can improve the energy density of the battery by reducing the average anodic potential, enhance the safety of the battery during operation when the potential might not be adequately controlled, and define a potential pathway for the innovation and development of carbon-based anode materials. Based on the material's chemistry and nanostructure, the findings here are expected to pave the way for developing high-performing electrodes with an extended operation window based on carbon-sulfur materials.

Bibliography for Chapter 3

- [1] R. Mishra, S. Panigrahy, S. Barman, *Energy Fuels* **2022**, *36* (19), 12310-12318.
- [2] J. Yang, X. Zhou, D. Wu, X. Zhao, Z. Zhou, *Adv. Mater.* **2017**, *29* (6), 1604108-1604108.
- [3] Z. Hong, Y. Zhen, Y. Ruan, M. Kang, K. Zhou, J.-M. Zhang, Z. Huang, M. Wei, *Adv. Mater.* **2018**, *30* (29), 1802035.
- [4] L. Qie, W. Chen, X. Xiong, C. Hu, F. Zou, P. Hu, Y. Huang, *Adv. Sci.* **2015**, *2* (12).
- [5] W. Li, M. Zhou, H. Li, K. Wang, S. Cheng, K. Jiang, *Energy Environ. Sci.* **2015**, *8* (10), 2916-2921.
- [6] X. Yuan, S. Chen, J. Li, J. Xie, G. Yan, B. Liu, X. Li, R. Li, L. Pan, W. Mai, *Carbon Energy* **2021**, *3* (4), 615-626.
- [7] B. Wan, H. Zhang, S. Tang, S. Li, Y. Wang, D. Wen, M. Zhang, Z. Li, *Sustain. Energy Fuels* **2022**, *6* (18), 4338-4345.
- [8] Q. Jin, K. Wang, P. Feng, Z. Zhang, S. Cheng, K. Jiang, *Energy Storage Mater.* **2020**, *27*, 43-50.
- [9] N. T. Aristote, C. Liu, X. Deng, H. Liu, J. Gao, W. Deng, H. Hou, X. Ji, *J. Electroanal. Chem.* **2022**, *923*, 116769.
- [10] a) Z. Li, C. Bommier, Z. S. Chong, Z. Jian, T. W. Surta, X. Wang, Z. Xing, J. C. Neufeind, W. F. Stickle, M. Dolgos, P. A. Greaney, X. Ji, *Adv. Energy Mater.* **2017**, *7* (18), 1602894-1602894; b) W. Chen, M. Wan, Q. Liu, X. Xiong, F. Yu, Y. Huang, *Small Methods* **2019**, *3* (4), 1800323-1800323.
- [11] L. Qie, W. Chen, X. Xiong, C. Hu, F. Zou, P. Hu, Y. Huang, *Adv. Sci.* **2015**, *2* (12), 1500195.
- [12] Y. Wang, D. Zhou, V. Palomares, D. Shanmukaraj, B. Sun, X. Tang, C. Wang, M. Armand, T. Rojo, G. Wang, *Energy Environ. Sci.* **2020**, *13* (11), 3848-3879.
- [13] J. Y. Hwang, S. T. Myung, Y. K. Sun, *Chem. Soc. Rev.* **2017**, *46* (12), 3529-3614.
- [14] C. Esen, M. Antonietti, B. Kumru, *ChemPhotoChem* **2021**, *5* (9), 857-862.
- [15] S. V. Selvaganesh, J. Mathiyarasu, K. L. N. Phani, V. Yegnaraman, *Nanoscale Res. Lett.* **2007**, *2* (11), 546-546.
- [16] X. Liu, N. Fechler, M. Antonietti, M. G. Willinger, R. Schlögl, *Mater. Horiz.* **2016**, *3* (3), 214-219.
-

CHAPTER 3. SULFUR-RICH CARBON ANODE

-
- [17] a) C. J. Jafta, A. Petzold, S. Risse, D. Clemens, D. Wallacher, G. Goerigk, M. Ballauff, *Carbon* **2017**, *123*, 440-447; b) D. Saurel, J. Segalini, M. Jauregui, A. Pendashteh, B. Daffos, P. Simon, M. Casas-Cabanas, *Energy Storage Mater.* **2019**, *21*, 162-173.
- [18] W. Ruland, *J. Appl. Crystallogr.* **1971**, *4* (1), 70-73.
- [19] V. Simone, A. Boulineau, A. de Geyer, D. Rouchon, L. Simonin, S. Martinet, *J. Energy Chem.* **2016**, *25* (5), 761-768.
- [20] C. Li, Y. Sun, Q. Wu, X. Liang, C. Chen, H. Xiang, *Chem. Commun. (Camb)* **2020**, *56* (45), 6078-6081.
- [21] A. C. Ferrari, J. Robertson, *Phys. Rev. B* **2000**, *61* (20), 14095-14107.
- [22] L. H. Cohan, *J. Am. Chem. Soc.* **1938**, *60* (2), 433-435.
- [23] J. Landers, G. Y. Gor, A. V. Neimark, *Colloids Surf., A* **2013**, *437*, 3-32.
- [24] a) C. Lastoskie, K. E. Gubbins, N. Quirke, *Langmuir* **1993**, *9* (10), 2693-2702; b) P. I. Ravikovitch, A. Vishnyakov, R. Russo, A. V. Neimark, *Langmuir* **2000**, *16* (5), 2311-2320; c) J. Jagiello, M. Thommes, *Carbon* **2004**, *42* (7), 1227-1232.
- [25] a) W. Luo, C. Bommier, Z. Jian, X. Li, R. Carter, S. Vail, Y. Lu, J. J. Lee, X. Ji, *ACS Appl. Mater. Interfaces* **2015**, *7* (4), 2626-2631; b) B.-H. Hou, Y.-Y. Wang, Q.-L. Ning, W.-H. Li, X.-T. Xi, X. Yang, H.-J. Liang, X. Feng, X.-L. Wu, *Adv. Mater.* **2019**, *31* (40), 1903125-1903125.
- [26] A. Beda, C. Vaultot, C. Matei Ghimbeu, *J. Mater. Chem. A* **2021**, *9* (2), 937-943.
- [27] a) J. Yang, X. Wang, W. Dai, X. Lian, X. Cui, W. Zhang, K. Zhang, M. Lin, R. Zou, K. P. Loh, Q.-H. Yang, W. Chen, *Nano-Micro Lett.* **2021**, *13* (1), 98-98; b) S.-W. Zhang, W. Lv, C. Luo, C.-H. You, J. Zhang, Z.-Z. Pan, F.-Y. Kang, Q.-H. Yang, *Energy Storage Mater.* **2016**, *3*, 18-23.
- [28] A. Karatrantos, Q. Cai, *Phys. Chem. Chem. Phys.* **2016**, *18* (44), 30761-30769.
- [29] T. Wu, M. Jing, L. Yang, G. Zou, H. Hou, Y. Zhang, Y. Zhang, X. Cao, X. Ji, *Adv. Energy Mater.* **2019**, *9* (9), 1803478-1803478.
- [30] Y. Dong, H. Pang, H. B. Yang, C. Guo, J. Shao, Y. Chi, C. M. Li, T. Yu, *Angew. Chem. Int. Ed.* **2013**, *52* (30), 7800-7804.
- [31] M. Smith, L. Scudiero, J. Espinal, J.-S. McEwen, M. Garcia-Perez, *Carbon* **2016**, *110*, 155-171.
- [32] a) I. Herrmann, U. I. Kramm, J. Radnik, S. Fiechter, P. Bogdanoff, *J. Electrochem. Soc.* **2009**, *156* (10), B1283-B1283; b) L. Hou, Q. Liang, F. Wang, *RSC Adv.* **2020**, *10* (4), 2378-2388.
-

CHAPTER 3. SULFUR-RICH CARBON ANODE

-
- [33] L. Ponsonnet, C. Donnet, K. Varlot, J. M. Martin, A. Grill, V. Patel, *Thin Solid Films* **1998**, 319 (1), 97-100.
- [34] a) J. T. Titantah, D. Lamoen, *Phys. Rev. B* **2004**, 70 (7), 75115-75115; b) D. A. Muller, Y. Tzou, R. Raj, J. Silcox, *Nature* **1993**, 366 (6457), 725-727.
- [35] A. B. Siddique, A. K. Pramanick, S. Chatterjee, M. Ray, *Sci. Rep.* **2018**, 8 (1), 9770-9770.
- [36] a) H. Hou, X. Qiu, W. Wei, Y. Zhang, X. Ji, *Adv. Energy Mater.* **2017**, 7 (24), 1602898-1602898; b) H. He, D. Sun, Y. Tang, H. Wang, M. Shao, *Energy Storage Mater.* **2019**, 23, 233-251; c) Y. Li, M. Chen, B. Liu, Y. Zhang, X. Liang, X. Xia, *Adv. Energy Mater.* **2020**, 10 (27), 2000927.
- [37] K. Li, J. Zhang, D. Lin, D.-W. Wang, B. Li, W. Lv, S. Sun, Y.-B. He, F. Kang, Q.-H. Yang, L. Zhou, T.-Y. Zhang, *Nat. Commun.* **2019**, 10 (1), 725-725.
- [38] L. Xiao, H. Lu, Y. Fang, M. L. Sushko, Y. Cao, X. Ai, H. Yang, J. Liu, *Adv. Energy Mater.* **2018**, 8 (20), 1703238.
- [39] I. Moez, H.-G. Jung, H.-D. Lim, K. Y. Chung, *ACS Appl. Mater. Interfaces* **2019**, 11 (44), 41394-41401.
- [40] J. Song, B. Xiao, Y. Lin, K. Xu, X. Li, *Adv. Energy Mater.* **2018**, 8 (17), 1703082.
- [41] Y. Li, M. Liu, X. Feng, Y. Li, F. Wu, Y. Bai, C. Wu, *ACS Energy Lett.* **2021**, 6 (9), 3307-3320.
- [42] T. S. Mathis, N. Kurra, X. H. Wang, D. Pinto, P. Simon, Y. Gogotsi, *Adv. Energy Mater.* **2019**, 9 (39), 1902007.
- [43] a) K. Wang, Y. Jin, S. Sun, Y. Huang, J. Peng, J. Luo, Q. Zhang, Y. Qiu, C. Fang, J. Han, *ACS Omega* **2017**, 2 (4), 1687-1695; b) Y. Li, Y.-S. Hu, M.-M. Titirici, L. Chen, X. Huang, *Adv. Energy Mater.* **2016**, 6 (18), 1600659.
- [44] L. F. Zhao, Z. Hu, W. H. Lai, Y. Tao, J. Peng, Z. C. Miao, Y. X. Wang, S. L. Chou, H. K. Liu, S. X. Dou, *Adv. Energy Mater.* **2020**, 11 (1), 2002704.
- [45] J. Qian, F. Wu, Y. Ye, M. Zhang, Y. Huang, Y. Xing, W. Qu, L. Li, R. Chen, *Adv. Energy Mater.* **2018**, 8 (16), 1703159.
- [46] J. Liu, J. Wang, C. Xu, H. Jiang, C. Li, L. Zhang, J. Lin, Z. X. Shen, *Adv. Sci.* **2018**, 5 (1), 1700322.
- [47] a) M. Messing, T. Shoa, S. Habibi, *J. Energy Storage* **2021**, 43, 103210-103210; b) A. Y. Kallel, V. Petrychenko, O. Kanoun, *Appl. Sci.* **2022**, 12 (2).
- [48] Z. H. Tian, Y. Zhang, J. X. Zhu, Q. Y. Li, T. X. Liu, M. Antonietti, *Adv. Energy Mater.* **2021**, 11 (47), 2102489.
-

- [49] Z. Mengqi, L. Songmei, L. Bin, G. Yongji, D. Zhiguo, Y. Shubin, *Sci. Adv.* **2022**, 5 (4), eaau6264.
- [50] H. Gong, Y. Chen, S. Chen, C. Xu, Y. Yang, Y. Ye, Z. Huang, R. Ning, Y. Cui, Z. Bao, *ACS Energy Lett.* **2022**, 7 (12), 4417-4426.
- [51] a) A. Brennhagen, C. Cavallo, D. S. Wragg, J. Sottmann, A. Y. Kuposov, H. Fjellvåg, *Batteries Supercaps* **2021**, 4 (7), 1039-1063; b) D. A. Stevens, J. R. Dahn, *J. Electrochem. Soc.* **2000**, 147 (12), 4428.
- [52] a) Y. Morikawa, S.-i. Nishimura, R.-i. Hashimoto, M. Ohnuma, A. Yamada, *Adv. Energy Mater.* **2020**, 10 (3), 1903176; b) D. Saurel, A. Pendashteh, M. Jáuregui, M. Reynaud, M. Fehse, M. Galceran, M. Casas-Cabanas, *Chemistry-Methods* **2021**, 1 (6), 249-260.
- [53] C. Prehal, D. Weingarth, E. Perre, R. T. Lechner, H. Amenitsch, O. Paris, V. Presser, *Energy Environ. Sci.* **2015**, 8 (6), 1725-1735.
- [54] K. Chayambuka, G. Mulder, D. L. Danilov, P. H. L. Notten, *Adv. Energy Mater.* **2020**, 10 (38), 2001310.

CHAPTER 4. HIGH-CAPACITY SUSTAINABLE HARD CARBON FOR SIBs.

Notion – The successful commercialization of SIBs relies heavily on designing and implementing highly efficient materials within the battery packs, from the electrode materials to supporting constituents. As stated in Chapter 1, the scope for improvement in the cathode materials is considerably constrained due to several limitations on the material side. However, research on the anode side is more expansive, mainly focusing on improving the performance of current carbonaceous materials. In this regard, hard carbons have emerged as a potential material for SIBs. Even within this category, there are subclasses of hard carbons, providing different electrochemical behaviors depending on the materials' structure.^[1]

Primarily, the current benchmark of hard carbons in SIBs comes from their superior performance compared to other carbonaceous materials, particularly graphite and soft carbons, which fail to deliver promising results in SIBs (**Figure 4.1**).^[2] Hard carbons typically exhibit higher specific capacities compared to the previous. A higher specific capacity combined with the diffusion-controlled storage mechanism directly corresponds to an increased energy density, a critical measure for practical applications.^[2-3] The structural characteristics of hard carbon also facilitate the efficient storage of sodium ions, encompassing processes such as ion insertion and micropore filling together.^[3]

The sodium storage behavior exhibited by hard carbons can be comparable to that observed in graphite within LIBs, providing a constant half-cell potential with a long plateau, thereby ensuring stable full-cell measures when combined with appropriate cathode materials. Another advantage associated with hard carbons lies in their synthesis processes, which can also be obtained from abundant sources, such as biowastes and industrial byproducts, as elucidated in the preceding chapters. Considering the trend in this field, there is still considerable room for further improvement of these materials, particularly through the introduction of more efficient synthesis and post-synthesis methods to control the chemistry and nanostructure of the carbonaceous materials towards improving the storage performances.^[2]

This dissertation explores several strategies aimed at enhancing the electrochemical performance of carbonaceous anode materials. Chapter 2 focuses on the post-synthetic approach, wherein CN is utilized as an *a*-SEI layer. By carefully adjusting the structural and electrical properties of the materials, significant improvements in sodium storage can be achieved. In Chapter 3, the sodium storage mechanism is evaluated within the concept of pore-filling while considering the sulfur heteroatom effect. Here, Chapter 4 elucidates a practical approach for fabricating a high-capacity anode material from sustainable sources for electrochemical sodium storage. A high-capacity hard carbon material is prepared through the one-step thermal condensation process utilizing 5-hydroxymethyl furfural (HMF), yielding high performances in SIBs and providing the requirements for being a potential anode material for commercial applications. In order to create a hard carbon material of choice, it is crucial to consider the potential methods available for enhancing performance metrics.

4.1. Parameters to improve the electrochemical performance

Hard carbon anodes in SIBs normally have specific capacities of 300 mA h g⁻¹ or lower, while some investigations have found values as high as 400 mA h g⁻¹.^[4] Enhancing the surface- and diffusion-controlled sodium storage will increase the specific capacity. However, due to different thermal treatment requirements, it is difficult to expand the capacity of both at once. Improving capacitive adsorption can be achieved with low-temperature heat treatment, heteroatom doping, and creating open surfaces, as discussed in Chapter 3, where the material pyrolyzed at lower temperatures provides much more sloping capacity (i.e., SC-800 vs. SC-1000). However, these methods significantly decrease the electrical conductivity and volumetric energy density, making them less practical for real applications.^[2] Also, the more open surface is one of the main reasons for the low initial Coulombic efficiency (ICE). Therefore, it is necessary to prepare hard carbon materials to tackle all the drawbacks above while maintaining the increased plateau capacities.

Although the mechanism for sodium storage in the plateau region is still partially elusive, the presence of closed pores and a larger interlayer spacing are frequently linked to higher plateau capacities.^[3] Increasing the interlayer spacing is typically achieved by introducing heteroatoms, which can be done through doping methods or using alkali-metal-containing substances from the beginning. In both cases, an increase in interlayer spacing has been reported to have an impact on the plateau capacity.^[2, 5] However, when compared to the effect of micropore volume, the influence of interlayer spacing is considerably less significant.^[2, 5]

An alternative approach to increasing the plateau capacity is to enhance the capacity through closed micropores. This can be accomplished by preventing the rearrangement of carbon atoms.^[5] Introducing oxygen through preoxidation or utilizing oxygen-rich precursors has been observed to restrict the graphitization process at high temperatures, resulting in the formation of more turbostratic domains. This, in turn, facilitates the formation of closed pores internally and leads to a significant increase in the plateau region.^[2, 5]

Due to their disordered structure, hard carbons naturally possess defects. These defects contribute to irreversible adsorption and, more significantly, consume the electrolyte, forming a thicker SEI.^[2] One effective method for mitigating these defects is to increase the carbonization temperature. However, excessively high temperatures promote graphitization, which has a negative impact on the specific capacity by reducing it and simultaneously increasing the diffusion barrier for sodium ions. It is crucial to control the condensation temperatures carefully to obtain good performance. In the case of hard carbons, the optimal heat treatment is usually around 1200°C and 1300°C.^[5] This range is significantly more energy-efficient when compared to the typical processes used for graphite anodes, which often require temperatures exceeding 2500°C.^[6] However, to promote the concept of more sustainable SIBs, it is still necessary to reduce the energy footprint of the fabrication process further. This will contribute to the overall goal of developing more environmentally friendly and sustainable energy storage solutions.

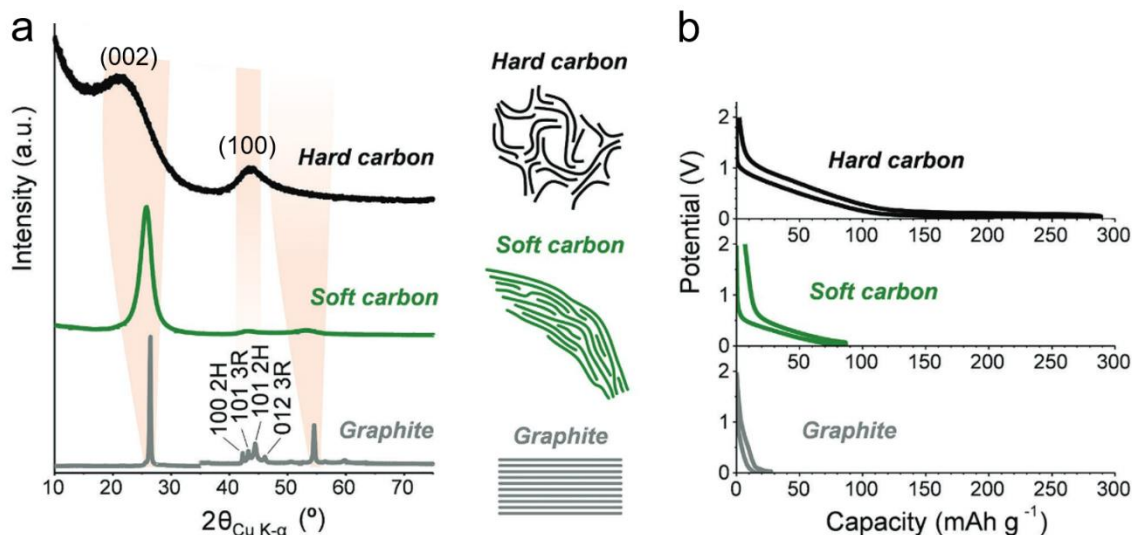


Figure 4.1. (a) The typical XRD patterns of hard carbon, soft carbon, and graphite. (b) Associated GCD curves in half-cell. Figure 1 in Saurel et al., *Adv. Energy Mater.*, **2018**, 8, 1703268. (Copyright (2018) Wiley)

A useful strategy for reducing defects in carbon materials is to optimize the carbonization atmosphere. In particular, using a reducing gas such as hydrogen is a viable option to mitigate the reactivity of defects at high temperatures.^[2] When exposed to a reducing atmosphere, functional groups that contain oxygen, such as C-O and C=O, and dangling bonds present in the carbon structure can undergo hydrogen reduction, converting them into volatile water and organic alkanes. This transformation helps eliminate defects and improves the overall quality of the carbon material. Additionally, it results in the formation of a significant number of nanopores within the structure, which can be utilized for efficient sodium-ion storage.^[2]

4.2. The effect of precursors on structure

Organic precursors are subjected to very high temperatures under an inert atmosphere to create graphitic carbons. These precursors are typically derived from biomasses, coal, or petroleum sources.^[7] During pyrolysis, volatile substances, i.e., hydrocarbons, water, methane, carbon dioxide, carbon monoxide, and ammonia, are released. The main loss in weight occurs within the temperature range of 250-500°C, and temperatures above 700°C are generally considered for the condensation of the precursors.^[2] However, oxygen or nitrogen heteroatoms could still be present in the remaining carbonaceous material. Higher temperatures must be attained before all of these components are released.^[2] After thermal condensation, the microstructure of the final carbon product can be categorized as either graphitizing carbons or non-graphitizing carbons, depending on the nature of the precursor. Non-graphitizing carbons exhibit a short-range arrangement with randomly oriented graphitic layers. Due to their low crystallinity and high amount of turbostratic disorder, these carbons exhibit broad X-ray diffraction peaks. The diffraction patterns of both graphitizing and non-graphitizing carbons change significantly when the temperature rises beyond 2500°C. In the case of graphitizing carbons, their X-ray diffraction peaks become sharper, which indicate the creation of a long-range graphitic order. (**Figure 4.1**). In contrast, non-graphitizing carbons experience a localized increase in crystallinity, yet their structure remains isotropic, with minimal interlayer reflections present.^[2]

The limited ability of non-graphitic carbons to undergo graphitization at elevated temperatures can be attributed to their unique microstructure. Initially, models proposed the randomly oriented graphitic domains interconnected within amorphous regions. This arrangement hinders the graphitization process and contributes to the development of a highly porous structure. Subsequent models now put the idea of a foam-like three-dimensional isotropic structure, wherein the walls of the micropores consist of curved carbon layers stabilized by non-hexagonal groups. As the temperature increases, the micropores gradually close and merge, but the resulting carbon material maintains a lower

density than graphite. This microstructural characteristic of non-graphitic carbons, featuring a foam-like structure with curved carbon layers and micropores, explains their inability to graphitize even at high temperatures fully.^[2]

Precursors containing heteroatoms that have the ability to remove a significant portion of hydrogen from the residue tend to yield non-graphitizing carbons. Examples of such precursors also include carbohydrates (e.g., sugars and cellulose).^[5, 8] Therefore, a practical guideline for predicting the type of carbon produced during thermal condensation is to estimate the excess hydrogen-to-carbon ratio. For instance, the presence of excess hydrogen following the initial mass loss is responsible for the formation of cokes.^[2] However, it is crucial to consider other aspects as well, as cross-linking can substantially impact the precursor's thermoplasticity. Despite a considerable excess of hydrogen, this cross-linking may occur in the precursor or in the initial stages of the heat treatment. The phenolic resins, lignin, and styrene-divinylbenzene polymers, among others, exhibit this

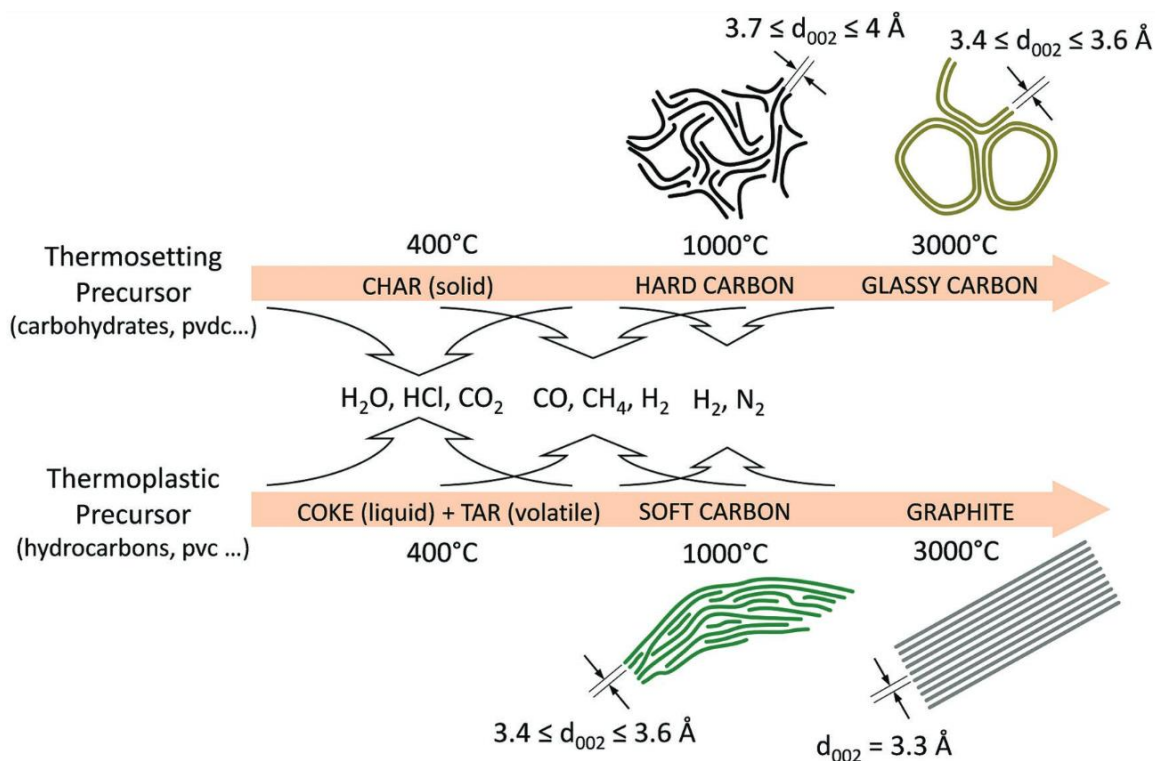


Figure 4.2. A diagram showing the carbonization process that takes place during the pyrolysis of organic materials, including thermosetting and thermoplastic polymers. The diagram also shows the typical carbon microstructure, along with the corresponding range of interlayer distances observed. Figure 2 in Saurel et al., *Adv. Energy Mater.*, **2018**, 8, 1703268. (Copyright (2018) Wiley)

behavior.^[9] Before carbonization, the precursor can also be intentionally induced to cross-link to stop further melting and impede the graphitization process. This effect is evident in materials such as PVC or polyethylene.^[10] In order to maintain the appropriate fiber morphology, a thermoplastic precursor is melted to create fibers, which are then cross-linked before carbonization. This process is known as oxidation-induced cross-linking. In general, the heat treatment processes create differences in morphology for thermosetting and thermoplastic precursors (**Figure 4.2**).

4.3. Production of HMF

A hydroxymethylfurfural (HMF) is a chemical compound that contains an aldehyde (CHO) and hydroxymethyl (CH₂-OH) groups on the furan ring.^[11] HMF represents a topic of considerable interest in chemistry as it is derived from biomasses and is an appealing candidate for many applications.^[11] Particularly in sustainable chemistry, HMF has a prominent role owing to its ability to be produced from renewable sources and its potential as a precursor for the synthesis of many valuable compounds. Extensive research has been conducted to explore HMF's potential for transformation into various biofuels, thereby offering a sustainable alternative to fossil fuels.^[11]

Hexoses, which are six-carbon sugars (i.e., glucose), are usually dehydrated to form HMF (**Figure 4.3**). The procedure entails putting the hexoses under a series of specific treatments and catalysts with specific functions.^[12] Pretreatment of lignocellulosic biomass, cellulose hydrolysis to glucose, glucose isomerization to fructose, and fructose dehydration are a few of the complex steps that the hexoses should undergo to create HMF.^[12b] Side reactions such as the condensation of sugars, reaction intermediates, the

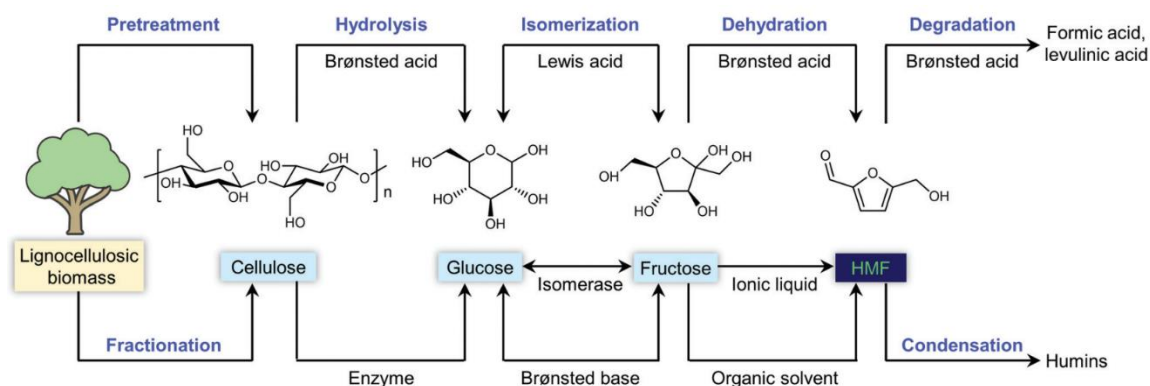


Figure 4.3. Synthesis of HMF from biomasses in different pathways. Figure 4 in Hou et al., *Green Chem.*, **2021**, 23, 119. (Copyright (2021) The Royal Society of Chemistry, copyright granted through Copyright Clearance Center, Inc.)

transformation of HMF into humins, and the degradation of HMF into formic acid or levulinic acid occur in parallel and reduce the HMF yield.

A viable approach to obtain HMF involves the catalytic dehydration of fructose. Several catalysts, including metal salts, ionic liquids, organic solvents, and Brønsted acid catalysts, facilitate the conversion of fructose to HMF.^[12b] Moreover, the fructose-based polysaccharide inulin can be used to form HMF through sequential hydrolysis to fructose and subsequent dehydration. Conversely, the conversion of glucose to HMF, despite its abundance and lower cost compared to fructose, presents challenges due to its more stable structure. Normally, the process of turning glucose into HMF happens in two steps; first, glucose is isomerized to fructose, then fructose is dehydrated to form HMF (**Figure 4.3**).^[12b] The isomerization of glucose to fructose often exhibits lower yields and efficiency compared to the HMF production directly from fructose. This isomerization process can be catalyzed by a number of catalysts, including Lewis acids, isomerases, and Brønsted bases. Direct conversion of glucose to HMF generally yields lower product yields and selectivity compared to conversion from fructose. HMF can also be generated as a byproduct during the pretreatment, hydrothermal processing, and carbonization of cellulose, hemicelluloses, and biomass.^[12b] Furthermore, chitin biomass derived from chitosan and crustacean shells can serve as alternative feedstocks for HMF production. Non-acidic catalysts, such as solid catalysts or ionic liquids, as well as alternative reaction conditions, are being investigated to enhance the selectivity, efficiency, and sustainability of HMF production.^[12b] These methods seek to enhance the HMF synthesis overall.

In a thermal polymerization process, the removal of OH groups initiates at approximately 170°C, and further heating of HMF to slightly above 250°C leads to dimerization.^[13] Subsequently, a significant portion of the molecules undergo char formation through the Diels-Alder reaction, resulting in the generation of a substantial amount of carbon as a final product, whether through hydrothermal carbonization (HTC) or conventional methods.^[14] HMF, being an oxygen-rich precursor, is an effective precursor for the production of non-graphitic carbons, as previously discussed. In this context, the presence of oxygen facilitates the formation of an extremely confined, porous, and interconnected structure, which can efficiently accommodate the sodium ions. Thus, based on the current benchmarks of saccharides in the SIBs,^[15] HMF is used in this Chapter as a sustainable precursor to producing high-capacity hard carbon electrodes.

4.4. Preparation of hard carbon derived from HMF

The hard carbon anode is synthesized from HMF precursor via one-step thermal condensation at 1100°C. The details of the synthesis method, electrochemical, and physico-chemical characterizations can be found in “**A4.1. Preparation of hard carbon**”

from HMF”, “A4.2. Electrode preparation and electrochemical characterizations”, and “A4.3. Physico-chemical characterizations” in Appendices.

4.5. Results and Discussion

4.5.1. Physico-chemical characterizations

Structure of carbon – Scanning electron microscopy (SEM) images reveal the material condensates, forming large particles characterized by distinct sharp edges and boundaries analogously to other hard carbons (**Figure 4.4a** and **Figure 4.4b**). Elemental analysis (EA) indicates that the composition consists of approximately 97.5 ± 1.0 wt. % carbon and 2.5 ± 1.0 wt. % oxygen, with a negligible amount of hydrogen. Energy-dispersive X-ray (EDX) spectroscopy confirms the homogeneous distribution of C and O within the material without any observed localization (**Figure 4.4a, inset**). The composition of the elements in the structure is further supported by EDX, yielding similar values of EA.

Structural analysis is conducted using high-resolution transmission electron microscopy (HRTEM) (**Figure 4.4c**). The obtained image verifies the non-graphitic nature of the hard carbon, revealing the short-range ordered structure with pseudo-graphitic planes throughout the structure.^[16] The absence of long-range order is indicated by a single diffuse ring in the fast Fourier transform (FFT) profile. Two broad peaks with centers at around 23° and 44° are visible in the X-ray diffraction (XRD) pattern and are attributed to the (002) and (100) reflections of non-graphitic carbons, respectively (**Figure 4.4d**).^[17] These broad peaks serve as confirmation of the short-range order present in the materials associated with the hard carbons. By employing a Gaussian fitting model on the diffraction pattern, the interlayer spacing of the (002) reflection is determined to be 0.39 nm (**Figure 4.4d, inset**). A less dense structure is evident because this computed gap is notably bigger than that of graphite (0.34 nm). Further investigation into the structure is conducted through Raman spectroscopy, wherein the *G* and *D* bands are analyzed utilizing the PseudoVoigt fitting model (**Figure 4.4e**). The material exhibits characteristic *D* and *G* bands with a peak intensity ratio (I_D/I_G) of 1.1 alongside a significantly broad 2D region, which is typical for non-graphitic carbons (**Figure 4.4e, inset**).^[18] Overall, the structure of the HMF-1100 aligns with the expected characteristics of other non-graphitic carbon materials.

Gas physisorption experiments with CO₂ and small-angle X-ray scattering (SAXS) measurements are carried out to investigate the porous structure of the material. The investigation of open and closed surface areas is important in designing high-performance anode materials for SIBs. In this particular context, the CO₂ physisorption proves to be more practical due to its smaller kinetic radius compared to that of N₂, allowing for easier access to the open micropores and even ultramicropores.^[19]

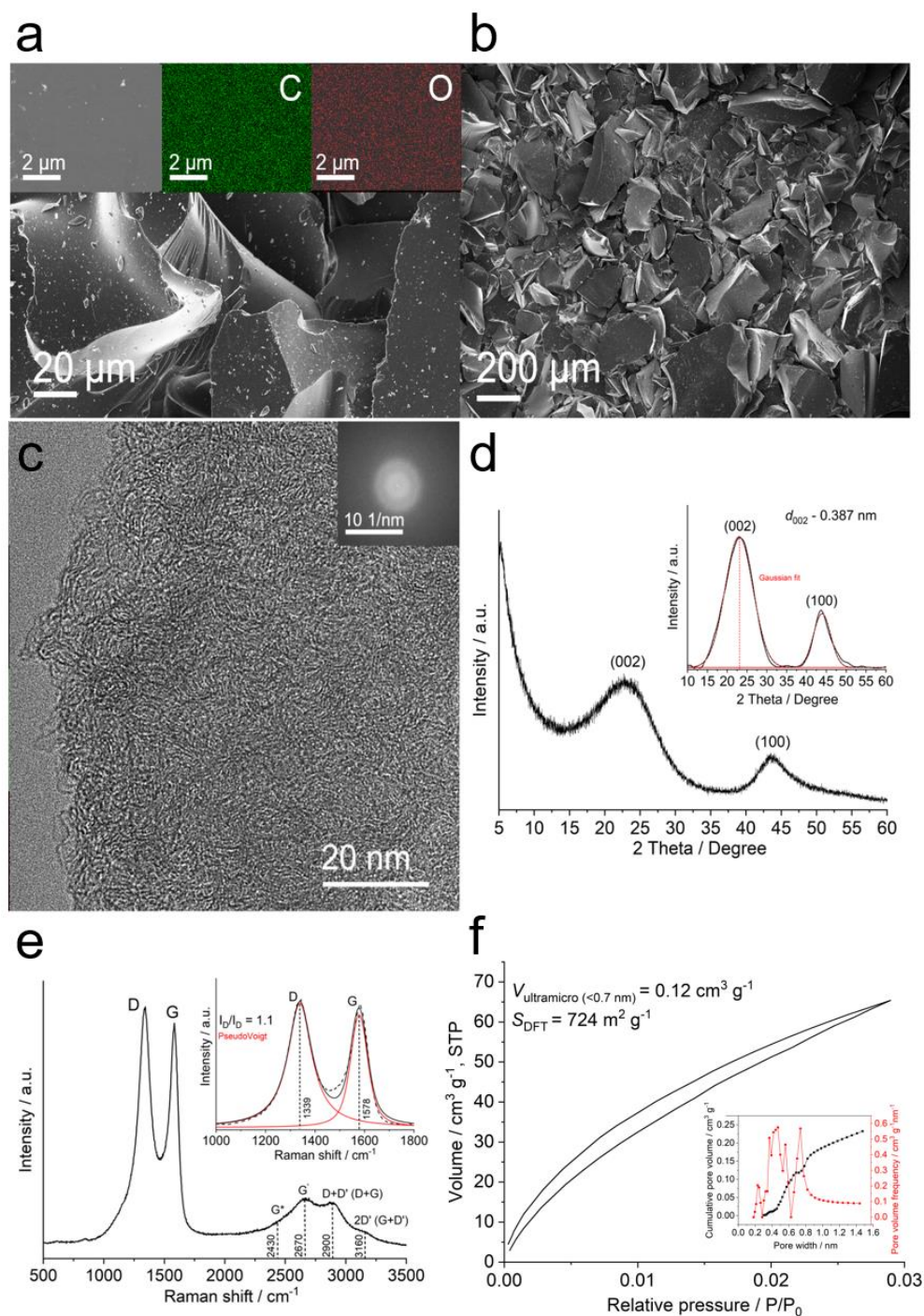


Figure 4.4. (a) and (b) SEM images of the HMF-1100 with different magnifications. Inset: EDX maps of C and O, showing the homogeneous distribution of the elements across the structure. (c) HRTEM image of the HMF-1100. Inset: FFT profile. (d) XRD pattern of the HMF-1100. Inset: Gaussian fitting model and calculated interlayer distance of (002) reflection. (e) Raman spectrum of HMF-1100. Inset: PseudoVoigt fitting of *D* and *G* with peak intensity ratios. (f) CO_2 gas physisorption of HMF-1100. Inset: Pore size distribution (PSD).

Analysis of the pore size distribution reveals that the material is predominantly composed of micropores smaller than 0.8 nm across the structure. The volume of accessible ultramicropores ($d_{\text{pore}} < 0.7$ nm (IUPAC)) is determined to be $0.12 \text{ cm}^3 \text{ g}^{-1}$ (**Figure 4.4f, inset**). Overall, the abundance of gas-accessible micropores facilitates diffusion-controlled storage of sodium ions, while the exclusion of macropores (i.e., those larger than 2.0 nm) enhances the first cycle efficiency by preventing the formation of excessive SEI within the macropores.^[20]

The evaluation of closed pores within the material is performed using SAXS, widely recognized as a robust technique for investigating topology at a broad scale.^[21] The SAXS pattern reveals two prominent contributions in the case of hard carbons: Porod's region that is associated with the scattering from sharp interfaces, such as macroscopic surfaces corresponding to a particular slope in q^{-4} at low angles, and the microporous region within the intermediate q ranges (**Figure A4.1**).^[21-22] Qualitative analysis indicates that the HMF-1100 possesses a considerable quantity of closed pores, even surpassing the SC-1000 described in Chapter 3. This significant presence of micropores is expected to enhance the diffusion-controlled sodium storage mechanism further, potentially exceeding the performance of the SC-1000 material in this specific scenario.

4.5.2. Sodium storage behavior of the material

Galvanostatic charge and discharge (GCD) measurements with different electrolytes –

The sodium storage performance of the HMF-1100 is evaluated using GCD measurements conducted at different current densities. In light of the promising outcomes associated with ether-based electrolytes, the electrochemical behavior of HMF-1100 as a sodium storage material is further investigated using an ether-based electrolyte. In general, ether-based electrolytes have demonstrated notable improvements in sodium storage performance when compared to traditional carbonate-based electrolytes.^[23] These improvements include a significant enhancement in sodium-ion diffusion kinetics and a reduction in charge-transfer resistance.^[24] To ensure comparability between the two different solvents, 1M NaPF₆ in Diglyme and 1M NaPF₆ in EC/EMC (3:7 in v) are studied. Electrochemical impedance spectroscopy (EIS) analysis reveals that the electrode-associated resistances are similar in both cases (R_1 in **Figure A4.2**). However, in terms of charge transfer resistance, the ether-based electrolytes exhibit superior performance, displaying substantially lower charge transfer resistance compared to the carbonate-based electrolyte (R_2 in **Figure A4.2**). This improvement has positive implications for the ion storage mechanism, as it facilitates an improved desolvation process and the rapid transfer of sodium ions.

The initial GCD curve reveals that HMF within the 1M NaPF₆ in Diglyme electrolyte exhibits a significantly higher capacity compared to the one with 1M NaPF₆ in EC/EMC (3:7 in v) (**Figure 4.5a**). Specifically, the former demonstrates a capacity of 376 mAh g⁻¹ in the second cycle, while the latter displays a capacity of 331 mAh g⁻¹. However, the first-cycle efficiencies (ICE) are observed to be similar (72% vs. 72%). The capacity increase is more pronounced within the plateau region, indicating that the ether-based electrolyte improves the kinetics of the diffusion-controlled plateau region. Once the SEI layer is stably formed, the HMF-1100 material exhibits a reversible capacity of more than 370 mAh g⁻¹. This high capacity, combined with a plateau capacity of more than 250 mAh g⁻¹, implies the significance of this carbon, equalizing the theoretical capacity of graphite in LIBs (372 mAh g⁻¹). Considering that HMF-1100 is derived from a sustainable and more energy-efficient production process, this high-capacity anode material holds potential for further advancements and innovation.

Regarding rate performance, the materials are cycled at different current densities ranging from 30 mA g⁻¹ (0.1C) to 600 mA g⁻¹ (2C) (**Figure 4.5b**). The superior performance observed at lower current densities persists even at higher current densities. Notably, even at rates exceeding 1C, the material maintains a prolonged plateau capacity, coming from its high diffusion-controlled storage characteristics. For instance, at 1C, it provides a capacity of approximately 300 mAh g⁻¹, while at 2C, it exhibits a capacity of around 250 mAh g⁻¹ (**Figure 4.5c**). These results are fascinating, considering that carbons of this nature typically exhibit significant decay at high currents due to the time-dependent nature of diffusion-controlled sodium storage.^[25] The unique structure of the carbon material is also found to be highly compatible with the ether-based electrolyte.

When considering cycling stability, it is essential to acknowledge that hard carbons have inherent limitations compared to graphite in LIBs due to the absence of a stable intercalation compound between sodium and carbon. As a result, the storage mechanism of hard carbons in SIBs primarily relies on harsh ion insertion and pore-filling mechanisms, which gradually distort the structure and lead to capacity degradation.^[26] HMF-derived carbon is subjected to cycling at high rates, specifically 600 mA g⁻¹ (2C) and 1 A g⁻¹ (3.3C), with a capacity retention of approximately 80% after 60 cycles in both cases (**Figure 4.5d**). Although the cycling stability of this material is lower than that of graphite in LIBs, it is still better than that of conventional HCs for SIBs. The cycle stability of hard carbons has been the subject of numerous investigations. Some approaches include further exfoliating graphitic layers and introducing sulfur heteroatoms into the carbon structure, as in Chapter 3, to improve safer surface-controlled storage or the utilization of more refined electrolytes.^[2] These strategies aim to mitigate the capacity fading issue and enhance the long-term stability of hard carbons in SIBs.

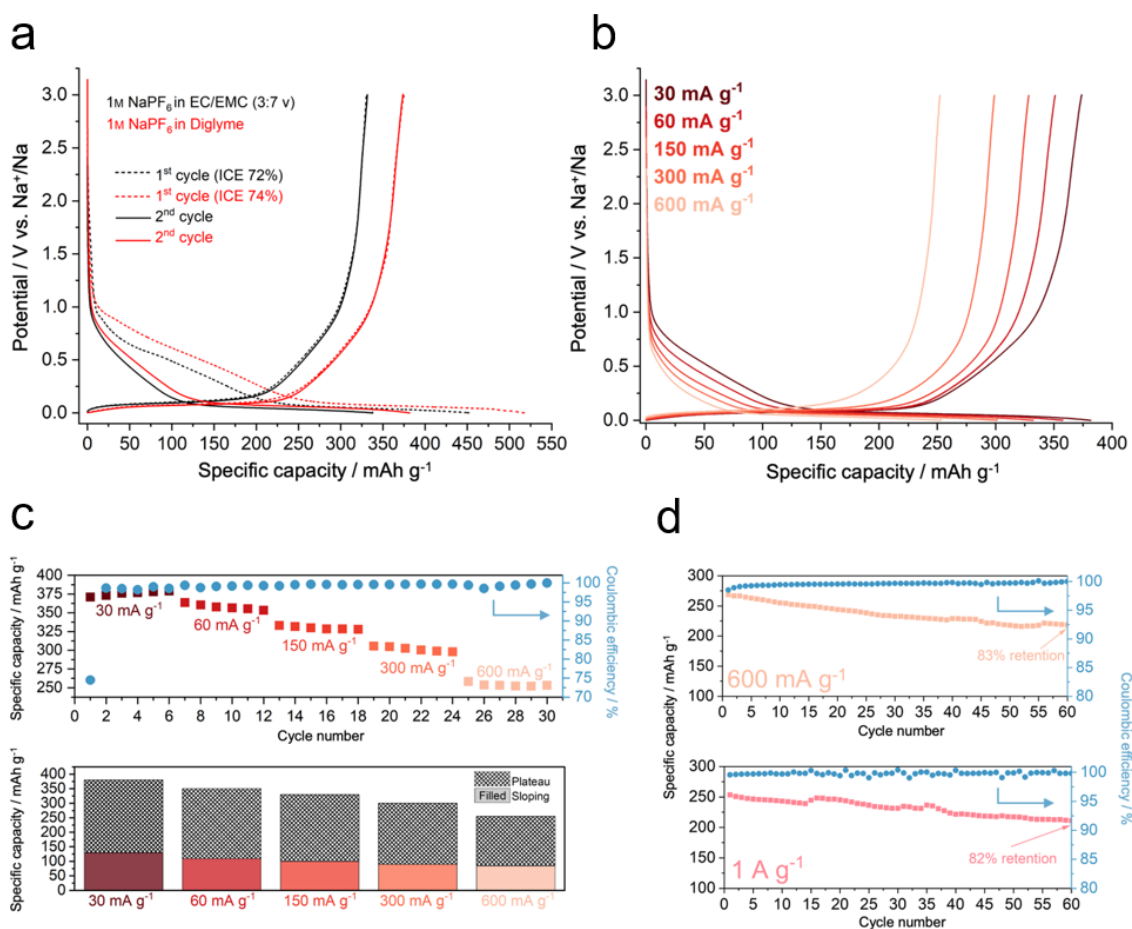


Figure 4.5. (a) Initial GCD curves of the HMF-1100 with different electrolytes showing the ICE and reversible capacity at 2nd cycle. (b) GCD cycles of HMF-1100 at different current rates. (c) Rate capability of the HMF-1100. (d) Cycling stability at 600 mA g⁻¹ and 1 A g⁻¹ showing capacity retention after 60 cycles.

A comparative analysis with carbons derived from glucose and fructose, treated at the same temperature of 1100°C, reveals that HMF-based carbon exhibits more promising results in terms of initial cycle efficiency and total capacity, even outperforming commercially available hard carbon in half-cell measurement (**Figure 4.6**).

Cyclic voltammetry (CV) and galvanostatic intermittent titration (GITT) measurement

– The sodium storage mechanism is investigated using GITT and CV measurements, following the experimental procedure outlined in Chapter 2. In the GITT experiments, the diffusion coefficients of sodium ions within the material are determined based on Fick’s law of diffusion. The sodium-ion diffusion coefficients of the HMF-1100 are found to be similar during both sodiation and desodiation processes, approximately on the order of 10⁻

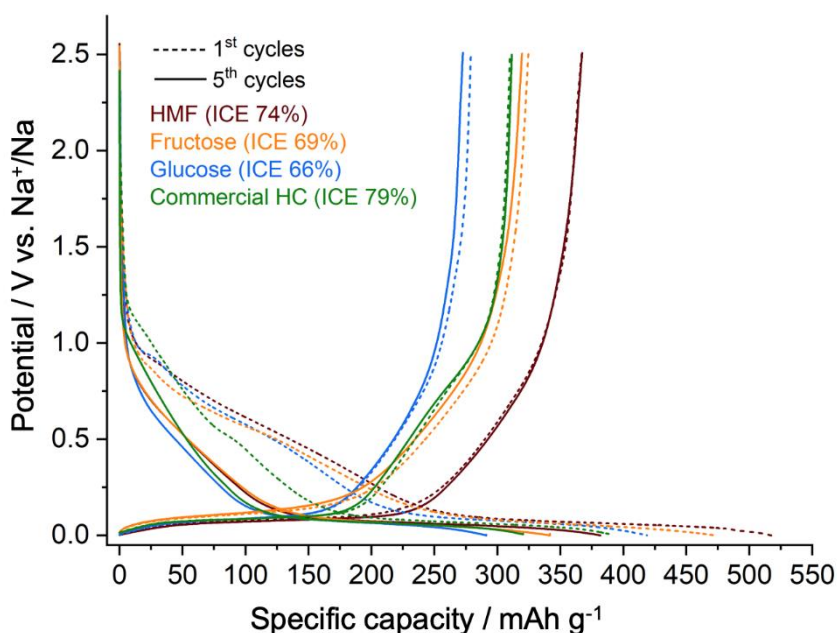


Figure 4.6. Initial and the 5th GCD curves of the hard carbons derived from HMF, Glucose, and Fructose, plus a commercial HC.

8 and $10^{-9} \text{ cm}^2 \text{ s}^{-1}$ (**Figure 4.7a**), which is consistent with the characteristics of hard carbons.^[27] However, as discussed earlier, a significant decrease in the diffusion coefficients is observed as the voltage approaches 0 V (vs. Na^+/Na) at the plateau region. This decrease provides evidence for the presence of electrochemical reactions that conflict with Fick's law of diffusion. Such behavior is commonly observed in diffusion-controlled sodium ion storage processes.^[27]

Additional evidence supporting the diffusion-controlled kinetics is obtained through CV analysis (**Figure 4.7b**). In this analysis, the concentration of sodium ions at the electrode-electrolyte interface is primarily influenced by time-dependent processes,^[28] which is the scan rate. The relationship between the logarithm of the peak anodic current ($\log(i)$) and the logarithm of the scan rate ($\log(v)$) in the CV plots allows for the examination of surface- or diffusion-controlled mechanisms of sodium-ion storage. The calculated slope (b -value) of the $\log(i)$ vs. $\log(v)$ plots indicates the nature of the dominant electrochemical process. A b -value close to 1 suggests a surface-controlled mechanism, like in capacitive behaviors, while a b -value close to 0.5 indicates a diffusion-controlled mechanism.^[28] The obtained b -value confirms that the diffusion-controlled mechanism is predominant in the sodium-ion storage process.

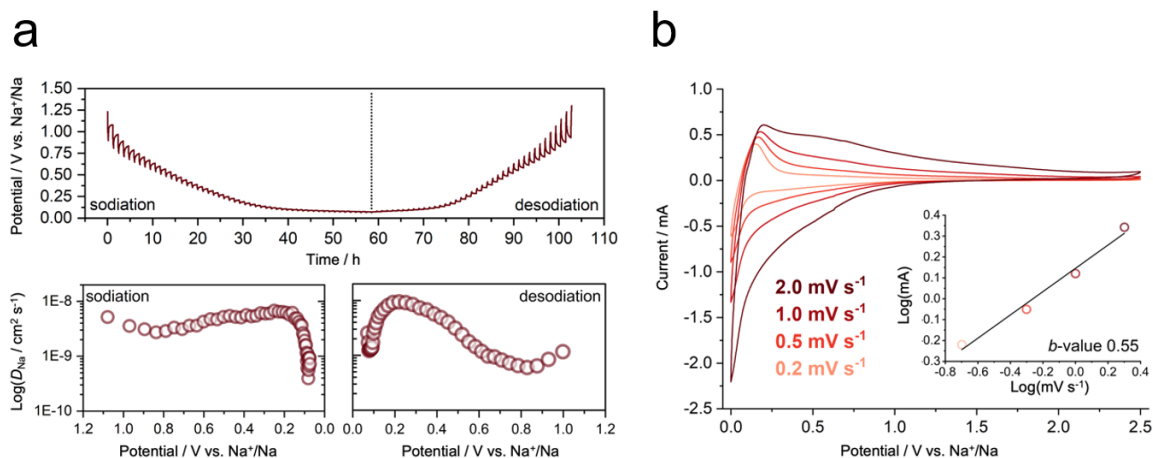


Figure 4.7. (a) GITT curves of HMF-1100 at 30mA g⁻¹. Bottom: Calculated diffusion coefficients during sodiation and desodiation processes. (b) CV plots of HMF-1100 at different scan rates. Inset: *b*-value plot.

4.6. Conclusions

This Chapter presents a one-step thermal condensation process for the fast and efficient synthesis of hard carbon from HMF. The quest for sustainable and efficient carbonaceous anode materials for SIBs poses significant challenges, making the exceptional performance exhibited by this material critical. The HMF-derived hard carbon demonstrates fascinating electrochemical characteristics, surpassing the theoretical capacity of graphite in LIBs. Additionally, the performance of this material is examined with different electrolyte solutions, where the ether-based electrolyte provides superior performance to the carbonate-based electrolyte. Notably, carbons of this nature typically exhibit limitations in delivering high cycling stability at high current densities, which is a critical factor for the commercialization of SIBs. However, further advancements are possible through alternative approaches. In conclusion, hard carbon made from HMF has the potential to be an anode material for SIBs and is flexible enough for future developments. Further investigations are ongoing to define the characteristics that enable large capacity and better rate performance towards high-performance SIBs.

Bibliography for Chapter 4

- [1] F. Xie, Z. Xu, Z. Guo, M.-M. Titirici, *Progress in Energy* **2020**, 2 (4), 042002.
- [2] D. Saurel, B. Orayech, B. Xiao, D. Carriazo, X. Li, T. Rojo, *Adv. Energy Mater.* **2018**, 8 (17), 1703268.
- [3] X. Chen, C. Liu, Y. Fang, X. Ai, F. Zhong, H. Yang, Y. Cao, *Carbon Energy* **2022**, 4 (6), 1133-1150.
- [4] a) C. Zhao, Q. Wang, Y. Lu, B. Li, L. Chen, Y.-S. Hu, *Sci. Bull.* **2018**, 63 (17), 1125-1129; b) A. Kamiyama, K. Kubota, D. Igarashi, Y. Youn, Y. Tateyama, H. Ando, K. Gotoh, S. Komaba, *Angew. Chem. Int. Ed.* **2021**, 60 (10), 5114-5120; c) A. Kamiyama, K. Kubota, T. Nakano, S. Fujimura, S. Shiraiishi, H. Tsukada, S. Komaba, *ACS Appl. Energy Mater.* **2020**, 3 (1), 135-140.
- [5] D. Alvira, D. Antorán, J. J. Manyà, *Chem. Eng. J.* **2022**, 447, 137468.
- [6] Q. Huang, S. L. Glazier, A. J. Louli, M. McArthur, C. Liu, J. Schrooten, J. R. Dahn, *J. Electrochem. Soc.* **2020**, 167 (8), 080543.
- [7] C. d. M. Saavedra Rios, V. Simone, L. Simonin, S. Martinet, C. Dupont, *Biomass Bioenergy* **2018**, 117, 32-37.
- [8] F. C. Cowlard, J. C. Lewis, *J. Mater. Sci.* **1967**, 2 (6), 507-512.
- [9] J. J. Kipling, J. N. Sherwood, P. V. Shooter, N. R. Thompson, *Carbon* **1964**, 1 (3), 321-328.
- [10] D. J. Johnson, I. Tomizuka, O. Watanabe, *Carbon* **1975**, 13 (4), 321-325.
- [11] A. A. Rosatella, S. P. Simeonov, R. F. M. Frade, C. A. M. Afonso, *Green Chem.* **2011**, 13 (4), 754-793.
- [12] a) Y. Nie, Q. Hou, C. Bai, H. Qian, X. Bai, M. Ju, *J. Clean. Prod.* **2020**, 274, 123023; b) Q. Hou, X. Qi, M. Zhen, H. Qian, Y. Nie, C. Bai, S. Zhang, X. Bai, M. Ju, *Green Chem.* **2021**, 23 (1), 119-231; c) S. Chen, R. Wojcieszak, F. Dumeignil, E. Marceau, S. Royer, *Chem. Rev.* **2018**, 118 (22), 11023-11117; d) C. Xu, E. Paone, D. Rodríguez-Padrón, R. Luque, F. Mauriello, *Chem. Soc. Rev.* **2020**, 49 (13), 4273-4306.
- [13] T. Nomura, E. Minami, H. Kawamoto, *ChemistryOpen* **2021**, 10 (6), 610-617.
- [14] a) Q. He, Y. Yu, J. Wang, X. Suo, Y. Liu, *Ind. Eng. Chem. Res.* **2021**, 60 (12), 4552-4561; b) N. Baccile, C. Falco, M.-M. Titirici, *Green Chem.* **2014**, 16 (12), 4839-4869; c) F. A. Kucherov, K. I. Galkin, E. G. Gordeev, V. P. Ananikov, *Green Chem.* **2017**, 19 (20), 4858-4864.
-

-
- [15] a) R. Väli, A. Jänes, T. Thomberg, E. Lust, *Electrochim. Acta* **2017**, 253, 536-544; b) M. Thompson, Q. Xia, Z. Hu, X. S. Zhao, *Mater. Adv.* **2021**, 2 (18), 5881-5905.
- [16] X. Liu, N. Fechler, M. Antonietti, M. G. Willinger, R. Schlögl, *Mater. Horiz.* **2016**, 3 (3), 214-219.
- [17] a) L. Qie, W. Chen, X. Xiong, C. Hu, F. Zou, P. Hu, Y. Huang, *Adv. Sci.* **2015**, 2 (12), 1500195; b) J. Yang, X. Zhou, D. Wu, X. Zhao, Z. Zhou, *Adv. Mater.* **2017**, 29 (6), 1604108-1604108; c) C. Li, Y. Sun, Q. Wu, X. Liang, C. Chen, H. Xiang, *Chem. Commun. (Camb)* **2020**, 56 (45), 6078-6081.
- [18] a) A. C. Ferrari, J. Robertson, *Phys. Rev. B* **2000**, 61 (20), 14095-14107; b) A. Kaniyoor, S. Ramaprabhu, *AIP Advances* **2012**, 2 (3), 032183.
- [19] A. Beda, C. Vaulot, C. Matei Ghimbeu, *J. Mater. Chem. A* **2021**, 9 (2), 937-943.
- [20] a) W. Luo, C. Bommier, Z. Jian, X. Li, R. Carter, S. Vail, Y. Lu, J. J. Lee, X. Ji, *ACS Appl. Mater. Interfaces* **2015**, 7 (4), 2626-2631; b) B.-H. Hou, Y.-Y. Wang, Q.-L. Ning, W.-H. Li, X.-T. Xi, X. Yang, H.-J. Liang, X. Feng, X.-L. Wu, *Adv. Mater.* **2019**, 31 (40), 1903125-1903125.
- [21] a) C. J. Jafta, A. Petzold, S. Risse, D. Clemens, D. Wallacher, G. Goerigk, M. Ballauff, *Carbon* **2017**, 123, 440-447; b) D. Saurel, J. Segalini, M. Jauregui, A. Pendashteh, B. Daffos, P. Simon, M. Casas-Cabanas, *Energy Storage Mater.* **2019**, 21, 162-173.
- [22] V. Simone, A. Boulineau, A. de Geyer, D. Rouchon, L. Simonin, S. Martinet, *J. Energy Chem.* **2016**, 25 (5), 761-768.
- [23] K. Li, J. Zhang, D. Lin, D.-W. Wang, B. Li, W. Lv, S. Sun, Y.-B. He, F. Kang, Q.-H. Yang, L. Zhou, T.-Y. Zhang, *Nat. Commun.* **2019**, 10 (1), 725-725.
- [24] J. Pan, Y.-y. Sun, Y. Yan, L. Feng, Y. Zhang, A. Lin, F. Huang, J. Yang, *JACS Au* **2021**, 1 (8), 1208-1216.
- [25] J. Liu, J. Wang, C. Xu, H. Jiang, C. Li, L. Zhang, J. Lin, Z. X. Shen, *Adv. Sci.* **2018**, 5 (1), 1700322.
- [26] S. Tan, H. Yang, Z. Zhang, X. Xu, Y. Xu, J. Zhou, X. Zhou, Z. Pan, X. Rao, Y. Gu, Z. Wang, Y. Wu, X. Liu, Y. Zhang, in *Molecules*, Vol. 28, **2023**.
- [27] a) K. Wang, Y. Jin, S. Sun, Y. Huang, J. Peng, J. Luo, Q. Zhang, Y. Qiu, C. Fang, J. Han, *ACS Omega* **2017**, 2 (4), 1687-1695; b) Y. Li, Y.-S. Hu, M.-M. Titirici, L. Chen, X. Huang, *Adv. Energy Mater.* **2016**, 6 (18), 1600659.
- [28] T. S. Mathis, N. Kurra, X. H. Wang, D. Pinto, P. Simon, Y. Gogotsi, *Adv. Energy Mater.* **2019**, 9 (39), 1902007.
-

CHAPTER 5. SUMMARY AND OUTLOOK

This dissertation systematically examines the strategies to improve the performance of carbonaceous anode materials in sodium-ion batteries (SIBs), including post-synthetic treatments, the effect of sulfur heteroatoms, and methods to prepare high-performing hard carbon anodes addressing structural requirements.

Chapter 2 focuses on the fabrication of a composite material consisting of sustainable carbon anode material derived from sodium lignosulfonate, with a conformal carbon nitride (CN) film serving as an artificial solid-electrolyte interphase (*a*-SEI) layer. The CN film is deposited using a chemical vapor deposition (CVD) method, known for its ability to generate highly uniform thin films. Within a specific range of thickness, the composite material exhibits exceptional performance in SIBs due to the heterojunction effect at the interface. This effect improves the ion transfer kinetics by facilitating improved solvation and effectively tunneling the sodium ions from the electrolyte to the electroactive material. Additionally, it reduces the open surface area that is available for electrolyte decomposition, thereby enhancing the first-cycle efficiency by mitigating the excessive SEI growth. By optimizing the thickness of the CN film, a substantial increase in specific capacity is observed, along with an increased plateau capacity, enabling more efficient storage of sodium ions. This is crucial for the further improvement of SIBs in high-energy-density applications. However, it should be noted that thicker layers of conformal CN do not present positive effects on diffusion-controlled sodium storage, as the CN layer itself is an electrically insulating material and is responsible for increasing the diffusion barrier of sodium ions. Nevertheless, even with thicker CN films, materials exhibit improved rate capability at high current densities, which is attributed to the fast kinetics of surface-controlled capacitive behavior. This approach is found promising in enhancing the performance of carbonaceous anode materials, particularly those derived from abundant sources or industrial byproducts.

The optimization of conformal *a*-SEIs represents a unique concept for improving electrochemical performance while minimizing the increase in material weight. Thus, in terms of increasing the energy density, this accomplishment is significant considering the

current challenges faced by SIBs, particularly the lack of suitable energy densities. To further enhance the electrochemical performance, the application of artificial SEIs opens space for further research and discussion, focusing on improving battery materials through the fine-tuning of electronic properties at the interface or redesigning the surfaces. Furthermore, this type of *a*-SEI can be further studied to accommodate a wide range of substrates, ranging from organic materials to inorganic electrode materials, especially on the cathode side.

In Chapter 3, high sulfur-content carbon anodes are synthesized from an oligomer precursor. Controlling the condensation temperature during synthesis changes the material's structure, resulting in a more ordered configuration with an increased microporosity. The material prepared at higher temperatures presents unique chemical and nanostructural characteristics, which enables more diffusion-controlled sodium storage compared to those treated at lower temperatures. With typical underpotential sodium deposition, the material demonstrates a reversible capacity exceeding 320 mAh g⁻¹ with an extended plateau capacity of 165 mAh g⁻¹, surpassing other sulfur-rich carbon materials in the field. The material's physicochemical and structural properties also contribute to its ability to achieve reversible overpotential sodium plating and stripping. This capability enhances the energy density, improves operational safety, and, among others, paves the way for further improvements in electrochemical sodium storage. Also, an *in-operando* SAXS method is developed here in order to prove the pore-filling mechanism. The findings of this study highlight the critical role of factors such as ultra-microporosity and the chemical environment in the design of effective anode materials for SIBs.

The introduction of sulfur-heteroatom in carbon electrode materials shows promise in certain aspects. However, it is important to note that its primary benefit lies in specific ion storage mechanisms, which may not be applicable in commercial applications due to low energy densities. Nevertheless, it could be well-suited for high-power applications due to a more surface-controlled mechanism provided at higher sulfur contents. The influence of heteroatoms should be further investigated within the context of other substances, as each energy storage mechanism possesses distinct chemical environments.

Chapter 4 introduces a one-step thermal condensation process, aiming to efficiently and rapidly synthesize hard carbon from 5-hydroxymethylfurfural (HMF). The development of sustainable and effective carbonaceous anode materials for SIBs poses significant challenges, highlighting the remarkable performance demonstrated by this particular carbon. The hard carbon derived from HMF exhibits fascinating electrochemical properties, surpassing the theoretical capacity of graphite in lithium-ion batteries (LIBs) (i.e., 376 mAh g⁻¹ vs. 372 mAh g⁻¹). The performance of this material is systematically evaluated with different electrolytes, revealing the superior performance of the ether-based electrolyte in comparison to the carbonate-based electrolyte in overall performance.

Notably, carbon materials of this nature often encounter difficulties in maintaining high cycling stability at high current densities, which is a critical consideration for the commercial viability of SIBs. To overcome this, more research should be conducted on the long-term effects of harsh ion insertion mechanism on the carbon structure, as the case of graphite in LIBs is inapplicable here. Also, a comparative study is conducted with different hard carbon materials, such as commercial wood-derived hard carbon and hard carbons derived from glucose and fructose, the main chemicals producing HMF. The results highlight the carbon derived from HMF provides better electrochemical performance, specifically in terms of total and plateau capacity, even surpassing the capacity of commercially available hard carbon. Overall, hard carbon from HMF is found promising as an anode material for SIBs and offers flexibility for further developments.

The results presented in this dissertation provide insights into enhancing the electrochemical performance of carbonaceous anode materials and have laid the foundation for the advancement of high-performance anode materials with extended operational windows.

APPENDICES

A1. Abbreviations and Variables

ADF	Annular dark-field
BWF	Breit-Wigner-Fano
CEI	Cathode electrolyte interphase
CMC	Carboxymethyl cellulose
CN	Carbon nitride
CNT	Carbon nanotube
CV	Cyclic voltammetry
CVD	Chemical vapor deposition
DEC	Diethyl carbonate
DFT	Density-functional-theory
DMC	Dimethyl carbonate
EA	Elemental analysis
EC	Ethylene carbonate
EDOT	3,4-Ethylenedioxythiophene
EDX	Energy dispersive X-ray
EELS	Electron energy loss spectroscopy
EIS	Electrochemical impedance spectroscopy
ELNES	Energy-loss near-edge structure
EMC	Ethyl methyl carbonate
ESR	Equivalent circuit resistance
EV	Electric vehicle
FEC	Fluoroethylene carbonate
FFT	Fast Fourier transform
FSI	Bis(fluorosulfonyl)imide
FTIR	Fourier-transform infrared spectroscopy
GCD	Galvanostatic charge and discharge
GITT	Galvanostatic intermittent titration test
HMF	5-Hydroxymethylfurfural
HRTEM	High-resolution transmission electron microscopy
HTC	Hydrothermal carbonization
ICE	Initial coulombic efficiency
ICP-OES	Inductively coupled plasma optical emission spectrometry
IUPAC	International Union of Pure and Applied Chemistry
KIB	Potassium-ion battery
LFP	Lithium iron phosphate
LIB	Lithium-ion battery

APPENDICES

LMO	Lithium manganese oxide
LSC	Lignosulfonate-derived carbon
NCA	Nickel, cobalt, and aluminum
NCM	Nickel, cobalt, and manganese
NMP	N-Methyl-2-pyrrolidone
NMR	Nuclear magnetic resonance
NVP	$\text{Na}_3\text{V}_2(\text{PO}_4)_3$
NVPF	$\text{Na}_3\text{V}_2(\text{PO}_4)_2\text{F}_3$
PAA	Polyacrylic acid
PC	Propylene carbonate
PSD	Pore size distribution
PVC	Polyvinyl chloride
PVDF	Polyvinylidene difluoride
RT	Room-temperature
RTIL	Room-temperature ionic liquid
SA	Sodium alginate
SAXS	Small-angle X-ray scattering
SBR	Styrene-butadiene rubber
SEI	Solid electrolyte interphase
SEM	Scanning electron microscopy
SIB	Sodium-ion battery
SoC	State of charge
SoH	State of health
TEM	Transmission electron microscopy
TFSI	Bis(trifluoromethanesulfonic)imide
TGA	Thermogravimetric analysis
TGA-MS	Thermogravimetric analysis mass spectroscopy
VEELS	Valence band electron energy loss spectroscopy
WAXS	Wide-angle X-ray scattering
XPS	X-ray photoelectron spectroscopy
XRD	X-ray diffraction

APPENDICES

A	Ampere
C	Celsius
D	Diffusion coefficient
D_0	Sample-detector distance (in SAXS)
E	Electrode potential
e	The thickness of the sample (in SAXS)
eV	Electron volt
F	Faraday constant
I_0	The intensity of the beam in cps (in SAXS)
i	Current
K	Kelvin
m	Mass
M	Molar mass
mAh	Milli ampere-hour
n	Charge number of transferred ionic species
$P(q)$	Form factor function
q	Scattering vector (in SAXS)
Q	Capacity
$S(q)$	Spatial distribution of particles
S_{BET}	BET surface area
t	Angle-dependent transmission (in SAXS)
T	Temperature
U	Cell voltage
V	Volt
v	Scan rate
V	Volume
W	Watt
Wh	Watt-hour
φ	Work function
z	Valency number
ΔE_τ	Cell voltage during a single GITT pulse
ΔN	Modified electron density difference
$\Delta \rho$	Electron density difference
$\Delta \Omega_{pixel}$	The solid angle of the pixel (in SAXS)
ΔE_s	Steady-state voltage during a single GITT pulse
ΔGr°	Standard Gibbs free energy
R_0	The average radius of particles
$d\Sigma/d\Omega$	Scattering cross-section per unit volume (in SAXS)

A2. Supplementary information for Chapter 2

A2.1. Preparation of sulfur-containing carbon and CN thin film application using the CVD method

A carbon source consisting of 58 wt. % of sodium-lignosulfonate from Domsjö Fabriker, a binder mixture comprising 4 wt. % of urea from Sigma-Aldrich and 4 wt. % of D-glucose anhydrous, also from Sigma-Aldrich, and 10 wt. % of deionized water, along with 24 wt. % of ZnO nanoparticles with a size of 20 nm from NanoAmor as a porogen are combined using a commercial kitchen kneader manufactured by Bosch, Germany. The mixture is then extruded and cut into pellets measuring 1 mm in diameter and 1.5 mm in length using a commercial noodle extruding machine (La Monferrina, Italy). The function of the glucose/urea binder is to induce crosslinking while carbonizing the pellets and producing a robust sulfur-rich carbon material. Without the glucose/urea binder, the physical mixture would lead to the arbitrary evaporation of Zn, and the intended interconnected hierarchical structure would not be realized. The extruded pellets are air-dried for 12 hours and subsequently placed in an ashing furnace (Nabertherm, Germany) under a nitrogen atmosphere. The pellets are crosslinked at 120 °C for 2 hours with a heating rate of 3 K min⁻¹ and then heated to 950 °C at the same rate and held at that temperature for 2 hours to achieve stepwise condensation. During this process, the ZnO nanoparticles undergo a carbothermal reduction, resulting in Zn metal, which is subsequently sublimated. The carbonization yield is found to be 30%. Finally, the carbonized pellets are ground into a powder and washed with a 0.1 M HCl solution under continuous stirring to eliminate any residual Zn. The carbon substrate material here is denoted as LSC.

The deposition of CN films on LSC is performed using a PlanarGROW-3S-OS (UK) chemical vapor deposition (CVD) system equipped with a 3-in. quartz tube. Typically, 150 mg of LSC powder is placed in the center of the second chamber, while a glass boat containing 1 g, 2 g, or 5 g of melamine (99%, Sigma-Aldrich) precursor is placed in the center of the first chamber for the LSC/ThinCN, LSC/MediumCN, and LSC/ThickCN samples, respectively. The vacuum is pulled down to 10 Torr, and the substrate temperature is increased to 550 °C with a nitrogen flow rate of 50 sccm serving as a carrier gas. Once the substrate reaches 550 °C, the melamine precursor is heated to 300 °C at a rate of 10 K min⁻¹ and held at that temperature for an additional 30 min. Subsequently, the samples are cooled naturally to room temperature. A notable color change from black to bluish is observed in the samples, which is dependent on the amount of melamine precursor used.

A2.2. Electrode preparation and electrochemical characterizations

The electrodes are produced by mixing LSC, LSC/ThinCN, LSC/MediumCN, and LSC/ThickCN with conductive carbon black (Super-P, Alfa Aesar) and polyvinylidene difluoride (PVDF, Kynar HSV-900) as a binding agent at a weight ratio of 8:1:1. The PVDF is dissolved in *N*-Methylpyrrolidone (NMP, Sigma-Aldrich). The slurry is then cast onto an aluminum foil (15 μm) using an automatic doctor blade film applicator (mtv messtechnik, Germany) and subsequently dried in a vacuum oven (Thermo Fisher, USA) at 80 $^{\circ}\text{C}$ overnight. The active materials are loaded onto the electrode at a final loading of approximately 1.0 mg cm^{-2} for all samples. Electrochemical measurements are performed using two-electrode Swagelok-type cells on a Biologic MPG-2 instrument (France). Swagelok-type cells are assembled in an argon-filled glovebox (MBRAUN, Germany) with an H_2O and O_2 content of less than 0.1 ppm. The electrolyte used is 1M NaPF_6 in ethylene carbonate (EC)/ethyl methyl carbonate (EMC) (3:7 in vol., E-Lyte GmbH, 200 μL), and glass fibers (Whatman GF/C) serve as the separators, while a thin piece of sodium metal (99.5%, Sigma-Aldrich) is employed as both the counter and reference electrode. For data reproducibility, at least four Swagelok-type cells are prepared for each sample. The galvanostatic charge-discharge (GCD) curves of the half-cells are measured in the potential range of 0.005-2.5 V (vs. Na^+/Na). Before the measurements, the half-cells are rested for at least three hours. Cyclic voltammetry (CV) measurements are conducted at scan rates of 0.5, 1.0, 2.0, and 5.0 mV s^{-1} in the potential range of 0.01-2.0 V (vs. Na^+/Na). Electrochemical impedance spectroscopy (EIS) is performed using an AC perturbation of 10 mV in the frequency range of 10 Hz to 20 kHz. The galvanostatic intermittent titration technique (GITT) is utilized to calculate the sodium-ion diffusion coefficients of the electrodes. During the experiments, current pulses (30 mA g^{-1}) are applied for 600 seconds, and relaxation potentials are measured for 3600 seconds. All electrochemical measurements are conducted at room temperature.

A2.3. Physico-chemical characterizations

X-ray photoelectron spectroscopy (XPS) is performed using the CISSY equipment (Helmholtz-Zentrum Berlin, Germany) with a SPECS XR 50 X-ray source using the Mg $\text{K}\alpha$ radiation. The hemispherical analyzer (CLAM4 by VG) is used to analyze photoelectrons. The binding energy calibration is performed using clean samples of gold, copper, and silver foil. Indium foil (99.99%, Sigma-Aldrich) is used as a substrate. The Shirley-type background and Lorentzian-Gaussian (mixed) models are used for the fittings. The crystallinity of the material is determined by X-ray diffraction (XRD) using Rigaku SmartLab (Japan, Cu $\text{K}\alpha$, 0.154 nm). Raman spectroscopy is obtained using a WITec Alpha 300 (Germany) confocal Raman microscope with an excitation wavelength

of 532 nm. Fourier-transform infrared (FTIR) spectrometry is performed using a Thermo Scientific Nicolet iD7 (USA) spectrometer. Thermogravimetric analysis (TGA) is conducted using NETZSCH TG-209 Libra (Germany) under a synthetic air and N₂ atmosphere at a heating rate of 10 K min⁻¹. Physisorption measurements are conducted on a Quantachrome Quadrasorb SI (Austria) at 77 K for N₂ and 273 K for CO₂. Samples are degassed overnight before the measurements. The density functional theory (DFT) method is used to evaluate the pore size distribution (PSD) of the materials employing adsorption isotherms. Inductively coupled plasma optical emission spectrometry (ICP-OES) is conducted with PerkinElmer Optima 8000 (USA). Scanning Electron Microscopy (SEM) imaging uses the Zeiss LEO 1550-Gemini (Germany) system with acceleration voltages of 3, 5, and 10 kV. An Oxford Instruments X-MAX (UK) 80 mm² detector collects the energy-dispersive X-ray (EDX) data. For the scanning transmission electron microscopy (STEM) observations, samples are embedded in Spurr resin (Electron Microscopy Sciences) polymerized at 65 °C. Ultrathin sections (80-100 nm thick) are obtained from trimmed resin blocks by ultramicrotomy (Leica Ultracut UCT, Germany) using an Ultra 35° diamond knife (Diatome). The STEM study is performed using a double Cs corrected JEOL JEM-ARM200F (Japan) (S)TEM operated at 80kV and equipped with a cold-field emission gun and high-angle silicon drift EDX detector (Jeol JED-2300 100 mm², Japan) (solid angle up to 0.98 steradians with a detection area of 100 mm²). Annular dark-field (ADF) STEM images are collected at a probe convergence semi-angle of 25 mrad. The so-called “beam shower” procedure is applied for 30 minutes, which is necessary for reducing hydrocarbon contamination during subsequent imaging at high magnification. Images are analyzed with Gatan’s microscopy suite (GMS) version 3.4.

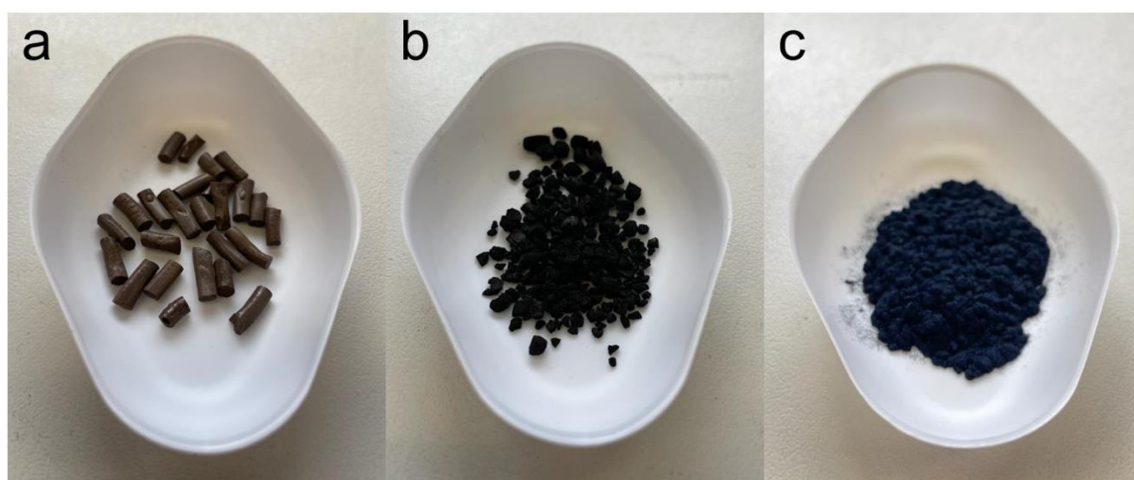


Figure A2.1. (a) The pellets after extrusion. (b) The pellets after pyrolysis, which results in the formation of LSC. (c) LSC after CN deposition (LSC/ThickCN) displays a dark bluish color. (Copyright (2023) The Royal Society of Chemistry)

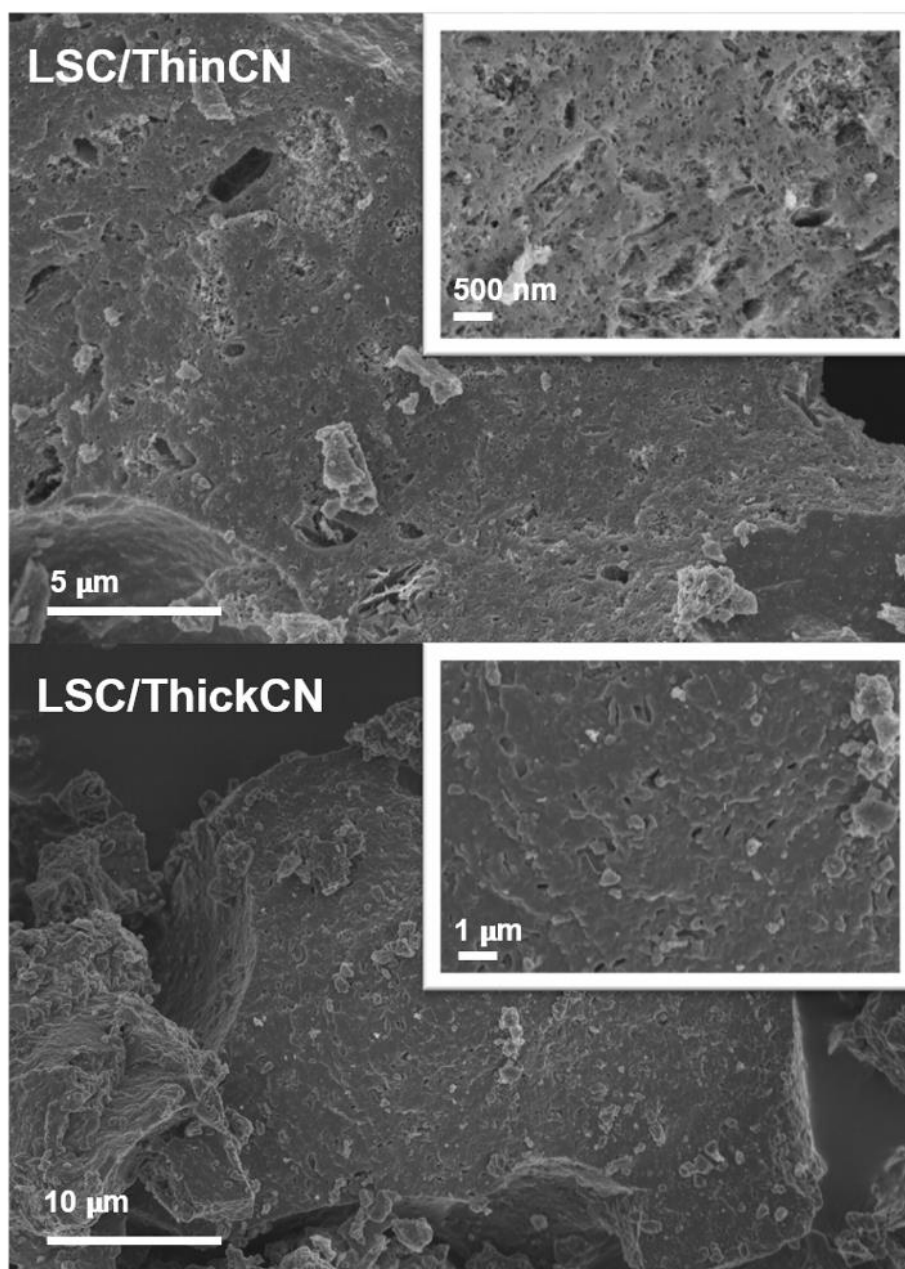


Figure A2.2. SEM images, captured at low and high magnifications, are used to examine the thin and thick CN coatings, respectively. The images reveal that both coatings are densely layered on a highly porous and rough surface. (Copyright (2023) The Royal Society of Chemistry)

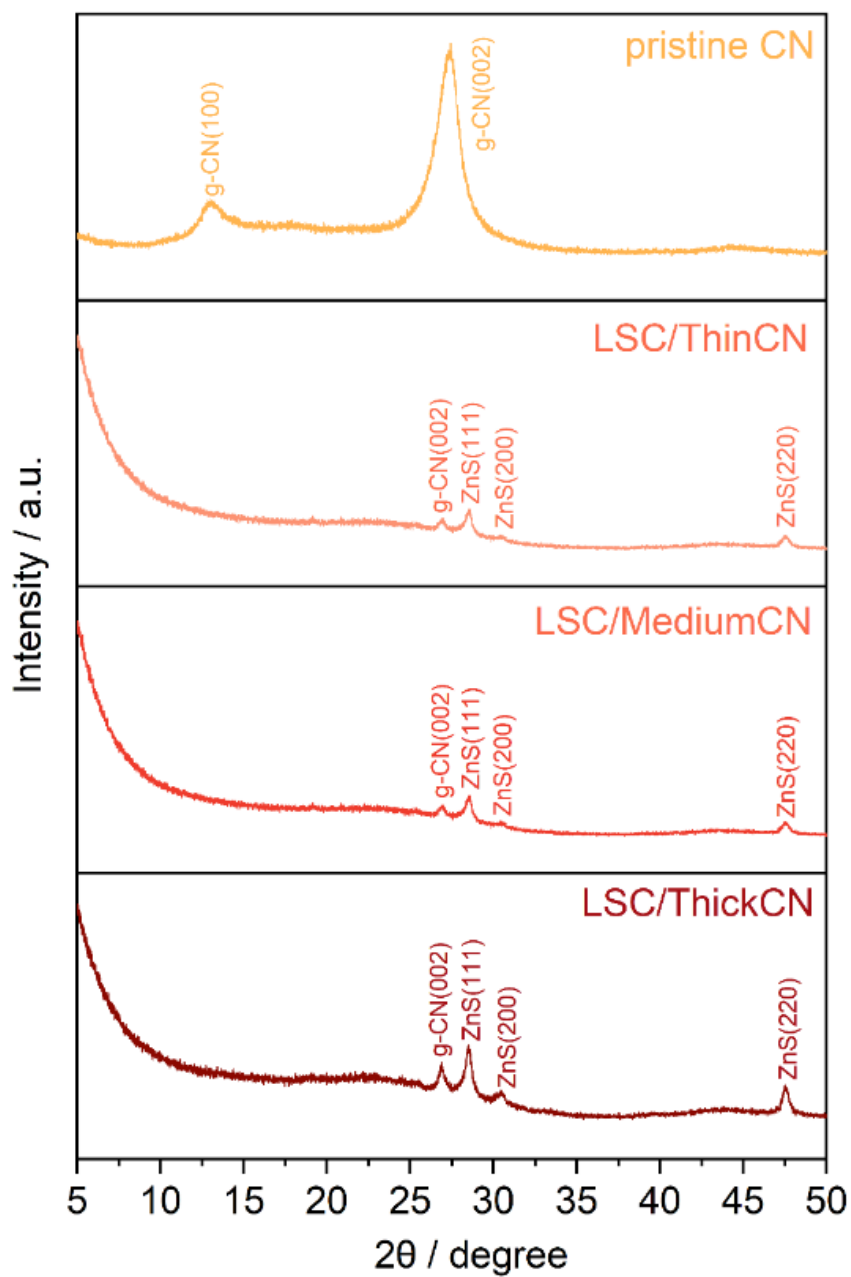


Figure A2.3. XRD patterns of the materials, which include pure CN that polymerized under the same thermal conditions. (Copyright (2023) The Royal Society of Chemistry)

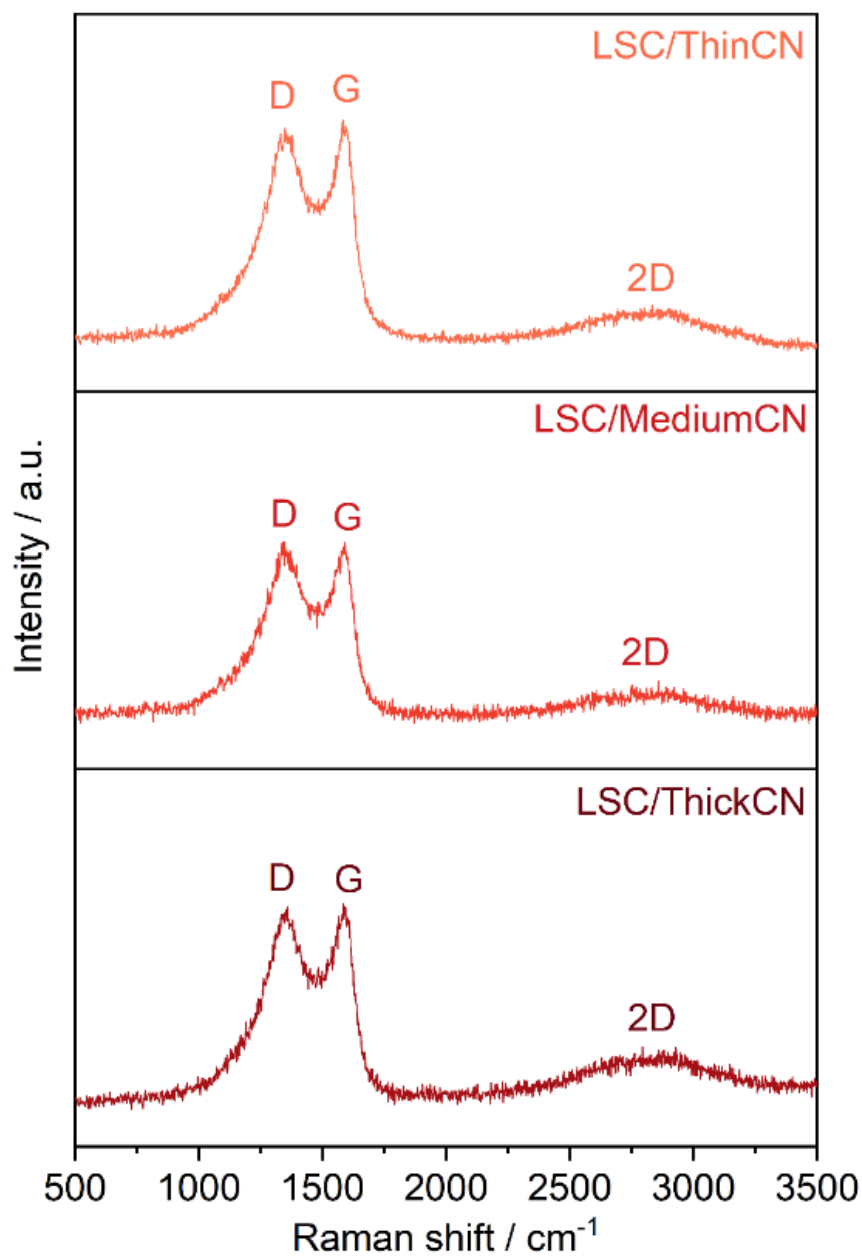


Figure A2.4. Raman spectra of the LSCs with different CN thicknesses. (Copyright (2023) The Royal Society of Chemistry)

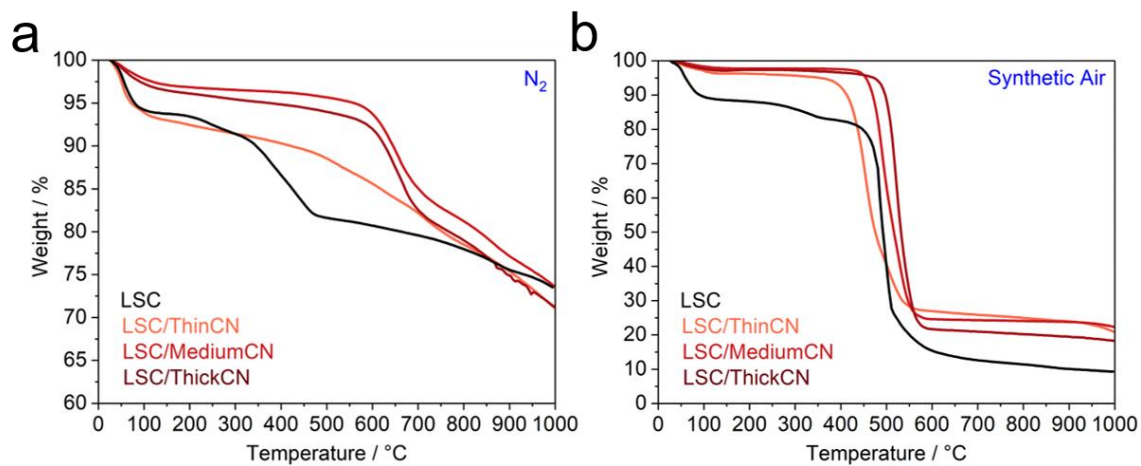


Figure A2.5. TGA profiles of the materials under both **(a)** N₂ and **(b)** synthetic air atmospheres demonstrate increased thermal stability. (Copyright (2023) The Royal Society of Chemistry)

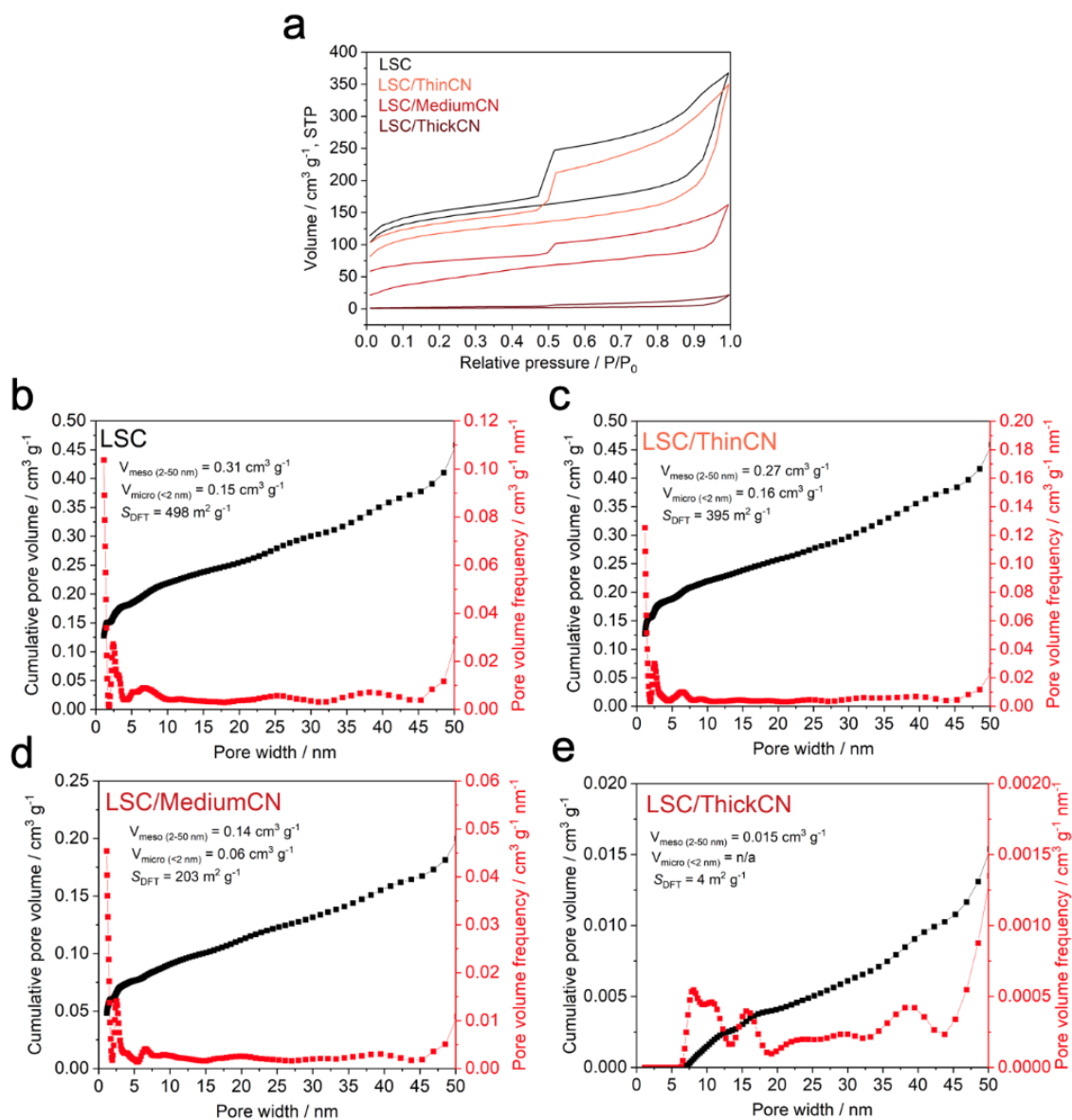


Figure A2.6. (a) Nitrogen adsorption and desorption isotherms (Type IV) of materials and pore size distribution (PSD) graphs with cumulative pore volume for (b) LSC, (c) LSC/ThinCN, (d) LSC/MediumCN, and (e) LSC/ThickCN. (Copyright (2023) The Royal Society of Chemistry)

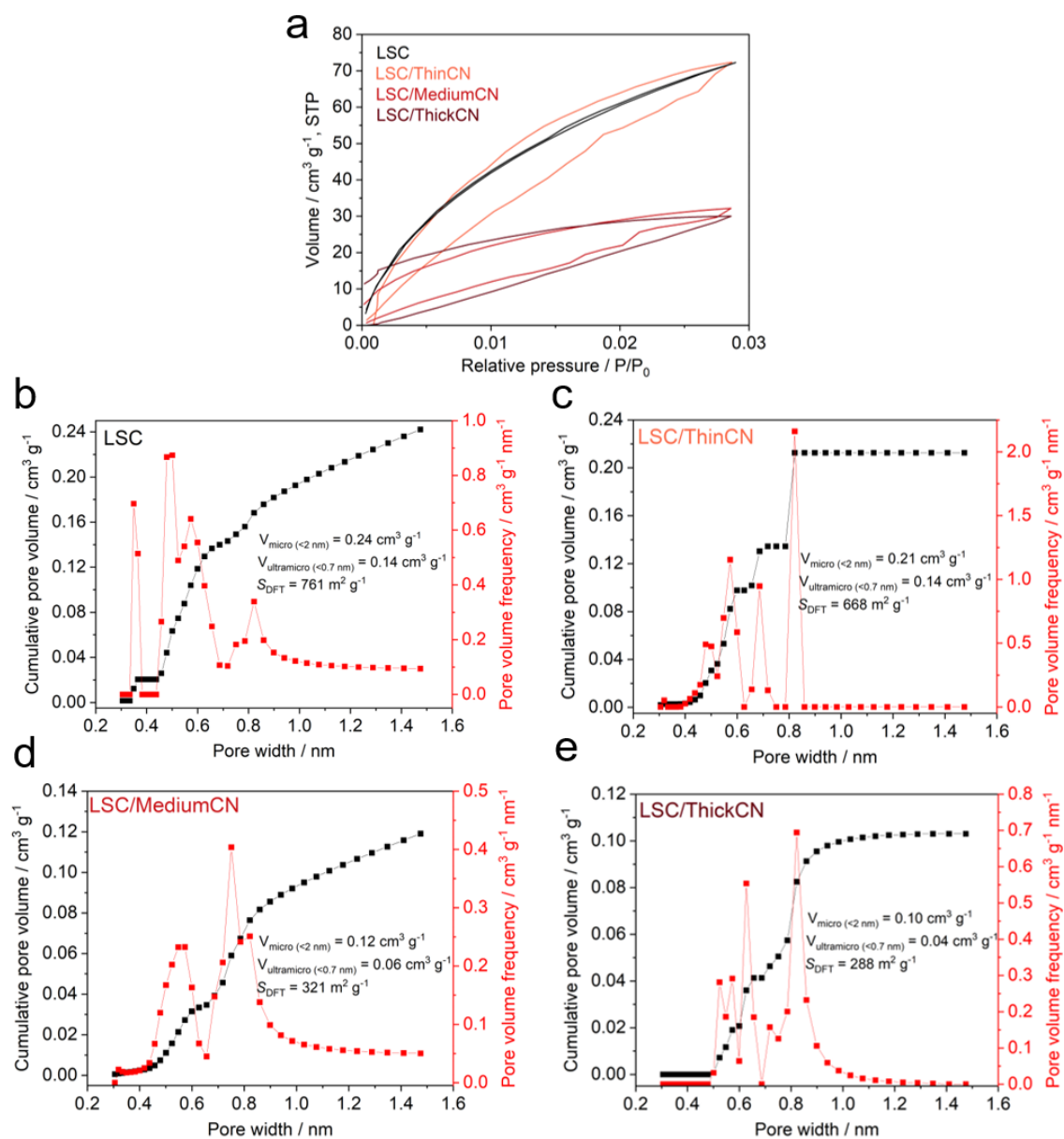


Figure A2.7. (a) CO₂ adsorption and desorption isotherms of materials and pore size distribution (PSD) graphs with cumulative pore volume for (b) LSC, (c) LSC/ThinCN, (d) LSC/MediumCN, and (e) LSC/ThickCN. (Copyright (2023) The Royal Society of Chemistry)

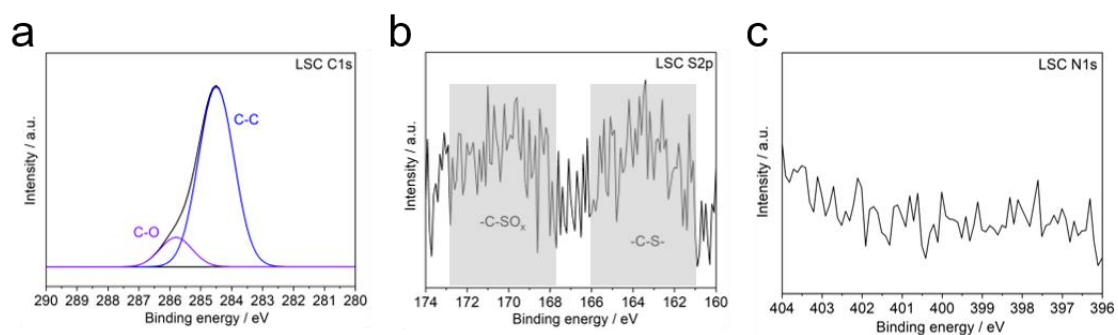


Figure A2.8. (a) XPS C2s core level spectra with the C-C and C-O peaks. (b) XPS S2p core level spectra demonstrate the presence of sulfur, which is attributed to the nature of the lignosulfonate. (c) XPS N1s core level demonstrates the absence of nitrogen prior to the deposition of CN, thereby confirming that the nitrogen content detected after the deposition is solely attributed to the CN film. (Copyright (2023) The Royal Society of Chemistry)

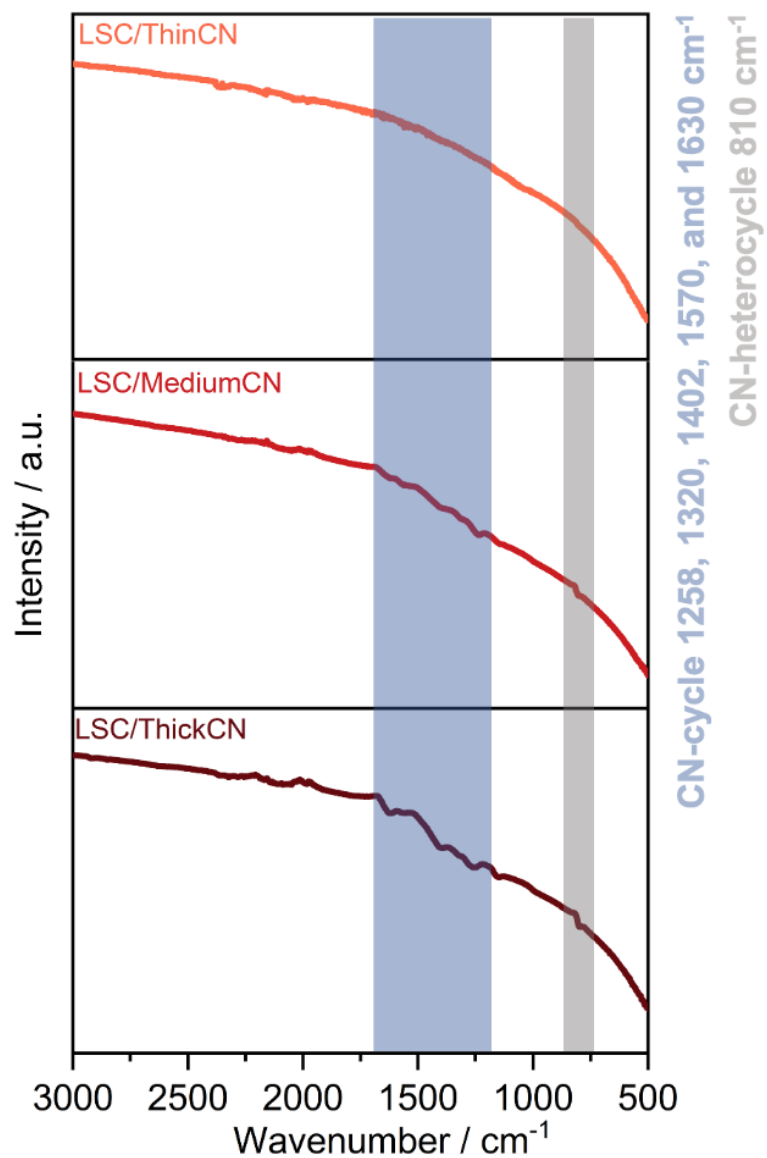


Figure A2.9. FTIR spectra of the materials. (Copyright (2023) The Royal Society of Chemistry)

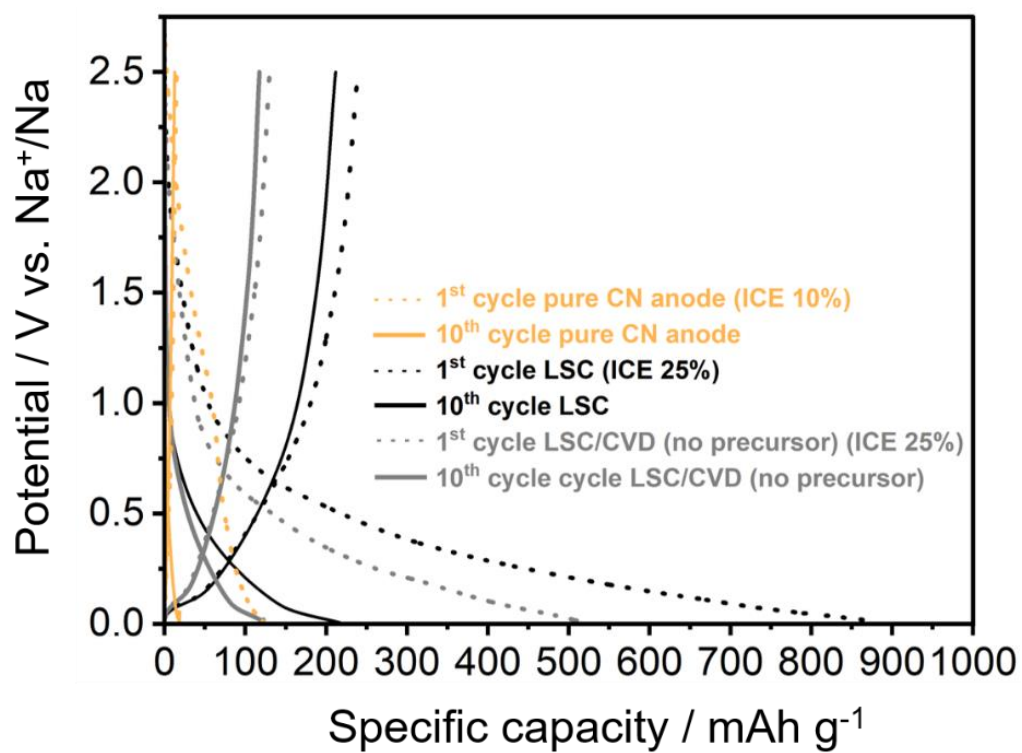


Figure A2.10. 1st and 10th GCD curves of the pure CN, LSC, and LSC/CVD (without melamine).
(Copyright (2023) The Royal Society of Chemistry)

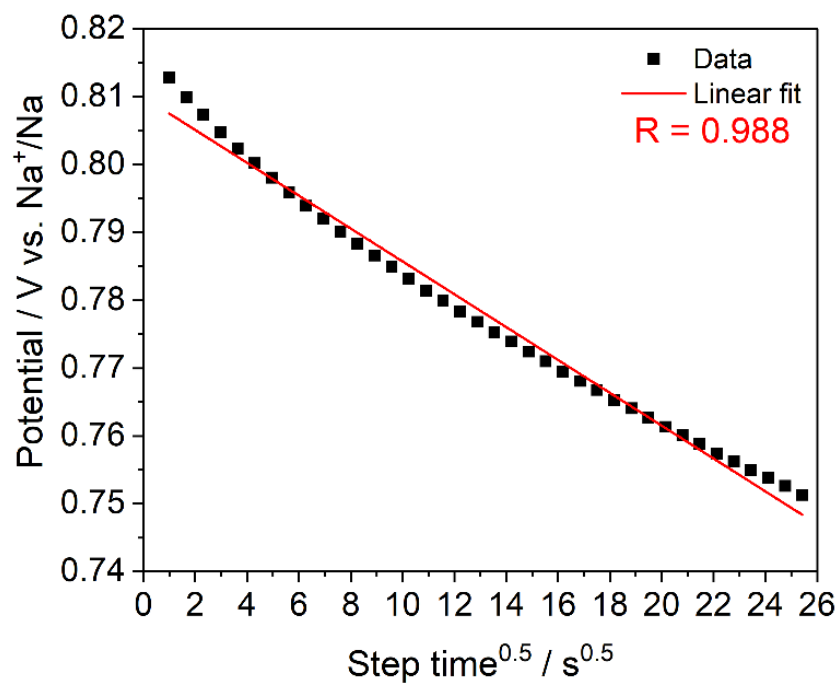


Figure A2.11. V vs. $s^{0.5}$ plot showing linear fit to simplify Weppner and Huggins model. (Copyright (2023) The Royal Society of Chemistry)

A3. Supplementary information for Chapter 3

A3.1. Electrode preparation and electrochemical characterizations

The electrodes are produced through a process that involves blending C-800, C-900, and C-1000 with conductive carbon black (Super-P, Alfa Aesar) and polyvinylidene difluoride (PVDF, Kynar HSV-900) as the binding agent in a weight ratio of 8:1:1. The PVDF is dissolved in *N*-Methylpyrrolidone (NMP, Sigma-Aldrich). The mixture is applied onto an aluminum foil (15 μm) using an automatic doctor blade film applicator (mtv messtechnik, Germany) and dried under vacuum at 80°C overnight. The electrodes' final active material mass is approximately 1.0 mg cm⁻² for all samples. Electrochemical measurements are conducted with two-electrode Swagelok-type cells on a Biologic MPG-2 instrument (France). Onsite in-operando SAXS measurements are performed using a portable potentiostat, Gamry Interface 1010 (USA). The Swagelok-type cells are assembled in an argon-filled glovebox (MBRAUN, Germany) with an H₂O and O₂ content of less than 0.1 ppm. The electrolyte used is 1M NaPF₆ in ethylene carbonate (EC)/ethyl methyl carbonate (EMC) (3:7 in vol., E-Lyte GmbH, 200 μL), with glass fibers (Whatman GF/C) serving as separators and a thin piece of sodium metal (99.5%, Sigma-Aldrich) as both counter and reference electrode. For the reproducibility of the data, at least four Swagelok-type cells are prepared for each sample. The commercial plant-based HC (Kuraray, Japan) is also used as a reference anode material for supportive measurements. The galvanostatic charge-discharge curves of the half-cells are collected in the potential range of 0.005-2.5 V (vs. Na⁺/Na), with half-cells resting for six hours before the measurements. The theoretical capacity of the electrodes is 300 mAh g⁻¹, which facilitates current densities in the form of C-rates. The rate performance of the electrodes is measured at 0.1C (30 mA g⁻¹), 0.2C (60 mA g⁻¹), 0.5C (150 mA g⁻¹), 1C (300 mA g⁻¹), and 2C (600 mA g⁻¹). Cyclic voltammetry (CV) measurements are carried out at scan rates of 0.5, 1.0, 2.0, and 5.0 mV s⁻¹ in the potential range of 0.01-2.0 V (vs. Na⁺/Na). Electrochemical impedance spectroscopy (EIS) is performed with an AC perturbation of 10 mV in the frequency range of 0.1 Hz to 20 kHz. The galvanostatic intermittent titration technique (GITT) is used to calculate the sodium-ion diffusion coefficients, where current pulses (30 mA g⁻¹) are applied for 1200 s, and relaxation potentials are measured for 3600 s. The full-cell demonstration is conducted with carbon-coated Na₃V₂(PO₄)₃ (NVP/C) cathode material (acquired from the Dalian Institute of Chemical Physics, Chinese Academy of Sciences). All electrochemical measurements are conducted at room temperature.

A3.2. Physico-chemical characterizations

X-ray photoelectron spectroscopy (XPS) is conducted using CISSY equipment (Helmholtz-Zentrum Berlin, Germany) featuring a SPECS XR 50 Mg K α gun and combined lens analyzer module (CLAM). Indium foil (99.99%, Sigma-Aldrich) is used as a substrate, and the Shirley-type background and Lorentzian-Gaussian (mixed) models are employed for the fittings. The crystallinity of the samples is determined by X-ray diffraction (XRD) using the Rigaku SmartLab (Japan, Cu K α , 0.154 nm). Small-angle X-ray scattering (SAXS) measurements of carbon powders are performed using the Bruker Nanostar II (USA, Cu K α , 0.154 nm), with a sample-detector distance of 283 mm, and calibrated with silver behenate. Raman spectroscopy is obtained using the WITec Alpha 300 (Germany) confocal Raman microscope with an excitation wavelength of 532 nm. Fourier-transform infrared (FTIR) spectrometry is conducted using the Thermo Scientific Nicolet iD7 (USA) spectrometer. Thermogravimetric analysis-mass spectroscopy (TGA-MS) is performed using NETZSCH TG-209 Libra (Germany) under a helium atmosphere with a heating rate of 10 K min⁻¹. Physisorption measurements are carried out on a Quantachrome Quadrasorb SI (Austria) at 77 K for N₂ and 273 K for CO₂, with samples degassed overnight before measurement. The density functional theory (DFT) method is employed to evaluate the pore size distribution (PSD) in the disordered carbons. Elemental analysis is conducted using the Elementar Vario EL III (Germany) with two different modes (combustive for carbon, hydrogen, nitrogen, and sulfur; non-combustive for oxygen). Scanning Electron Microscopy (SEM) imaging is performed using the Zeiss LEO 1550-Gemini (Germany) system with acceleration voltages of 3, 5, and 10 kV, and the energy-dispersive X-ray (EDX) data are collected using an Oxford Instruments X-MAX (UK) 80 mm² detector. High-resolution transmission electron microscopy (HRTEM) imaging and electron energy loss spectroscopy (EELS) are conducted using the double aberration-corrected Jeol JEM ARM200F (Japan) microscope, equipped with a cold field emission gun and a GIF Quantum from Gatan (USA). The acceleration voltage is set to 80 kV, and HRTEM images are acquired on a Oneview (4k x 4k), while EEL spectra are collected on a US1000 (2k x 2k) camera, both from Gatan. Data analysis is carried out using Gatan's microscopy suite (GMS) version 3.4.

In-operando SAXS measurements – In-operando SAXS measurements of the half-cells are conducted under synchrotron light at BESSY II (Helmholtz-Zentrum Berlin, Germany). Experiments are performed using a monochromatic X-ray beam at 18.0 keV, and scattered intensities are collected with a Dectris Eiger 9M detector. Transmission through the sample is calculated from an X-ray fluorescence signal collected from a lead beam stop using a RAYSPEC Sirius SD-E65133-BE-INC detector equipped with an 8 μ m beryllium window. The sodiation and desodiation processes are carried out at a current density of 30 mA g⁻¹. In order to address the inhomogeneity issues resulting from the

APPENDICES

amorphous nature of carbon, the sample electrode is mapped at 16 distinct points to monitor consistency in the structural changes. Throughout the sodiation and desodiation processes, scattering data is collected at a time resolution of 2 minutes.

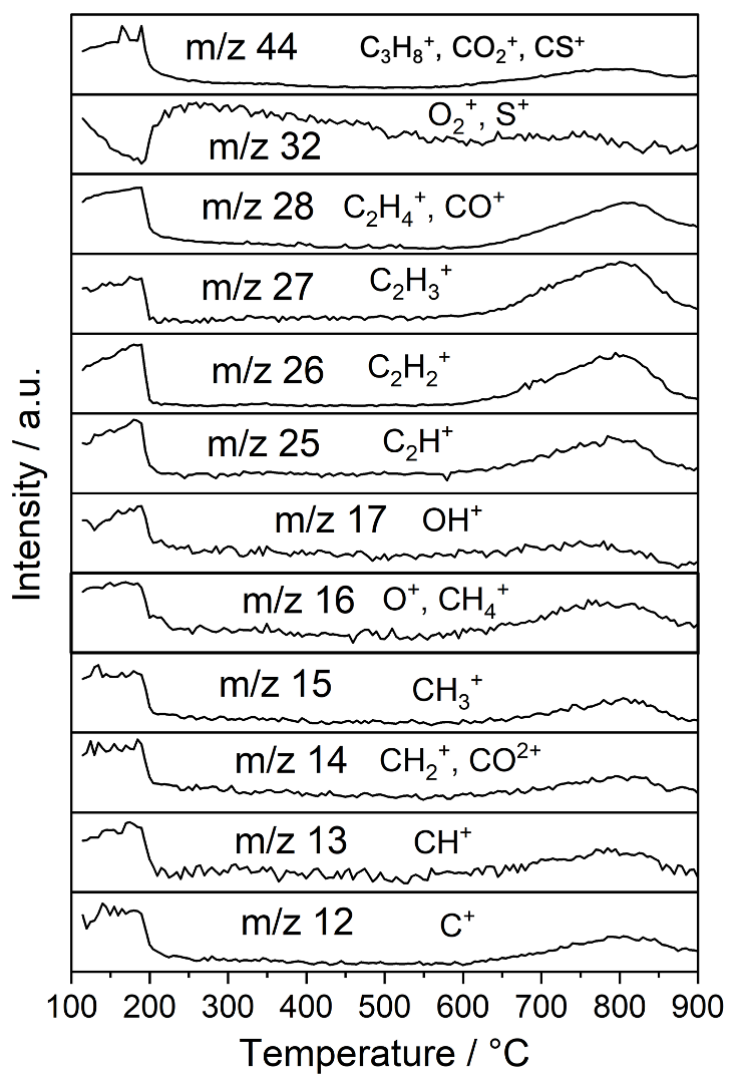


Figure A3.1. TGA-MS profile of oligo-EDOT. (Copyright (2024) Wiley)

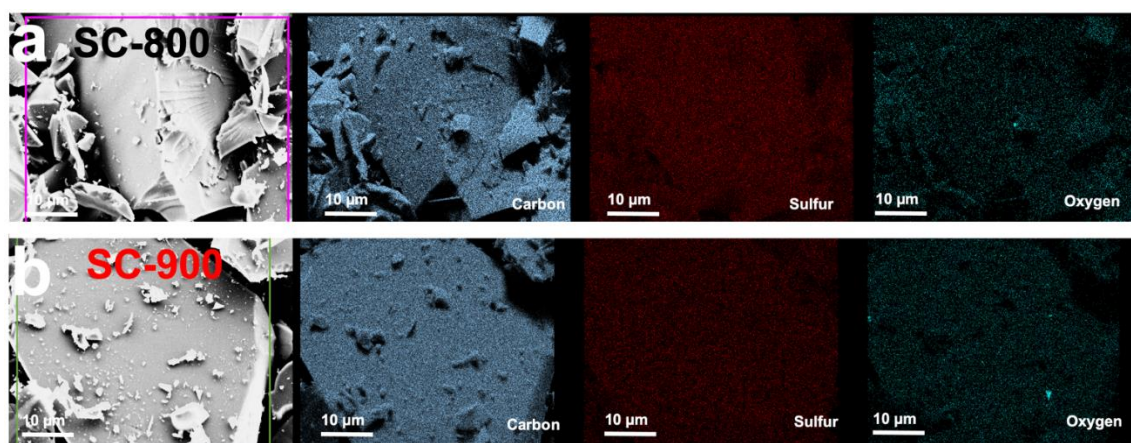


Figure A3.2. Elemental mappings of (a) SC-800 and (b) SC-900 from EDX spectroscopy. (Copyright (2024) Wiley)

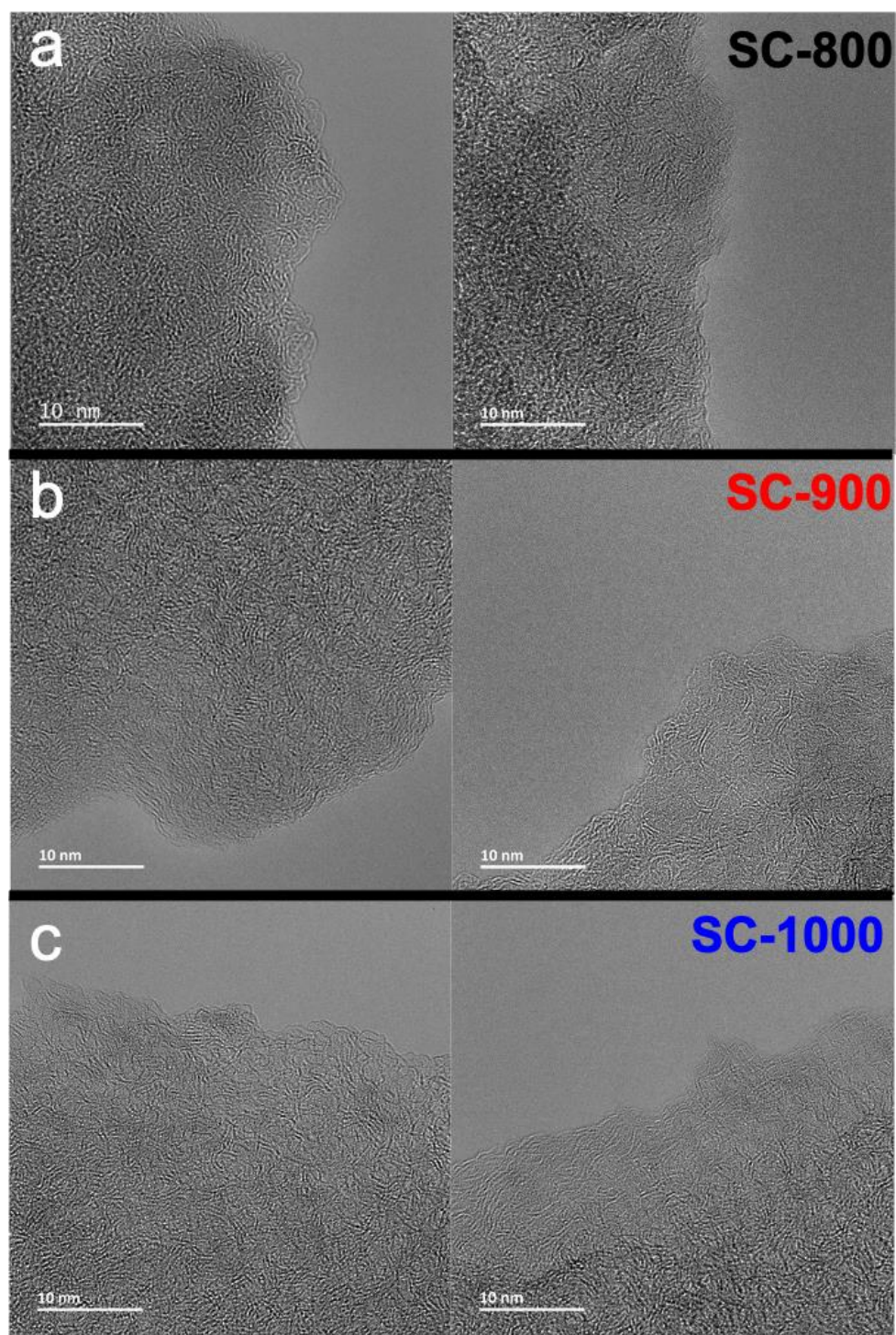


Figure A3.3. HRTEM images of **(a)** SC-800, **(b)** SC-900, and **(c)** SC-1000 from two different locations. (Copyright (2024) Wiley)

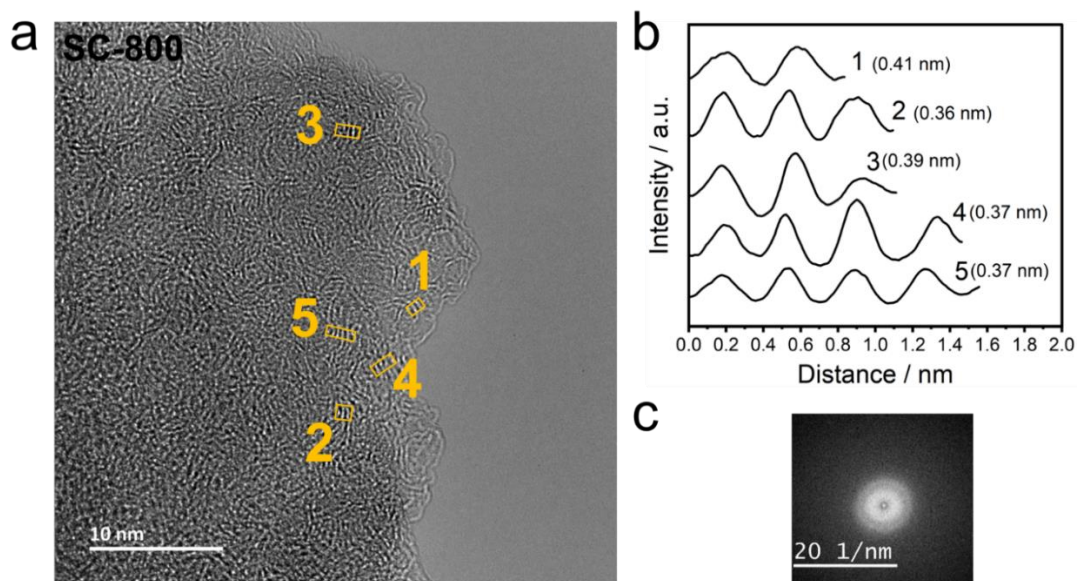


Figure A3.4. (a) HRTEM image of the SC-800; (b) image intensity periodicity; (c) FFT pattern. (Copyright (2024) Wiley)

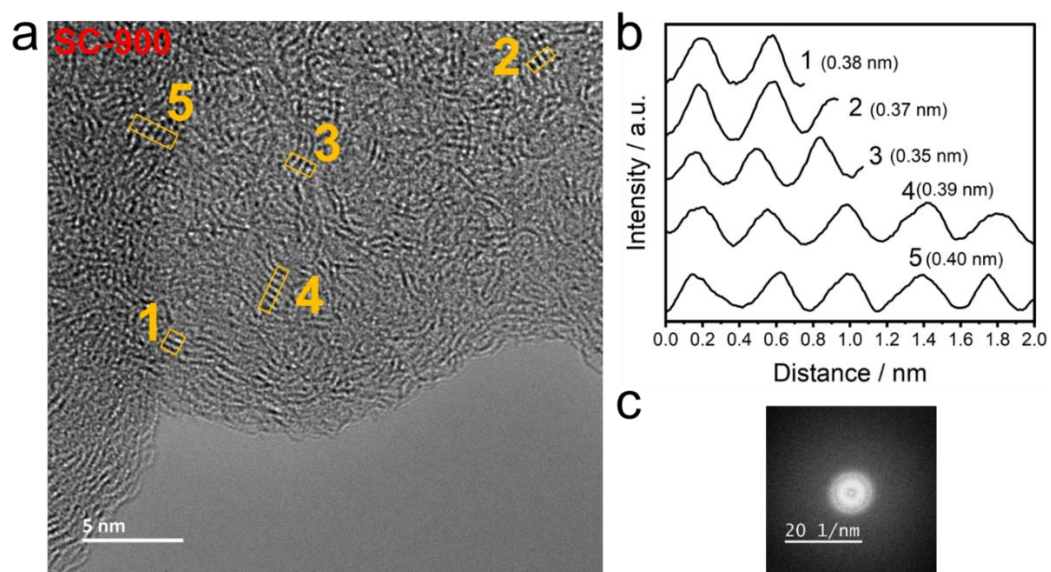


Figure A3.5. (a) HRTEM image of the SC-900; (b) image intensity periodicity; (c) FFT pattern. (Copyright (2024) Wiley)

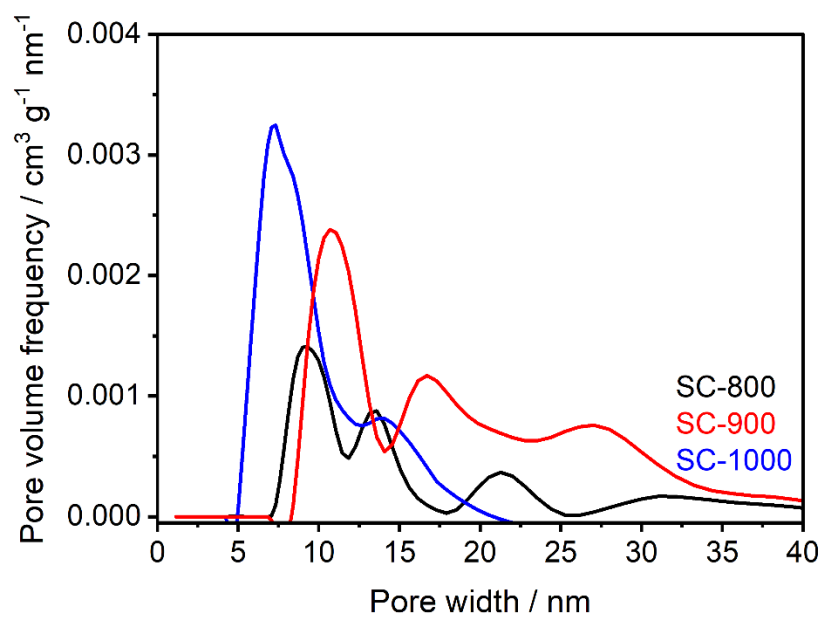


Figure A3.6. PSD from N_2 sorption measurements. (Copyright (2024) Wiley)

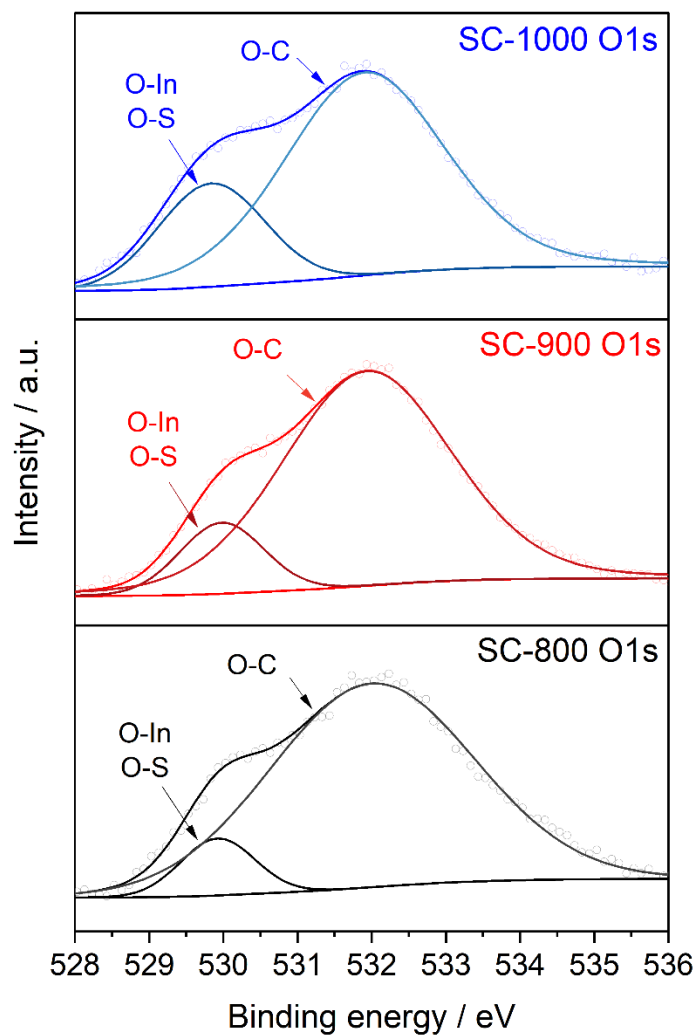


Figure A3.7. XPS spectra of materials display a pair of robust peaks in the O1s core level. (Copyright (2024) Wiley)

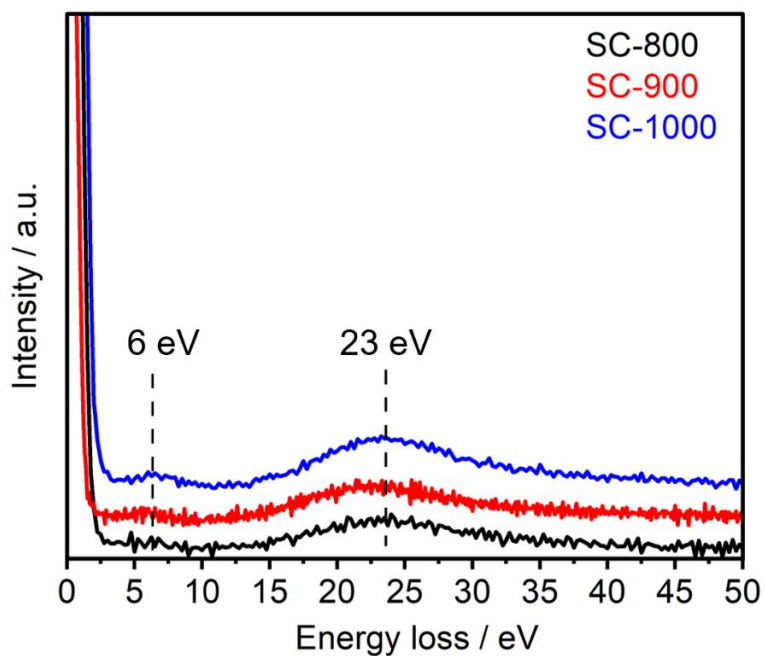


Figure A3.8. Low-loss EELS exhibit plasmon peaks, and the signals are normalized and vertically shifted to emphasize the differences between the materials being analyzed. (Copyright (2024) Wiley)

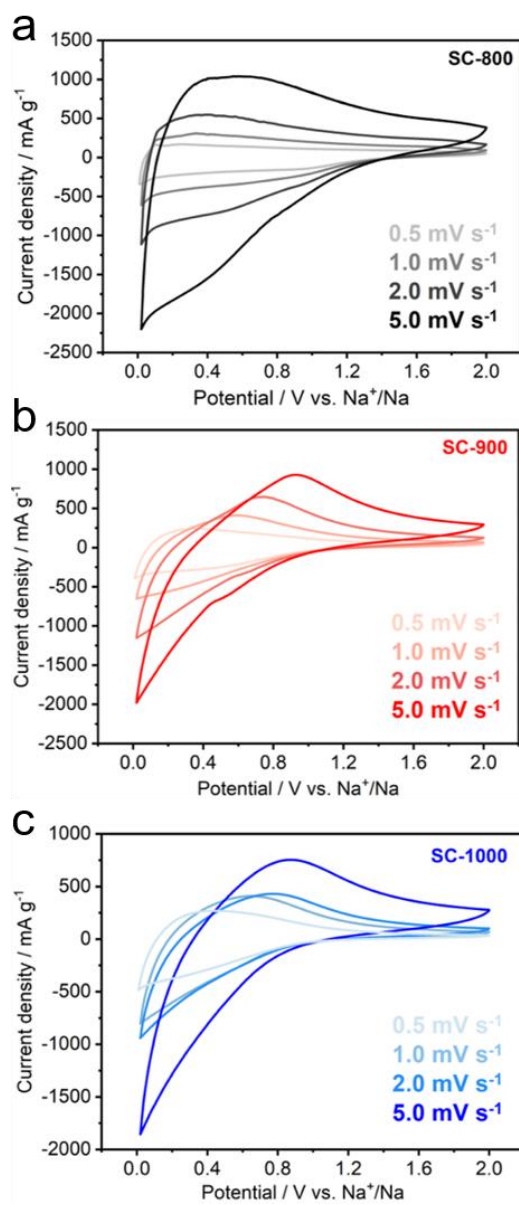


Figure A3.9. CV curves of (a) SC-800, (b) SC-900, and (c) SC-1000 at different scan rates. (Copyright (2024) Wiley)

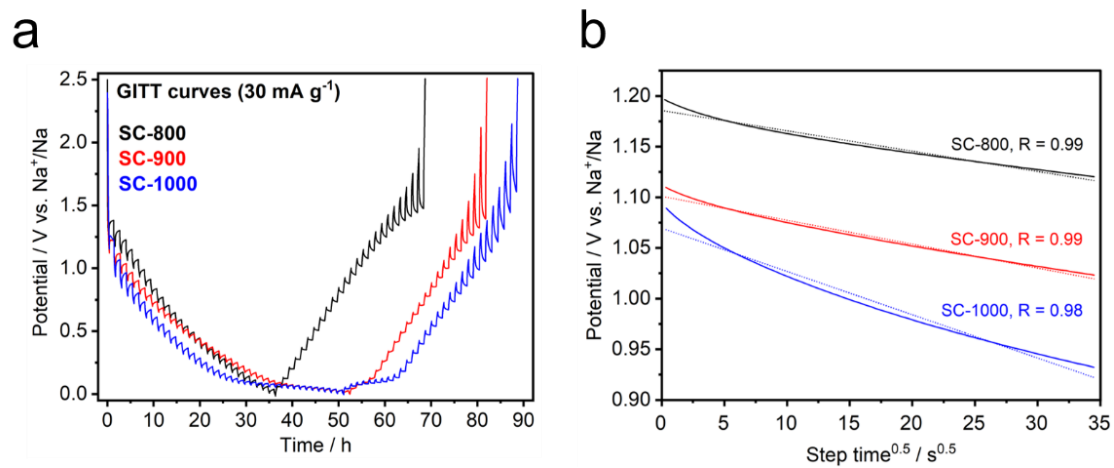


Figure A3.10. (a) GITT curves of the materials. (b) Linear relationships between V vs. $s^{0.5}$ from single step GITT curve. (Copyright (2024) Wiley)

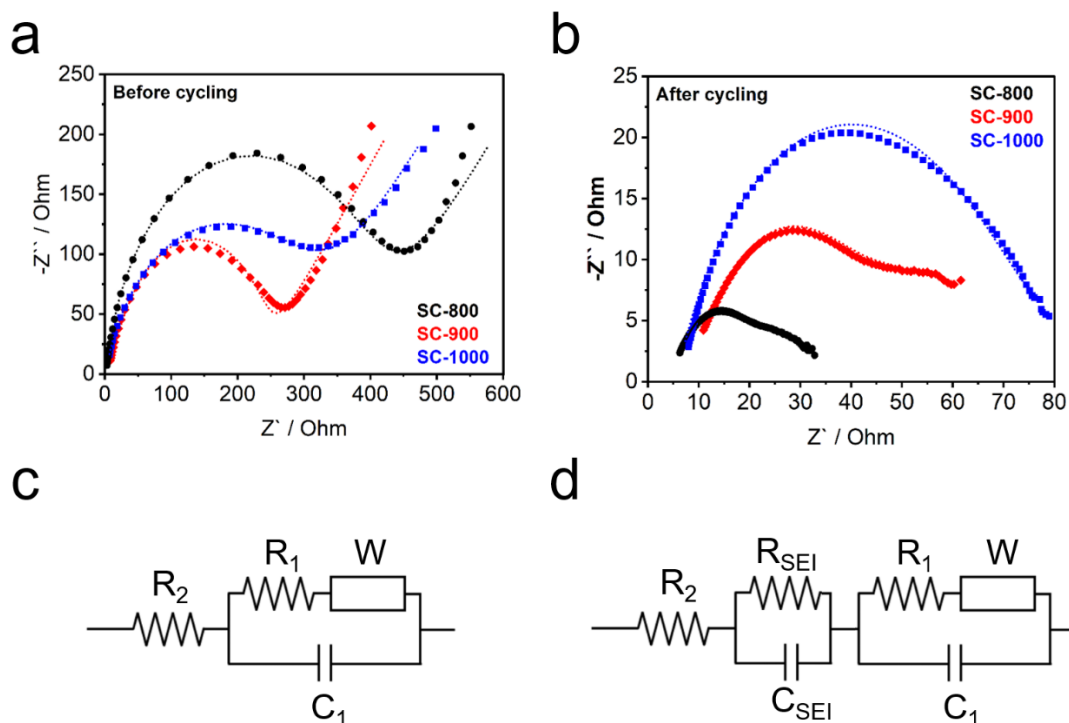


Figure A3.11. Nyquist plots and relative Randles circuit models of SC-800, SC-900, and SC-1000. Panel (a) and (b) represent the Nyquist plots before and after cycling (60 cycles), respectively. Panel (c) exhibits the Randles circuit model for precycling, where R_2 denotes the resistance associated with the electrolyte and electrode, whereas R_1 is linked to the charge transfer of the electrode. Panel (d) shows the Randles circuit model for after-cycling, revealing a second semi-circle that is associated with the growth of the passivation layer, represented by R_{SEI} . (Copyright (2024) Wiley)

Table A3.1. The internal, charge transfer, and SEI-related resistivity of the materials in Ohm cm^{-2} can be calculated from the Randles circuit model (electrode area, 1.13 cm^2).

Sample	Before cycling (Ohm cm^{-2})		After cycling (Ohm cm^{-2})		
	R_2	R_1	R_2	R_1	R_{SEI}
SC-800	2.0	354.8	4.8	14.9	4.2
SC-900	6.0	176.1	6.5	33.5	7.3
SC-1000	0.8	273.9	5.0	56.6	7.4

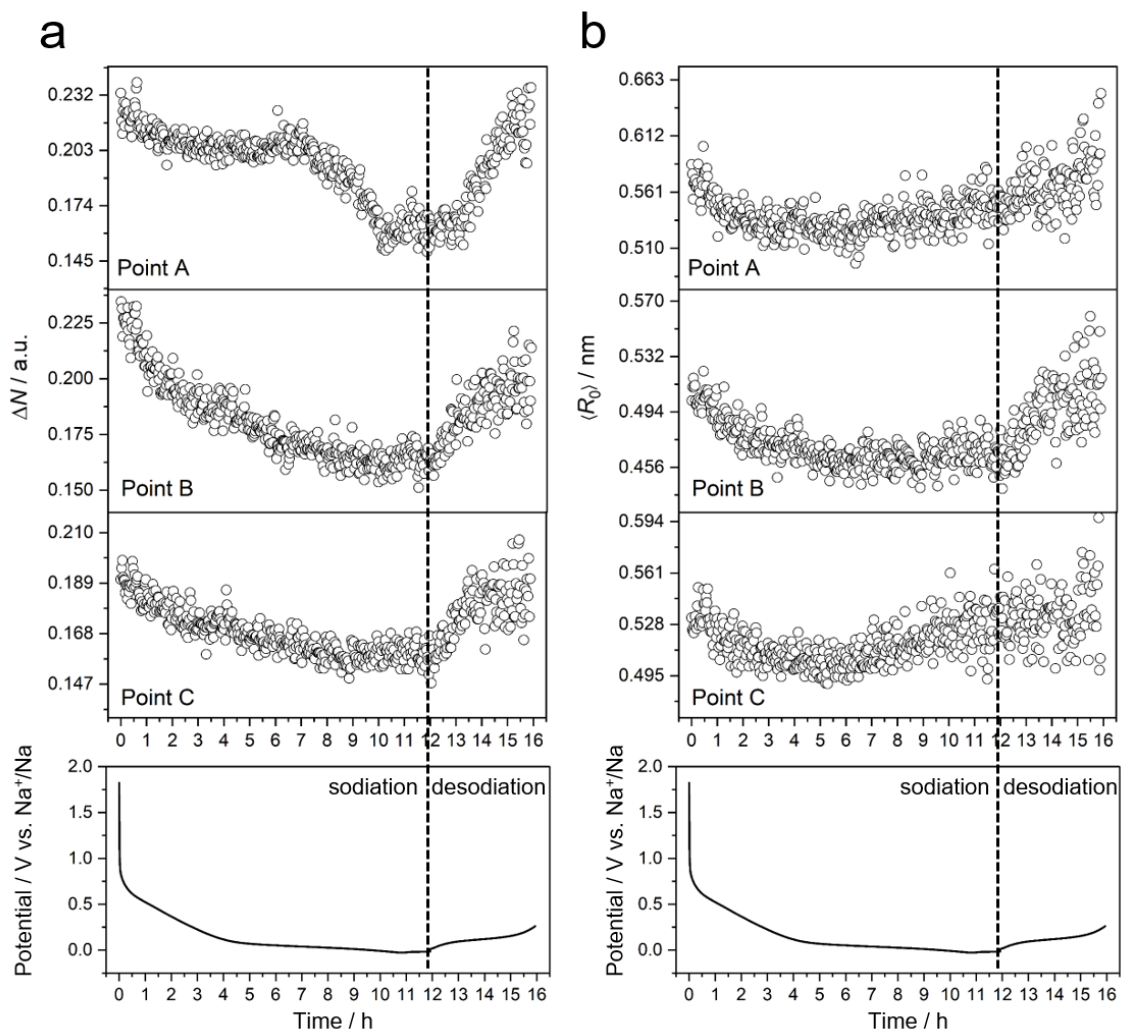


Figure A3.12. This figure illustrates the reproducibility of scattering profiles with respect to the parameters ΔN and $\langle R_0 \rangle$. Three random points, A, B, and C, are chosen from a set of 16 points for analysis. (Copyright (2024) Wiley)

A4. Supplementary information for Chapter 4

A4.1. Preparation of hard carbon from HMF

2 gr. of 5-(Hydroxymethyl)furfural (HMF, Sigma-Aldrich, >99%) is introduced into an alumina crucible. Subsequently, the crucible is placed within a tube furnace. The temperature of the furnace is gradually increased at a rate of 10°C per minute until it reaches 1100°C. The furnace is maintained at this temperature for about four hours while a nitrogen atmosphere is maintained. The resulting carbon material, denoted as HMF-1100, demonstrates a measured yield of approximately 30%. In order to establish a comparative analysis, hard carbons derived from D-(+)-Glucose (Sigma-Aldrich, >99%) and D-(-)-Fructose (Sigma-Aldrich, >99%) are also synthesized utilizing the same recipe.

A4.2. Electrode preparation and electrochemical characterizations

The electrodes are produced through a process that involves blending HMF-1100 with conductive carbon black (Super-P, Alfa Aesar) and polyvinylidene difluoride (PVDF, Kynar HSV-900) as the binding agent in a weight ratio of 80:15:5. The PVDF is dissolved in *N*-Methylpyrrolidone (NMP, Sigma-Aldrich). The mixture is applied onto an aluminum foil (30 μm) using an automatic doctor blade film applicator (mtv messtechnik, Germany) and dried under vacuum at 100°C overnight. The electrodes' final active material mass is approximately 1.2 mg cm^{-2} for all samples. Electrochemical measurements are conducted with three-electrode Swagelok-type cells on a Biologic MPG-2 instrument (France). The Swagelok-type cells are assembled in an argon-filled glovebox (MBRAUN, Germany) with an H_2O and O_2 content of less than 0.1 ppm. The electrolytes used are 1M NaPF_6 in ethylene carbonate (EC)/ethyl methyl carbonate (EMC) (3:7 in vol.) and 1M NaPF_6 in Diglyme (E-Lyte GmbH, 200 μL), with glass fibers (Whatman GF/C) serving as separators and a thin piece of sodium metal (99.5%, Sigma-Aldrich) as both counter and reference electrode. The commercial plant-based HC (Kuraray, Japan) is also used as a reference anode material for supportive measurements. The galvanostatic charge-discharge curves of the half-cells are collected in the potential range of 0-3.0 V (vs. Na^+/Na), with half-cells resting for six hours before the measurements. Cyclic voltammetry (CV) measurements are carried out at scan rates of 0.2, 0.5, 1.0, and 2.0 mV s^{-1} in the potential range of 0.01-2.5 V (vs. Na^+/Na). Electrochemical impedance spectroscopy (EIS) is performed with an AC perturbation of 10 mV in the frequency range of 0.1 Hz to 20 kHz. The galvanostatic intermittent titration technique (GITT) is used to calculate the sodium-ion diffusion coefficients, where current pulses (30 mA g^{-1}) are applied for 1200 s, and relaxation potentials are measured for 3600 s.

A4.3. Physico-chemical characterizations

The crystallinity of the samples is determined by X-ray diffraction (XRD) using the Rigaku SmartLab (Japan, Cu K α , 0.154 nm). Small-angle X-ray scattering (SAXS) measurements of carbon powders are performed using the Bruker Nanostar II (USA, Cu K α , 0.154 nm), with a sample-detector distance of 283 mm, and calibrated with silver behenate. Raman spectroscopy is obtained using the WITec Alpha 300 (Germany) confocal Raman microscope with an excitation wavelength of 532 nm. Physisorption measurements are performed on a Quantachrome Quadrasorb SI (Austria) at 273 K for CO₂, with samples degassed overnight before measurement. The density functional theory (DFT) method is employed to evaluate the pore size distribution (PSD) in the disordered carbons. Elemental analysis is conducted using the Elementar Vario EL III (Germany). Scanning Electron Microscopy (SEM) imaging is performed using the Zeiss LEO 1550-Gemini (Germany) system with acceleration voltages of 3, 5, and 10 kV, and the energy-dispersive X-ray (EDX) data are collected using an Oxford Instruments X-MAX (UK) 80 mm² detector. High-resolution transmission electron microscopy (HRTEM) is conducted using the double aberration-corrected Jeol JEM F200 (Japan) microscope.

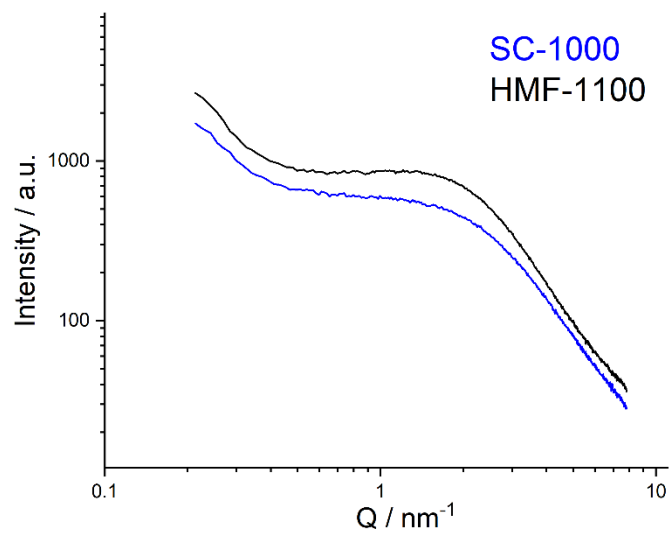


Figure A4.1. SAXS profiles of the HMF-1100 and SC-1000.

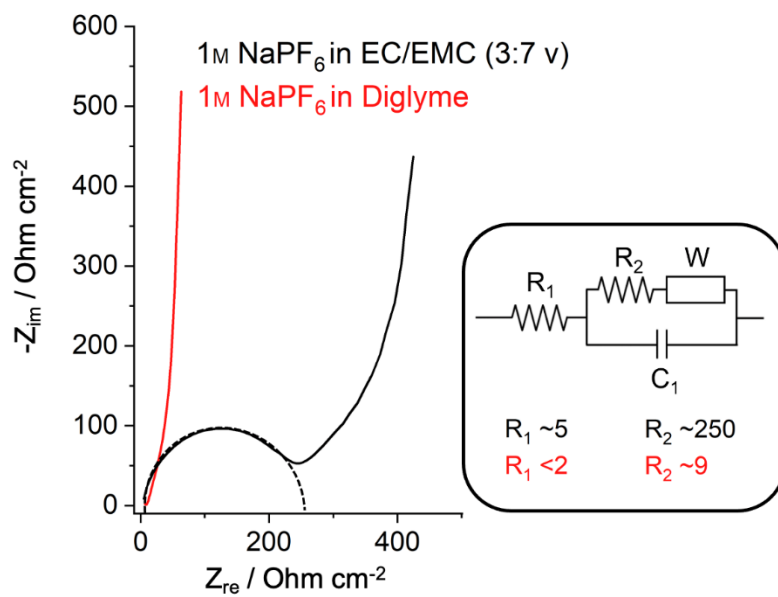


Figure A4.2. EIS measurements of the HMF-100 in different electrolytes. And associated Randle's circuit model for electrode resistance (R_1) and charge transfer resistance (R_2).

LIST OF PUBLICATIONS

As a first author

- ❖ E. O. Eren, C. Esen, E. Scoppola, Z. Song, E. Senokos, H. Zschiesche, D. Cruz, I. Lauer mann, N. V. Tarakina, B. Kumru, M. Antonietti, P. Giusto, Microporous sulfur-carbon materials with extended sodium storage window. *Adv. Sci.*, **2024**, In press.
- ❖ E. O. Eren, E. Senokos, Z. Song, E. B. Yilmaz, I. Shekova, B. Badamdorj, I. Lauer mann, N. V. Tarakina, M. Al-Naji, M. Antonietti, P. Giusto, Conformal carbon nitride thin film inter-active interphase heterojunction with sustainable carbon enhancing sodium storage performance. *J. Mater. Chem. A*, **2023**, 11 (3), 1439-1446.
- ❖ E.O. Eren, S. Özkar, Recent advances in heterogeneous catalysts for the effective electroreduction of carbon dioxide to carbon monoxide. *J. Power Sources*, **2021**, 506, 230215.
- ❖ E.O. Eren, N. Özkan, Y. Devrim, Polybenzimidazole-modified carbon nanotubes as a support material for platinum-based high-temperature proton exchange membrane fuel cell electrocatalysts. *Int. J. Hydrogen Energy*, **2021**, 46(57), 29556-29567.
- ❖ E.O. Eren, N. Özkan, Y. Devrim, Development of non-noble Co–N–C electrocatalyst for high-temperature proton exchange membrane fuel cells. *Int. J. Hydrogen Energy*, **2020**, 47(58), 33957–33967.
- ❖ E.O. Eren, N. Özkan, Y. Devrim, Preparation of polybenzimidazole/ZIF-8 and polybenzimidazole UiO-66 composite membranes with enhanced proton conductivity. *Int. J. Hydrogen Energy*, **2022**, 47(45), 19690–19701.

As a co-author

- ❖ Z. Song, J. Hou, E. Raguin, A. Pedersen, E. O. Eren, E. Senokos, N. V. Tarakina, P. Giusto, M. Antonietti, Triazine-based graphitic carbon nitride thin film as a homogeneous interphase for lithium storage, *ACS Nano*, **2024**, In press.
- ❖ G. N. B. Durmuş, E.O. Eren, Y. Devrim, C. Ö. Çolpan, N. Özkan, High-temperature electrochemical hydrogen separation from reformat gases using PBI/MOF composite membrane. *Int. J. Hydrogen Energy*, **2023**, 48(60), 23044-23054.

DECLARATION

Die vorliegende Dissertation entstand in dem Zeitraum zwischen März 2021 und Juni 2023 am Max-Planck-Institut für Kolloid- und Grenzflächenforschung unter Betreuung von Prof. Dr. Dr. h.c. Markus Antonietti.

Hiermit erkläre ich, dass die vorliegende Arbeit selbstständig angefertigt wurde und keine anderen als die angegebenen Hilfsmittel und Quelle verwendet wurden. Die Arbeit wurde bisher weder im Inland noch im Ausland in gleicher oder ähnlicher Form einer anderen Prüfungsbehörde vorgelegt. Es habe bisher keine früheren erfolglosen Promotionsverfahren stattgefunden.

The present work was carried out during the period between March 2021 and June 2023 at the Max Planck Institute of Colloids and Interfaces under the supervision of Prof. Dr. Dr. h.c. Markus Antonietti.

I declare that I have written this thesis on my own and used no other than the named aids and references. This thesis was not submitted to another examination board in this or other countries. There were no unsuccessful examination processes.

Potsdam, 01.08.2023

Ort, Datum

Name, Unterschrift